Title
Novel Scanning Strategies in x-Space Magnetic Particle Imaging for Improved Imaging Performance and Theranostic Applications

Author
Tay, Zhiwei

Publication Date
2018

Peer reviewed|Thesis/dissertation

Novel Scanning Strategies in x-Space Magnetic Particle Imaging for Improved Imaging Performance and Theranostic Applications

By

Zhi Wei Tay

A dissertation submitted in partial satisfaction of the

requirements for the degree of

Joint Doctor of Philosophy
with University of California, San Francisco

in

Bioengineering

in the

Graduate Division

of the

University of California, Berkeley

Committee in charge:

Professor Steven Conolly, Chair
Professor Chris Diederich
Professor Seth Sanders

Spring 2018

Novel Scanning Strategies in x-Space Magnetic Particle Imaging for Improved Imaging Performance and Theranostic Applications

Abstract

Novel Scanning Strategies in x-Space Magnetic Particle Imaging for Improved Imaging Performance and Theranostic Applications

by

Zhi Wei Tay

Joint Doctor of Philosophy
with University of California, San Francisco in Bioengineering

University of California, Berkeley

Professor Steven Conolly, Chair

Magnetic particle imaging (MPI) is an emerging tracer imaging modality. In this work, we develop novel scanning strategies to improve the imaging performance of MPI and explore novel methods to use MPI for theranostic applications. A major focus is inventing and exploring different scanning strategies to overcome or leverage the magnetic relaxation dynamics associated with the tracers used in MPI in order to find optimal tradeoffs in imaging performance metrics such as spatial resolution, SNR and scanning time. In the first part of this thesis, we perform an experimental study to underscore the significant discrepancy between experimental performance of large core size tracers and their theoretical performance, and demonstrate that this is a major obstacle to improving MPI performance. Subsequently, we describe the hardware design and construction of a frequency-flexible, arbitrary waveform tabletop scanner to enable the investigation of novel scanning strategies to help address this issue. Conventional MPI uses a single frequency excitation wave around 20 kHz. With this new device, we show the first study of non-sinusoidal excitation waveforms such as square, trapezoidal, triangle waveforms, and based on this, we design a novel approach to scanning and signal encoding in MPI which we name pulsed MPI (pMPI). Subsequently, we show that pMPI unlocks the potential of large core size nanoparticles by suppressing deleterious relaxation-based blurring effects. This enabled the first viable use of these nanoparticles which previously have been unusable in MPI. We also exploit the frequency-flexibility to optimize parameters for continuous (sinusoidal)

wave MPI and elucidate an optimal waveform that achieves both good resolution and SNR where previous work has suboptimally traded-off one for another. Lastly, we show how inter-particle interactions can be exploited to generate another new form of MPI which we term strongly-interacting MPI (SiMPI). Despite apparent issues with lack of LSI properties, we develop strategies to modify the tracers and scanning / reconstruction to enable LSI scanning with SiMPI in order to exploit its extraordinary characteristics of positive feedback (Schmidtt trigger) for over 10-fold improvement in both spatial resolution and SNR.

In the second part, we perform extensive preclinical studies as the first *in vivo* proof-of-concept of theranostic MPI. We show that MPI is unique as a theranostic modality due to many key advantages such as precise localization of therapy *in vivo*, an ability to receive measure and predict dosage based on image-guidance, and finally elucidate an approach for future development of real-time feedback for fine control and definite quantification of dosage. Our *in vivo* proof-of-concept results show robust localization of the heating dose deposited as well as therapeutic outcomes in a dual tumor xenograft rodent model. Importantly, we prove that this localization method can address one key challenge in Magnetic Hyperthermia, which is to avoid collateral damage to off-target organs such as the liver which tends to accumulate magnetic nanoparticles and is prone to unintended heat damage. Furthermore, we investigate aerosolized magnetic nanoparticles as a method to image the lungs with MPI. We demonstrate that MPI lung imaging with magnetic aerosol can be a viable alternative to clinically established radioaerosol procedures. This lays important groundwork for use of magnetic aerosols and MPI for safer lung imaging and lung theranostics in combination with the abovementioned work.

We believe a major takeaway from this work is that there remains numerous unexplored possibilities within MPI that can only be discovered by breaking away from conventional scanning strategies and current dogma behind the optimal MPI tracer. We believe exploration of these exotic scanning strategies and nanoparticle formulations will result in significant advances in our field.

Acknowledgements

My work at the Berkeley Imaging Systems Lab (BISL) has been an incredible journey of discovery and learning. I am grateful to the many people who have guided me along the way and have made this journal possible.

Specifically, I would like to say thank you to my wonderful girlfriend, Mika Tei. She has allowed me to share the joys of intellectual discovery and helped me through the most frustrating and trying times in the Ph.D. journal.

To all my close friends and family – thank you for your support. Special thanks to my parents for raising me and for always being so confident of and supportive of me.

To the wonderful group of people at BISL, I appreciate your kindness, collaboration and support through the years. I recall your patience and help when I was first learning the ropes and I could not have become so productive so quickly without your support. Special thanks to Daniel Hensley, without whom I would not be able to discuss and improve the many novel MPI scanning methods we came up with together. Your patience and openness to my many crazy ideas allowed me to be courageous in trying out many different ideas. In particular, Daniel and I have worked in close partnership to develop various aspects of pMPI and SiMPI, both of us making significant contributions to these two novel MPI methods. Special thanks as well to Patrick Goodwill for helping me in getting started up in the lab and always being a person to look up to. Special thanks to Bo Zheng for always being helpful and patient with my many hardware troubleshooting struggles as we developed a large amount of new hardware together - the arbitrary waveform relaxometer, the hyperthermia MPI setup, pMPI hardware and more. Furthermore, it has been a pleasure to work with BISL colleagues Paul Keselman, Ryan Orendorff, Elaine Yu, Prashant Chandrasekharan, and Xinyi Zhou.

A very special thanks to my mentor Steve Conolly. Steve you have provided an excellent work culture that is the foundation of such a warm, nurturing and friendly lab. You care deeply about your students and seek to help us in every way, and our many conversations about startup ideas always remind me to be creative and have the end-user in mind when designing or engineering any device.

"I am enough of the artist to draw freely upon my imagination. Imagination is more important than knowledge. Knowledge is limited. Imagination encircles the world."

Albert Einstein

Preface

Magnetic particle imaging has been developed extensively over the last decade. However, most of the research has been focused on designing and building the first generation of MPI hardware as well as conducting proof-of-concept implementations of various imaging only applications. Recent research has expanded to alternative applications of MPI such as magnetic steering and magnetic targeting. However, there has been limited exploration of the scanning strategies of MPI as well as the nanoparticles used. The first generation of MPI scanners and nanoparticles have quickly converged to using a stable and acceptable level of performance without much regard to further optimization of the available scanning parameters and nanoparticle designs.

In this work, we set out to comprehensively explore a relatively unexplored area of MPI - the scanning strategy which is mainly defined by the magnetic excitation waveform. We believe that the conventional thinking that a narrow set of sinusoidal waveforms as well as an optimal nanoparticle core size is a very limiting perspective: 1) the excitation waveform can be tailored to unlock the potential of non-standard nanoparticles 2) different excitation waveforms should be implemented in one scanner in order to enable flexibility in MPI applications, in particular the theranostics application where excitation can be changed to provide a ”heating mode” and ”imaging mode”.

In Chapter 1, we give a general introduction to MPI and outline its key advantages and niche in medical imaging, an explanation of its key principles for implementation, some of the applications work that MPI is well-suited for, and finally a listing of the open challenges in MPI. The subsequent dissertation is organized into two main parts: (1) exploration of different scanning strategies and nanoparticle formulations (2) proof-of-concept studies showing important preclinical applications of MPI with special focus on theranostics MPI where having differential scanning strategies for ”imaging mode” and ”therapy mode” is important.

In **Part I**, we investigate different novel strategies for MPI scanning.

In Chapter 2 we describe the design and construction of an arbitrary waveform and frequency flexible relaxometer. We term our device the Arbitrary Waveform Relaxometer (AWR). This device enables subsequent investigations into novel MPI scanning strategies.

In Chapter 3 we experimentally show the performance discrepancy between Langevin Theory and experimentally achieved MPI performance of

large core size tracers. This investigation provides critical insight into why successful MPI nanoparticles fall within a certain size range and provides the first experimental evidence of a ”relaxation wall” that is a barrier to improving MPI performance. Prior work has not experimentally investigated the effect of nanoparticle core size on MPI performance.

Chapter 4 focuses on the development of a novel scanning strategy we term pulsed MPI (pMPI) in order to break past the ”relaxation wall” and unlock the potential of large core size nanoparticles. This strategy is based on designing the excitation waveform to minimize blurring resulting from the sluggish large core nanoparticles. A section is also dedicated to exploring the requisite hardware changes required to perform this new scanning strategy on a rodent and eventually human scale.

In recognition of the hardware challenges of pMPI, Chapter 5 focuses on optimization of the MPI scanning waveform within constraints of a single tone excitation. Single tone excitation is significantly easier to implement especially in terms of power (due to resonant design) and also for feedthrough suppression on the receive end. However, prior work has not comprehensively optimized the effect of frequency and amplitude of sinusoidal excitation. Here, we detail the first comprehensive optimization exploiting the frequency-flexibility and high-throughput nature of the AWR and show how to optimally tailor sinusoidal excitation to both small size and large size nanoparticles.

Up to this point, MPI tracers have generally been understood as single core nanoparticles with a fixed magnetization behavior. The performance of multi-core particles have been modeled as an effective single core and there has been insufficient investigation into inter-particle interactions and how to optimally modify them to enhance MPI performance. Chapter 6 goes into our discovery of a new class of strongly-interacting nanoparticles and the development of a positive feedback theoretical model explaining their dramatically improved MPI performance with more than 10-fold improvements in both spatial resolution and SNR over conventional. We discuss strategies in nanoparticle formulation as well as reconstruction to address some of the non-LSI characteristics of these particles and develop essentially a new type of MPI that has scanning and reconstruction strategies tailored to the unique nanoparticle properties. We term this new type of MPI as strongly-interacting magnetic particle imaging (SiMPI).

We hope that one takeaway from Part 1 is a sense that MPI has many unexplored aspects and that MPI should not be understood as a single optimal scanning method. With the advent of pMPI and SiMPI, we hope that this opens up a new period of investigation in MPI pulse sequences

tailored to different nanoparticles and different applications of MPI, much in the same way pulse programming quickly became a very extensive region of research in MRI after its introduction.

In **Part II**, we focus on performing proof-of-concept studies on key applications of MPI, namely theranostics MPI for cancer as well as lung MPI. These applications are especially compelling as MPI's unique niche. Furthermore, the requirement that the "imaging mode" and "therapy mode" have different MPI scanning strategies allows us to build our application work off the knowledge created from the waveform optimization research in Part 1.

In Chapter 7, we show *in vivo* proof-of-concept of theranostic MPI where we show MPI image-guidance for MPI-gradient localization of magnetic hyperthermia. This application is compelling as one of MPI's unique niches because of the fact that MPI's imaging mechanism closely matches the heating mechanism behind magnetic hyperthermia. This provides an especially robust basis for quantification of heating dose and also implies that the MPI hardware and scanning enabling imaging resolution improvements can immediately be recycled to provide precise localization of heat deposition. In our study, we show robust image-guided localization of heat *in vivo* and show, critically, that thermal damage and therapy of xenograft tumors is localized to only our targeted region. This has important implications in addressing a major obstacle to clinical translation of magnetic hyperthermia, which is to precisely localize heating and avoid collateral damage to healthy organs. Furthermore, the same localization concept can be extended to localize actuation of drug release nanocarriers and other biomechanical stimuli for a variety of other applications.

In Chapter 8, we show *in vivo* proof-of-concept that MPI can track inhaled aerosol as a radiation-free alternative to clinical nuclear medicine (radioaerosol) methods for tracking inhaled therapeutics as well as clinical tests such as the pulmonary radioaerosol mucociliary clearance (PRMC) tests. This application is compelling as one of MPI's unique niches because of lung imaging is difficult for many other modalities and since the lung is one of the more sensitive organs to radiation damage, a radiation-free alternative to the nuclear medicine clinical standard is certainly safer and desirable. In our study, we show that (1) MPI can replicate the performance of nuclear medicine in evaluating the delivery efficiency of different aerosol delivery methods, (2) MPI can track biodistribution and quantify delivery of model therapeutics such as doxorubicin and ICG, (3) MPI is well-suited for timecourse imaging to measure mucociliary clearance and thus serve as a radiation-free alternative to the clinical PRMC test.

We believe this work lays essential groundwork and proof-of-concept for whole new families of MPI approaches (pMPI and SiMPI). The applications work provide critical *in vivo* proof-of-concept of MPI's clinical potential and is the first step towards bringing MPI closer to benefiting human patients.

Zhi Wei Tay
Berkeley, CA
Apr 27, 2018

Contents

Abstract 1

Acknowledgements i

Preface iii

1 Introduction and Background 1
- 1.1 Medical Imaging . . . 1
  - 1.1.1 Anatomical Imaging Techniques . . . 1
  - 1.1.2 Functional Imaging Techniques . . . 3
- 1.2 LSI Imaging Systems and LSI Analysis . . . 4
- 1.3 Magnetic Particle Imaging . . . 5
  - 1.3.1 Basic Principles . . . 6
  - 1.3.2 Imaging Metrics of MPI . . . 6
  - 1.3.3 Key Characteristics of MPI . . . 9
- 1.4 MPI Applications . . . 10
  - 1.4.1 Angiography and Perfusion Imaging . . . 10
  - 1.4.2 Cell Tracking . . . 11
  - 1.4.3 Lung Imaging . . . 11
  - 1.4.4 Cancer and Theranostics . . . 12
- 1.5 Open Challenges in MPI . . . 13
- 1.6 Path Towards Clinical Implementation of MPI . . . 13
  - 1.6.1 Specific absorption rate (SAR) Limits . . . 13
  - 1.6.2 Maintaining Good Performance while Scaling up to Human Size . . . 14

I Novel Scanning Strategies to Improve MPI Imaging Performance 17

2 Design and Construction of the Arbitrary Waveform Relaxometer 20
- 2.1 Attribution . . . 20
- 2.2 Introduction . . . 20

2.3 Background . . . 21
2.4 Design and Methods . . . 23
2.4.1 Working Principles of Magnetic Particle Imagers . . . 23
2.4.2 Design of the Arbitrary Waveform Spectrometer / Relaxometer . . . 25
2.4.3 Nanoparticle Tracers . . . 28
2.4.4 Animal Procedures . . . 29
2.4.5 MPI Tracer Characterization using Sinusoidal Drive Waveform . . . 29
2.4.6 Novel Implementation of Arbitrary Drive Waveforms 31
2.5 Results . . . 32
2.5.1 Validation of the Accuracy of the Arbitrary Waveform Relaxometer . . . 32
2.5.2 Limit of Detection of 20 ng Fe . . . 33
2.5.3 Automated High-Throughput Processing . . . 33
2.5.4 Arbitrary Drive Waveforms . . . 35
2.5.5 Wideband Feedthrough Attenuation . . . 35
2.5.6 First Experimental Verification of x-space DC Recovery Algorithm . . . 35
2.5.7 First Experimental Demonstration of Triangular Wave Drive Waveform . . . 37
2.6 Discussion . . . 37
2.7 Conclusion . . . 39
2.8 Acknowledgments . . . 40

3 The Relaxation Wall: Experimental Limits to Improving MPI Spatial Resolution by Increasing Nanoparticle Core size 41
3.1 Attribution . . . 41
3.2 Introduction . . . 41
3.3 Background . . . 42
3.3.1 Spatial Resolution in Magnetic Particle Imaging . . . 42
3.4 Materials and Methods . . . 45
3.4.1 Magnetic Nanoparticles . . . 45
3.4.2 Magnetic Particle Relaxometer Experiments . . . 46
3.4.3 Magnetic Particle Imager Experiments . . . 47
3.4.4 Calculation of Langevin Spatial resolution curves . . . 48
3.5 Results . . . 48
3.5.1 Spatial resolution stops improving beyond 25 nm core diameter . . . 48
3.5.2 Verification of trend with MPI imaging results . . . 51

3.5.3 Magnetic relaxation limits improvement of spatial resolution . . . 51
3.5.4 Strategies for mitigation of magnetic relaxation do not work fully . . . 53
3.6 Discussion . . . 55
3.7 Conclusions . . . 58
3.8 Acknowledgments . . . 59

4 Pulsed Magnetic Particle Imaging in 1D **60**
4.1 Attribution . . . 60
4.2 Introduction . . . 60
4.3 Background . . . 62
4.4 The Pulsed MPI Approach . . . 64
4.4.1 Magnetic Relaxation . . . 64
4.4.2 Square Wave Signal and Imaging Equations . . . 65
4.4.3 Resolution . . . 71
4.4.4 SNR and Bandwidth . . . 72
4.5 Experimental Methods . . . 73
4.5.1 Implementing pMPI Excitation Pulse Sequences . . . 73
4.5.2 Nanoparticles . . . 76
4.5.3 Testing of 1D pMPI . . . 76
4.5.4 Testing of 2D pMPI . . . 79
4.5.5 pMPI reconstruction . . . 81
4.6 Experimental Results . . . 82
4.6.1 Comparison of Pulsed MPI and Standard MPI . . . 82
4.6.2 Effect of Drive Frequency (Wait Time) on Pulsed MPI . 83
4.6.3 Effect of Drive Amplitude (Step Size) on Pulsed MPI . 84
4.6.4 Effect of Rise Time (Sharpness of Square Wave) on Pulsed MPI . . . 84
4.6.5 Harmonic Analysis and Resolution-Bandwidth Relationship . . . 85
4.7 Discussion . . . 86
4.7.1 Magnetostimulation Safety Considerations . . . 86
4.7.2 SAR Safety Considerations . . . 88
4.7.3 Receive Chain Modifications for pMPI . . . 90
4.7.4 Maximum Theoretical Resolution Gain with pMPI . . . 92
4.8 Implementation on the 3D preclinical scanner - Preliminary Data . . . 93
4.9 Conclusion . . . 97
4.10 Acknowledgments . . . 97

5 Optimal Drive Waveforms for High Resolution and High Sensitivity MPI **100**
5.1 Attribution . . . 100
5.2 Introduction . . . 100
5.3 Background . . . 101
5.4 Resolution and Sensitivity in MPI . . . 103
5.4.1 Spatial Resolution in X-space Reconstruction . . . 105
5.4.2 Signal-to-Noise Ratio (SNR) in Magnetic Particle Imaging . . . 106
5.4.3 Incomplete Magnetization Significantly Decreases Sensitivity and Further Worsens Blurring . . . 108
5.4.4 Multi-objective Optimization for Both Spatial Resolution and Sensitivity Creates Optima Due To Opposing Trends . . . 114
5.4.5 Loss of Higher Harmonic Information is Partially Compensated by Decreasing Receive Bandwidth . . . 114
5.4.6 Magnetic Slew Rate Alone Cannot Predict MPI Performance . . . 116
5.4.7 Similar Conclusions are expected for System Matrix Reconstruction . . . 116
5.5 Methods . . . 117
5.5.1 Berkeley 3D MPI Scanner . . . 117
5.5.2 Berkeley Arbitrary Waveform Relaxometer . . . 118
5.5.3 Magnetic Nanoparticles . . . 118
5.5.4 Calculation of Resolution . . . 120
5.5.5 Calculation of Sensitivity . . . 120
5.5.6 Calculation of Phase Lag . . . 120
5.6 Results . . . 120
5.6.1 Small Core SPIOs: Low Amplitude and Low Frequency both improve resolution at the cost of sensitivity 120
5.6.2 Large Core SPIOs have higher sensitivity to frequency than small core SPIOs . . . 123
5.6.3 Small Core SPIOs: Low amplitude (2.5 – 5.0 mT) and high frequency (80 – 160 kHz) approach is optimal . . . 124
5.6.4 Large Core SPIOs: Low amplitude ($\sim$ 8 mT) and medium frequency ($\sim$ 6 kHz) approach is optimal . . . 125
5.6.5 Expanded MPI resolution model matches well with measured data . . . 126
5.6.6 Small Particles: Proof of global bound on error . . . 127

5.6.7 Large Particles: LAHF failure due to incomplete magnetization of the SPIO at pFOVs centered at or near the SPIO particle . . . 127
5.7 Discussion . . . 127
5.7.1 Low Amplitude, High Frequency Drive Waveforms are Optimal . . . 127
5.7.2 Magnetostimulation and SAR Safety Considerations . 129
5.7.3 Relationship to System Matrix Reconstruction 129
5.7.4 Implementation on Preclinical Scanners and Path to Clinical Application . . . 130
5.8 Conclusion . . . 131
5.9 Acknowledgments . . . 131

6 Strongly Interacting Magnetic Particle Imaging (SiMPI) 132
6.1 Introduction . . . 132
6.2 Theory . . . 133
6.2.1 Conventional Magnetic Particle Imaging vs Strongly Interacting Magnetic Particle Imaging . . . 133
6.2.2 Requirements for SiMPI, Challenges and Initial Solutions . . . 134
6.2.3 Model for Inter-Particle Magnetic Interactions when Particles are in Close Proximity . . . 135
6.2.4 Theoretical Conditions Necessary for Local Clustering of Nanoparticles . . . 137
6.2.5 Close Proximity and Stable Relative Geometry of Particles Generates Large Local Fields Requiring A Coercive External Field to Overcome . . . 138
6.2.6 Implications and Re-modeling as a Positive Feedback System - Schmidtt Trigger . . . 141
6.2.7 Analysis involving SPIO relaxation . . . 144
6.2.8 Parameters governing SiMPI . . . 145
6.2.9 Recommended Modifications to X-Space Scanning . . 147
6.2.10 Recommended Modifications to X-Space Reconstruction . . . 147
6.3 Experimental Results . . . 149
6.3.1 Drive Amplitude Needs to Be Higher Than Coercive Threshold . . . 149
6.3.2 Lower Drive Frequencies Decrease The Coercive Threshold . . . 149
6.3.3 Requirement of A Minimum Particle Concentration . . 149

6.3.4 2D Imaging . . . 151
6.3.5 TEM images prove chain formation . . . 151
6.3.6 Prepolarizing pulse can help ensure SiMPI behavior by giving time for chain formation . . . 151
6.3.7 SiMPI behavior requires nanoparticle chain to have its axis parallel to RF excitation axis . . . 154
6.4 Conclusion . . . 154
6.5 Acknowledgment . . . 155

II Theranostics and Therapeutic Tracking Applications of MPI 156

7 Magnetic Particle Imaging Theranostics: *In Vivo* Proof-of-concept using Gradient Fields For Arbitrary Localization of Therapy 158
7.1 Attribution . . . 158
7.2 Introduction . . . 158
7.3 Background . . . 159
Limitations of Current Magnetic Hyperthermia Methods . . . 164
Signal Localization in MPI can also be used to Localize Heating in Magnetic Hyperthermia . . . 164
7.4 Methods . . . 169
7.5 Superparamagnetic Iron Oxide Nanoparticles (SPIONs) . . . 169
7.5.1 SPION Synthesis . . . 169
7.5.2 SPION Surface Modification with PEGsilane . . . 169
7.5.3 SPION Characterization . . . 170
7.5.4 Dynamic Magnetization Response in Different Locations in the MPI Gradient . . . 171
7.6 Animal Procedures . . . 172
7.6.1 Development of Tumor Xenograft . . . 172
7.6.2 Animal Preparation for MPI-magnetic hyperthermia Procedure . . . 173
7.6.3 Histological Assessment . . . 174
7.6.4 Imaging and Magnetic Hyperthermia . . . 175
7.6.5 *In Vivo* Temperature Measurement . . . 176
7.6.6 Predictive Algorithm for Thermal Dose Planning . . . 176
7.7 Results and Discussion . . . 177
7.7.1 User-defined, Arbitrary Localization of Heating *In Vitro* 177
7.7.2 Image-guided, Arbitrary Localization of Heating *In Vivo* 178

7.7.3 Robustness of Dose Planning and Heat Localization *In Vivo* . . . 180
7.7.4 Predictive Algorithm for the *In Vivo* Distribution of Heating . . . 182
7.7.5 Luciferase Assay shows Localized Therapy *In Vivo* . . . 182
7.7.6 Histological Assessment Verifies Localization of Thermal Damage to Target Region Only . . . 183
7.7.7 Discussion . . . 184
Precision of Localization Linearly Improves with Gradient Strength . . . 184
Implementation of Real-time MPI-magnetic hyperthermia . . . 185
Real-time Temperature Feedback with MPI Thermometry . . . 186
SAR and Magnetostimulation Safety Considerations . . . 187
Path to Clinical Implementation . . . 188
7.8 Conclusions . . . 189
7.9 Acknowledgment . . . 190

8 In Vivo Tracking and Quantification of Inhaled Aerosol using Magnetic Particle Imaging towards Inhaled Therapeutic Monitoring 191
8.1 Attribution . . . 191
8.2 Introduction . . . 191
8.3 Background . . . 192
8.4 Methods . . . 196
8.4.1 Hardware . . . 196
8.4.2 Nanoparticles . . . 196
8.4.3 Ventilation Experimental Setup . . . 196
8.4.4 Animal Experimental Groups . . . 197
8.5 Results . . . 197
8.5.1 Evaluation of delivery efficiency . . . 197
8.5.2 Tracking and quantification of inhaled therapeutics . . . 199
8.5.3 Timecourse MPI to monitor clearance rates from the lung . . . 200
8.6 Discussion . . . 202
8.7 Conclusions . . . 203
8.8 Acknowledgments . . . 203

Bibliography 204

List of Figures

1.1 Comparison of anatomic vs. functional images. Anatomic imaging (left) can provide visualization of internal bodily structures such as the skeleton in this case but is unable to clearly visualize the tumor or liver. Functional or molecular imaging techniques (center), which often use contrast agents or tracers specifically target certain organs such as the liver in the case or may have antibodies that target the tumor. This provides clear visualization of pathology, such as the tumor, and specific organs, such as the liver, which may not be highlighted or clearly visualized in the anatomic image. However, functional images typically do not have visualization of the entire body. The image here is a result of intratumoral injection of MPI tracer, but similar results are expected from a tumor targeted contrast agent. (Right) Overlay of the anatomic image and the functional image allows a spatial reference for the highlighted pathology/organ, and helps the physician accurately locate the tumor for diagnosis and treatment. These images are part of the data from the 'MPI theranostics' study in Chapter 7. 2

1.2 Spatial localization of the MPI signal via Langevin physics. (left) Typical raster trajectory of the field-free-point or field-free-line used in MPI imaging (right) How the non-linear ensemble magnetization response of the magnetic nanoparticles can be translated by the inductive receive coils into a Langevin point-spread-function (red plot) centered at the precise location of the nanoparticles. This forms the basis of signal localization in x-space MPI. 7

1.3 (Top) Approximate equation for MPI limit of detection in terms of grams of Fe (assuming SNR = 1). Assumptions are coil noise dominance, and that the $-H_{\text{sat}}$ to $+H_{\text{sat}}$ region of the M-H curve approximates the SPIO peak response. Variables are NF = noise factor of preamplifier; ρ = density of SPIO; k_B = Boltzmann constant; T,R,B = temperature, resistance and sensitivity (T/A) of the receive coil respectively; H_{sat} and M_{sat} refers to the applied field needed to reach M_{sat} and the 90% saturation magnetization value respectively; BW = final receive bandwidth after digital windowing; ω is the MPI excitation frequency in radians and H_{ampl} is the MPI excitation amplitude. (Bottom) Approximate equation for MPI spatial resolution. Variables are μ_0 = vacuum permeability; k is a proportionality constant modulating the blurring effect of magnetic relaxation; τ is the (Debeye) magnetization time constant of the SPIO that causes delays in magnetization leading to relaxation-induced blurring; G is the MPI gradient strength in Tesla/meter. 14

2.1 A representative MPI image showing visualization of the biodistribution of magnetic particle labeled stem cells after they were injected into the tail vein of a rat. This image demonstrates the high sensitivity and contrast of MPI and the capability to perform long-term, *in vivo* biodistribution studies without the exponential loss of signal typical in nuclear medicine studies. However, as shown by the image of the lung, liver and spleen in Figure 1, the spatial resolution of MPI is limited and a prime target for improvement. We demonstrate in this paper that the AWR enables high-throughput drive waveform optimization for better MPI resolution. 21

2.2 **a.** To-scale Solidworks™ drawing of our arbitrary waveform relaxometer (AWR) accurately representing the actual physical device. It comprises a miniature drive coil (Tx) with a low net inductance of 2.5 μH, two receive coils in gradiometric configuration (Rx1, Rx2), and a biasing coil to extend the applied field range. The gradiometer-shimming mechanism shifts Rx2 relative to Tx2 in increments of 22 μm to fine-tune the Tx2-Rx2 coupling to match that of Tx1-Rx1, minimizing net Tx-Rx coupling. The concept of cancellation amplitude adjustment for inductive decoupling is not new (Goodwill et al., 2011a; Graeser et al., 2013), but our novel mechanical implementation allows for in-bore facile precision "spatial-shimming" allowing for simultaneous feedback of gradiometer performance during adjustment. The in-bore adjustment is important because removing, adjusting then reinserting the receive coil into the MPS setup may incur placement error and we have shown in Figure 2.3a that even tens of microns can affect gradiometer performance. Prior hardware using inductive decoupling (Goodwill et al., 2011a; Behrends, Graeser, and Buzug, 2015; Graeser et al., 2013) do not allow in-bore adjustment. **b.** Prior sinusoidal MPI spectrometers/relaxometers requires capacitors in the transmit chain to reduce reactive power and/or a band-stop filter (BSF) in the receive chain to reduce feedthrough. However, arbitrary drive waveforms precludes the use of tuned circuit elements. Instead, the AWR's novel untuned design relies on a very low coil inductance of 2.5 μH coupled with a high coil efficiency of 1.06 mT/ampere for transmit power handling. An improved gradiometer is used for broadband feedthrough attenuation on the receive. 24

2.3 **a.** Demonstration of improved gradiometer performance via fine "spatial-shimming" the cancellation coil (Rx2) location relative to the transmit coil (Tx). This has the effect of fine adjusting the Rx2-to-Tx coupling factor for improved inductive decoupling reaching up to -67 dB (10 kHz). **b.** The gradiometer is capable of wideband feedthrough attenuation which is essential in the AWR's wideband excitation context. **c.** The very low drive coil inductance of $2.5\ \mu$H coupled with high coil efficiency of 1.06 mT/ampere enables high field amplitudes across an unprecedented DC – 400 kHz despite not using resonant circuits for reactive power handling. When compared to the safe scanning limits for a human (Saritas et al., 2013a), we see that the AWR's unprecedented drive-field flexibility allows for testing of almost any drive waveform that would be used in a safe human scanning context, enabling comprehensive drive waveform optimization. In contrast, conventional VSM (Mészáros, 2007) and AC Susceptometry (Chen, 2004) are unable to cover the MPI-relevant parameter space. We limit our device design to below 400 kHz because near zero-field, the delay from magnetic relaxation is expected to be $> 2\ \mu$s (Deissler, Wu, and Martens, 2014), surpassing a half-period of the drive waveform and causing poor resolution. 26

2.4 **a.** High-throughput magnetic particle spectrometry is enabled by the lack of tuned circuit elements in the AWR. In a single automated acquisition (500 ms total time), we discretely sample 100 drive frequencies from 16 kHz to 115 kHz at 25 mT. The data from this single acquisition is shown as a stack plot of Resovist fourier spectra for 100 discrete drive frequencies (after background correction and removal of out-of-band signal). **b.** Analysis of the spectra in Fig. 3a shows the expected steeper slope of harmonic decay with higher drive frequencies. This matches the findings of prior work (Kuhlmann et al., 2015). A steeper slope implies a poorer modulation transfer function response leading to poorer spatial resolution. **c.** From a single automated acquisition, 33 unique sets of drive parameters were tested (n = 3) on 125 μg of Resovist. The optimal drive waveform (gray arrow) with best resolution is with a 17 kHz, 8.5 mT amplitude waveform. The FWHM resolution (mm) assumes a 3.5 T/m gradient. **d.** The same dataset from part c is plotted for both spatial resolution and signal strength. While the lowest amplitude and frequency (gray arrow) gives the best spatial resolution, this is at a significant cost of almost 10-fold lower signal strength which has implications for MPI sensitivity. The high-throughput and denser sampling of frequency uniquely allows the AWR to better optimize for both spatial resolution and signal strength. This reveals the 100 kHz, 8.5 mT amplitude waveform (black arrow) which shows almost as good resolution improvement as the gray arrow while having *no loss in signal strength*, therefore having better overall MPI performance than the waveform obtained from simply optimizing for one parameter. 28

2.5 **a.** Reconstructed PSF from data obtained by the AWR compares well to the theoretical expected PSF with magnetic relaxation of a first-order Debye model. The calculation used the same value of τ (2.3 μs) validated in prior work (Croft et al., 2016). **b.** The FWHM of reconstructed PSFs from AWR data (n = 3) closely matches ($R^2 = 0.972$) actual spatial resolution measured from MPI scanner *images* (3.5 T/m gradient 23 kHz)Croft et al., 2016. This shows the AWR can accurately predict for MPI tracer *imaging* performance. **c.**The AWR signal (PSF peak amplitude) is linear with Resovist iron mass with sensitivity of 13.1 μV/μg for sine wave and 8.3 μV/μg for triangular wave before amplification. Three experimental repeats were taken per data point (n = 3). We estimate the detection limit (SNR = 1) to be $\sim$ 20 ng and $\sim$ 30 ng respectively with 6.25 s total acquisition time (25 averages). The AWR is thus a sensitive and quantitative sensor for magnetic particles. The difference in sensitivity between sine and triangular wave is due to differences in the waveform velocity at the zero-crossing point. 32

2.6 **a.** Experimental data showing the linear chirp from $1 - 400$ kHz produced by the AWR (spectrogram obtained from short-time Fourier Transform of AWR current monitor trace). Although the maximum slew rate of the power amplifier limits chirp amplitude beyond 200 kHz, this amplitude never falls below the SAR safety limits (Fig. 2.3) even at 400 kHz, thus covering the entire *safe* parameter space. **b.** The AWR is capable of arbitrary waveforms as shown by this composite waveform made up of arbitrary waveform parts: (1) triangular wave (2) linear chirp (3) ramp and (4) composite waveform made up by direct addition of 3 sine waves of equal amplitude but different frequencies (5, 7 and 12 kHz). The drive waveform shape is validated by the internal current monitor of the AE Techron 7224. 34

2.7 **a.** First experimental validation of the DC recovery algorithm used in x-space reconstruction. DC recovery of the discarded first harmonic information produces a nearly identical PSF to a PSF where the analog received signal at the first harmonic was retained. **b.** Experimentally reconstructed PSF for Triangle and Sine drive wave showing only minor differences. This is expected because a triangle and sine wave are similar, and the x-space theory in 1D shows that various trajectories with similar spatial sampling densities should yield the same reconstructed results, excepting variable impacts of magnetic relaxation. Importantly, this shows the triangle wave maintains conventional MPI performance while obviating velocity compensation which is a major reconstruction step. 36

3.1 (a) Calculated Langevin curves (using eqn. 3) for different nanoparticle core sizes. The shape of the curves show a dramatic change with nanoparticle core size due to the cubic relationship between nanoparticle core size and saturation field. (b) Calculated MPI steady-state PSFs show a dramatic narrowing with increased core size. This is in contrast to the strategy of increasing MPI gradient strength shown in (c) where only a linear improvement of the PSF width is observed with increases in gradient strength. Because spatial encoding in MPI is a linear function of the magnetic field gradient, conversion between x-axis units of applied field (mT/μ_0) and distance (mm) is done simply by dividing by the gradient strength ($T/\mu_0 m$). 44

3.2 MPI hardware. (a) Magnetic Particle Relaxometer used to obtain point spread functions of SPIOs to measure the full-width-at-half-maximum spatial resolution. (b) Magnetic Particle Imager used to obtain images of SPIOs to validate the measurements of the relaxometer as well as provide visual images of the differences in spatial resolution as core size changes. (c) MPI obtains an image by rastering the field-free-point across the field of view as shown in the figure. The field-free-point can be considered a sensitive detection point in 3D space. In x-space reconstruction, the time-domain received voltage signal is gridded to the instantaneous location of the field-free-point to make an image. 47

3.3 (a) Table of nanoparticle properties and experimental measurements (b) TEM of Imagion Biosystems PrecisionMRX® SPIOs showing narrow size variation and constant spherical shape as evidenced by the isoperimetric quotients (thus implying constant shape anisotropy). A representative M vs. H plot ($M_{sat} = 0.551T/\mu_0$) is also plotted. See Section 2.1 for more details. 49
3.4 (a) Experimental 1D point spread functions of Imagion Biosystems PrecisionMRX®SPIOs measured on the Magnetic Particle Relaxometer at 20.25 kHz and 20 mT/μ_0. The PSF narrows as core size increases from 18 to 24 nm, but stops narrowing and starts widening beyond 25 nm. This shift is concomitant with a marked displacement of the PSF in the direction of the scan which is similar to that seen in prior work on MPI relaxation (Croft et al., 2016; Croft, Goodwill, and Conolly, 2012), suggesting a marked increase in magnetic relaxation processes. Data is represented by the smooth solid lines while the markers are just a visual guide to differentiate the curves. (b) Comparison of the experimentally achieved spatial resolution (n = 3) with the predicted spatial resolution from the Langevin model shows an increasing disparity with increasing core size after 24.4 nm. 50
3.5 Magnetic Particle Imager scan of point sources of different SPIO core sizes. The experimental imaging results have good agreement with the Relaxometer measurements, showing the same trend of optimal resolution with 24.4 nm SPIOs. 52

3.6 Trace of the *experimental* time-domain MPI signal. Data is represented by the smooth solid lines while the markers are just a visual guide to differentiate the curves. **a)** From 18.5 nm to 24.4 nm, a slight increase in delay is seen in the peaks of each subsequent trace. This is indicative of magnetic relaxation processes increasing in magnitude. However, this effect is surpassed by the narrowing of the signal peak by Langevin physics. Thus, the narrowest peak and best resolution is seen at 24.4 nm. **b)** From 24.4 nm to 32.1 nm however, magnetic relaxation increases dramatically as evidenced by the very large time delay (phase delay of almost 40 degrees) of the 27.4 nm and 32.1 nm signal peaks. This is indicative of strong magnetic relaxation processes that clearly dominate the expected peak narrowing from Langevin physics. As a result, the signal peak is spread out and worse resolution occurs when going from 24.4 nm to 32.1 nm. 53

3.7 Low amplitude and low frequency drive waveform strategies have been shown in prior work to reduce the negative impact of magnetic relaxation (Kuhlmann et al., 2015; Croft et al., 2016). Both approaches were tested separately (n=3, error bars are small and within the shape markers). (a) In the low amplitude approach, frequency is held constant at 20.25 kHz and amplitudes of 20.0, 4.0 and 0.5 mT/μ_0 were used. (b) The low frequency approach keeps amplitude constant at 20 mT/μ_0 while frequencies of 20.25, 2.0 and 0.4 kHz were used. While both strategies help achieve better spatial resolution overall, spatial resolution still stops improving after a certain core size. These strategies are unable to fully mitigate the negative impact of the large amount of relaxation seen by larger core size particles and are unable to achieve the cubic spatial resolution improvements predicted by the Langevin model. 54

4.1 MPI rasters a sensitive point (the zero-field point or field-free-point) across a 3D volume to form an image of the superparamagnetic iron oxide nanoparticles (SPIONs) present. Here, a sensitive line setup is shown, which obtains projection images through the sample like CT. MPI's inductive signal is generated by the SPION magnetization response to the fast raster from the sinusoidal drive waveform. In this work, we show that by changing the sinusoid drive waveform to a pulsed waveform (square wave), we are able to significantly improve MPI resolution by circumventing relaxation-induced blurring. 61
4.2 Although the Langevin Theory for MPI predicts cubic resolution improvement with increasing nanoparticle core size, in practice, resolution gains with increasing core size are limited. Furthermore, beyond the optimal 24.4 nm core size, spatial resolution is observed to worsen rather than improve with core size. This is demonstrated by the stark difference between the measured image resolution and the Langevin theoretical resolution of a point source phantom of 27.4 nm SPIOs (ImagionBio, PrecisionMRX^{TM}). This disparity can be attributed to relaxation-induced blurring, where blurring worsens with larger core sizes due to their increasingly sluggish response to the excitation drive field. In this work, we propose a new drive waveform to circumvent this problem and achieve the ideal (Langevin) spatial resolution. Because this will unlock the potential of cubic improvement of resolution with core size, significant improvements in resolution are expected, especially for large core size SPIOs such as the 27.4 nm. 63
4.3 Pulsed encoding in MPI acquisition. We can describe an MPI acquisition scheme in terms of a choice of fast excitation encoding waveform, FOV sampling strategy, and reconstruction formulation. pMPI replaces the canonical sinusoidal fast excitation encoding with pulsed waveforms. Subsequent aspects of the acquisition scheme such as FOV sampling strategy and reconstruction method may be chosen as desired as long as the pMPI constraints described herein are respected. For example, slew rates involved in FOV sampling cannot compromise steady-state induction. pMPI may be incorporated into the x-space or system matrix paradigm. 66

4.4 The strategy behind pulsed MPI explained in 1D. The key principle is a step-and-wait net excitation trajectory (formed from a square wave fast excitation + ramp for large FOV sampling). The wait time must be long enough to allow any delays in magnetization to reach steady-state (the Langevin magnetization). Instead of making the raw received signal (instantaneous dM/dt) as our MPI signal, we integrate the raw signal over the wait time to obtain a ΔM for that step. This measured ΔM is exactly the change in magnetization of the ideal Langevin M-H curve as we step from x to x+Δx. As a result, **pulsed MPI is a discrete sampling of the ideal Langevin dM/dH curve**. With finer and finer sampling (Δx $\rightarrow$ 0), the 1D image approaches the continuous, ideal dM/dt plot. Because for waiting for steady-state at each step, pulsed MPI completely circumvents any relaxation-induced blurring that is commonly observed in conventional MPI due to the "no-wait" sinusoidal trajectory. This conventional blurring can be understood as delays in magnetization resulting in the dM/dt signal being spread across a larger distance in x. 67

4.5 Hardware implementation of pulsed MPI. (a) Arbitrary waveform relaxometer (AWR) used in this work. The AWR is a benchtop MPI system with a frequency-flexible drive coil that can provide square wave excitation and configurable with or without field-free line (FFL) producing magnets. (b) Pre-emphasized voltage waveforms sent to linear amplifiers in voltage-control mode are used to create square waveforms in the drive coil. (c) Experimental data from implementation of pulsed MPI. Current monitor measurements (AE Techron 7224) verified that a square drive field of 1 mT amplitude was achieved with a rise time of $\sim$ 2 μs. The measured MPI raw inductive signal from the magnetization response of a 32 nm core SPIO is shown in blue. The characteristic peak-and-decay signal expected from SPIOs with significant magnetic relaxation is observed in the raw data. Integrating the blue plot over the wait time of a step gives the net SPIO magnetization change (red plot). We observe that magnetization reaches steady-state as desired (magnetization plateaus) . . . 74

4.6 Square Wave data acquisition and image reconstruction using the AWR. (a) In acquisition, a slowly-varying bias field allows us to sample a large magnetic FOV over time with the faster square wave excitation (Tx). This pulse sequence leads to a dense sampling of points in the applied magnetic field domain. (b) In a simple x-space reconstruction, we can integrate the signal for each square wave half-period and grid this value to the mean field location. In a final step we can interpolate the gridded data onto a desired 1D pixel grid. The result is a 1D square wave PSF. If we divide the applied field by an assumed gradient, we arrive at a 1D spatial PSF. 77
4.7 (a) Feedthrough in pulsed MPI manifests as a narrow spike coinciding with the pulse. The experimentally measured feedthrough is greatly attenuated by fine gradiometer tuning as described in prior work (Tay et al., 2016). (b) Without removal of the feedthrough before reconstruction, this results in a benign, fixed DC value added to each pixel (variation is due to noise). (c) Reconstructed point-spread-functions from experimental data (27nm SPIO, 2.5 kHz 0.5 mT step). Unlike standard MPI that requires a more complex partial FOV DC recovery algorithm (Lu et al., 2013), the feedthrough in pulsed MPI reconstructs as a benign global DC offset that can be removed using robust *a priori* assumptions of zero signal at the edges of the imaging FOV (simple subtraction of the DC value across the entire FOV). Thus, time-domain baseline subtraction is not required in pMPI. 78

4.8 Experimental comparison between conventional sinusoidal MPI at 25 kHz, 20 mT with square wave pulsed MPI at 2.5 kHz, 1 mT step size.
(a) Standard MPI data shows that resolution stops improving after 24.4 nm (PSF widens) and significant relaxation-induced blurring occurs. (b) Pulsed MPI data for the same range of magnetic core sizes show constant improvement of resolution (PSF narrows) with core size as predicted by the Langevin Model (c) Comparison of experimental sinusoidal MPI FWHM resolution, square wave pMPI FWHM resolution, and theoretical Langevin prediction as a function of tracer core size. Note the inflection point in sinusoidal MPI resolution such that larger tracers have worse resolution while square wave pMPI allows us to realize with Langevin theoretical prediction (solid red line) with a small offset (dashed red line) due to the contribution of the excitation amplitude to FWHM. 79

4.9 Square wave MPI experimental results as a function of hold time (half-period of square wave) – the length of time at a constant applied field to establish steady-state – and comparison with theory for 27.4 nm particles. Step size of 1 mT was used. (a) 1D point spread function with varying hold time. Resolution and signal strength worsens with shorter hold times as the SPIO is unable to reach steady-state magnetization, resulting in relaxation-induced blurring and lower peak signal. This is in part due to long relaxation times at low field strength leading to the observed 'peak depression' of the PSF for shorter hold times. (b) Spatial resolution improves and approaches that of the Langevin Model as hold time increases $\rightarrow 3\tau$. The results match our theory that pMPI relies critically on waiting long enough for SPIO magnetization to reach steady-state. (c) pMPI peak signal worsens with shorter hold time as the SPIO does not have enough time to reach steady-state magnetization, resulting in a lower measured ΔM than $M_{\mathrm{steady-state}}$. The results show that long hold times are desirable, but this must be traded-off against longer scan times. Because the resolution and signal strength plots asymptotically approach Langevin values, the optimal hold time should correspond to the start of the asymptotic approach to steady-state because diminishing returns occur thereafter. A good rule-of-thumb for hold time should be 2 – 5 τ where τ is the Debeye relaxation time constant. 80

4.10 pMPI experimental results as a function of excitation step size and comparison with theory for 27.4 nm particles. 2.5 kHz square wave with varying amplitudes was used. (a) pMPI 1D point spread functions show higher signal but worse resolution with increasing step size. (b) Spatial resolution improves and approaches that of the Langevin Model as step size decreases $\rightarrow 0$. The results match our theory that pMPI is a discrete sampling of the ideal Langevin dM/dH curve, and the large step sizes equate coarse discrete sampling that incurs a rect convolution blurring effect. (c) pMPI peak signal improves with increasing excitation step size as a larger portion of the SPIO's M-H magnetization curve is covered per step. This implies a spatial resolution and SNR trade-off in optimizing the excitation step size. 82

4.11 Experimental analysis of the effect of rise time using trapezoidal excitation waveforms with different rise times. The hold time was kept at 1 ms with a fixed step size of 10 mT. (a) Experimental excitation waveforms measured by the current monitor (AE Techron 7224) and converted to magnetic field by calibration with a gaussmeter probe (Lakeshore Instruments™). (b) Measured 1D point spread functions show that varying rise time has very little effect on the pMPI performance. (c) Relative SNR changes very little with increasing rise time. The slight change is from longer square wave period (fixed flat top hold time + varying rise time) because the same signal is spread over a larger amount of time. The results here show that perfect square waves are not required to realize the benefits of pMPI, thus the hardware criteria for pMPI is much less stringent as compared to hardware required for near perfect square waves. 85
4.12 Experimental signal and resolution bandwidth relationships. (a) PSFs constructed from the same dataset but using only 1 (red) or 15 (blue) harmonics of the fundamental square wave excitation frequency in reconstruction. (b) PSF FWHM resolution as a function of the number of harmonics used in reconstruction. (c) Peak signal intensity as a function of the number of harmonics used in reconstruction. Unlike in continuous wave MPI, resolution worsens with increasing receive bandwidth and the inclusion of more harmonics. Peak signal does, however, improve. This peculiar resolution-bandwidth relationship is a function of the temporo-spatial encoding of the signal due to the field dependence of the tracer magnetic relaxation. Tracer located far from the FFR is characterized by fast relaxation due to the high field conditions while tracer near the FFR is characterized by slower relaxation. Faster relaxation processes equate to higher harmonic information in the Fourier domain. In this manner, signal from tracer near the FFR center is relatively concentrated at the lower harmonics. 88

4.13 Safety limits for pMPI waveforms. Because optimal pMPI waveforms use low amplitudes < 5 mTpp and there is negligible effect of rise time on pMPI performance, optimized pMPI waveforms are safe. In general, any pMPI waveform that is designed to improve resolution better than Resovist™ will require < 10 mTpp step size and will be safe as long as the rise time is > 2 μs. 90

4.14 The resolution gains of pulsed MPI are verified using two-line phantoms with various distances between the lines. The AWR used to obtain 1D point-spread-functions with pulsed waveforms was outfitted with permanent magnets to generate a field-free-line scanner geometry similar to the preclinical scanner described in Fig. 7.3 and in (Yu et al., 2017b). Because the same drive coil is maintained as in the AWR, this small-bore scanner is able to implement pulsed waveforms in a 2D FFL-based scanning trajectory (Fig. 7.3). Projection MPI images are taken of the phantom using standard MPI and pulsed MPI. The results show that while standard MPI has significant blurring and is unable to resolve the two lines, pulsed MPI produces sharp images that are able to resolve the two lines. In addition, the measured images are very similar to the simulated images where the phantom used was 2D convolved with the ideal Langevin point spread function. This verifies that pulsed MPI approaches the spatial resolution predicted by the ideal Langevin model in 2D. The results also show a significant resolution gain of almost 8-fold when comparing standard MPI (27.4 nm SPIO) and pulsed MPI (27.4 nm SPIO). This clearly illustrates the large amount of relaxation-induced blurring present that was circumvented by the pulsed MPI strategy. Comparing to a typical Ferucarbotran tracer (vivotrax™) commonly used in MPI studies, pulsed MPI still maintains a 5-fold improvement in resolution over standard MPI, achieving 0.6 mm resolution with a 3.5 T/m gradient. This is almost two-fold better better than the 1D scans predict because leaving out a bit more of very initial part of the signal in each half-period improves resolution beyond that achievable by the Langevin model because it removes the ”long tails” of the Langevin that cause blur because the signal from these regions completes very quickly and is found almost completely in the initial part. By using only the later parts, we restrict our signal to only the parts of the Langevin curve that have the largest magnetization change *i.e.* when the FFP is just above the SPIO. We name this strategy *tau-weighting* as it exploits the difference in magnetization time constant between the Langevin tails and the Langevin middle section, and we show that it improves resolution at the cost of some SNR. Using a 7 T/m gradient would give a very good 0.3 mm resolution *before deconvolution*. Further resolution improvements could be achieved with deconvolution by trading-off SNR. 91

4.15 Block Diagram showing the overall hardware changes necessary to implement pMPI on the existing 3D scanner 93
4.16 Linear circuit design for implementation of pMPI 94
4.17 Switched circuit design for implementation of pMPI. The switches turn the circuit into a resonant one when rapid transitions of current through the inductor transmit is required and switch it back to a linear voltage-powered circuit when piecewise constant pMPI phases are required. 95
4.18 Receive circuit design for pMPI to deal with the different (pulsed) nature of direct feedthrough. 96
4.19 Preliminary results from testing of a variable gain amplifier (VGA) on the receive chain to mitigate pMPI direct feedthrough. 98

5.1 MPI rasters a sensitive point (the zero-field point or field-free-point) across a 3D volume to form an image of the superparamagnetic iron oxide nanoparticles (SPIONs) present. MPI's inductive signal is generated by the SPION magnetization response to the fast raster from the sinusoidal drive waveform. While the MPI imaging performance is highly dependent on the drive waveform, a comprehensive optimization of the drive waveform has yet to be done. In this work, we optimize the MPI drive waveform across an unprecedented 0.4 kHz - 416 kHz and 0.5 mT - 40 mT for *both* improved resolution and high sensitivity. 102

5.2 Because MPI uses inductive pick-up coils to receive the signal, the MPI signal is proportional to drive waveform slew rate by Faraday's law of induction. Thus, high sensitivity MPI needs high slew rate drive waveforms. However, as slew rate increases, we do not observe a perfectly linear gain in sensitivity as the ensemble magnetization of the SPIOs cannot keep up with the drive waveform slew rate due to (ensemble) magnetic relaxation. Magnetic relaxation at high drive waveform slew rates leads to blurring of the MPI signal because of delays in SPIO magnetization. As a result, low slew rates are favorable for resolution, but high slew rates are better for SNR and sensitivity. Because either frequency or amplitude can be adjusted to change the slew rate, and because the trends are not linear, this manifests as a non-trivial optimization problem to find the best trade-off for *both* good resolution and high sensitivity MPI. 103

5.3 Our model for MPI resolution expands upon the model from Croft et al. 2016 (Croft et al., 2016) describing the effect of amplitude on MPI resolution. The base model describes the measured resolution as a weighted sum of the base resolution at steady-state (no blurring) and a blurring term that is dependent on the measured SPIO phase lag and drive amplitude applied. To demonstrate drive amplitude blurring, we show experimental point-spread-function of IB 32.1 nm SPIOs with the same drive frequency but varying drive amplitudes. The PSFs are normalized to a peak value set by Faraday's law. The results show increased blurring with higher drive amplitudes with negligible deviation of peak intensity from Faraday's Law. To expand upon the base model, we found that another effect should be added which we term 'peak depression'. This effect is necessary to account for the high frequency sensitivity of larger core size SPIOs as well as for the much larger range of frequencies used in this study. In essence, peak depression highlights the inability of the SPIO to magnetize fully when the applied field drive excursion is centered at the SPIO. This is because the SPIO has to rotate its magnetic moment through the largest angle here (180^o) and rotation is incomplete when the SPIO cannot keep up with the applied drive field. However, when the drive excursion is off-center, the SPIO does not have to rotate through a full 180^o and it keeps up with the drive field better, therefore obtaining magnetization changes closer to that predicted by the ideal Langevin. The result is less-than-expected ΔM / less signal at the peak while full ΔM / normal signal at the sides, giving a point spread function that only has its peak depressed. This effectively worsens resolution as the originally intense signal peak now blends into the background blur. To demonstrate peak depression, we show experimental point-spread-function of IB 32.1 nm SPIOs with the same drive amplitude but varying drive frequency. PSFs are normalized to a peak value set by Faraday's law. The results show that an increasing inability to keep up with higher frequencies, as shown by a deviation of the peak signal from Faraday's law. For instance, doubling the frequency should achieve twice the MPI signal peak, but the measured peak is less than twice. 109

5.4 (A) Photo of the modified Arbitrary Waveform Relaxometer described in previous work (Tay et al., Sci Rep, 2016). While the drive coils are kept the same, permanent magnets and selection field coils were installed to create a small bore scanner. (B) Because the same drive coil and drive transmit chain was maintained, the modified device retains all the frequency flexibility and drive waveform versatility of the previous device. This plot shows that our modified device is able to test a wide variety of drive waveforms. The capability region covers almost all drive waveforms possible within the human safety limits and encompasses a much larger range than the drive waveforms investigated in prior MPI literature. Therefore, using this device, we are able to do a comprehensive optimization of the drive waveform (within safety limits) for MPI by investigating an unprecedented 0.4 – 416 kHz and 0.5 – 40 mT amplitude. (C) We verify the accuracy of resolution measurements from our modified device by comparing the measurements to that obtained from our preclinical scanner that has been extensively validated in prior work. The results show that the resolution measurements are in good agreement. 113

5.5 Experimental results from varying the drive amplitude over a wide range (0.5 mT – 40 mT) while keeping drive frequency constant at 20 kHz. A wide range of nanoparticles with a spread of magnetic core sizes were used (Vivotrax, 18.5 nm, 24.4 nm, 27.4 nm, 32.1 nm ImagionBio SPIOs). (a) Resolution generally improves with lower amplitudes and the trend is similar to the main conclusion reported by Croft et al. (Croft et al., 2016). A near 2-fold improvement was observed for Vivotrax. (b) Similar trends in resolution was observed across the wide range of nanoparticles used. Some SPIOs, such as IB 27.4 nm and IB 32.1 nm had larger improvements in resolution as drive amplitude was lowered. Solid lines represent our theoretical resolution model. (c) However, sensitivity decreases essentially linearly with amplitude, showing that sensitivity has to be sacrificed for resolution improvement for the low amplitude strategy. Solid lines represent the linear trend expected from the SPIO's dM/dt response to the decreased slew rate drive field by Faraday's law. Interestingly, while there is less phase lag (relaxation) at higher amplitudes, the resolution is worse. As Croft et al. 2016 has shown, this is because the blurring effect is amplified for larger amplitudes because the MPI trajectory is correspondingly wider and the blur is mapped onto a larger region in space. This amplification effect outweighs the drop in relaxation. 115

5.6 Experimental results from varying the drive frequency over a wide range (0.5 kHz – 416 kHz) while keeping drive amplitude constant at 20 mT. A wide range of nanoparticles with a spread of magnetic core sizes were used (Vivotrax, 18.5 nm, 24.4 nm, 27.4 nm, 32.1 nm ImagionBio SPIOs). (a) Resolution generally improves with lower frequencies and significant phase lag, where the MPI signal lags behind the applied field resulting in an offset point spread function, is observable at high frequencies of 96 kHz. A 4-fold improvement was observed for IB 32.1 nm going from 96 kHz to 0.5 kHz, showing the high sensitivity of large core SPIOs to drive frequency. (b) For smaller core SPIOs (Vivotrax™, IB 18.5 nm and IB 24.4 nm), the results show that resolution improves with lower frequencies, although to a lesser extent than an equal change in amplitude as shown in Fig. 5.5. (c) Sensitivity decreases with frequency, showing that low frequency approaches also sacrifice sensitivity for resolution improvement. However, unlike the varying amplitude strategy in Fig. 5.5, at high frequencies sensitivity no longer varies linearly with drive frequency and falls away from Faraday's law. This is because the SPIO rotation cannot keep up with the high drive frequency. This is confirmed by phase lag measurements that show significant increases in phase lag with increasing frequency. This increased phase lag also leads to worse resolution from relaxation-induced blurring. 117

5.7 Experimental Results when using the low amplitude high frequency strategy. This strategy is found to be optimal for small core size SPIOs (Vivotrax™, IB 18.5 nm, IB 24.4 nm). Optimal points are marked with asterisks and the optimal overall region considering all the 3 SPIOs is shaded in grey. For small SPIOs, decreasing amplitude and adapting the frequency to maintain a fixed slew rate of 400 T/s shows that resolution improves with lower amplitudes. Importantly, we see that sensitivity stays approximately the same following Faraday's law, achieving our objective of improving resolution without trading-off sensitivity. Beyond 160 kHz, the sensitivity starts to drop and depart from Faraday's law while resolution shows no improvement. Thus, we obtain an optimum parameter set of 2.5 mT – 5 mT and 160 kHz – 80 kHz. Similar trends were observed for the IB 18.5 nm and IB 24.4 nm with a very similar optimum parameter set. The phase delay plot shows that the optimal performance parameter set does not correlate well with the minimal phase delay point, again emphasizing that relaxation alone (phase delay) is a limited metric for MPI performance. In contrast, for large core size SPIOs (IB 27.4 nm and IB 32.1 nm), decreasing amplitude and adapting the frequency to maintain a fixed slew rate of 400 T/s shows a significant drop in sensitivity everywhere across the tested parameter range. Unlike the smaller cores, we are unable to maintain high sensitivity by using high frequency to offset lower amplitudes. This is because the larger nanoparticles simply cannot rotate well when pushed to a faster frequency. Thus, the low amplitude high frequency strategy does not work as well for large core sizes. 119

5.8 Experimental Results when using the low frequency high amplitude strategy. This strategy is found to be optimal for large core size SPIOs (IB 27.4 nm and IB 32.1 nm). Optimal points are marked with asterisks and the optimal overall region considering all the 3 SPIOs is shaded in grey. Because large core sizes have increased sensitivity to frequency, we need to use lower frequencies. However, we cannot use too high an amplitude as well, thus we change the slew rate to be lower at 50 T/s so as to enable low frequency and medium amplitudes. We observe that this experimental series works much better for larger cores, obtaining an optimum parameter set of 10 mT and 5 kHz. We see that sensitivity remains constant up to approximately 5 kHz beyond which large deviations from Faraday's law is observed. 5 kHz is optimal because spatial resolution is the best for 32.1 nm and very close to the best resolution for 27.4 nm. For small core sizes, decreasing frequency and adapting the amplitude to maintain a fixed slew rate of 50 T/s does not improve resolution with decreasing frequency, underscoring that for small core sizes, amplitude is the dominant factor affecting resolution. Because sensitivity is lower than the low amplitude high frequency approach while resolution did not improve, this low frequency high amplitude series is not optimal for small cores. This shows that for small core sizes, it is better to ensure small drive amplitudes and to have a very high frequency even if the net slew rate is high. 121

5.9 Experimental data from Fig 4 - 7 are plotted on resolution vs. sensitivity axes for easier visualization of optimal points. (a) Low amplitude only experimental series. The plot shows that decreasing the amplitude while keeping frequency constant results in monotonically better resolution but worse sensitivity. There are no optimal points observed and resolution is traded off for sensitivity. (b) Low frequency only experimental series. Similar to (a), no optimal points are observed and low frequency incurs a significant trading off of sensitivity for resolution. 123

5.10 Experimental data from Fig 4 - 7 are plotted on resolution vs. sensitivity axes for easier visualization of optimal points. (a) In contrast with Fig 5.9, with a low amplitude high frequency approach (constant slew rate of 400 T/s), we observe optimal points in the plot. The steep valley like plots show that good resolution can be obtained at a optimal parameter set with a minimal cost in sensitivity. Comparison to the 20 kHz 20 mT standard MPI parameters (*Typ marking) show that resolution is significantly improved and sensitivity is negligibly affected. (b) Similar results are observed for large SPIOs when a constant slew rate of 50 T/s is used. Optimal points are easily identified on the plots. Very significant improvements in resolution are achieved over standard MPI but at some cost of sensitivity. This is mainly because a 8-fold lower slew rate is used to match the large core SPIOs that are not normally suitable for conventional MPI at 400 T/s slew rate. 126
5.11 MPI drive waveform safety limits in a human compared to the optimal drive waveforms obtained in this study. The experimental series of the low amplitude high frequency series and the high amplitude low frequency series are plotted, showing that the optimal points obtained for the respective series fall within safety limits. The optima for low amplitude high frequency are on the edge of the safety limits but because this is in the SAR dominated regime and the 4 W/kg SAR limit used for this plot is relatively conservative, the optimal waveform here can be considered to be safe. 128

6.1 Initial results showing the large improvement in resolution with SiMPI over the best-performing nanoparticles with conventional MPI. This is the main motivation of developing SiMPI. 133
6.2 (left) Illustration showing the advantage of an emulsion formulation for SiMPI. This is just an initial solution, more robust solutions could potentially have the oil phase replaced by some other (more solid) matrix that sets the nanoparticles in a chain geometry. (middle) Photo of the shaken emulsion (right) Light microscopy (100x) of the shaken emulsion. 135

6.3 (left) Block diagram showing how our model works. (right) Since the Langevin function saturates and the delay term introduces hysteresis, we see that the output will be very similar to a Schmidtt trigger, whose symbol is an op-amp with a hysteresis curve. Essentially, like a Schmidtt trigger which is a comparator circuit with hysteresis that occurs via applying positive feedback to the noninverting input of the amplifier, our SiMPI multi-particle structure applies positive feedback via local fields to the input field felt by each particle, and the Langevin behavior of each individual particle gives us the saturator component. Experimental data showing hysteresis curves from our nanoparticles that look a lot like Schmidtt trigger input-output curves is shown in Fig. 6.8 142
6.4 Simulated plots of the input u(t) and output p(t) of the SiMPI positive feedback system without considering relaxation delays (the Debeye relaxation term is ignored). 100 recursions of the positive feedback loops was used in the simulation. As β approaches and goes above unity, the SiMPI system becomes more and more like a step function, which promises near infinitely good SNR and spatial resolution for MPI in theory. In practice however, relaxation delays limit the number of recursions through the feedback loop and therefore limit the output of the positive feedback since scanning times must be realistic and cannot afford to "wait" forever for near infinite feedback loops to occur. 144

6.5 Plots of the input u(t) and output p(t) of the SiMPI positive feedback system with relaxation taken into account. Upon taking into account relaxation, hysteretic behavior is observed which is similar in appearance to experimentally obtained data and point-spread-function. Simulation parameters use a linear $u(t)$ slew from -5 to 5 over a duration of 25μs which is a half-period of the typical 20 kHz MPI excitation. The reverse slew is then performed to complete the slew in the other direction and finish off a full period, forming complete hysteretic loops. $\beta = 1$ was assumed and strong field dependence of the time constant was assumed: $\tau(u(t)) = \tau_{\text{base}} exp(-10u(t)/u_{\max}$ if $u(t)$ is opposite sign of $p(t)$, otherwise $\tau(u(t)) = \tau_{\text{base}}$. Various (Debeye) relaxation time constant τ_{base} was used, showing the dependence of the hysteresis width on relaxation time constant. The shorter the relaxation time constant, the better the SiMPI performance. . . . 146

6.6 Effect of drive/excitation amplitude on SiMPI. If drive amplitude is below the threshold, SiMPI behavior is lost and the conventional MPI response is seen, which is a few orders of magnitude weaker in SNR and almost an order of magnitude poorer in resolution. To show that SiMPI is not merely a reconstruction artifact or trick, we show raw time-domain data from the MPI receiver coil as drive amplitude is changed. As time passes, the background near-DC field is very slowly ramped down and passes zero. The zero point of the background field corresponds to center of the time course. We observe broad envelopes and then a very sharp peak as the drive amplitude reaches the threshold, showing the switch from conventional MPI to SiMPI behavior. The strength of the raw signal changes by orders of magnitude as well. The slight broadening of the envelope in 15 mT plot is due to the envelope widening since there is more leeway above the coercive threshold of 14 mT and thus MPI signal is seen when the the background field is at zero and when it is near zero ($< 1mT$ away as well, hence, the broadening of the envelope. Critically, this suggests that with a drive amplitude equal to the SiMPI amplitude threshold, we can directly form an image from the raw time domain envelope, opening opportunities to reduce reconstruction computational load and time as well as possibility of demodulation of our AM signal (the envelope) and thus using a much lower receive bandwidth. . 148
6.7 Effect of drive/excitation frequency on SiMPI. Lower frequencies lower the coercive threshold, and this is likely due to there being more time to deal with the delay in the positive feedback loop, therefore less applied field is needed for the input argument to switch sign and saturate in the other direction (thus generating the step response and the sharp dM/dt peak we receive in MPI). However, the spatial resolution also worsens, possibly because there is more time spent near zero field where thermal forces are able to break apart the chain structure, therefore resulting in a mix of SiMPI and non-SiMPI behavior. 150

6.8 Concentration latching in SiMPI. Below a certain threshold concentration, the dynamic hysteresis curves no longer show "step-like" behavior and the point spread functions become broader. SiMPI behavior is lost and MPI performance degrades to conventional levels. Note the dynamic hysteresis curves at high concentrations look very similar to the input-output function of a Schmidtt trigger. 150
6.9 Various 2D Phantoms show dramatic improvement in imaging performance with SiMPI 152
6.10 TEM imaging show clear chain formation when magnetic field is applied. At low concentrations, chains barely form due to abovementioned concentration latching effects. 153
6.11 Temperature was used to change the toluene viscosity to affect the SiMPI nanoparticles. Higher viscosity shows poorer SiMPI performance as the nanoparticles have greater difficulty coming together to form chains needed for SiMPI. 153
6.12 (left) prepolarizing pulse to form the SiMPI chain before performing the MPI scanning and readout. (middle) The prepolarizing pulse generates SiMPI behavior where there was no SiMPI before due to lack of a pre-existing chain. (right) The prepolarizing pulse has to be parallel to the drive field direction to work. The perpendicular case actually suppresses SiMPI behavior completely. 155

7.1 Simple Pictorial Representation of how theranostic MPI uses MPI gradients to selectively treat the tumor while avoiding potential damage to healthy organs like the liver. 159

7.2 Theranostic Workflow demonstrated experimentally on a U87MG xenograft mouse model with SPIONs present in the liver and tumor. Step 1: an MPI image scan at 20 kHz, 20 mT enables clear visualization with high contrast of the SPION biodistribution in regions of pathology (tumor) and also in healthy clearance organs (liver). Imaging parameters are such that SPIONs do not heat. Step 2: the user selects a region, in this case the tumor, to localize the magnetic hyperthermia to. Step 3: The MPI gradients are shifted to center the field-free region (FFR) on the target. This magnetically saturates SPIONs away from the FFR to prevent heating. Step 4: Heat scan at 354 kHz, 13 mT is performed while the MPI gradients are on and held in position. Heating is experimentally localized in the FFR (centered at tumor) while minimizing collateral heat damage to the liver. 161
7.3 Hardware setup of the MPI scanner and the image-guided magnetic hyperthermia scanner. Images are first obtained on our Berkeley MPI Scanner (validated in prior work (Yu et al., 2017b)). To obtain an image, the sensitive field-free-region (FFR) is rastered through a volume. In this study, a field-free-line geometry is used, and images obtained are similar to projection scintigraphy. A separate higher-frequency MPI scanner is used for application of magnetic hyperthermia but has the same geometry, field-free-line. The coordinates are matched to the coordinates of the field-free-line (FFL) of the imaging scanner so as to enable image-guidance from the first scanner. The user is able to pick a target from the image, and the corresponding coordinates on the image is sent to the MPI heating scanner. The robot arm shifts the co-registered animal bed to center the FFL of the heating scanner to the requested coordinates. To locally heat only the target spot, the field-free-line is held in place over the spot while a higher frequency (354kHz) excitation is performed. 163

7.4 Illustration of MPI-localized heating in the tumor while sparing the liver. This is compared to a surface coil method that can localize excitation near the body surface, but is unable to maintain narrow excitation deep within the body due to the field spreading and drop-off with distance. Furthermore, since $\lambda/2 \approx 50$ m for typical heating frequencies, the excitation field cannot be focused into a narrow spot. Collateral damage may done to healthy tissues with non-specific SPION accumulations i.e. clearance organs. In contrast, MPI gradients localizes heating by a completely different mechanism, which is to suppress nanoparticle rotation rather than shaping the excitation wave. Like MPI which can image at depth, heating is localized to the field-free-line (narrow axis) without spreading or attenuation with depth. With a 7 T/m gradient, localization to within a 4 mm diameter cylinder is expected. 165

7.5 Experimental results demonstrating the mechanism behind MPI gradient-based localization of heating.(a) Magnitude of the MPI gradient in the x-z plane (Lakeshore^{TM}Gaussmeter). The gradient field has zero magnetic field at the center and a high magnitude everywhere else. Due to the field-free-line geometry along the y-axis, each x-z slice along y has the same magnetic field profile. (b) SPION dynamic hysteresis loops was simulated at different positions in the gradient field. The hysteresis loops are most open at position A ($|H| = 0$) while the hysteresis loops are closed at other positions. Because heating depends on the area bounded by the hysteresis loop, the gradient field localizes heating to the field-free-line where $|H| \approx 0$. Different drive frequencies have the same trend, showing that this localization method is flexible and works for a range of MPI drive fields. (c) Nanoparticles were put at different locations in the gradient field and heated with 354 kHz, 13 mT excitation. The measured temperature rise and SAR (Neoptix^{TM}probes) is observed to be highest when the nanoparticle is located at position A (field-free-line), in line with simulations in (b). Heating was suppressed at other positions due to the large $|H|$ away from the field-free-line. The 2.35 T/m gradient used here localizes heating to within a 7 mm radius region, but doubling the gradient to 7 T/m will improve localization to 2.3 mm radius. 166

7.6 *in vitro* experimental demonstration of localization of magnetic hyperthermia. A 3 x 3 grid phantom was used where each well was filled with 100 μl of 25 mg/ml SPIONs. The temperature of each well was measured by Neoptix^{TM}fiber optic temperature sensors under different imaging or heating conditions. During a standard MPI scan, no heating was observed due to the low frequency (20 kHz) and raster trajectory. During a high frequency (354 kHz) heating scan without MPI gradients, all the wells heat up. When the MPI gradients are used, the user is able to selectively heat up only the well where the field-free-line is located, with negligible heating in all neighboring wells. Because the wells are spaced 7 mm apart, we demonstrated that heating is localized to within 7 mm for a 2.35 T/m MPI gradient. Higher gradients at 7 T/m can improve this value to 2.35 mm. 168

7.7 Experimental characterization of the magnetic nanoparticles used in this study. The nanoparticles are PEG coated, single crystalline core, superparamagnetic iron oxide. (a) TEM of the nanoparticles. (b) Histogram of the core size distribution gives a nominal core size of 13 nm with effective magnetic core size of 11.7 nm. DLS analysis of the hydrodynamic diameter with number weighted distribution gives a value of $\sim$ 40 nm. (c) Magnetization response of the SPIONs. Inset shows a zoom in of the region close to zero field. 171

7.8 This study used 5 groups of athymic nude mice. Groups 1 and 2 had a single U87MG xenograft and received tail vein injections and intratumoral injection of 1.25 mg Fe SPION each. Bioluminescence imaging was performed for groups 3 and 4 that had luciferin-competent dual MDA-MB-231-luc xenografts (each intratumorally injected with 1.25 mg Fe SPION). Group 5 had a double U87MG xenograft and received intratumoral injection of 1.25 mg Fe SPION in each tumor. MPI and projection X-ray was performed for all groups. Groups 1 & 3 had gradient-localized heating while Groups 2 & 4 had gradient-localization off during heating. Group 5 had gradient-localized heating that sequentially targeted one tumor then another. For all groups, post-euthanasia, the liver and tumor were excised for histology. 173

7.9 *In vivo* experimental demonstration of localization of magnetic hyperthermia. The tumor was heated while sparing the liver. All *in vivo* local temperatures were measured by Neoptix™ fiber optic temperature sensors. During a standard MPI scan, negligible heating was observed in the mouse to the low frequency (20 kHz) and raster trajectory. During a high frequency (354 kHz) heating scan without MPI gradients, all *in vivo* locations with nanoparticles heat up (thus damaging the healthy liver). When the MPI gradients are used, only the tumor is heated while the liver is spared. Lastly, we used a dual tumor mouse to demonstrate arbitrary user control of which tumor to heat. We first centered the field-free-line over the bottom tumor. Only the bottom tumor heated up while the top tumor was spared. Subsequently, without removing the mouse, we shifted the field-free-line over the top tumor. Only the top tumor heated up while the bottom tumor was spared, demonstrating arbitrary control of the site of heating just by shifting the MPI field-free-line. . . . 178

7.10 Experimental demonstration of MPI's potential for dose planning, image guidance and actuation localization. (a) The MPI image is linearly quantitative (R^2 = 0.996) for the amount of SPION. (b) The MPI image intensity is well correlated (R^2 = 0.964) with the deposited SAR measured *in vivo*, demonstrating robustness for dose planning and image guidance. (c) Robust localization of the heating to the targeted location is demonstrated (n = 14, p-value of < 0.001 with Welch's t-test). Localization is clearly attributed to the MPI gradient, since there is no localization of heating when the gradients are off. This implies that MPI gradients can robustly spare the liver while treating the tumor 1 – 2 cm away. 180

7.11 Experimental demonstration that MPI can predict the spatial distribution of heating for image-guided, gradient-localized magnetic hyperthermia. Because MPI is quantitative for the mass of SPION, and since SAR is proportional to the SPION mass, we can obtain a SAR image from the MPI image (no gradients and localization yet). To predict the localization effect of the MPI gradients, we dot multiply the SAR image with suppression effect of the MPI gradient which is in essence a SAR spatial filter. We thus obtain a prediction of the SAR dose after gradient localization. Finally, to account for heat spreading through tissue from the SPION mass, we convolve the previous image with a temperature spatial point spread function (PSF). Our predicted spatial distribution of heating matches experimental data in that the liver was heated by less than $0.8\%^oC$ as predicted by the calculated temperature map. 181
7.12 Experimental assessment of localized heat therapy using a bioluminescence-competent MDA-MB-231-luc xenograft model. (a) MPI image of the dual tumor MDA-MB-231-luc xenograft mice. The bottom tumor is targeted during gradient-localized heating. *in vivo* temperature at both tumors and the rectum measured by NeoptixTM fiber optic temperature probes. The greatest heating occurred in the targeted bottom tumor, while the upper tumor received negligible heating. The total CEM43 achieved was 79.3 minutes in the targeted bottom tumor. The core body temperature, however, was slightly elevated and likely due to the homeostatic response distributing heat from the heated bottom tumor to the rest of the body. (b) Luciferase bioluminescence activity of the tumor was measured before and after treatment. The results show significant decrease in activity for the treated bottom tumor, while the untreated tumor had almost no change in bioluminescence activity. Thus, this demonstrates the utility of MPI gradients in localizing tumor therapy. (c) Statistics (n = 3, p-value = 0.05 with Welch's t-test) show that localization of therapy is robust. 183

7.13 Histological assessment of MPI localization of thermal damage. (a) Apoptosis assay (red) and DAPI stain (blue) shows apoptosis only occurs in the targeted tumor but not in the neighboring off-target tumor, verifying localization of heat damage by the MPI gradients. The liver is also damaged when MPI gradients are turned off and uniform heating of the tumor and all other locations occurs. In contrast, no damage is observed in the liver when the MPI gradient is turned on and targeted at the tumor. (b) Statistics (n = 3, p-value = 0.005 with Welch's t-test) show that localization of thermal damage by MPI gradients is robust. The liver sustains significant damage if MPI gradients are off due to collateral heating of the SPIONs cleared to the liver. In contrast, the liver is negligibly damaged if MPI gradients are on (p-value = 0.026). These results validate the ability of MPI gradients to robustly localize thermal damage to the tumor while sparing the liver 1 – 2 cm away. (c) Prussian Blue stain confirms that SPIONs are successfully delivered to both the tumor and liver (clearance organ). 185

8.1 Magnetic Particle Imaging (MPI) applied to *in vivo* tracking of inhaled aerosol. (a) MPI / CT imaging visualizes the *in vivo* distribution of the inhaled aerosol in the lung airspace (maximum intensity projection). (b) The MPI scanner uses electromagnets to generate a field-free-line (FFL) magnetic field gradient with an effective trajectory as shown. This generates one MPI projection image and multiple projections can be used to reconstruct a 3D image. (c) TEM of the multicore clustered superparamagnetic iron oxide nanoparticles used. (d) Dynamic magnetization curves of the SPION measured at an AC excitation field of 20.225 kHz and 40 mTpp to match the MPI drive field. (e) MPI is linearly quantitative for aerosol mass. MPI's high contrast, high sensitivity and quantitative nature enables it as a radiation-free alternative to radioaerosol scintigraphy and PET for *in vivo* quantification of therapeutic aerosol dose, visualization of biodistribution, assessment of delivery efficiency and finally timecourse evaluation of clearance rates. 194

8.2 Magnetic Particle Imaging (MPI) is able to assess the delivery efficiency of different methods. (a) Experimental setup showing how the aerosol is delivered by controlled ventilation to the rodent. (b) MPI assessment of the delivery efficiency of three different methods. Method 1 uses a slow controlled ventilation rate. This enables the aerosol to be more evenly distributed in the lung. Method 2 uses a fast controlled ventilation rate, resulting in more inertial impactation of the aerosol in the central conducting airways as opposed to the finer airways in the lung periphery. Method 3 increases the size of the aerosol droplets and therefore significantly increases the probability of inertial impactation in the central airways, resulting in poor delivery to lung periphery. 198
8.3 Magnetic Particle Imaging (MPI) is able to quantify the delivery of aerosolized therapeutics. (a) Experimental setup. The MPI imaging agent (SPIONs) is mixed with the model drug, doxorubicin hydrochloride, then aerosolized. The aerosol is inhaled by the animal or deposited on surgical gauze for the *in vitro* experiment. (b) Fluorescence measurements of deposited doxorubicin hydrochloride for the *in vitro* experiment shows good correlation with the MPI signal, confirming that the MPI image can quantify drug deposition. (c) The MPI image clearly visualizes the drug deposition *in vivo* while fluorescence imaging of the drug is difficult at depth. *Ex vivo* imaging of the lungs confirm that the MPI image and the fluorescence image match, showing that MPI images the drug distribution in the lungs and provides clearer visualization *in vivo* and at-depth. 199
8.4 MPI is able to track with high contrast and sensitivity the clearance of delivered aerosol. The clearance pathway is clearly visualized by visible boli in the trachea and in the gastrointestinal tract. Because SPIONs do not radioactively decay over time, MPI is suitable for longitudinal imaging of aerosol clearance. The visible attenuation of the signal is due to mucociliary clearance from the lung, as the lost signal is accounted for by MPI signal in excreta. MPI thus has the potential to be a radiation-free alternative to current pulmonary radioaerosol mucociliary clearance clinical tests. 201

8.5 MPI quantification of the SPION biodistribution over time. (a) Change in biodistribution of SPIONs and two-compartment model fitting shows SPIONs are cleared from the lung and through the GI tract into excreta. The quantitative nature and high sensitivity of MPI shown here makes it a promising radiation-free alternative to radioaerosol procedures. (b) *Ex vivo* MPI validation shows SPIONs in only the lungs and excreta. Prussian Blue stains of lung histological sections verify that SPIONs were successfully delivered to the lung. 202

List of Tables

List of Abbreviations

1D	**1 D**imensional
2D	**2 D**imensional
3D	**3 D**imensional
AWR	**A**rbitrary **W**aveform **R**elaxometer
BISL	**B**erkeley **I**maging **S**ystems **L**ab
DI	**D**e-**I**onized
DSP	**D**igital **S**ignal **P**rocessing
EMF	**E**lectro**m**otive **F**orce
EPR	**E**hanced **P**ermeability (and) **R**etention
FFL	**F**ield-**F**ree **L**ine
FFP	**F**ield-**F**ree **P**oint
FFR	**F**ield-**F**ree **R**egion
FOV	**F**ield **o**f **V**iew
FWHM	**F**ull **W**idth (at) **H**alf **M**aximum
LSI	**L**inear (and) **S**hift **I**nvariant
MAA	**M**acro**a**ggregated **A**lbumin
MFH	**M**agnetic **F**luid **H**yperthermia
MNP	**M**agnetic **N**ano**p**article
MPI	**M**agnetic **P**article **I**maging
MRI	**M**agnetic **R**esonance **I**maging
PEG	**P**oly**e**thylene **G**lycol
PET	**P**ositron **E**mission **T**omography
pFOV	**p**artial **F**ield **o**f **V**iew
pMPI	**p**ulsed **M**agnetic **P**article **I**maging
PSF	**P**oint **S**pread **F**unction
ROI	**R**egion **o**f **I**nterest
Rx	**R**eceive
SAR	**S**pecific **A**bsorption **R**ate
SNR	**S**ignal (to) **N**oise **R**atio
SPECT	**S**ingle **P**hoton **E**mission **C**omputed **T**omography
SPIO	**S**uper**p**aramagnetic **I**ron **O**xide
Tx	**T**ransmit or excitation

Physical Constants

Boltzmann constant	$k = 1.380\,648\,527\,9 \times 10^{-23}\ \mathrm{J\,K^{-1}}$
Vacuum permeability	$\mu_0 = 4\pi \times 10^{-7}\ \mathrm{H\,m^{-1}}$

List of Symbols

B	induction field magnitude	T
B_1	coil sensitivity	$\mathrm{T\,A^{-1}}$
f	frequency	Hz
f_0	fundamental excitation frequency	Hz
G	linear magnetic gradient magnitude	$\mathrm{T\,m^{-1}}$
H	magnetic field magnitude	$\mathrm{A\,m^{-1}}$
I	moment of inertia	$\mathrm{kg\,m^2}$
k	magnetic Langevin constant	$\mathrm{m\,A^{-1}}$
$\mathcal{L}$	Langevin function	none
m	magnetic moment	$\mathrm{A\,m^2}$
M	magnetization magnitude	$\mathrm{A\,m^{-1}}$
x_s	location of MPI field-free region center	m
η	viscosity	$\mathrm{Pa\,s}$
γ	gyromagnetic ratio	$\mathrm{rad\,s^{-1}\,T^{-1}}$
ρ	particle density	$\mathrm{particles\,m^{-3}}$
ω	angular frequency	rad
τ	time constant	s

Dedicated to Mika Tei, Ricky Tay Kwee Lee and Esther Lim Beng Hwee

Chapter 1

Introduction and Background

1.1 Medical Imaging

Medical imaging can be broadly defined as forming images of the human body, interior or exterior, that provides anatomic or functional information leading to diagnosis of pathology or damage in the body. There are a variety of medical imaging modalities, each of which has its own strengths and weaknesses. Common imaging modalities are Projection X-ray, Computed Tomography (CT), Magnetic Resonance Imaging (MRI), Nuclear Medicine (which encompasses Positron Emission Tomography - PET, scintigraphy and Single-Photon Emission Computed Tomography - SPECT), and Ultrasound. The imaging modalities can be broadly classified into anatomic and functional imaging modalities.

1.1.1 Anatomical Imaging Techniques

Anatomical imaging modalities derive signal from the biological material such as tissue and organs in the subject. Typical modalities include magnetic resonance imaging (MRI), X-ray projection imaging, X-ray computed tomography (CT), and ultrasound. Depending on the modality and scanning parameters, contrast between different tissue types can be achieved. For example, X-ray has excellent visualization of bone but soft tissues do not show up as brightly. These modalities typically enable high resolution visualization (spatial and/or temporal) about the internal anatomy and structures. For pathologies that show up as a clear structural change or defect, for example a bone fracture, anatomic imaging alone is sufficient to inform a diagnosis.

While indispensable to any imaging study, there are often limitations to the contrast achievable by anatomic imaging even after adjusting the relevant imaging parameters. In addition, small amplitude signals carrying

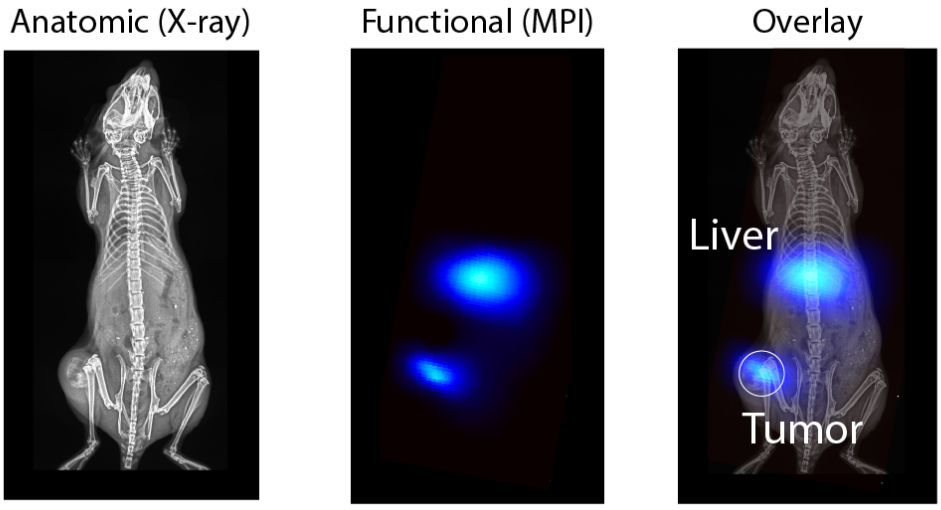

FIGURE 1.1: Comparison of anatomic vs. functional images. Anatomic imaging (left) can provide visualization of internal bodily structures such as the skeleton in this case but is unable to clearly visualize the tumor or liver. Functional or molecular imaging techniques (center), which often use contrast agents or tracers specifically target certain organs such as the liver in the case or may have antibodies that target the tumor. This provides clear visualization of pathology, such as the tumor, and specific organs, such as the liver, which may not be highlighted or clearly visualized in the anatomic image. However, functional images typically do not have visualization of the entire body. The image here is a result of intratumoral injection of MPI tracer, but similar results are expected from a tumor targeted contrast agent. (Right) Overlay of the anatomic image and the functional image allows a spatial reference for the highlighted pathology/organ, and helps the physician accurately locate the tumor for diagnosis and treatment. These images are part of the data from the 'MPI theranostics' study in Chapter 7.

vital information about hidden pathologies are often masked by the large volume of surrounding (healthy) tissue. In such situations where additional specific contrast is required, functional imaging of contrast agents and tracers comes into play.

1.1.2 Functional Imaging Techniques

In comparison to anatomic imaging, functional and molecular imaging methods and modalities specifically target defined physiologic, functional, or pathological information in the image which are then highlighted for visualization through the use of contrast agents, dyes or tracers. An anatomic imaging modality can also be used for functional imaging with the use of contrast agents, which strongly highlight the defined target, but at the cost of losing visibility and contrast of other anatomic information (an issue often solved by simple overlaying of the anatomic and functional images). Some examples include gadolinium contrast in MRI or microbubbles in ultrasound (James and Gambhir, 2012).

Contrast agents modify the anatomic image, much like emboldening the outlines of a pencil sketch or deepening the shade of select regions of the sketch. Positive contrast agents raise local pixel intensity in the image (*e.g.*, gadolinium T1 agent in MRI) while negative contrast agents reduce local pixel intensity (*e.g.*, T2* iron oxide tracers in MRI). Typically, positive contrast agents are preferred because negative contrast agents are often confused with empty spaces or airspaces in the anatomy which almost always show up as hypointense or dark regions regardless of imaging modality.

Tracer modalities are different from the abovementioned case of contrast agents in anatomic modalities because tracer modalities do not receive any signal from biological tissue and only receive signal from the tracer itself. This manifests as an image where the body is effectively fully transparent and only the tracer is visualized. Examples of such modalities include MPI and nuclear medicine modalities positron emission tomography (PET), scintigraphy, and single photon emission computed tomography (SPECT). Tracer modalities are powerful because they offer very high contrast of the target pathophysiology (*e.g.*, 18-FDG in PET) and correspondingly higher sensitivity as small amplitude signals are not swamped by background signal from surrounding tissue. As a result, typically orders of magnitude lower concentrations of tracer are required than in the case of contrast agents, and this helps avoid typical side-effects such as contrast agent nephrotoxicity that partially result from the high concentrations required.

One key drawback is that tracer modalities completely lack anatomic information and physicians lack a spatial context or map if looking at the tracer image alone. For this reason, combined anatomic and molecular imaging overlays are common as in PET/CT and MPI/CT (James and Gambhir, 2012; Zheng et al., 2016).

1.2 LSI Imaging Systems and LSI Analysis

Linear and Shift Invariance is highly desirable for medical imaging (Gaskill, 1978; Prince and Links, 2006) for many reasons. Key within these is that images reconstructed from LSI modalities do not depend on *a priori* assumptions about the imaged object and can faithfully provide accurate information to aid diagnosis while avoiding non-linear artifacts that can mislead diagnoses. Because LSI systems can be completely described by its response to a point source which is an easy experimental calibration, the expected (and obtained) image from a theoretical object can be easily and accurately modeled, allowing easy verification of the accuracy of medical images and leading to confidence in the accuracy of the technique. While LSI systems are powerful, it is important to acknowledge that due to inevitable noise in any imaging detector/system, no realistic medical imaging can be considered to be perfectly LSI. Noise can be minimized to a level where errors resulting from LSI assumptions are negligible and thus provide accurate enough imaging of the human subject in a clinical setting.

Linearity can be defined as compliance to the following equation:

$$H(\alpha\rho(x) + \beta\rho(x)) = \alpha H(\rho(x)) + \beta H(\rho(x)) \quad \forall\alpha, \beta \in \mathbb{R} \tag{1.1}$$

If $\tilde{\rho}(x) = H(\rho(x))$, then shift invariance is compliance to the following equation:

$$H(\rho(x - x_0)) = \tilde{\rho}(x - x_0) \tag{1.2}$$

The power of LSI systems can be mathematically visualized in the fact that the relationship of object to image can be simply summed up in one elegant equation:

$$y = Ax \tag{1.3}$$

where A (*e.g.*, represented as a matrix) is a linear operator that acts on the input x to produce the output y. The operator A describes everything that occurs in the process of creating an image from the object. For example,

in MPI, the operator A describes the magnetization point-spread-function of the magnetic nanoparticle, the conversion of spatial information to temporal information by the receiver coils, and the information encoding the scanning trajectory(Goodwill and Conolly, 2011b; Rahmer et al., 2009).

Solving a linear system, involves inverting the linear system. This is the basis of the system matrix reconstruction concept in MPI, but this can run into problems if A does not have a good conditional number which in turn means the inverse problem is not well-posed. The deleterious effects of trying to solve such a problem has been extensively investigated (Shahram and Milanfar, 2004) and typical issues include dramatic magnification of noise and other sources of coherent error.

To address this, we consider that the operator A can be broken down into a product of individual operators, each representing the linear operation that results from each physical mechanism occurring in the chain of events from scanning the object to image generation:

$$A = A_N A_{N-1} \dots A_1$$

As a result, we can choose to only perform inverse problem solution on the well-posed operators within this cascade, and accept a net solution that is not exactly the object but something close, for example, the object spatial distribution convolved with the magnetization point-spread-function, which if narrow enough, will approximately equal the actual spatial distribution of the object. This is the concept behind x-space reconstruction in MPI, where inversion only occurs for the well-posed operators such as MPI trajectory spatio-temporal encoding. This is powerful as it avoids the amplification of noise during image reconstruction and significantly reduces the computational load of reconstruction.

1.3 Magnetic Particle Imaging

Here we introduce the field of MPI broadly, starting with the physical principles underlying MPI, then describing the advantageous characteristics resulting from this that give MPI it's unique niche amongst imaging modalities, and finally complete the introduction with a listing of some of the open challenges remaining.

1.3.1 Basic Principles

MPI is a fundamentally a tracer-based modality that directly visualizes magnetic nanoparticles. The MPI signal comes from applying an excitation magnetic field which magnetizes the magnetic nanoparticles. The resultant change in nanoparticle ensemble magnetization is measured and recorded as the MPI signal. To interrogate only a single point in 3D space at a time, MPI relies on strong magnetic gradients that magnetically saturate all magnetic nanoparticles except those located at the field-free-point of the magnetic gradient. This key aspect of MPI depends critically on the non-linear magnetic response of the superparamagnetic iron oxide nanoparticles typically used in MPI - in the sense that these nanoparticles can become saturated and magnetize no further at some point. As a result, only unsaturated nanoparticles, which are those located at the field-free-point, can change their magnetization in response to the excitation. To form an image, the field-free-point is rastered across the entire 3D volume to interrogate each point in space in turn.

1.3.2 Imaging Metrics of MPI

In any imaging modality, there are a few key metrics of interest that determine the performance of that modality and serve as a basis for comparison between modalities. One key metric is spatial resolution, which is the ability of the imaging modality to resolve two separate points. This is critical in medical imaging to visualize and diagnose pathology, for example, being able to see a fine crack in the bone for x-ray diagnosis of fracture. Finer resolution allows the use of smaller pixels leading to a better resolution image (similar scenario as the usage of a computer screen with more pixels per square inch) where smaller features can be visualized and resolved. Strictly speaking, digital images can use pixels of any size desired, but if the analog received data from the imaging device has a certain blur, then having very small pixels in the digitization does not increase the perspicuity of the image and the blur from the device is still observed. As such, it is typical to match the pixel size to the analog resolution. In this thesis, we will use the Houston criterion Houston, 1927 of resolution, which defines two points as resolved if they are separated by at least a full-width-half-maximum distance (FWHM). This in turn is defined as the distance from the point source where the image intensity falls to half of the (central) maximum.

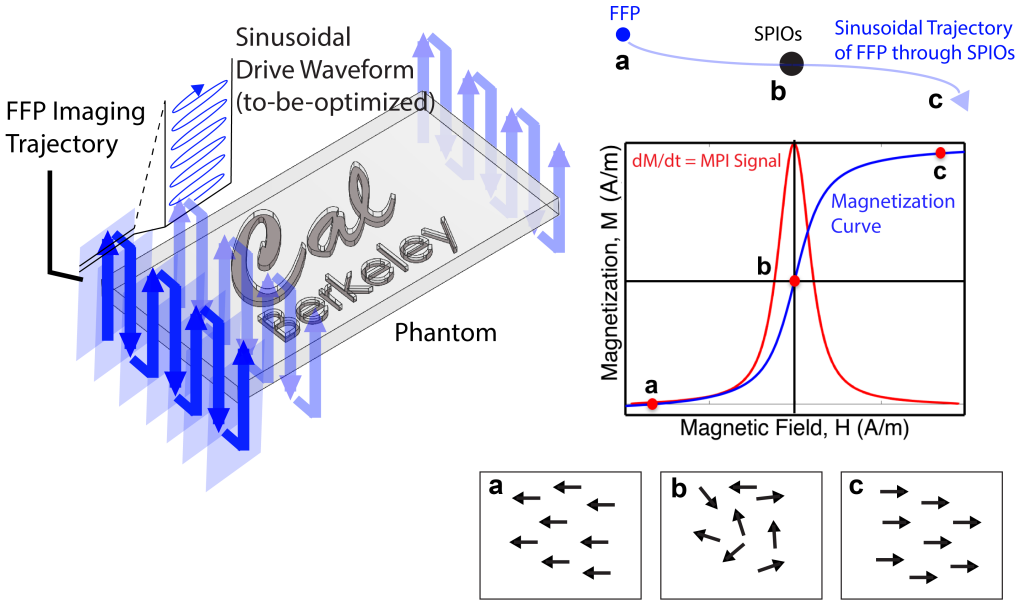

FIGURE 1.2: Spatial localization of the MPI signal via Langevin physics. (left) Typical raster trajectory of the field-free-point or field-free-line used in MPI imaging (right) How the non-linear ensemble magnetization response of the magnetic nanoparticles can be translated by the inductive receive coils into a Langevin point-spread-function (red plot) centered at the precise location of the nanoparticles. This forms the basis of signal localization in x-space MPI.

Another key metric is sensitivity or signal-to-noise (SNR). This defines if very low concentrations of the imaging agent can be detected and visualized, and is critical for medical imaging because it is desirable to visualize pathologies in their early stages / screening purposes, where either the mass of the pathology (i.e. tumor) is small or the available binding sites for targeted imaging agents (18-FDG PET) are very limited. Here, we report sensitivity in terms of MPI signal (in volts) per gram of nanoparticle, or as a dimensionless SNR number. For reference, the minimum acceptable SNR is 5 by the Rose criterion but typically, medical imaging requires an SNR of 10 or above. SNR will differ between different MPI devices, but in our analysis, we seek to normalize for this effect by ensuring all our results are taken on the same device with the same amount of averaging.

Other important metrics are contrast-to-noise ratio, temporal resolution and safety. MPI has very good contrast-to-noise ratio because there is zero tissue signal. Thus, if the imaging agent is targeted to the pathology, the contrast between pathology and background tissue can be very high. This excellent contrast is a hallmark of tracer modalities such as nuclear medicine, where only the radioactive imaging agent is visualized (body tissue has negligible radiation output). MPI is the same, since it only visualizes the non-linear magnetic flux response from the magnetic nanoparticles (the paramagnetic response from the body tissue is removed together with the direct feedthrough from the MPI excitation wave). As such, one can consider MPI to be at least conceptually, a magnetic version of nuclear medicine (exact performance of resolution, sensitivity etc may differ, but the key hallmark of excellent contrast and zero tissue background signal is the same). MPI has been shown recently to have good temporal resolution of 46 frames per second too (within a limited FOV) Ludewig et al., 2017. Temporal resolution is needed to resolve fast changing phenomenon in the body, such as blood flow and perfusion. Lastly, the safety of MPI is relatively good since it uses FDA and EU approved imaging agents (for MRI) such as Resovist ™. These magnetic nanoparticles are safely cleared and broken down by the liver into iron for bodily uptake or excretion. Because the nanoparticles are very small ($< 100nm$) in hydrodynamic size, they do not clog capillaries and can move around freely with the blood circulation. Critically, as a "magnetic tracer modality", MPI is not restricted by the same radiation dose constraints as nuclear medicine and avoids radiation related health risks from imaging. Lastly, the low frequency magnetic fields used in MPI do not cause magnetostimulation or heating (SAR) hazards as long as a maximum amplitude of excitation is observed.

We will not go in detail about what factors determine the MPI performance for each metric here, as the subsequent chapters will discuss all of these at length in the introduction/theory sections in order to provide a context for the spatial resolution or SNR optimization that we perform when creating novel scanning strategies that try to improve MPI performance in these key metrics. Notably, resolution is discussed at length in Chapter 3, SNR is discussed at length in Chapter 5, and safety (magnetostimulation and heating) is discussed in the end of Chapter 4.

1.3.3 Key Characteristics of MPI

MPI has several intrinsic advantages. First, because MPI images the electronic magnetic moment which is 22 million times stronger than nuclear magnetic moment imaged in MRI, MPI has high sensitivity. MPI has been shown recently to approach near picogram sensitivity Graeser et al., 2017; Them et al., 2016a; Them et al., 2016b. Furthermore, MPI has high temporal resolution, with real-time MPI image-guidance of catheters demonstrated Salamon et al., 2016; Rahmer et al., 2017. Temporal resolutions of 46 frames per second have been shown in recent state-of-the-art scanners Ludewig et al., 2017.

Second, MPI has been demonstrated to be high-contrast since it only images magnetic nanoparticles. The human body has no native magnetic sources and is therefore entirely invisible to MPI. The iron in hemoglobin is not ferromagnetic because it does not associate together to form magnetic domains and therefore do not show the non-linear magnetization behavior requisite for MPI. Ferrohemoglobin (without oxygen attached) is weakly paramagnetic and its paramagnetic response is removed together with the excitation feedthrough by analog filtering and thus does not appear in the MPI signal.

Third, MPI is quantitative for the SPION mass Zheng et al., 2015; Zheng et al., 2016; Yu et al., 2016; Ludewig et al., 2017; Tay et al., 2016 because the strength of the induced magnetization is linearly proportional to the mass of magnetic tracer present. Furthermore, the low excitation frequencies used imply that the magnetic flux lines emitted by the magnetized tracer fully penetrate through the body and is picked up by the receive coil without any attenuation unlike the gamma rays used in nuclear medicine. In addition, the tracer nature of MPI means that quantification is not hindered by surrounding background tissue signal.

Fourth, MPI is robust anywhere in the body and can image at-depth without any signal attenuation. Because of the low excitation frequencies

used, the excitation magnetic fields and the signal magnetic fields penetrate fully through tissue and bone. Because MPI can be thought of as imaging the very strong susceptibility of the magnetic nanoparticles, small changes in susceptibility resulting from air-tissue interfaces that have a large impact on image quality in MRI have zero impact on the MPI image.

Fifth, the magnetic tracers used in MPI do not radioactively decay over time unlike radiotracers used in nuclear medicine. As a result, tracers can be stored and taken out for use just before the imaging procedure, while the only other tracer modality, nuclear medicine, needs to prepare a fresh batch of tracer before every scan. Furthermore, due to the radioactive nature of the tracers, extensive facilities (in-house cyclotron, radiation shielding) is required, and time-consuming, cumbersome hot chemistry is needed to link the radiotracer to molecules of interest such as antibodies or albumin just before the study.

Lastly, magnetic tracers used in MPI are proven to be safe. Resovist, which is a typical tracer in MPI, has been FDA approved for prior use in MRI. The iron oxide in MPI tracers is broken down safely in the liver. This is in contrast to the radiation dose requisite in any nuclear medicine study, where lifetime dose limits severely limit the total number and frequency of nuclear medicine studies possible.

1.4 MPI Applications

As a result of the key characteristics of MPI described above, MPI is well-suited for several imaging applications.

1.4.1 Angiography and Perfusion Imaging

Key advantages of MPI specific to this application are the high contrast, quantitative nature and safety. Because of its tracer nature, capillary level perfusion can be imaged where otherwise impossible because there is no background tissue signal to mask the weak capillary signal. As a result, direct quantification of perfusion is possible where other modalities must rely on indirect methods to calculate local perfusion from major vessel input and output measurements. A recent stroke and brain perfusion study has demonstrated real-time MPI with 46 fps (Ludewig et al., 2017). Recently, we have shown the first *in vivo* traumatic brain injury imaging in MPI (Orendorff et al., 2017). MPI tracers may also have important safety advantages

over the contrast agents, such as gadolinium and iodine, that are used in other contrast agent-based angiographic methods.

1.4.2 Cell Tracking

Amongst all the applications, cell tracking can be considered one application uniquely suited to MPI. Cell tracking critically requires safety and long lifetime of the tracers, since it is important to minimally affect the function of tracked cells, especially stem cells, yet monitor their biodistribution over long periods of time. Due to the small numbers of cells, sensitivity and high contrast is also highly desirable. However, the only other tracer modality, nuclear medicine, is fundamentally ill-suited for this application due to the radioactive decay of the tracers. If tracers with very long half-life are used (such as Indium-111), there is a significant trade-off in SNR because there are much few photons available during the scan duration.

Recently, our group showed MPI's promise for cell tracking with the first *in vivo* MPI cell tracking studies (Zheng et al., 2015; Zheng et al., 2016). Sensitivity of 200 labeled cells was reported with linear quantification of the stem cell number. It is important to note that this incredible MPI sensitivity is achieved with a heterogenous tissue background. While MRI may achieve single cell sensitivity, this requires a very homogeneous tissue background such that the signal from the cell will not be confused with natural anatomic variation. Furthermore, the fate of neural stem cells injected into the brain was tracked over the course of three months. This clearly shows the longitudinal and quantitative capabilities of MPI.

Lastly, MPI's capability to have image-guided, localized heating of the nanoparticles can serve as a much-needed kill switch that is vital in stem cell translation to the clinic. One major issue is stem cells going rogue and generating teratomas. MPI's ability to selectively heat and kill teratomas formed from the initially injected labeled stem cells could be crucial in assuring safety of stem cell therapies.

1.4.3 Lung Imaging

The lung is also a key niche for MPI. In general, the lung is a relatively inaccessible organ for many imaging modalities such as MRI and Ultrasound. CT and Nuclear Medicine are typically used, but pose significant radiation risk especially since the lung is well-known to be one of the more sensitive organs to radiation damage. MPI's robustness anywhere in the body and its relative safety pose it as a promising alternative to the current procedures

used. For example, traditionally, nuclear medicine 'V/Q' techniques have been used for diagnosis of pulmonary embolism. The 'Q' or perfusion scan uses macro-aggregated albumin entities tagged with a radiotracer. Upon injection, the aggregates get stuck in the capillaries of the lung and allow visualization of the lung perfusion, with empty spots indicating blockage of perfusion. Zhou et al. were able to show the use of MPI for this application in a recent paper from our group (Zhou et al., 2017). The 'V' or ventilation scan using aerosolized MPI tracers is detailed in Chapter 8. Combining the two is a potential future work, allowing us to provide a fully MPI alternative to clinical VQ studies.

MPI is also a promising alternative to gamma scintigraphy tracking of inhaled therapeutics. Currently, radioaerosols are used to evaluate mucociliary clearance, assess delivery efficiency of inhaler devices and finally to track deposition of inhaled therapeutics. Chapter 8 provides *in vivo* proof-of-concept of MPI being a viable alternative to these nuclear medicine procedures.

1.4.4 Cancer and Theranostics

Tracer modalities are very useful in the early diagnosis of cancer. While anatomic imaging modalities can provide some visualization of the tumor when it reaches a large size, tracer modalities such as 18FDG PET are well-known to be sensitive for smaller tumors. Our lab has investigated the potential of MPI as an alternative to nuclear medicine for the imaging of cancer. Recently, our group has shown the first *in vivo* cancer imaging in MPI (Yu et al., 2016). Here, tumor xenografts in a rat were imaged with high contrast and sensitivity. Notably, the nanoparticles were untargeted and accumulation in the tumor came from the enhanced permeability and retention (EPR) effect exhibited by *some* lesions. The excellent visualization of the tumor over the imaging timecourse confirms that MPI, like PET, is able to provide superior imaging of cancer.

In addition to imaging, MPI can be leveraged for cancer theranostics. After confirming the presence of cancer, the magnetic tracer already present at the tumor can be selectively heated for thermal therapy of the cancer. *In vivo* proof-of-concept of MPI cancer theranostics, complete with proven therapy of tumors in a rat model, is detailed in Chapter 7.

1.5 Open Challenges in MPI

The MPI field has made a lot of progress since its invention in 2005 by Gleich and Wiezenecker (Gleich and Weizenecker, 2005). But many open challenges still remain.

One key challenge is MPI's relatively mediocre spatial resolution. Current preclinical resolution is limited to around 1 mm. While deconvolution to improve resolution is possible, this often comes at a steep price for SNR. In this dissertation, we investigate novel scanning methods to improve spatial resolution in other ways such as mitigating relaxation-based blurring (pMPI) as well as leveraging the positive feedback in nanoparticle magnetization (SiMPI).

Another key challenge is "Color MPI", where MPI provides additional sensing of several microenvironment parameters such as viscosity, binding state, pH and temperature. "Color MPI" could also refer to the generation of different magnetic tracers, each with its own MPI signature where the resultant MPI image can be unmixed into its component tracers, each tracer thus being assigned a "color". This would be very powerful and a at-depth, magnetic version of fluorescence imaging. While much recent research has been directed towards developing MPI techniques and tracers for "Color MPI", there still remains a lot of work to be done to make "Color MPI" viable and powerful.

1.6 Path Towards Clinical Implementation of MPI

Here we briefly discuss key issues in the path towards clinical implementation.

1.6.1 Specific absorption rate (SAR) Limits

Like MRI, MPI must address magnetic-based safety parameters such as magnetostimulation and tissue heating as measured by SAR. This is because MPI, like MRI, exposes the human body to time-varying magnetic fields (excitation field). (Saritas et al., 2013a) has shown that certain MPI excitation limits need to be observed to stay within safety limits. Key in this is a reduction in excitation amplitude but this can be compensated by a possible increase in excitation frequency (Gleich and Weizenecker, 2005) since MPI

$$Limit\ of\ Detection \approx 2\,\rho\sqrt{k_B} \cdot \frac{NF\sqrt{T_{coil}R_{coil}}}{B_{coil}} \cdot \frac{H_{sat}}{M_{sat}} \cdot \frac{\sqrt{\mathrm{BW}}}{\omega H_{ampl}}$$

Hardware Parameters | Nanoparticle Parameters | Scanning Parameters

$$Spatial\ Resolution \approx \mu_0 \cdot (H_{sat} + k \cdot \tau_{SPIO}\omega H_{ampl}) \cdot G^{-1}$$

Nanoparticle Parameters | Scanning Parameters | Hardware Parameters

FIGURE 1.3: (Top) Approximate equation for MPI limit of detection in terms of grams of Fe (assuming SNR = 1). Assumptions are coil noise dominance, and that the $-H_{\mathrm{sat}}$ to $+H_{\mathrm{sat}}$ region of the M-H curve approximates the SPIO peak response. Variables are NF = noise factor of preamplifier; ρ = density of SPIO; k_B = Boltzmann constant; T,R,B = temperature, resistance and sensitivity (T/A) of the receive coil respectively; H_{sat} and M_{sat} refers to the applied field needed to reach M_{sat} and the 90% saturation magnetization value respectively; BW = final receive bandwidth after digital windowing; ω is the MPI excitation frequency in radians and H_{ampl} is the MPI excitation amplitude. (Bottom) Approximate equation for MPI spatial resolution. Variables are μ_0 = vacuum permeability; k is a proportionality constant modulating the blurring effect of magnetic relaxation; τ is the (Debeye) magnetization time constant of the SPIO that causes delays in magnetization leading to relaxation-induced blurring; G is the MPI gradient strength in Tesla/meter.

uses very low frequencies ($\sim$ 20 kHz). This should not negatively affect MPI performance since recent work has shown that low excitation (drive) amplitude helps, rather than hinder, MPI spatial resolution (Croft et al., 2016). As such, a human-safe MPI scanner using safe excitation sequences should perform well at least on the MPI excitation parameters (barring sensitivity changes due to receive coil scaling).

1.6.2 Maintaining Good Performance while Scaling up to Human Size

Next, it is important to discuss the factors that affect MPI performance in general to understand the problems associated with scaling the hardware up to human-size. Fig. 1.3 shows the generic equations governing MPI sensitivity (limit of detection at SNR = 1) and MPI spatial resolution, and these were derived with reference to prior mathematical work from (Gleich, 2014; Goodwill and Conolly, 2010).

Current MPI preclinical scanners are able to produce a high gradient field of 6.3 T/m (Yu et al., 2017a) and it is known that MPI spatial resolution

scales linearly with gradient strength. When scaling up to human-size, it is a challenge to maintain the same high gradient field strength. Gradient coil design has been analyzed in-depth for MRI (Turner, 1993), and coil efficiencies scale as $1/r^2$, which means power requirements in scaling-up to human scale as r^5 since current required scales with r^2, coil resistance scales as r and overall power dissipated scales as I^2R. But having at least reasonable gradient strengths of > 3.5 T/m is necessary for competitive spatial resolution. As with MRI scanners, superconducting main (gradient) magnets may thus be an important cost-cutting measure for human MPI scanner designs.

Another approach towards human MPI is to develop better MPI-tailored SPIOs. Improving MPI resolution from the SPIO quality can then be traded-off for lower gradients to ease implementation of human-size MPI scanners. For instance, improving the phase purity of the SPIO tracer have resulted in better MPI spatial resolution. The MPI performance showed almost 2-fold better spatial resolution than Resovist™. (Ferguson et al., 2015a) This can then be traded-off for a 2-fold weaker gradient which will dramatically reduce hardware requirements for a human scanner.

One important factor is the FDA approval of these new MPI-tailored SPIOs. Iron oxide nanoparticles have already been approved clinically for various uses. For example, Resovist™is approved in Japan as an MRI contrast agent, Feraheme™is approved in North America for anemia treatment and Nanotherm™is approved in Europe for magnetic hyperthermia treatment. It has also been shown that the very rare cases of anaphylactic shock from SPIO injections can be attributed to the surface coating on the nanoparticles. We believe that with careful biocompatibility and anti-immunogenic design of the SPIO coating, the path to FDA approval for new MPI-tailored SPIOs should be smooth.

Lastly, MPI is still a relatively new field and is far from completing hardware, scanning and SPIO optimization for MPI performance. From the equations shown in Fig. 1.3, MPI performance could still improve in each of the color-coded sections. For example, use of 77K cryogenic litz / HTS receive coils which have not been implemented yet could improve MPI sensitivity. As noted above, optimizing the SPIO could lead to large gains in MPI performance. Lastly, while there is some work already done in optimizing MPI scanning sequences, as the Part 1 of this dissertation will show, MPI scanning strategies are mostly unexplored and there are still large gains possible from investigating this field. In Part 1, we investigate 3 different and novel MPI scanning strategies (pulsed MPI, optimized continuous-wave MPI and strongly-interacting MPI) to improve MPI performance. We hope that the work presented in this dissertation will demonstrate the vast

unlocked potential in each of the possible color-coded ”improvement regions” for MPI and contribute towards existing and future work towards improving MPI to become a more attractive and compelling modality to be added to the repertoire of clinical imaging modalities such as CT, MRI, Ultrasound and Nuclear Medicine.

Part I

Novel Scanning Strategies to Improve MPI Imaging Performance

Part 1 Preface

This part of the dissertation aims to elucidate several novel MPI scanning strategies I developed over the course of my graduate school career. In Chapter 2, I describe the design and construction of a miniature arbitrary waveform relaxometer (AWR) with unprecedented frequency flexibility and ability to perform non-conventional, arbitrary waveforms. These new capabilities will prove vital to the development and testing of all the novel scanning strategies in this chapter. Chapter 3 describes a short study on MPI tracers (superparamagnetic iron oxide nanoparticles or SPIOs) that investigates the failure of MPI theory to achieve cubic spatial resolution gains with larger SPIO core sizes. The obstacles discovered and outlined in this short study will serve as motivation for the new scanning strategy in Chapter 4 that seeks to circumvent these obstacles. Chapter 4 describes this new scanning strategy, which we call pulsed MPI (pMPI), and demonstrates how it circumvents the problems discovered in Chapter 3. pMPI is a huge departure from conventional continuous-wave MPI (cwMPI), with its hallmark being square-like pulsed excitation waveforms. Its ability to unlock the cubic scaling potential of large core size SPIOs will prove enabling for nanoparticle development that has been unable to proceed past ~ 25 nm core sizes. Furthermore, the transition of MPI from continuous wave to pulsed excitation sequences could mark the beginning of pulse sequencing in MPI, with parallels to pulse sequencing in MRI, which is an extremely vast and still growing field.

Chapter 5 takes a step back into conventional cwMPI, and exploits the high-throughput and frequency-flexible nature of the AWR to perform an optimization of the MPI excitation/drive waveform across an unprecedentedly large parameter space and across a wide range of SPIOs. The results will prove useful for MPI system designers to improve current MPI scanners with minimal hardware modifications.

Chapter 6 challenges the commonly held notion in MPI that each SPIO nanoparticle exists as non-interacting entities. SPIO nanoparticles were made to strongly interact with each other during MPI scanning, and the results from this Strongly-Interacting MPI (SiMPI) show dramatic improvements in both SNR and spatial resolution. The crux of this MPI scanning strategy depends on creating favorable conditions for individual SPIOs to gather and strongly interact. The resultant system was modeled as a positive feedback system, taking inspiration from Schmidtt triggers in electrical engineering, and this positive feedback enables near-step-function-like

magnetization response which in turn becomes a delta-function-like point-spread-function which closely approaches the MPI ideal point-spread-function. Initial results are very promising, with two orders of magnitude improvement in SNR and 10-fold improvement in spatial resolution over the current gold standard of Resovist^{TM}with cwMPI.

I hope the several novel scanning strategies demonstrated in this work will serve to advance Magnetic Particle Imaging (MPI) and make it a more compelling imaging modality. There is still so much to discover and create in MPI and I believe that the breadth of work presented here is only the tip of the iceberg and will help to demonstrate the vast area still unexplored in MPI that could be harnessed for dramatic improvements in MPI performance.

Chapter 2

Design and Construction of the Arbitrary Waveform Relaxometer

2.1 Attribution

2.2 Introduction

To enable investigations in novel scanning strategies, new hardware must be designed and constructed that is capable of flexible, almost arbitrary, scanning and excitation trajectories. The current MPI hardware available are all single tone or have a handful of limited frequencies that are swapped by changing the tuning capacitor (Croft et al., 2016). As such, in this chapter, we detail the design of novel hardware capable of arbitrary waveform excitation. This device is a tabletop scanner capable of assessing the MPI performance of many different types of MPI waveforms. To make the design specifications realistic, we limited the specifications to only cover the human-safe parameter space for MPI waveforms (in terms of effective amplitude and frequency) as outlined in prior work (**saritas˙2013**). Regardless, this parameter space is still very large. We demonstrated an unprecedented 400 kHz excitation bandwidth and capability of high-throughput acquisition of harmonic spectra (100 different drive-field frequencies in only 500 ms). We also demonstrate the first capability of arbitrary drive-field waveforms which have not been experimentally evaluated in MPI to date. The

high-throughput capability, frequency-agility and tabletop size makes this Arbitrary Waveform Relaxometer/Spectrometer (AWR) constructed in this study a significant advance in MPI hardware and a convenient yet powerfully flexible tool to enable high-throughput, comprehensive investigation and optimization of the MPI excitation waveform / scanning strategy.

2.3 Background

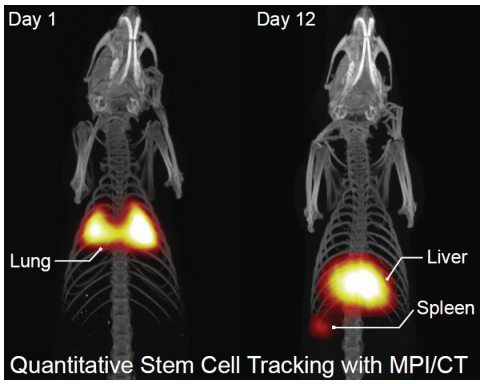

FIGURE 2.1: A representative MPI image showing visualization of the biodistribution of magnetic particle labeled stem cells after they were injected into the tail vein of a rat. This image demonstrates the high sensitivity and contrast of MPI and the capability to perform long-term, *in vivo* biodistribution studies without the exponential loss of signal typical in nuclear medicine studies. However, as shown by the image of the lung, liver and spleen in Figure 1, the spatial resolution of MPI is limited and a prime target for improvement. We demonstrate in this paper that the AWR enables high-throughput drive waveform optimization for better MPI resolution.

The spatial resolution of native MPI images, limited by scanner hardware and the magnetic behavior of MPI tracers at around 1 mm currently, is a prime target for improvement. This is an important limitation especially when MPI is used for visualization of anatomy. For example, in Figure 2.1, which is a representative MPI *in-vivo* image of stem cell tracking, the shape of the spleen is not well resolved. Most of the effort to-date has been directed to designing better MPI tracers (Ferguson et al., 2015b; Ferguson et al., 2013b; Ferguson, Khandhar, and Krishnan, 2012; Ferguson et al., 2013a; Ludwig et al., 2014; Khandhar et al., 2013; Arami et al., 2013; Dhavalikar and Rinaldi, 2014) and improved scanner hardware with higher magnetic gradients (Yu, Goodwill, and Conolly, 2015; Goodwill, Yu, and Conolly,

2015; Lyu et al., 2014). Recent literature have shown that the drive waveform affects MPI spatial resolution (Kuhlmann et al., 2015; Croft, Goodwill, and Conolly, 2012; Shah, Ferguson, and Krishnan, 2014; Tomitaka et al., 2015; Vogel, 2014; Croft et al., 2016; Sarica and Saritas, 2015). Unfortunately, current MPI hardware is limited to only sinusoids at a few discrete frequencies (Ludwig, Wawrzik, and Schilling, 2012; Wawrzik, Ludwig, and Schilling, 2010; Schilling et al., 2013; Biederer et al., 2009a; Lyu et al., 2014; Goodwill and Conolly, 2010; Buzug et al., 2012; Saritas et al., 2013b; Goodwill et al., 2012d; Yu, Goodwill, and Conolly, 2015; Goodwill, Yu, and Conolly, 2015; Goodwill et al., 2012b). Multiple simultaneous frequencies (Philips-Bruker 3D Fast MPI demonstrator scanner (Rahmer et al., 2015)) is limited to a narrow range (24.51 kHz, 25.25 kHz, and 26.04 kHz). Discrete drive frequencies at 10, 25, 50 and 100 kHz was shown by Kuhlmann et al. (Kuhlmann et al., 2015), although denser frequency sampling is helpful in optimizing for both spatial resolution and signal strength. Also, the use of two frequencies to decouple signal intensity and SPIO mobility information by Kuhlmann et al. (Kuhlmann et al., 2016) suggests that denser frequency sampling could further optimize color MPI contrast. Furthermore, the use of square waves in the ferrofluid literature (Shliomis, 1974; Shliomis and Raikher, 1980) and constant velocity scanning (same scanning trajectory as triangular drive wave) by Vogel et al. (Vogel et al., 2014) showing benefits of simplified reconstruction suggest that various unexplored arbitrary drive-field waveforms could be useful in MPI.

All of these recent studies suggest that a high-throughput, frequency-flexible, arbitrary-waveform MPS device will be of significant interest to the MPI community for optimizing drive waveforms for spatial resolution, signal strength and contrast. In order to build hardware capable of arbitrary drive frequencies, the main technical challenges are to generate MPI drive fields with a wide bandwidth while reducing direct feedthrough and reactive power. Previous MPI hardware have been unable to meet this requirement as bandstop filters are used to deal with feedthrough and/or tuned circuit elements are used for reactive power handling (Graeser et al., 2013; Behrends, Graeser, and Buzug, 2015; Goodwill et al., 2011a; Erbe, Sattel, and Buzug, 2012; Fidler et al., 2015; Debbeler et al., 2015). Figure 2.2b shows a typical circuit design in conventional MPI hardware. Thus, prior work has been limited to a few discrete drive frequencies. Changing frequencies require time-consuming switching of tuning capacitors (Behrends, Graeser, and Buzug, 2015; Goodwill et al., 2011a), although some frequency-tunability within a small bandwidth (19 – 25 kHz) is possible (Behrends, Graeser, and Buzug, 2015).

In this paper, we present a novel Magnetic Particle Spectrometer that is uniquely capable of high-throughput and comprehensive optimization of the MPI drive waveform. We greatly expand the optimizable parameter space with unprecedented frequency agility across DC – 400 kHz (Figure 2.3c) and capability for non-conventional drive waveforms. We also obtain harmonic spectra at 100 different drive frequencies ($16 - 115$ kHz) within a single 500 ms acquisition (Figure 2.4a), demonstrating more than 100-fold improvement in throughput due to time savings from instantaneous frequency switching. Because we have validated against an MPI imager the accuracy of spatial resolution measurements from this device (Figure 2.5b), this hardware allowed for the first time experimental evaluation of MPI performance under arbitrary drive waveforms (Fig. 2.6 and Fig. 2.7). Thus, the AWR's tabletop size without need for dedicated facilities poses it as a convenient yet powerfully flexible tool for nanoparticle experts looking to characterize magnetic nanoparticles as well as MPI systems designers looking to optimize drive waveforms for MPI resolution and signal strength.

2.4 Design and Methods

2.4.1 Working Principles of Magnetic Particle Imagers

The basis of MPI is the non-linear magnetization response of superparamagnetic iron oxide (SPIO) tracers. Magnetic gradient fields are applied in order to magnetically saturate SPIOs in all spatial regions other than the field-free-region (FFR) of the gradient field. The FFR may be shaped as a line (FFL) or as a point (FFP). The FFR is then shifted rapidly (at frequencies of 10 – 25 kHz) by a drive coil and the corresponding induced signal from the magnetization response of SPIOs spatially located at the FFR is picked up by an inductive receive coil. The combination of the gradient and drive coils shift the FFR across the entire field of view and allows reconstruction of the image from the voltage time series. Reconstruction can be done in the frequency domain by obtaining a system function and then solving the inverse problem of the spectral image data (Rahmer et al., 2009). This can also be done in the time domain by mapping the time domain signal to a spatial grid through knowledge of the instantaneous FFR location (Goodwill and Conolly, 2010). In the literature the former approach is often referred to as system matrix reconstruction while the latter is referred to as x-space reconstruction (Goodwill and Conolly, 2010; Goodwill et al., 2012d; Goodwill et

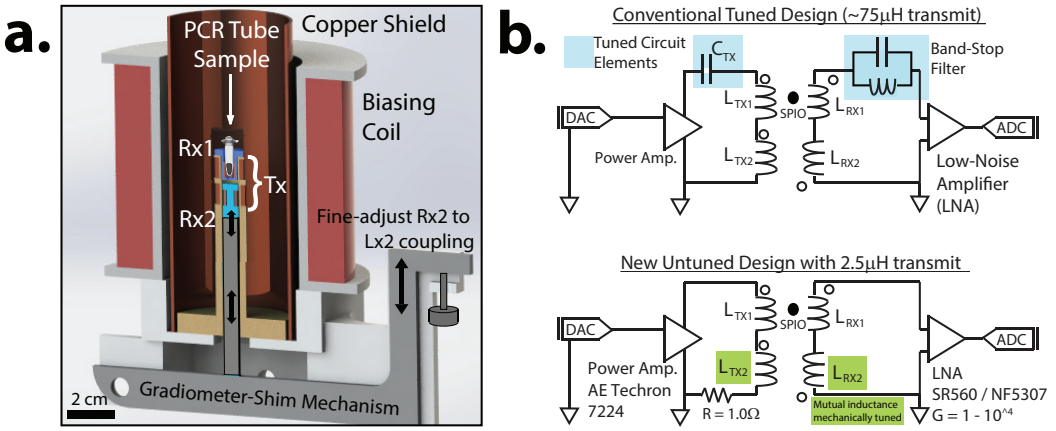

FIGURE 2.2: **a.** To-scale Solidworks™ drawing of our arbitrary waveform relaxometer (AWR) accurately representing the actual physical device. It comprises a miniature drive coil (Tx) with a low net inductance of 2.5 μH, two receive coils in gradiometric configuration (Rx1, Rx2), and a biasing coil to extend the applied field range. The gradiometer-shimming mechanism shifts Rx2 relative to Tx2 in increments of 22 μm to fine-tune the Tx2-Rx2 coupling to match that of Tx1-Rx1, minimizing net Tx-Rx coupling. The concept of cancellation amplitude adjustment for inductive decoupling is not new (Goodwill et al., 2011a; Graeser et al., 2013), but our novel mechanical implementation allows for in-bore facile precision "spatial-shimming" allowing for simultaneous feedback of gradiometer performance during adjustment. The in-bore adjustment is important because removing, adjusting then re-inserting the receive coil into the MPS setup may incur placement error and we have shown in Figure 2.3a that even tens of microns can affect gradiometer performance. Prior hardware using inductive decoupling (Goodwill et al., 2011a; Behrends, Graeser, and Buzug, 2015; Graeser et al., 2013) do not allow in-bore adjustment. **b.** Prior sinusoidal MPI spectrometers/relaxometers requires capacitors in the transmit chain to reduce reactive power and/or a band-stop filter (BSF) in the receive chain to reduce feedthrough. However, arbitrary drive waveforms precludes the use of tuned circuit elements. Instead, the AWR's novel untuned design relies on a very low coil inductance of 2.5 μH coupled with a high coil efficiency of 1.06 mT/ampere for transmit power handling. An improved gradiometer is used for broadband feedthrough attenuation on the receive.

al., 2012b; Croft, Goodwill, and Conolly, 2012; Lu et al., 2013; Goodwill and Conolly, 2011a; Tamrazian et al., 2011).

High quality MPI requires a large magnetic moment and a steep dynamic magnetization curve or M(H) response. This yields a sharp Langevin curve. In the frequency domain, this implies higher amplitudes for all harmonics and a gentle slope of the harmonic decay envelope (Kuhlmann et al., 2015). In x-space reconstruction, this corresponds to a tall and narrow point-spread function (PSF) where spatial resolution is quantified with the

Houston criterion (Houston, 1927). In this paper, we will use x-space reconstruction. Similar conclusions may be obtained with harmonic or system-matrix reconstruction.

As such, the non-normalized peak height of the x-space PSF and its FWHM are thus key parameters for characterizing tracer performance in MPI. Deconvolution could be applied in post processing to improve resolution as demonstrated in prior MPI work (Weizenecker et al., 2009; Rahmer et al., 2009; Rahmer et al., 2012; Knopp et al., 2011).

2.4.2 Design of the Arbitrary Waveform Spectrometer / Relaxometer

To measure these key MPI performance metrics, an MPI relaxometer or spectrometer is necessary. Magnetic Particle Spectrometers (MPS) were first developed in 2009 by Biederer et al. (Biederer et al., 2009a) and 2010 by Wawrzik et al. (Wawrzik, Ludwig, and Schilling, 2010) and measures the SPIO response to a pure tone drive field. Because no gradients are used, the response is that of a SPIO point source located at the FFP (or another location if a homogeneous biasing field is applied). Other magnetization characterization devices are typically inadequate in obtaining these MPI performance metrics because the field amplitudes needed to reach the non-linear regions of the tracer magnetization curve are not achieved in AC susceptometry (Kuhlmann et al., 2015). Furthermore, static measurements such as Vibrating Sample Magnetometry (VSM) are inaccurate in predicting MPI performance at 10 – 25 kHz because of temporal relaxation effects (Croft et al., 2016). Figure 2.3 compares the capabilities of an MPI relaxometer and other characterization tools and shows that AC susceptometry and Vibrating Sample Magnetometry (VSM) only cover a small fraction of the MPI-relevant parameter space.

To achieve the high magnetic field amplitudes needed to excite the MPI tracers, reducing reactive power required by the drive coil is necessary. While prior work uses tuned circuit elements to achieve this (Graeser et al., 2013; Behrends, Graeser, and Buzug, 2015) (Fig. 2.2), arbitrary drive waveforms need a wideband method to reduce reactive power. Miniaturizing the MPI drive coil (Tay et al., 2015a) is one way to do this.

All transmit and receive coils were wound on custom-designed, miniature 3D-printed bobbins or scaffolds depicted in Figure 2.2. Our solenoidal drive coil has 18 turns of 175/44 served litz copper wire with 8.4 mm inner diameter and 1.9 cm length. The detector (receive) coil fits inside the drive

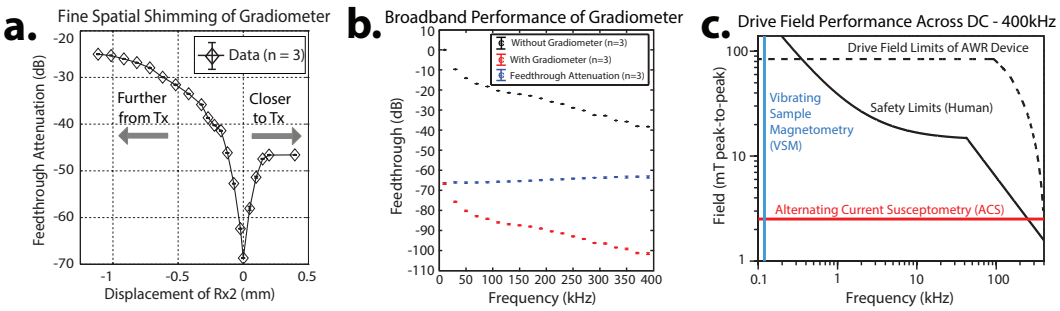

FIGURE 2.3: **a.** Demonstration of improved gradiometer performance via fine "spatial-shimming" the cancellation coil (Rx2) location relative to the transmit coil (Tx). This has the effect of fine adjusting the Rx2-to-Tx coupling factor for improved inductive decoupling reaching up to -67 dB (10 kHz). **b.** The gradiometer is capable of wideband feedthrough attenuation which is essential in the AWR's wideband excitation context. **c.** The very low drive coil inductance of 2.5 μH coupled with high coil efficiency of 1.06 mT/ampere enables high field amplitudes across an unprecedented DC – 400 kHz despite not using resonant circuits for reactive power handling. When compared to the safe scanning limits for a human (Saritas et al., 2013a), we see that the AWR's unprecedented drive-field flexibility allows for testing of almost any drive waveform that would be used in a safe human scanning context, enabling comprehensive drive waveform optimization. In contrast, conventional VSM (Mészáros, 2007) and AC Susceptometry (Chen, 2004) are unable to cover the MPI-relevant parameter space. We limit our device design to below 400 kHz because near zero-field, the delay from magnetic relaxation is expected to be > 2 μs (Deissler, Wu, and Martens, 2014), surpassing a half-period of the drive waveform and causing poor resolution.

coil and has 20 turns of 100/44 served litz copper wire shaped to the sample holder (0.2 mL PCR tube) dimensions. A duplicate set of detector coil is spaced ~ 4 mm away and connected in series to the primary for gradiometric cancellation. The net drive coil inductance and efficiency are 2.5 μH and 1.06 mT/A respectively. This results in significantly lower reactive power compared to prior work with 75 μH inductance and 0.77 mT/A drive coil efficiency (Behrends, Graeser, and Buzug, 2015). Thus, the AWR is capable of wideband excitation at any frequency between $DC - 400$ kHz and at field amplitudes of up to 86 mTpp (Fig. 2.3). The limit of 400 kHz is because magnetic relaxation times (Deissler, Wu, and Martens, 2014) approach the drive wave period causing poor resolution and SAR safety limits are < 1 mTpp beyond 400 kHz (Saritas et al., 2013a).

The spatially homogenous drive field is generated by an untuned solenoid powered by a DC-coupled power amplifier (AE Techron 7224) with pulsed power of up to 1.2 kW. Drive field inhomogeneity within the sample volume of 25 μL is $< 1\%$. While the small dimensions reduces sample

capacity to 25 μL, SNR per unit volume is improved (Webb, 2007), and sufficient SNR (> 10) even for cell labeling studies ($\sim$20 μg/mL) (Minard et al., 2013) is achieved. To match the load to the AE Techron 7224 optimal load range, a $1.0\ \Omega$ heatsink-mounted non-inductive resistor (LPS800 thick film resistor, Vishay Sfernice) was added in series to the transmit coil (Fig. 2.2b).

The next technical challenge is to deal with direct feedthrough interference which is typically many orders of magnitude higher than the SPIO signal (Behrends, Graeser, and Buzug, 2015). For single tone excitation, the signal lost when filtering out the first harmonic can be recovered by a continuity algorithm (Lu et al., 2013) since first harmonic information lost corresponds to a local DC offset. Therefore prior relaxometers using monotonal excitation have relied on analog bandstop filters (Fig. 2.2) to remove the excitation feedthrough (Croft, Goodwill, and Conolly, 2012).

Unfortunately, in an arbitrary drive waveform context, the excitation feedthrough is wideband and analog bandstop filtering across such a wideband would likely render recovery of the tracer signal impossible. Therefore, gradiometric (wideband) attenuation of the direct feedthrough is the only practical method to reduce field feedthrough interference from tracer signal. A duplicate setup as cancellation unit idea (Graeser et al., 2013; Behrends, Graeser, and Buzug, 2015) perpendicular Tx and Rx (Reeves and Weaver, 2014) idea, and three-section gradiometer (Schulz et al., 2015; Utkur and Saritas, 2015) have been proposed. We chose a two-section gradiometer design that is conceptually similar to first idea but with implementation of a novel mechanical design to adjust cancellation signal amplitude. This improved our wideband analog gradiometric attenuation of direct feedthrough to around -67 dB (-67 dB at 10 kHz and -63 dB at 400 kHz) as shown in Figure 2.3.

After analog gradiometric attenuation, the received SPIO response is (analog) amplified by the SR560 low-noise preamplifier (Stanford Research Systems, USA) at 1 MHz bandwidth or the NF5307 differential amplifier (NF Corporation, Japan) at 10 MHz bandwidth. The amplified signal is then digitized at 10 MSPS by a 12-bit ADC (National Instruments PCI-6115, Austin, TX, USA). A baseline subtraction (background correction) is then performed digitally to further reduce residual feedthrough interference. To expand the field of view, we use a bias coil (Fig. 2.2) that produces up to $\pm$ 120 mT homogeneous field when driven by a current-controlled amplifier (AE Techron LVC5050, Elkhart, IN, USA). The system is controlled using custom software written in MATLAB (Mathworks MATLAB, Natick, MA, USA).

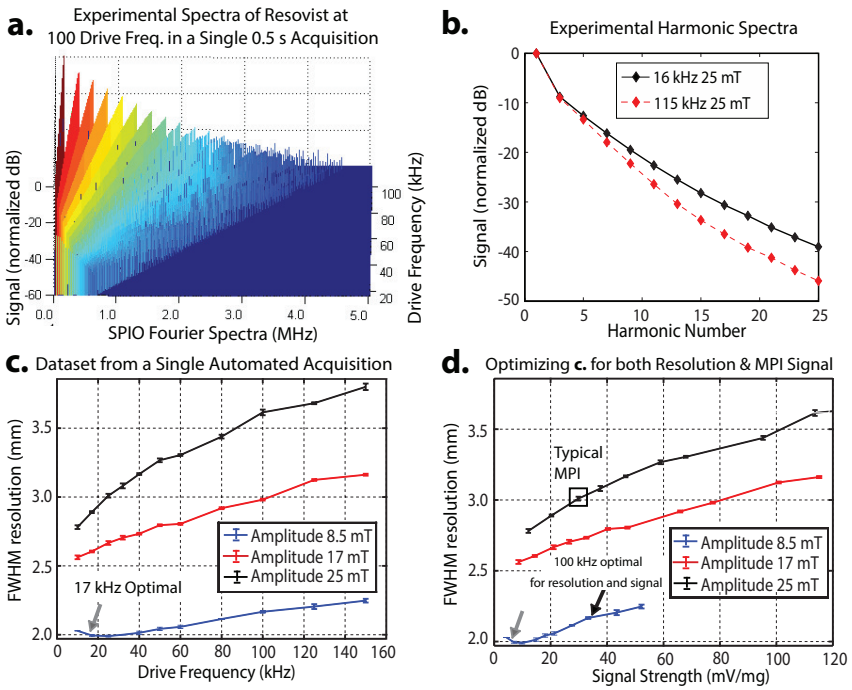

FIGURE 2.4: **a.** High-throughput magnetic particle spectrometry is enabled by the lack of tuned circuit elements in the AWR. In a single automated acquisition (500 ms total time), we discretely sample 100 drive frequencies from 16 kHz to 115 kHz at 25 mT. The data from this single acquisition is shown as a stack plot of Resovist fourier spectra for 100 discrete drive frequencies (after background correction and removal of out-of-band signal). **b.** Analysis of the spectra in Fig. 3a shows the expected steeper slope of harmonic decay with higher drive frequencies. This matches the findings of prior work (Kuhlmann et al., 2015). A steeper slope implies a poorer modulation transfer function response leading to poorer spatial resolution. **c.** From a single automated acquisition, 33 unique sets of drive parameters were tested (n = 3) on 125 μg of Resovist. The optimal drive waveform (gray arrow) with best resolution is with a 17 kHz, 8.5 mT amplitude waveform. The FWHM resolution (mm) assumes a 3.5 T/m gradient. **d.** The same dataset from part c is plotted for both spatial resolution and signal strength. While the lowest amplitude and frequency (gray arrow) gives the best spatial resolution, this is at a significant cost of almost 10-fold lower signal strength which has implications for MPI sensitivity. The high-throughput and denser sampling of frequency uniquely allows the AWR to better optimize for both spatial resolution and signal strength. This reveals the 100 kHz, 8.5 mT amplitude waveform (black arrow) which shows almost as good resolution improvement as the gray arrow while having *no loss in signal strength*, therefore having better overall MPI performance than the waveform obtained from simply optimizing for one parameter.

2.4.3 Nanoparticle Tracers

Aqueous suspensions of Resovist^{TM} superparamagnetic iron oxide particles (Bayer Healthcare, Germany; 0.5 mmol Fe/mL) were used. Resovist is

widely used in MRI (Reimer and Balzer, 2003; Schmitz et al., 2006; Wang, 2011) and in MPI (Nohara et al., 2013; Ishihara et al., 2013; Kuhlmann et al., 2015; Croft, Goodwill, and Conolly, 2012; Shah, Ferguson, and Krishnan, 2014; Croft et al., 2016). Although Resovist is known to have a very heterogeneous nature, the representative core diameter is $\sim 17 \pm 4$ nm (Croft et al., 2016). Unless otherwise stated, all experimental measurements employed 25 μL of Resovist diluted to 5 mg Fe / mL.

Senior Scientific Precision MRX^{TM} SPIOs (Azano Biotech, Albuquerque, NM, USA) with carboxylic acid coated outer shell and 32.1 nm core diameter was also used. Unless otherwise stated, all experimental measurements employed 25 μL SPIOs at 5 mg Fe / mL.

2.4.4 Animal Procedures

All animal procedures were approved by the Animal Care and Use Committee at UC Berkeley and carried out in accordance with the National Research Councils Guide for the Care and Use of Laboratory Animals. For figure 2.1, immunocompetent 7-week old female Fischer 344 rats weighing approximately 130 g were imaged with MPI. Animals were fed on a diet of Teklad Rodent Diet 2018 (Harlan, Indianapolis, IL) ad libitum. The rats (2 groups of n = 3) received tail vein injections of 5×10^6 to 8×10^6 Resovist-labeled hMSCs in 1 mL PBS. The hMSCs used were labeled with 40 μg Fe / mL of Resovist in cell culture solution using methodology similar to previous studies (Hsiao et al., 2007). A custom animal bed was used to support the animal under isoflurane anesthesia (2%, 1.5 L/min) within a MPI scans used a $4 \times 3.75 \times 10$ cm FOV and a 9 minute acquisition. Although MPI scans have been performed *in vivo* on live animals (Zheng et al., 2015), for figure 2.1 the animals were sacrificed using isoflurane overdose for postmortem co-registered MPI and CT imaging at 1 day and 12 days post-injection. CT images were acquired (RS9-80 CT, 25 min acquisition, 184 μm isotropic resolution) as an anatomic reference and the resultant MPI-CT 3D images were co-registered visually using SPIO-glass fiducial markers with Osirix Imaging Software (Pixmeo SARL, Switzerland).

2.4.5 MPI Tracer Characterization using Sinusoidal Drive Waveform

The AWR measures the PSF of the SPIO sample, from which we can measure signal strength, spatial resolution and relaxation time constant (Croft et

al., 2016). Since it is not an MPI scanner, there are no gradient fields and the PSF is reported in units of magnetic field (mT). This can be easily translated to spatial distance (mm) by dividing by the MPI scanner gradient. The AWR drive coil produces a sinusoidal magnetic drive field at frequencies between 1 – 400 kHz with 1 – 43 mT peak amplitude. The bias coil simultaneously applies a linear ramp from 40 mT to -40 mT in 250 ms to ensure that the entire magnetic behavior of the sample, including the saturation regions, is interrogated. To reconstruct a PSF, we grid the velocity-compensated instantaneous induced voltage signal from our receive pick-up coil to the bins of a magnetic field grid via interpolation from the instantaneous applied field magnitude to the grid. We only use data corresponding to the center 10% of each half-period bracketing the zero-crossing for higher SNR. As the first harmonic is kept, DC recovery (Lu et al., 2013) is not applied to each partial FOV or imaging station (Lu et al., 2013; Croft et al., 2016; Gleich et al., 2010; Rahmer et al., 2011; Schmale et al., 2011). Overlapping points are averaged within each 0.1 mT wide bin to form the resultant PSF with edges set to zero. Positive and negative velocity scans are reconstructed separately.

Theoretical x-space PSFs were computed using MATLAB software (Mathworks MATLAB, Natick, MA). To model the effect of relaxation with any arbitrary transmit pulse sequence, we use the MPI Debye model for magnetic relaxation validated in Croft et al. (Croft, Goodwill, and Conolly, 2012; Croft et al., 2016) with the specific equation:

$$\frac{\mathrm{d}M(t)}{\mathrm{d}t} = -\frac{M(t) - M_{\mathrm{ss}}(t)}{\tau_{\mathrm{eff}}} \tag{2.1}$$

where $M(t)$ is the instantaneous magnetization as a function of space, $M_{\mathrm{ss}}(t)$ is the steady-state (Langevin) magnetization, and τ_{eff} is an effective, phenomenological magnetic relaxation time constant. Since there is no gradient that is present, M and M_{ss} have no spatial dependence.

The exact pulse sequence used in the AWR was used for simulations. The inductive signal for a point source under the AWR pulse sequence was calculated by equation 2.1 under a finite difference method at 10 MHz sampling rate. This is equal to the AWR analog sampling rate and sufficient to capture the dynamics of relaxation times of more than 0.2 μs. As with experimental data, the simulated data was reconstructed using the gridding procedure outlined above. To validate our AWR hardware, we replicated the sinusoidal excitation parameters of 30 mT and 9.3 kHz used in prior work (Croft et al., 2016). For theoretical PSF modeling we used the validated relaxation time constant of 2.3 μs and Resovist parameters of 17 nm

mean core size with 4 nm standard deviation from prior work (Croft et al., 2016). We then compared the PSF from AWR data to the theoretically calculated PSF.

To further verify the accuracy of spatial resolution predictions from our novel relaxometer (AWR), we compare resolution predictions of the AWR to measured *image* resolution in our Berkeley MPI imager (23 kHz and varying field strengths). The imaging scanner has been validated in our previous publications (Saritas et al., 2013b; Goodwill et al., 2012b; Croft et al., 2016). We use the image resolution values of the scanner from prior work (Croft et al., 2016) and compare them to the PSF FWHM from our AWR data by dividing by the scanner gradient (3.5 T/m). To ensure an accurate comparison, we used the same frequency (23 kHz) and field strengths that were used to obtain the image resolution values in Croft et al. (Croft et al., 2016). To account for the finite size of the phantoms used in the MPI imager, the AWR-measured PSF was convolved with the dimensions of the phantom in the measurement direction (1.0 mm diameter) before measurement of FWHM. The coefficient of determination (R^2) between the imager-measured FWHM and AWR-measured FWHM was then calculated.

2.4.6 Novel Implementation of Arbitrary Drive Waveforms

To demonstrate frequency-agility, we implemented on the AWR a linear chirp across DC – 400 kHz (amplitude 10 mT). We also implemented a composite arbitrary waveform composed of four contiguous parts: (1) triangular wave at 10 kHz and 25 mT amplitude (2) linear chirp running from 10 kHz to 50 kHz at 25 mT amplitude (3) ramp running from -25 mT to 25 mT over 0.2 ms (4) composite waveform made up by adding sine waves of 8.3 mT amplitude at 5, 7 and 12 kHz. All drive waveforms were verified by the real-time current monitor on the AE Techron 7224 power amplifier. The real-time SPIO response to the arbitrary waveform was recorded for Resovist and Senior Scientific 32 nm SPIOs and plotted on the same graph. The SPIO signal traces are normalized for better visibility.

To measure the triangular wave PSF, the entire acquisition and reconstruction uses the same sine wave protocol described in the previous section but with the drive waveform changed to that of a triangular wave.

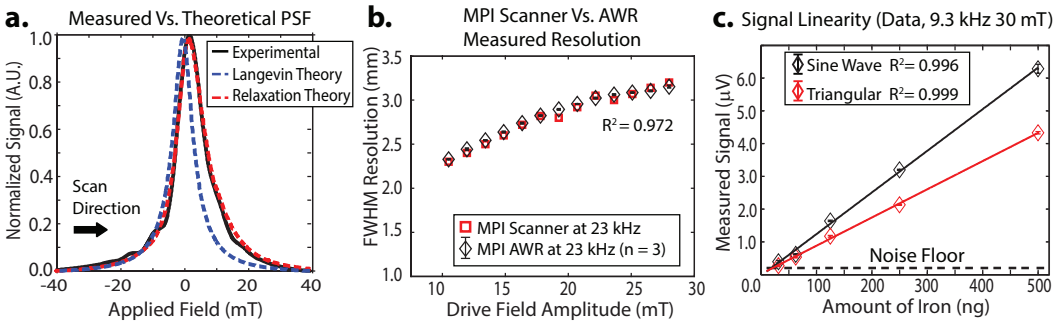

FIGURE 2.5: **a.** Reconstructed PSF from data obtained by the AWR compares well to the theoretical expected PSF with magnetic relaxation of a first-order Debye model. The calculation used the same value of τ (2.3 μs) validated in prior work (Croft et al., 2016). **b.** The FWHM of reconstructed PSFs from AWR data (n = 3) closely matches ($R^2 = 0.972$) actual spatial resolution measured from MPI scanner *images* (3.5 T/m gradient 23 kHz)Croft et al., 2016. This shows the AWR can accurately predict for MPI tracer *imaging* performance. **c.**The AWR signal (PSF peak amplitude) is linear with Resovist iron mass with sensitivity of 13.1 μV/μg for sine wave and 8.3 μV/μg for triangular wave before amplification. Three experimental repeats were taken per data point (n = 3). We estimate the detection limit (SNR = 1) to be $\sim$ 20 ng and $\sim$ 30 ng respectively with 6.25 s total acquisition time (25 averages). The AWR is thus a sensitive and quantitative sensor for magnetic particles. The difference in sensitivity between sine and triangular wave is due to differences in the waveform velocity at the zero-crossing point.

2.5 Results

2.5.1 Validation of the Accuracy of the Arbitrary Waveform Relaxometer

To validate the AWR, we compare data taken from the AWR with theory, prior work and imaging results. Figure 2.5a shows that the reconstructed PSF from AWR data closely matches the PSF calculated from theory (Croft et al., 2016). Figure 2.5b shows that the predicted resolution from the AWR closely matches ($R^2 = 0.972$) the measured resolution from scanner *imaging results*, demonstrating that the AWR can accurately predict *imaging* spatial resolution in MPI. This verification allows us to use the AWR to predict MPI performance with arbitrary drive waveforms that cannot be performed on any current MPI scanner to-date. Hence, the AWR is a powerful investigation tool to evaluate the pros and cons of arbitrary drive waveforms for MPI before scaling up to animal-size scanning.

2.5.2 Limit of Detection of 20 ng Fe

Different amounts of Resovist was diluted in DI water to $25\ \mu$L volume and measured for 6.25 seconds. The peak amplitude of the reconstructed PSF is linear with the amount of iron (Fig. 2.5), demonstrating the AWR is quantitative for SPIO amount. We observed the limit of detection (SNR = 1) to be $\sim$20 ng, showing more than 10-fold improvement from prior relaxometers (Goodwill et al., 2011a; Bauer et al., 2016a)

The improved sensitivity is likely due to these factors: (1) The small size of the receive coil increases SNR per unit volume (Webb, 2007). (2) improvements in gradiometer performance (Fig. 2.3) shifts the ADC dynamic range lower to capture weaker SPIO signals. (3) The signal at the first harmonic is kept and not discarded unlike prior relaxometers with bandstop filters at the first harmonic.

2.5.3 Automated High-Throughput Processing

Because the AWR does not rely on the tuned circuit elements used in all prior work, it is capable of a continuous and wide range of frequencies and thus well positioned to conduct digitally automated, high-throughput studies of drive waveform parameters. In prior work, changing drive frequencies typically required time-consuming manual switching of tuned circuit elements. Even if this process could be automated, having tuned circuit elements limits the available frequencies to discrete values and precludes arbitrary waveforms.

To demonstrate potential for automated and high-throughput studies, in Fig. 2.4 we acquire the Fourier spectra of Resovist at 100 different drive-field frequencies (sinusoidal drive-field) that was automatically taken in a single acquisition (total acquisition time of 500 ms). There is no manual hands-on requirement except for an initial sample insertion of the Resovist probe. With automated frequency switching and good SNR with only 5 ms per drive-field frequency, the AWR is more than 100-fold faster than prior work (Croft, Goodwill, and Conolly, 2012; Goodwill et al., 2011a; Tamrazian et al., 2011) requiring multiple capacitor exchanges to cover the same frequency range. The main time savings come from the rapid, capacitor-free frequency switching. Thus, measurement time can be increased above 5 ms if more SNR is desired. This demonstrates that the AWR can be automated to rapidly investigate the entire parameter space of drive frequency and amplitude for one tracer. Although not shown here, this could be easily extended to the parameter of arbitrary waveform shape as well.

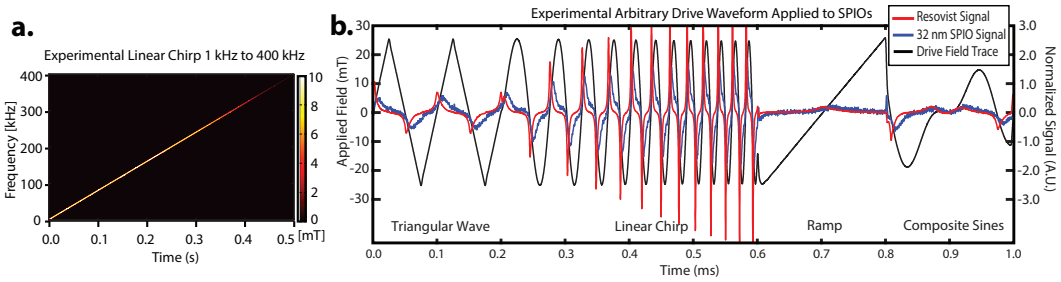

FIGURE 2.6: **a.** Experimental data showing the linear chirp from $1 - 400$ kHz produced by the AWR (spectrogram obtained from short-time Fourier Transform of AWR current monitor trace). Although the maximum slew rate of the power amplifier limits chirp amplitude beyond 200 kHz, this amplitude never falls below the SAR safety limits (Fig. 2.3) even at 400 kHz, thus covering the entire *safe* parameter space. **b.** The AWR is capable of arbitrary waveforms as shown by this composite waveform made up of arbitrary waveform parts: (1) triangular wave (2) linear chirp (3) ramp and (4) composite waveform made up by direct addition of 3 sine waves of equal amplitude but different frequencies (5, 7 and 12 kHz). The drive waveform shape is validated by the internal current monitor of the AE Techron 7224.

In addition, we demonstrate optimization of drive waveforms for better spatial resolution in Fig. 2.4c that plots FWHM resolution of Resovist against 33 sets of drive parameters (frequency and amplitude). Crucially, this dataset was obtained from a *single* AWR acquisition, demonstrating capability for high-throughput optimization. Because lower drive amplitudes were investigated here, the biasing coil was used to extend the applied field and limits throughput to the biasing coil slew rate. As a result, a longer acquisition time of 8.25 s is required. The data shows a trend of worsening resolution with larger drive-field frequency and/or amplitude. This matches the conclusions from prior work (Kuhlmann et al., 2015; Croft et al., 2016) and validates the accuracy of the AWR. For example, our data at 25 kHz and for amplitudes of 8.5, 17, 25 mT, have FWHM of 7.0, 9.4, 10.5 mT respectively. This closely matches the values of 7.0, 9.1, 10.3 mT from Croft et al. (Croft et al., 2016).

Furthermore, as a result of denser sampling of the drive frequencies, we are able to optimize the trade-off between spatial resolution and signal strength. For example, Fig. 2.4d shows a non-obvious drive waveform that gives the best resolution while having the same signal strength as a conventional MPI waveform.

2.5.4 Arbitrary Drive Waveforms

The AWR is capable of a linear chirp drive waveform from 1 kHz to 400 kHz (Fig. 2.6) within 500 ms, demonstrating the frequency-flexibility of the AWR. The chirp waveform amplitude starts to drop above 200 kHz due to power amplifier voltage slew rate limitations (Fig. 2.3). Furthermore, the AWR is capable of arbitrary drive waveforms as demonstrated by a waveform made up of contiguous arbitrary waveform parts: (1) triangular wave (2) linear chirp (3) ramp and (4) composite waveform (tri-tone). All drive waveform shapes are validated by the internal current monitor of the AE Techron 7224.

The response of two different SPIOs (Resovist and Senior Scientific 32 nm) are recorded. Visibly different responses to the arbitrary waveform in can be observed between Resovist and Senior Scientific 32 nm SPIOs because the larger 32 nm magnetic core SPIOs are known to have Brownian-dominant relaxation mechanisms and thus have a significantly delayed reaction to the applied field. These results suggest that the AWR is a good platform to test if non-sinusoidal waveforms may provide even better contrast between different SPIOs for colorized MPI imaging first pioneered by Rahmer et al. (Rahmer et al., 2015).

2.5.5 Wideband Feedthrough Attenuation

Because the analog feedthrough interference is no longer at a single frequency, bandstop filters cannot be used and the gradiometer becomes the only way to reduce analog feedthrough interference. In Fig. 2.3, we demonstrate that the gradiometer achieves wideband feedthrough attenuation of about -67 dB (-67 dB at 10 kHz and -63 dB at 400 kHz). We show similar limit of detection (SNR = 1) for a sine wave excitation (without bandstop filters) as that of a triangular wave excitation (Figure 2.5), demonstrating that the combination of inductive decoupling and baseline subtraction is effective regardless of monotonal or wideband feedthrough interference.

2.5.6 First Experimental Verification of x-space DC Recovery Algorithm

In prior work, feedthrough corruption of the first harmonic signal usually required analog bandstop filtering at the first harmonic. The lost first harmonic information is recoverable by a DC-recovery continuity algorithm during x-space reconstruction (Goodwill et al., 2012b; Lu et al., 2013). While

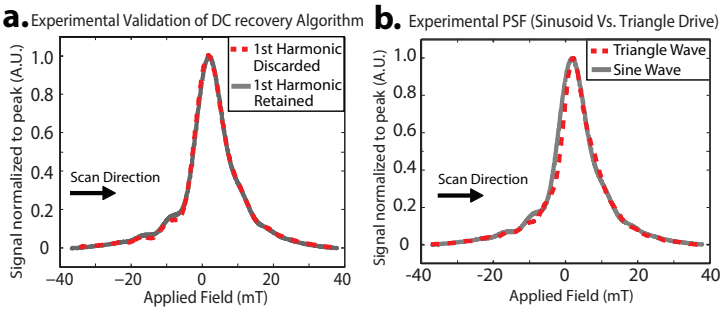

FIGURE 2.7: **a.** First experimental validation of the DC recovery algorithm used in x-space reconstruction. DC recovery of the discarded first harmonic information produces a nearly identical PSF to a PSF where the analog received signal at the first harmonic was retained. **b.** Experimentally reconstructed PSF for Triangle and Sine drive wave showing only minor differences. This is expected because a triangle and sine wave are similar, and the x-space theory in 1D shows that various trajectories with similar spatial sampling densities should yield the same reconstructed results, excepting variable impacts of magnetic relaxation. Importantly, this shows the triangle wave maintains conventional MPI performance while obviating velocity compensation which is a major reconstruction step.

this approach is well-posed and robust, removing this x-space reconstruction step could improve SNR and speed up reconstruction time. The theory and experimental demonstration of LSI properties are shown in Lu et al. (Lu et al., 2013), but due to prior relaxometer hardware limitations it was not possible to experimentally compare the DC recovery PSF to a PSF with first harmonic information retained.

Our AWR is able to perform this first x-space experimental comparison due to the improvements in gradiometer design as outlined in Fig. 2.2 that obviates the use of bandstop filter on the receive chain. As a result, the AWR is able to reconstruct the PSF while keeping the first harmonic information. In Fig. 2.7 we show this *first experimental* comparison of the reconstructed PSFs using (1) x-space DC recovery method and (2) without DC recovery (first harmonic information was not filtered out). The results demonstrate that the DC recovery algorithm is robust and produces a nearly identical PSF as the PSF from retaining the first harmonic information.

However, because the DC recovery stitching operation of partial FOVs depends on an edge continuity condition, the noise at higher harmonics will be propagated when recovering the first harmonic. Our experiments show an estimated 4-fold SNR boost when retaining the first harmonic information at low iron content (< 100 ng Fe).

2.5.7 First Experimental Demonstration of Triangular Wave Drive Waveform

Triangular drive waveforms are useful as MPI drive waveforms because they imply fully linear motion of the MPI field-free-point (FFP across the field-of-view (FOV) in the presence of linear background magnetic gradients. The benefits of simplified reconstruction due to constant velocity have been shown in the work on Traveling Wave MPI by Vogel et al. (Vogel et al., 2014) where a dynamic linear gradient array (replacing both drive and background gradient) generates constant velocity motion of the FFP while using sinusoidal drive for each element. To assess the performance of the SPIO under a triangular drive waveform, we tested the same Resovist sample with a sinusoidal and triangular excitation. Both drive waves have exactly the same frequency and amplitude (9.3 kHz and 30 mT), differing only in their shape. The PSFs are nearly identical showing that a triangle wave excitation has a similar MPI performance as that of a sine wave (Fig. 2.7) but with simplified reconstruction (constant velocity).

2.6 Discussion

The characteristics of the SPIO tracers used are critical to the imaging performance of MPI. While there are many tools available for analysis of these tracers such as Vibrating Sample Magnetometry, an MPI-specific tool is necessary for measurement of the *imaging performance* of tracers. Therefore, the main role of a magnetic particle relaxometer is to rapidly and accurately characterize MPI tracer performance in a convenient fashion. Here, we have demonstrated that our relaxometer is able to accurately obtain the PSF of the tracer of a gold-standard particle Resovist™ and these measurements matches well with theory, prior work (Croft et al., 2016), and most importantly, *imaging results* (Fig. 2.5). The actual measurement (without biasing coil) only takes $250 - 500$ ms and even with computation, time writing data to disk, and 25 averages, it takes less than 30 seconds to measure a sample at a 100 drive frequencies (Fig. 2.3a). The table-top size of our AWR, the relative simplicity of construction (no tuned circuit elements), and the combination of speed and unprecedented frequency-flexibility make it a powerful and convenient tool for MPI researchers.

Up till recently, Magnetic Particle Spectrometers only used very few discrete frequencies and were mainly for particle characterization at conventional MPI drive waveforms. However, recent work in the MPI literature

using Magnetic Particle Relaxometers / Spectrometers have demonstrated that both drive frequency and amplitude have a significant effect on MPI spatial resolution (Kuhlmann et al., 2015; Croft, Goodwill, and Conolly, 2012; Shah, Ferguson, and Krishnan, 2014; Tomitaka et al., 2015; Vogel, 2014; Croft et al., 2016). Furthermore, Vogel et al. (Vogel et al., 2014) showed through the work on Traveling Wave MPI the many compelling benefits of linear motion of FFP (achievable with triangular drive waveforms) due to the constant FFP velocity that simplifies the mathematics and facilitates image reconstruction. In addition, the use of two different frequencies to decouple signal intensity and SPIO mobility information as shown by Kuhlmann et al. (Kuhlmann et al., 2016) demonstrates the importance of varying drive frequency for contrast in color MPI. All of these suggest that it is of significant interest for Magnetic Particle Spectrometers (MPS) to take on a new and additional role of optimizing the MPI drive waveform as well.

An ideal MPS hardware for comprehensive optimization of the drive waveform would be high-throughput, frequency-flexible across a wide range of parameters and also capable of arbitrary waveforms. Towards this goal, we consider that the 3D MPI platform from Bruker and Philips (Gleich et al., 2010) is capable of 3 simultaneous drive frequencies (excitation field) but the frequencies are very close (24.51 kHz, 25.25 kHz, and 26.04 kHz). The MPS platform from Kuhlmann et al. (Kuhlmann et al., 2015) is capable of 4 discrete frequencies of 10, 25, 50 and 100 kHz, but it is of interest to more finely sample within this frequency range and beyond as shown by the non-obvious optimization results in Figure 2.4d. To date, there has been no MPS hardware with the above-mentioned ideal specifications of full frequency-flexibility, high-throughput and arbitrary waveforms.

In response to this, we have designed our AWR to have unprecedented frequency-flexibility across DC-400 kHz (up to 86 mTpp), unprecedented arbitrary-waveform capability with orders of magnitude higher throughput than prior spectrometers. Although there may be no resonant effects expected from the SPIO tracer, due to the multitude of performance metrics to simultaneously optimize for, there is significant utility in high-throughput, dense sampling of the frequency parameter. We demonstrate this by revealing an optimum waveform of 100 kHz, 8.5 mT for Resovist that allows for significantly improved spatial resolution without compromising signal strength. In contrast, optimizing only for spatial resolution (lowest frequency and amplitude) incurs a significant 10-fold loss in signal strength (Fig 2.4c) for marginal improvement in resolution.

While the wide, continuous frequency range of the AWR is useful, the

most unique feature of the AWR is the capability to generate and apply arbitrary drive waveforms. Such waveforms have never been experimentally evaluated in an MPI context and may contain much potential since recent pioneering work by Vogel et al. (Vogel et al., 2014) has increasingly pointed to the benefits of non-sinusoidal drive waveforms, in particular triangular waves. Since it is technically challenging and expensive to implement arbitrary waveforms on an imaging scanner, our novel AWR is an indispensable tool to evaluate the pros and cons of a proposed arbitrary drive waveform before implementing on a small-animal or human-scale. For example, in our comparison of a triangle drive waveform to an equivalent sine drive waveform (Fig. 2.7), we show that triangular drive waveforms are able to maintain similar MPI performance to conventional sinusoids while significantly reducing reconstruction computational load. In addition, as shown by the Arbitrary Waveform in Figure 2.6, the differing responses of Resovist and Senior Scientific 32 nm SPIOs to the different arbitrary waveforms suggests potential of our device to optimize waveform shape, amongst other parameters, to improve contrast between tracers for color MPI applications first pioneered by Rahmer et al. (Rahmer et al., 2015). The capability of the AWR is not limited to classic waveforms such as triangle and square waves, and more complex waveforms constructed by summing multiple basic or primitive waveforms are also possible as shown in Figure 2.6. While the full optimization of arbitrary waveforms for MPI performance is outside the scope of this paper, we have demonstrated the hardware capability to conduct this study.

2.7 Conclusion

Recent work from Kuhlmann et al. and Vogel et al. (Kuhlmann et al., 2016; Kuhlmann et al., 2015; Vogel et al., 2014) have pointed towards the importance of frequency-flexible and non-sinusoidal drive waveforms for improved MPI spatial resolution and SPIO relaxation contrast. As a result, it is of interest for Magnetic Particle Spectrometers (MPS) to optimize the drive waveform in addition to its basic role of particle characterization. Unfortunately, to date, there has been no MPS hardware capable of the wide-range frequency-flexibility or the arbitrary drive waveforms required for a comprehensive optimization. In response to this, we have designed a novel tabletop magnetic particle spectrometer and relaxometer (AWR) with high-throughput capability, unprecedented frequency-agility (DC – 400 kHz) and unique capability for arbitrary drive waveforms. This greatly expands the

parameter space available for drive waveform optimization. We believe the unprecedented flexibility of the AWR will be of interest to MPI system designers and nanoparticle experts seeking to optimize and tailor MPI drive waveforms to the SPIO tracers for improved spatial resolution, signal strength and microenvironment contrast.

2.8 Acknowledgments

I would like to thank Laura Taylor for her help in acquiring some of the datasets discussed in this chapter and Daniel Hensley for helping significantly with the software necessary to remotely operate and run the device smoothly and at high-throughput capability. Also, I would like to acknowledge Dr. Erika Vreeland and associates at Imagion Biosystems who provided us with a wide range of tracer samples to use in this study. Most importantly, I would like to thank Patrick Goodwill for inspiring me to the initial idea and design and Bo Zheng for all the advice to improve my device through its many prototypes. I would also like to thank all the AWR users in the BISL lab who have provided invaluable feedback needed to improve the instrument.

Chapter 3

The Relaxation Wall: Experimental Limits to Improving MPI Spatial Resolution by Increasing Nanoparticle Core size

3.1 Attribution

3.2 Introduction

Before embarking on an exploration of novel MPI scanning waveforms, we investigate the theoretical MPI performance predicted by Langevin theory and compare theory against experimental measurements of MPI performance. This lays the groundwork and motivation for subsequent chapters, as the realistic limitations and barriers that are experimentally proven in this study become the target for engineering a circumventing solution.

According to Langevin theory, one method to improve spatial resolution is to increase the magnetic core size of the superparamagnetic nanoparticle tracers. The Langevin model of superparamagnetism predicts a cubic improvement of spatial resolution with magnetic core diameter. However, prior work has shown that the finite temporal response, or magnetic relaxation, of the tracer increases with magnetic core diameter and eventually

leads to blurring in the MPI image. Here we perform the first wide ranging study of 5 core sizes between 18–32 nm with experimental quantification of the spatial resolution of each. Our results show that increasing magnetic relaxation with core size eventually opposes the expected Langevin behavior, causing spatial resolution to stop improving after 25 nm. Different MPI excitation strategies were experimentally investigated to mitigate the effect of magnetic relaxation. The results show that magnetic relaxation could not be fully mitigated for the larger core sizes and the cubic resolution improvement predicted by the Langevin was not achieved. This suggests that magnetic relaxation is a significant and unsolved barrier to achieving the high spatial resolutions predicted by the Langevin model for large core size SPIOs.

3.3 Background

3.3.1 Spatial Resolution in Magnetic Particle Imaging

Spatial resolution in MPI is closely linked to the shape of the M-H magnetization curve of the SPIO. A steeper M-H curve results in a narrower x-space point spread function. This also implies stronger higher harmonics leading to a better modulation transfer function for frequency domain reconstruction. This results in a more well-posed inverse problem leading to better SNR and less artifacts in the reconstructed image and therefore improved effective resolution. For an ensemble of ideal superparamagnetic nanoparticles, each with magnetic moment m, the M-H curve can be described by the Langevin function as follows:

$$M(H) = Nm\,\mathcal{L}(k_{\mathrm{sat}}H) \tag{3.1}$$

where $\mathcal{L}(x)$ is the Langevin function which is analytically defined as $coth(x) - 1/x$. The constant k_{sat} is determined by the magnetic properties of the nanoparticle and defined as:

$$k_{\mathrm{sat}} = \frac{\mu_0 m}{k_{\mathrm{B}}T} \tag{3.2}$$

The steepness of the M-H curve is closely linked to m which is defined as:

$$m = \frac{M_{\mathrm{sat}}\pi d^3}{6} \tag{3.3}$$

The magnetic core diameter d has a profound impact on the M-H curve and, correspondingly, spatial resolution in MPI. Previous studies on SPIO sizes from 13–19 nm have shown improved MPI resolution with increasing core size to 19 nm (Ferguson, Minard, and Krishnan, 2009; Ferguson et al., 2010). Similarly, studies on the Feraspin series (size-fractionated Resovist) show improved MPI spectra with increased size-fraction (Ludwig et al., 2012).

Rahmer et al., 2009 showed that MPI spatial resolution should be inversely proportional to the cube of the magnetic core diameter using the System Matrix MPI reconstruction method. Knopp et al., 2011 also showed the width of the convolution kernel highly depends on the particle size. Precisely the same resolution limit was derived for the x-space MPI reconstruction method (Goodwill and Conolly, 2010). For x-space reconstruction, the point spread function (PSF) that defines the spatial resolution of MPI is simply the derivative of the M-H curve. One can analytically solve for the full-width-half-maximum (FWHM), which is the standard Houston resolution criterion (Houston, 1927)). If the effects of magnetic relaxation are neglected, the 1D spatial resolution of MPI, for *both* System Matrix (Rahmer et al., 2009) and x-space MPI reconstruction (Goodwill and Conolly, 2010), is

$$\Delta x = \left(\frac{24\, k_{\mathrm{B}}\, T}{\mu_0\, \pi\, M_{\mathrm{sat}}} \right) \frac{1}{G d^3} \tag{3.4}$$

where G is the gradient strength in T/(μ_0m). This equation shows that MPI spatial resolution should improve *cubically* with increasing magnetic core diameter. Because resolution only scales linearly with gradient strength G, we are limited by cost, power and cooling constraints when improving MPI spatial resolution with stronger gradients (above 5 T/(μ_0m)). The gradient strength is also constrained by human safety limits, magnetostimulation and SAR limitations (Saritas et al., 2013a). Hence, it is enormously important to investigate the limits of the resolution improvement by increasing magnetic core diameter, and this will be even more important for scaling up to a human MPI scanners.

There have been numerous works on modeling the MPI nanoparticle response (García-Palacios and Lázaro, 1998; Weizenecker et al., 2010; Weizenecker et al., 2012; Graeser, Bente, and Buzug, 2015). Weizenecker et al. modeled the effect of anisotropy and frequency on the MPI performance for 20,25,30 nm particles. The study noted that high levels of anisotropy

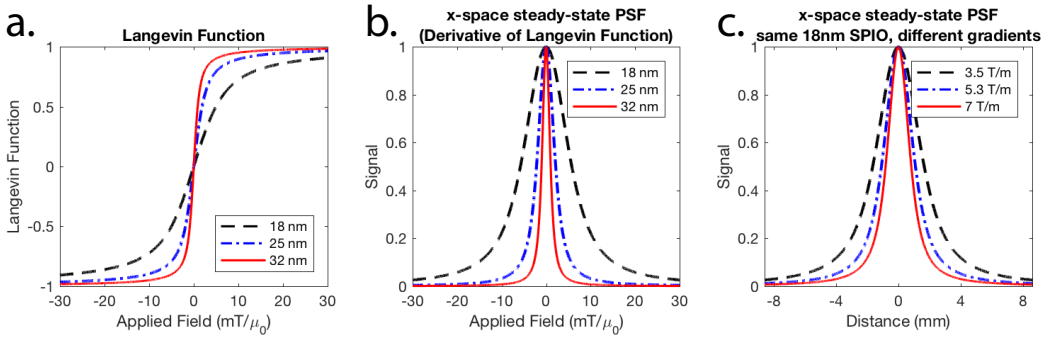

FIGURE 3.1: (a) Calculated Langevin curves (using eqn. 3) for different nanoparticle core sizes. The shape of the curves show a dramatic change with nanoparticle core size due to the cubic relationship between nanoparticle core size and saturation field. (b) Calculated MPI steady-state PSFs show a dramatic narrowing with increased core size. This is in contrast to the strategy of increasing MPI gradient strength shown in (c) where only a linear improvement of the PSF width is observed with increases in gradient strength. Because spatial encoding in MPI is a linear function of the magnetic field gradient, conversion between x-axis units of applied field (mT/μ_0) and distance (mm) is done simply by dividing by the gradient strength (T/μ_0m).

reduced the MPI performance to worse than the Langevin model prediction. Graeser et al. extended the Weizenecker model for 30 nm particles and showed how proper superimposition of shape semi-axis and the crystal axes during particle synthesis can give optimal MPI performance. Other research groups (Croft, Goodwill, and Conolly, 2012; Croft et al., 2016; Dieckhoff et al., 2016; Deissler, Wu, and Martens, 2014; Deissler and Martens, 2015; Dhavalikar et al., 2016) have also modeled how MPI spatial resolution varies with NP size, and with drive field frequency and amplitude. In general, all these studies have noted that larger SPIOs have longer magnetic relaxation times. While there are a multitude of models concerning the exact physical causes of magnetic relaxation, from an imaging perspective we are most concerned about time-delays and spreading of the MPI signal that will directly impact the reconstructed image. As such, we will define magnetic relaxation using the most general definition: the non-instantaneous response of the ensemble magnetization to the applied field (Croft, Goodwill, and Conolly, 2012). The general Néel and Brownian time constants involved in magnetic relaxation can be written as follows:

$$\tau_{\mathrm{N}} = N(H) \cdot \tau_0 \exp\left(\frac{KV_{\mathrm{c}}}{k_{\mathrm{B}}T}\right) \tau_B = B(H) \cdot \frac{3\eta V_{\mathrm{h}}}{k_{\mathrm{B}}T} \tag{3.5}$$

where $N(H)$ and $B(H)$ are functions that account for the effect of applied field, H, on the time constants.

These equations show that both relaxation mechanisms have longer time constants when the nanoparticle grows larger. When these relaxation times approach the period of the excitation waveform, a noticeable blurring effect results that reduces achievable resolution. Hence, larger NPs should improve resolution, but relaxation-induced blurring of larger NPs may obviate the improvements in spatial resolution. Here, we expand upon prior modeling work (listed above) by performing the first experimental study on the MPI imaging performance of nanoparticles across a wide range of core sizes from 18 to 32 nm. By observing these two opposing effects in practice, we determine the practical limits to improving MPI spatial resolution by increasing core size.

3.4 Materials and Methods

3.4.1 Magnetic Nanoparticles

Imagion Biosystems PrecisionMRX® superparamagnetic iron oxide nanoparticles (Imagion Biosystems, Inc. Albuquerque, NM, USA) with carboxylic acid coated outer shell and varying core diameters were used. The core is single crystalline magnetite (Fe_3O_4) for all core sizes. This is experimentally confirmed by prior work (Vreeland et al. 2015) with high resolution transmission electron microscopy (HRTEM) and X-ray diffraction. A representative data sample is found in the supplementary information of this reference. The nanoparticle shape and hence the shape anisotropy remains approximately uniform and does not change significantly with core size. This is evidenced by the TEM (JEOL 1200EX) images in Fig. 3.3a showing uniform spherical shape across all core sizes. The high isoperimetric quotients tabulated in Fig. 3.3b show that the deviation from an ideal sphere with increasing core size is very low.

To determine the particle core size distribution, synthesized nanoparticles were analyzed using small angle X-ray scattering (SAXS) with a Rigaku SmartLab diffractometer system and SmartLab Guidance system control software. Data analysis was performed using Rigaku NANO-Solver v3.5 software that uses a spherical particle shape with a Gaussian size distribution. The spherical shape assumption was experimentally confirmed by TEM analysis (see Fig. 3.3b.) Statistically, SAXS is a more rigorous technique for measuring size distribution because it is possible to measure a

large ensemble of particles with SAXS while TEM image analysis is practically limited to 100 – 1000 particles.

All SPIOs have same outer coating material and differ only in the magnetic core size. The core is covered by an inner monolayer of oleic acid coating and then encapsulated within a monolayer of a carboxylic acid functionalized amphiphilic polymer. The hydrodynamic diameter and zeta potential of all SPIOs was measured in deionized water pH 6.0 using a Malvern Zetasizer Nano ZS system. The zeta potentials of all SPIOs ranged between -40 and -50 mV. Hydrodynamic diameter scales with core size as described in Fig. 3.3a. This scaling is necessary to maintain a large enough coating buffer to prevent inter-particle aggregation.

Magnetization measurements were collected using a Quantum Design MPMS-7 SQUID magnetometer. The precise mass of iron in the sample was determined using a colorimetric assay as described previously (Vreeland et al., 2015). Magnetization curves were recorded from -4000 kA/m to +4000 kA/m at 293K. The field-dependent magnetization data was normalized to the mass of iron in the sample to determine the saturation magnetization (σ_{sat}). The measured saturation magnetization is $M_{sat} = 0.551T/\mu_0$ which is $\sim 92\%$ of the bulk magnetite value of $0.6T/\mu_0$ (Cullity and Graham, 2011). A representative M vs. H magnetization plot (25.0 nm particles) is also plotted in Fig. 3.3b. The exact synthesis and more characterization of the nanoparticles can be found in detail in the main article and supplementary information of (Vreeland et al., 2015). The MPI performance of the SPIOs was also measured using a magnetic particle spectrometer/relaxometer described in (Tay et al., 2016) as well as the x-space MPI scanner described in (Croft et al., 2016). Unless otherwise stated, all experimental measurements employed 25 μL SPIOs at 5 mg Fe / mL.

3.4.2 Magnetic Particle Relaxometer Experiments

The SPIOs of different core sizes were first tested on our arbitrary waveform relaxometer (AWR) which is described in detail in our prior work (Tay et al., 2015b; Tay et al., 2016). The AWR includes a non-resonant transmit coil design to enable frequency agility as well as arbitrary excitation waveforms. This table-top system does not have gradient fields for signal localization; instead, a sinusoidal excitation and linear bias field are superimposed to test the aggregate response of a sample in the applied magnetic field space. This system can reconstruct a 1D point-spread function (PSF) characteristic of the entire sample supplied to the device. To interrogate the entire Langevin M-H curve and even up to the saturation regions of the SPIOs, we scan with

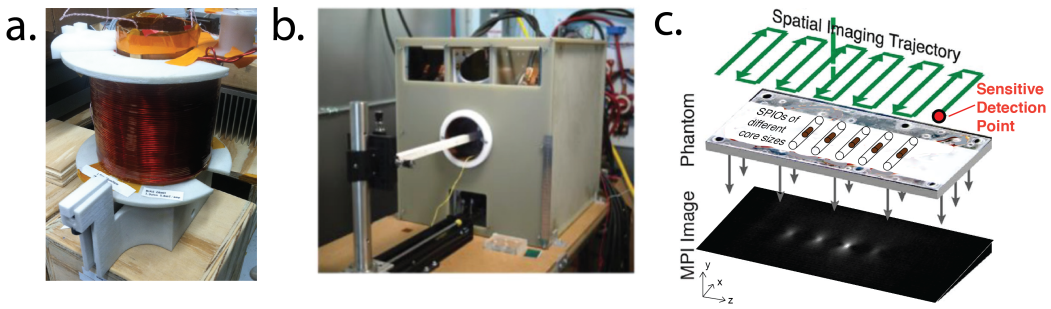

FIGURE 3.2: MPI hardware. (a) Magnetic Particle Relaxometer used to obtain point spread functions of SPIOs to measure the full-width-at-half-maximum spatial resolution. (b) Magnetic Particle Imager used to obtain images of SPIOs to validate the measurements of the relaxometer as well as provide visual images of the differences in spatial resolution as core size changes. (c) MPI obtains an image by rastering the field-free-point across the field of view as shown in the figure. The field-free-point can be considered a sensitive detection point in 3D space. In x-space reconstruction, the time-domain received voltage signal is gridded to the instantaneous location of the field-free-point to make an image.

the background (bias) field slowly decreasing from 60 mT to -60 mT across 0.2s. We have demonstrated the AWR measured 1D PSFs agree with 1D PSFs obtained using our gradient-based imaging systems (Tay et al., 2016). To translate the AWR PSF to a true imaging PSF, we only need to divide the DC field by the gradient strength. Reconstruction uses the middle 60 percent of the time-domain signal within a half-period, centered about the sinusoidal zero-crossing in order to maximize SNR. The 60 percent value is chosen to be similar to that used in the Berkeley 3D Magnetic Particle Imager. For Fig. 3.4, the drive waveform is a 20.25 kHz, 20 mT sine wave to match the drive field of the 3D imaging scanner used. For Fig. 3.7, the drive frequency and amplitude are as specified in the figure.

3.4.3 Magnetic Particle Imager Experiments

To verify the findings from the relaxometer experiments, we imaged a point source phantom by lining up 5 tubes (ID 0.7 mm, OD 1.3 mm) with 1 μL of 5 mg/mL SPIO inside each as shown in Fig. 3.5. We used our 3D MPI scanner with a 7 T/(μ_0m) FFP selection field, comprised of permanent magnet pair. An MPI image is formed by rastering the sensitive field-free-point (FFP) across the entire field-of-view and gridding the received voltage in an inductive pick-up coil to the instantaneous field-free-point position. The FFP is shifted by electromagnetic shift coils in the x and y directions and by the drive coil in z. A robot arm moves the sample in discrete steps in z to

compensate for limited amplitude of the transmit coil. The scanning setup is shown in Fig. 2c, where the green trajectory represents the field-free-point location in a y-plane. A homogeneous transmit solenoid adds a 20.25 kHz, 20 mT sine wave excitation along the z-axis, thus making the FFP zigzag (in the z-axis) as it moves along the green trajectory. This is done to sample the regions between the green trajectory lines. The magnetic field gradient is 7 T/(μ_0m) in the x-axis, and 3.5 T/(μ_0m) in the y- and z-axes. The field of view is $14.56 \times 4 \times 3.75cm^3$ and the total scan time is 9 minutes. Details on the 3D MPI scanner hardware and the image reconstruction algorithm have been published (**lu˙2013**; Saritas et al., 2013b; Goodwill et al., 2012a).

3.4.4 Calculation of Langevin Spatial resolution curves

In this paper, we use the Houston criterion for spatial resolution (Houston, 1927) that uses the full-width-half-maximum of the point spread function or imaging point source. The Langevin spatial resolution (red) curves plotted in Fig. 3.4 and Fig. 3.7 was calculated using the equation 3.4 (Langevin model of an ensemble of ideal magnetic nanoparticles) where the gradient strength G is 3.5 T/(μ_0m) to match the Berkeley Magnetic Particle Imager gradient. We use the experimentally measured nanoparticle $\mu_0 M_{\text{sat}}$ value of $0.551\ T$ for these calculations. T is set as 293 K.

3.5 Results

3.5.1 Spatial resolution stops improving beyond 25 nm core diameter

Imagion Biosystems PrecisionMRX® nanoparticles with core diameters between 18 to 32 nm were measured on the AWR and 1D point-spread-functions plotted. The results in Fig. 3a show that while the PSF narrows when core diameter increases from 18 nm to 24 nm, this trend reverses after 25 nm. This is concomitant with an increasing displacement in the direction of the scan. This behavior is similar to results from prior work (Croft et al., 2016; Croft, Goodwill, and Conolly, 2012) and is indicative of delay between the time-domain MPI signal and the applied field due to increasing magnetic relaxation. This results in blurring of the 1D PSF in the direction of the scan when the time-domain MPI signal is gridded to applied field values during reconstruction. As a result, the improved spatial resolution predicted by the steady-state Langevin PSF is not realized. The steady-state

a.

Core Diameter (SAXS)	Core Diam. σ (SAXS)	Hydrodynamic Diameter (Z-avg intensity)	PDI of coated particle (Z-avg intensity)	Concentration of Fe_3O_4	MPI Relaxometer FHWM*	Isoperimetric Quotient (1 denotes perfect circle)	
						Mean	σ
18.5 nm	1.5 nm	40.5 nm	0.106	5 mg/mL	16.7 mT/μ_0	0.97	0.03
21.6 nm	1.6 nm	35.9 nm	0.059	5 mg/mL	14.2 mT/μ_0	0.97	0.03
24.4 nm	1.6 nm	41.0 nm	0.029	5 mg/mL	12.0 mT/μ_0	0.94	0.03
27.6 nm	2.1 nm	56.2 nm	0.180	5 mg/mL	19.7 mT/μ_0	0.92	0.05
32.1 nm	2.2 nm	68.0 nm	0.200	5 mg/mL	25.1 mT/μ_0	0.91	0.03
					*At 20.2 kHz, 20mT/μ_0		

b.

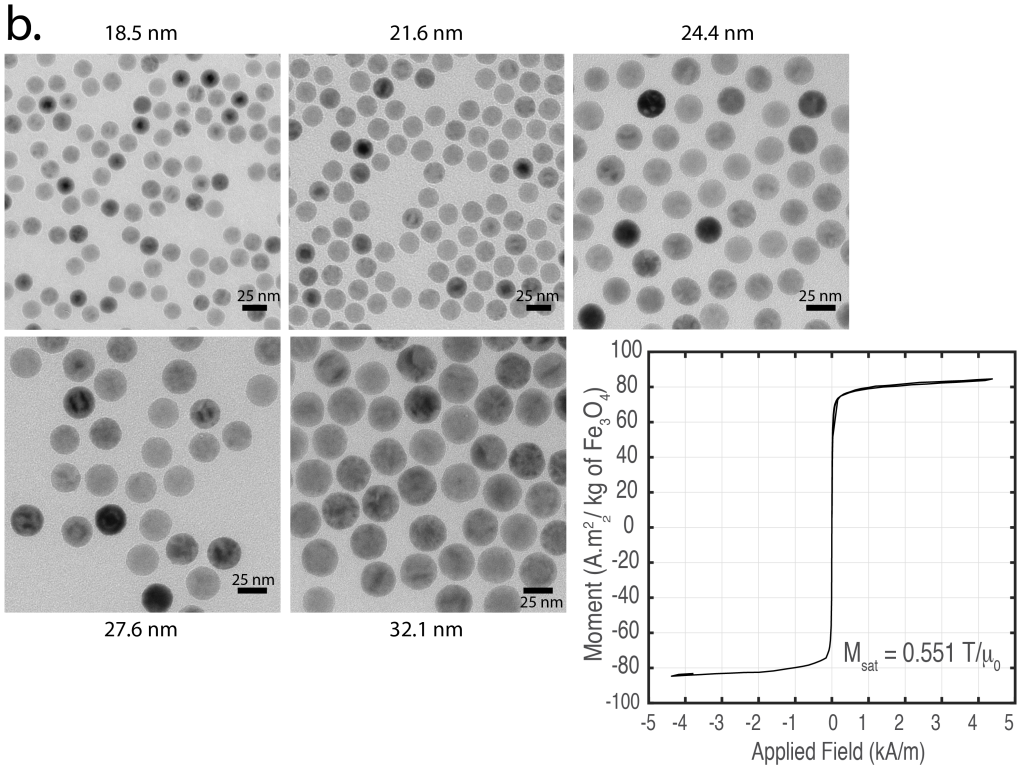

FIGURE 3.3: (a) Table of nanoparticle properties and experimental measurements (b) TEM of Imagion Biosystems PrecisionMRX® SPIOs showing narrow size variation and constant spherical shape as evidenced by the isoperimetric quotients (thus implying constant shape anisotropy). A representative M vs. H plot ($M_{sat} = 0.551T/\mu_0$) is also plotted. See Section 2.1 for more details.

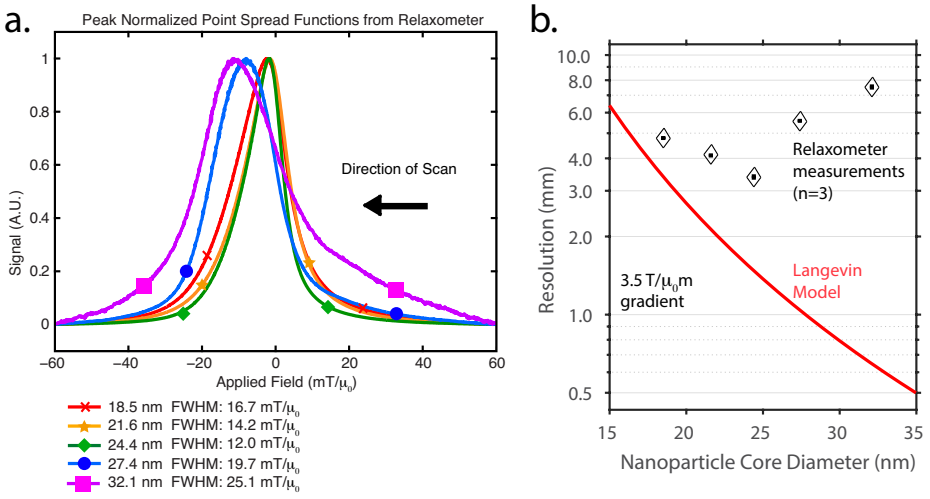

FIGURE 3.4: (a) Experimental 1D point spread functions of Imagion Biosystems PrecisionMRX®SPIOs measured on the Magnetic Particle Relaxometer at 20.25 kHz and 20 mT/μ_0. The PSF narrows as core size increases from 18 to 24 nm, but stops narrowing and starts widening beyond 25 nm. This shift is concomitant with a marked displacement of the PSF in the direction of the scan which is similar to that seen in prior work on MPI relaxation (Croft et al., 2016; Croft, Goodwill, and Conolly, 2012), suggesting a marked increase in magnetic relaxation processes. Data is represented by the smooth solid lines while the markers are just a visual guide to differentiate the curves. (b) Comparison of the experimentally achieved spatial resolution (n = 3) with the predicted spatial resolution from the Langevin model shows an increasing disparity with increasing core size after 24.4 nm.

Langevin theory assumes the SPIOs instantaneously respond to the applied field. Fig. 3.4b shows an increasing disparity between the Langevin model and the experimentally measured spatial resolution as core size increases. For example, the Langevin model predicts that 700-micron resolution is achievable with 32 nm SPIOs, while the experimental resolution achieved was around 7 mm, assuming a 3.5 T/(μ_0m) gradient.

3.5.2 Verification of trend with MPI imaging results

We confirmed our relaxometer measurement results with an imaging scan using the Berkeley MPI scanner. The images are shown in Fig. 3.5. The same trend of worsening resolution beyond 24.4 nm is observed and measurement of the FWHM from a line plot (blue dashed line) through the image are in good agreement with the AWR results. The 32.1 nm particles are not visible because the large relaxation time constants leads to very low induced signal in the MPI receive coil (MPI signal $\propto \frac{dM}{dt}$). 32.1 nm particles are visible in the relaxometer because a much larger volume ($25\mu L$) is used.

3.5.3 Magnetic relaxation limits improvement of spatial resolution

To verify that magnetic relaxation is the mechanism behind the limiting of spatial resolution as core size increases, the raw time-domain signal across a half-period of drive field was investigated. Any magnetic relaxation will cause a delay of the time-domain signal in the direction of the scan. In Fig. 3.6a, while an increase in magnetic relaxation can be inferred from the slight delay of the peak going from 18.5 nm to 24.4 nm, the signal peak has an overall narrowing leading to overall better resolution. This suggests that the effect of Langevin physics dominates over magnetic relaxation in this range of core sizes.

From 24.4 nm to 32.1 nm, however, there is a dramatic increase in peak delay (Fig. 3.6b). The signal is delayed by $\sim 6\mu s$ and is spread out across almost twice the time as 24.4 nm. These results show that magnetic relaxation is dramatically more significant beyond 24.4 nm and clearly dominates over Langevin physics.

The raw MPI time-domain data shown here also provides an intuitive explanation of worsening resolution. Since the signal is spread out over more time for 27.4 nm and 32.1 nm, the signal is associated with more voxels in x-space reconstruction because $signal(t)$ is directly gridded to the voxels

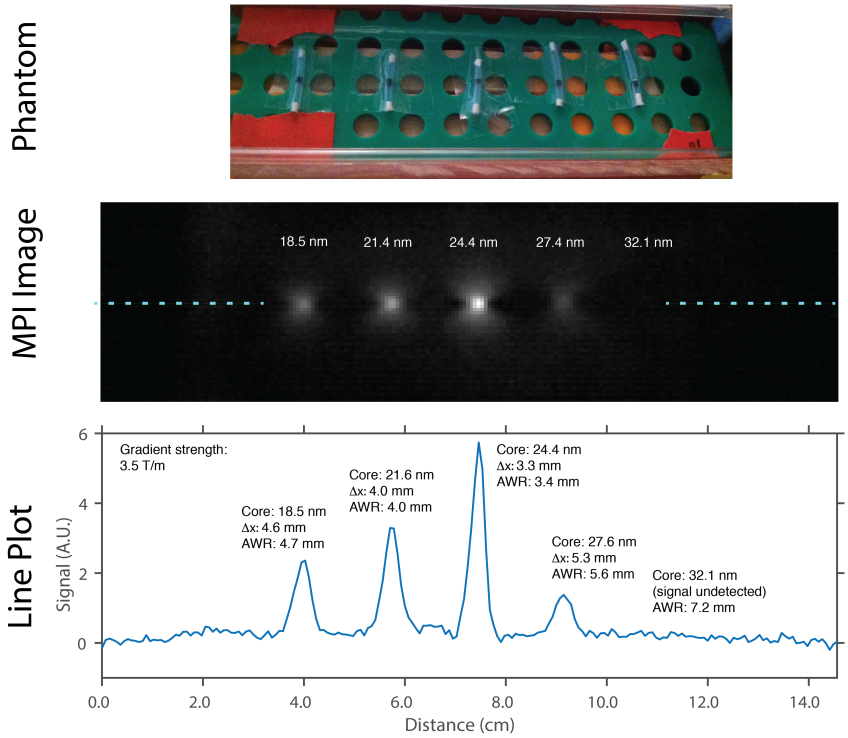

FIGURE 3.5: Magnetic Particle Imager scan of point sources of different SPIO core sizes. The experimental imaging results have good agreement with the Relaxometer measurements, showing the same trend of optimal resolution with 24.4 nm SPIOs.

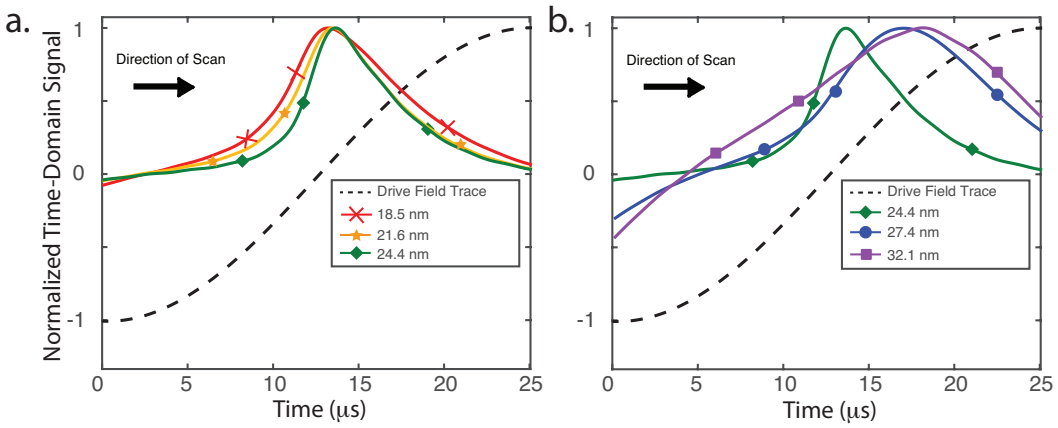

FIGURE 3.6: Trace of the *experimental* time-domain MPI signal. Data is represented by the smooth solid lines while the markers are just a visual guide to differentiate the curves. **a)** From 18.5 nm to 24.4 nm, a slight increase in delay is seen in the peaks of each subsequent trace. This is indicative of magnetic relaxation processes increasing in magnitude. However, this effect is surpassed by the narrowing of the signal peak by Langevin physics. Thus, the narrowest peak and best resolution is seen at 24.4 nm. **b)** From 24.4 nm to 32.1 nm however, magnetic relaxation increases dramatically as evidenced by the very large time delay (phase delay of almost 40 degrees) of the 27.4 nm and 32.1 nm signal peaks. This is indicative of strong magnetic relaxation processes that clearly dominate the expected peak narrowing from Langevin physics. As a result, the signal peak is spread out and worse resolution occurs when going from 24.4 nm to 32.1 nm.

that the field-free-point bypassed in that time. Similarly, for system matrix reconstruction, a spread-out signal peak corresponds to a steeper decay in the Magnetic Particle Spectrometry spectra and thus a more poorly conditioned system matrix during image reconstruction.

3.5.4 Strategies for mitigation of magnetic relaxation do not work fully

Prior work has demonstrated that the MPI drive waveform significantly affects the MPI performance of SPIOs (Croft et al., 2016; Kuhlmann et al., 2015). Here, we investigate if low amplitude and low frequency approaches can help mitigate magnetic relaxation and achieve the Langevin model spatial resolution. For the low amplitude approach, the frequency was kept constant at the original 20.25 kHz while amplitudes of 20.0, 4.0 and 0.5 mT/μ_0 were used. For the low frequency approach, the amplitude was maintained at the original 20 mT/μ_0 while frequencies of 20.25, 2.0 and 0.4 kHz were used.

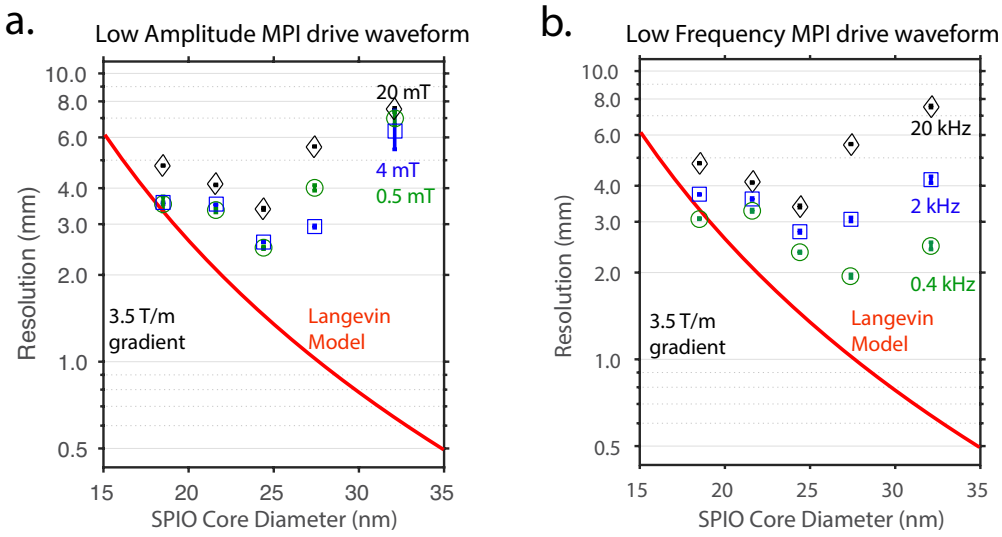

FIGURE 3.7: Low amplitude and low frequency drive waveform strategies have been shown in prior work to reduce the negative impact of magnetic relaxation (Kuhlmann et al., 2015; Croft et al., 2016). Both approaches were tested separately (n=3, error bars are small and within the shape markers). (a) In the low amplitude approach, frequency is held constant at 20.25 kHz and amplitudes of 20.0, 4.0 and 0.5 mT/μ_0 were used. (b) The low frequency approach keeps amplitude constant at 20 mT/μ_0 while frequencies of 20.25, 2.0 and 0.4 kHz were used. While both strategies help achieve better spatial resolution overall, spatial resolution still stops improving after a certain core size. These strategies are unable to fully mitigate the negative impact of the large amount of relaxation seen by larger core size particles and are unable to achieve the cubic spatial resolution improvements predicted by the Langevin model.

The results show that low amplitude approaches do not work well at larger core sizes. This can be attributed to the strong field strength dependence of Néel and Brownian time constants as described in equation 5.1 and (Deissler, Wu, and Martens, 2014; Dieckhoff et al., 2016), where the smaller AC drive amplitudes mean that the time constants remain relatively large throughout the entire AC period. In contrast, low frequency approaches work better at larger core sizes. The spatial resolution minima of the curve is shifted to 27.4 nm at 0.4 kHz and there is significantly improved spatial resolution by almost 2-fold from the optimal resolution at 20-kHz curve. This can be attributed to the fact that the temporal blurring has a lower impact on the time-domain raw MPI signal shape when the drive waveform period is longer, which in turn results in less blurring during image reconstruction as shown by Croft et al., 2016. Overall, while both approaches help mitigate magnetic relaxation and improve spatial resolution, the general trend of worsening spatial resolution beyond 27.4 nm still remains. Notably, the fact that low frequency approaches work well at core sizes past the minima of the 20 kHz curve while low amplitude approaches do not (relaxation time constants are longer at low fields) lends further credence to the idea that increasing magnetic relaxation from larger core sizes is the main cause of worsening spatial resolution. In essence, these results suggest that magnetic relaxation is a significant spatial resolution barrier that is not easily resolved by current approaches.

3.6 Discussion

As shown in Fig. 3.1, the ideal steady-state Langevin model for an ensemble of nanoparticles predicts a highly desirable cubic improvement in MPI resolution with core size (Rahmer et al., 2009; Goodwill and Conolly, 2010). However, in practice, relaxation-induced blurring of the MPI signal also occurs and is known to also increase with core size as described in equation 5. Blurring of the MPI image by magnetic relaxation (Neel and/or Brownian mechanisms) is a well-known phenomenon that has been shown in prior work for both system matrix (Schmidt et al., 2015) and x-space reconstruction approaches (Croft, Goodwill, and Conolly, 2012; Croft et al., 2016). Our key result, shown in Fig. 3.4, is the first experimental study of SPIOs in aqueous solvent showing the interplay of these two effects resulting in optimal resolution being achieved at 24.4-nm core size, with worsening resolution beyond 24.4 nm. We presented experimental evidence that the resolution improving effect of the ideal Langevin model for an ensemble

of particles is increasingly mitigated and dominated by relaxation-induced blurring. For example, in Fig. 6a, it can be observed there is an increase in time-delay of the MPI signal as core size increases from 18.5 nm to 24.4 nm indicating an increasing delay in ensemble magnetization (magnetic relaxation). Notably, the signal response is still narrower in time for 24.4 nm, suggesting that both the resolution improvement from the Langevin model and relaxation-induced blurring are affecting the MPI signal.

While magnetic core size is a major factor in influencing the Neel and Brownian relaxation time constants as described in equation 5, there are other factors that may affect these time constants and therefore the MPI resolution. One possible factor is the shape anisotropy constant. While the particles used in this study are all spherical, larger core sizes are slightly less so (see Fig. 3a). However, the maximum shape anisotropy calculated from this factor is $2341 Jm^{-3}$ which is only a small fraction (< 0.172) compared to the magnetocrystalline anisotropy. Equation 10 and 11 of Graeser, Bente, and Buzug, 2015 and magnetocrystalline anisotropy of magnetite $K_1 = -13600 Jm^{-3}$ was used. Therefore, the increase in shape anisotropy contributes only minimally and cannot be solely responsible for the two-fold worsening of spatial resolution between 24.4 nm and 32.1 nm particles. Another possible factor is the changing hydrodynamic sizes between different core sizes (see Fig. 3.3a). Hydrodynamic size has a large impact on the Brownian relaxation time constant but is does not affect the Néel relaxation time constant (equation 5). While there is a poor correlation between the measured hydrodynamic size and measured MPI resolution for the 18.5 - 24.4 nm range of particles, the correlation is better for the 24.4 - 32.1 nm range of particles. The results suggests that the impact of hydrodynamic size on MPI resolution is modulated by the relative dominance of Néel and Brownian relaxation mechanisms which in turn is most dependent on magnetic core size due to the exponential dependence of the Néel time constant on the magnetic core volume. While it is possible that hydrodynamic size contributes towards the worsening resolution going from 24.4 nm to 32.1 nm and that better resolution could be obtained with very thin coatings, in practice, a minimum coating thickness is required in synthesis for successful phase transfer as well as to prevent spontaneous aggregation of nanoparticles. Yet another factor to consider is the width of the particle size distribution. From Knopp et al., 2011, there is less than a two-fold improvement in resolution of the normalized convolution kernel between a 15 nm monosized ensemble and a polysized ensemble (lognormal with 16.4 nm mean with 4 nm standard deviation). For the particles used in this study, the standard deviation is constant at 1.5 nm and only increases to 2.1 and 2.2 nm at

27.6 nm and 32.1 nm core sizes respectively (see Fig. 3.3a). The variation in size distribution for this study is thus much lower than that shown by Knopp et al., and therefore this factor can be considered to contribute only minimally to the spatial resolution trend measured in this study.

The results of our study show that with current typical MPI imagers operating around 20 kHz and 20 mT drive amplitude, spatial resolution on a typical 7 T/(μ_0m) gradient is limited to about 1.5 mm. For preclinical applications, this spatial resolution is not ideal. This is especially so for smaller rodents such as mice and also when investigating disease models of the vasculature. This resolution challenge of MPI is valid with both methods of reconstructing the MPI image. For example, Weizenecker and Rahmer's 2009 landmark paper on the System Matrix (Rahmer et al., 2009) noted that while a 5.5 T/(μ_0m) gradient and dominant particle diameter of 30 nm theoretically allows a resolution better than 0.5 mm, experimentally, due to the wide distribution of particle sizes and the regularization applied in reconstruction to mitigate limited SNR, the observed resolution was not better than 1.5 mm.

Many approaches have been taken to improve the spatial resolution of MPI. One approach is to increase the gradient strength of the MPI imager (Vogel et al., 2015b; Yu, Goodwill, and Conolly, 2015; Goodwill et al., 2015). Gradients of up to 7 T/(μ_0m) have been achieved on murine scanners at Berkeley (Yu, Goodwill, and Conolly, 2015; Goodwill et al., 2015). Notably, Vogel et al., 2015b achieved a gradient strength of 85 T/(μ_0m) which will theoretically achieve 29 μm resolution with a 30 nm magnetite core particle (assuming instantaneous relaxation). However, the bore size of the device is very small (6-mm diameter) and cannot fit small animals. Such high gradients for a small animal-sized bore would require superconducting magnets, with increased cost and complexity. In addition, the high gradients imply that the rate of scanning across the entire field-of-view will have to be proportionally slowed down due to obey magnetostimulation and SAR safety limits (Saritas et al., 2013a). Finally, as demonstrated in Fig. 3.1, like MRI, the spatial resolution of MPI improves only *linearly* with increasing gradient strength.

Deconvolution approaches could potentially obtain significant spatial resolution improvements. However, our knowledge of the *in vivo* PSF and relaxation behavior is imperfect, and also the conditioning of the computation could damage final SNR, especially with relaxation-induced blurring of the MPI signal. The fundamental SNR versus resolution tradeoffs with sophisticated deconvolution algorithms has been studied specifically for MPI by Knopp et al., 2011 and in general by Shahram and Milanfar, 2004.

Other approaches include optimizing the drive waveform to mitigate the blurring effects of magnetic relaxation. Notably, low amplitude or low frequency approaches have been investigated before (Croft et al., 2016; Kuhlmann et al., 2015; Murase et al., 2014; Shah, Ferguson, and Krishnan, 2014). In our study, we tested out these strategies on our range of magnetic core sizes. Unfortunately, while some improvement in spatial resolution was observed, Fig. 3.7 shows that neither approach is able to fully mitigate the blurring from magnetic relaxation in order to achieve the theoretical Langevin spatial resolution for larger core sizes. Very low frequencies (< 400 Hz) could show promise for MPI, but MPI uses an inductive pick-up coil today, so SNR will be reduced. SQUID detectors have SNR independent of frequency, so they may mitigate this challenge.

Perhaps the most promising approach is to optimize novel magnetic nanoparticle tracers for great resolution and minimal relaxation-induced blurring (Ferguson, Minard, and Krishnan, 2009; Ferguson et al., 2010; Ferguson, Khandhar, and Krishnan, 2012; Hufschmid et al., 2015). Here, the nanoparticle synthesis will involve attention to particle phase purity. Furthermore, as Weizenecker et al., 2012 has shown, optimizing the particle anisotropy can prove valuable. In addition, Graeser, Bente, and Buzug, 2015 has shown that superimposing of shape semi-axis and crystal axes during crystal growth can improve the MPI performance. For very large core sizes, because the Néel time constant is larger than Brownian time constant for low applied fields (Deissler, Wu, and Martens, 2014), Brownian relaxation will be dominant. Hence, tailored SPIOs with the smallest hydrodynamic radius possible while still maintaining a thick enough coating to prevent aggregation may also show resolution improvements.

3.7 Conclusions

In this study, we perform the first experimental study on the interplay of Langevin steady-state physics and magnetic relaxation as particle core size is increased and measure its effects on MPI spatial resolution. The experimental results show that magnetic relaxation limits the optimal core size of MPI nanoparticle tracers to ~ 25 nm. We experimentally observe a significant disparity, consistent with trends from prior modeling work, between the resolution predicted by the steady-state Langevin physics model and that achieved experimentally for SPIOs with core size larger than 25 nm. For example, the steady-state Langevin predicts ~ 600 micron resolution with a 3.5 T/(μ_0m) gradient and 32 nm SPIO, but experimentally ~ 7 mm

resolution is achieved. This spatial resolution disparity remains even after optimizing the drive waveform to reduce the impact of relaxation-induced blurring, suggesting that magnetic relaxation is a potent and unresolved barrier to unlocking the potential of large core size particles. We hope that in the near future, MPI researchers will invent new methods to overcome magnetic relaxation-induced blurring for larger core sizes. This will allow us to unlock the highly desirable cubic improvement of MPI spatial resolution with nanoparticle core size.

3.8 Acknowledgments

We are extremely grateful to Dr. Erika Vreeland and associates at Imagion Biosystems who provided us with a wide range of nanoparticle core sizes, without which this study would not be possible.

Chapter 4

Pulsed Magnetic Particle Imaging in 1D

4.1 Attribution

Reproduced in part from the Journal Publication:
Tay ZW, Hensley DW, Ma J, Zheng B, Goodwill P, Conolly S. Pulsed Magnetic Particle Imaging in 1D. IEEE Transactions of Medical Imaging. 2018. In submission.

4.2 Introduction

To address the relaxation wall described in the previous chapter, we use the AWR described in Chapter 2 to develop a novel scanning method. Instead of using conventional sinusoidal excitation waves, we exploit the flexibility of the AWR to implement square-like excitation waves. The piecewise-constant portions of the square waves manifest as a scan-and-wait effect, where the dynamic processes of SPIO magnetization that normally cause blurring are allowed to complete. This prevents magnetization delays from causing MPI signal to blur from the first voxel to subsequent voxels, and therefore enables achievement of the native Langevin resolution without the associated relaxation-based blurring. In this chapter, we provide an explanation of this approach, which we term pMPI due to the "pulsed" steps before the constant hold. We also show experimental data demonstrating improved spatial resolution, circumvention of the relaxation-based blurring to achieve the Langevin model of cubic improvement of resolution with SPIO core size. Finally, we show proof-of-concept 2D images of pMPI.

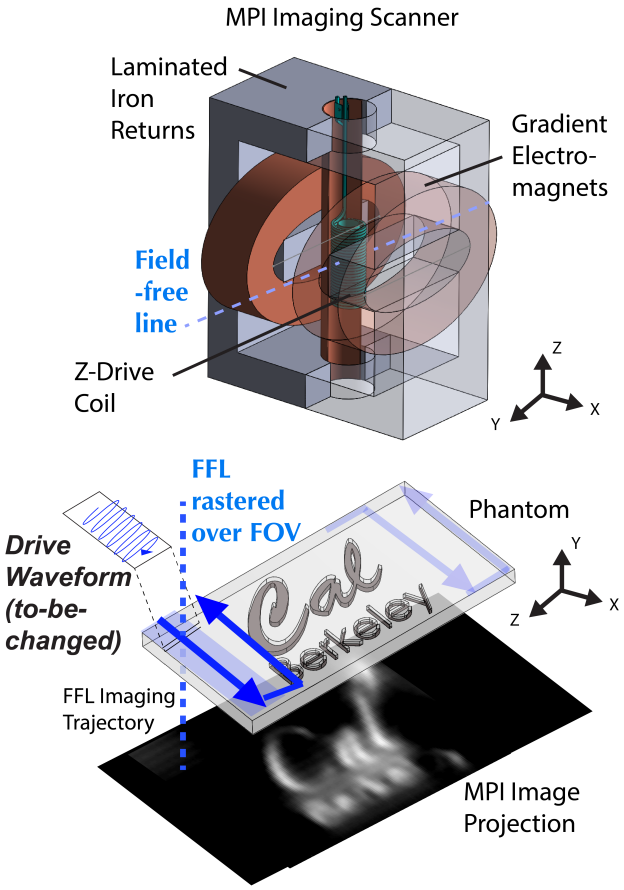

FIGURE 4.1: MPI rasters a sensitive point (the zero-field point or field-free-point) across a 3D volume to form an image of the superparamagnetic iron oxide nanoparticles (SPIONs) present. Here, a sensitive line setup is shown, which obtains projection images through the sample like CT. MPI's inductive signal is generated by the SPION magnetization response to the fast raster from the sinusoidal drive waveform. In this work, we show that by changing the sinusoid drive waveform to a pulsed waveform (square wave), we are able to significantly improve MPI resolution by circumventing relaxation-induced blurring.

4.3 Background

Using typical excitation parameters in standard MPI, we have found that improved resolution with increasing magnetic core size follows the Langevin prediction up to approximately 25 nm. After this inflection point, we see reduced performance and worsening resolution as shown in Fig. 4.2(c) and which is in direct conflict with the Langevin theory. At this point, relaxation dynamics start to play an increasingly important roll, breaking the steady-state assumption and leading to significant secondary blurring. The precise location of this inflection point is dependent on various tracer properties and the magnetic slew rates used in excitation. But accounting for the effect of dynamic physics in MPI data acquisition as currently performed establishes a 'relaxation wall' that limits the achievable resolution in MPI (Tay et al., 2017).

While magnetic relaxation has a deleterious effect on achievable resolution as described thus far, it can also be leveraged to provide powerful contrast and molecular imaging capabilities. For example, colorized contrast for multiplexing tracers, unmixing tracer species, and sensing temperature have recently been described (Cho, Cho, and Cho, 2014; Perreard et al., 2014b; Hensley et al., 2015; Rahmer et al., 2015; Stehning, Gleich, and Rahmer, 2016). Additionally, new theranostic applications that combine MPI and heating actuation rely on the lossy, non-instantaneous nature of the tracer response (Murase et al., 2013; Hensley et al., 2016).

Many of these newer developments as well as the distinction between x-space and system matrix MPI can be described in terms of differences in signal encoding. This is possible because there is great flexibility in how the FFR can be used to sample an imaging field-of-view (FOV). And paramount for this work, the way in which relaxation information is encoded in the raw signal is a strong function of the excitation waveform.

Here we propose a new excitation approach for MPI which allows direct encoding of steady-state Langevin information into the acquired time domain signal. This enables reconstruction of images that asymptotically approach the theoretical Langevin resolution, even for large particles with significant magnetic response times. It also provides an ability to temporally separate excitation feedthrough from the MPI signal.

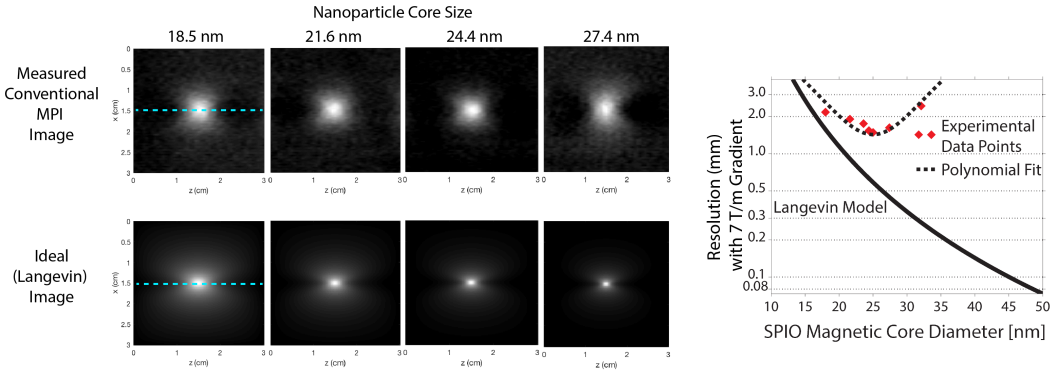

FIGURE 4.2: Although the Langevin Theory for MPI predicts cubic resolution improvement with increasing nanoparticle core size, in practice, resolution gains with increasing core size are limited. Furthermore, beyond the optimal 24.4 nm core size, spatial resolution is observed to worsen rather than improve with core size. This is demonstrated by the stark difference between the measured image resolution and the Langevin theoretical resolution of a point source phantom of 27.4 nm SPIOs (ImagionBio, PrecisionMRX^{TM}). This disparity can be attributed to relaxation-induced blurring, where blurring worsens with larger core sizes due to their increasingly sluggish response to the excitation drive field. In this work, we propose a new drive waveform to circumvent this problem and achieve the ideal (Langevin) spatial resolution. Because this will unlock the potential of cubic improvement of resolution with core size, significant improvements in resolution are expected, especially for large core size SPIOs such as the 27.4 nm.

4.4 The Pulsed MPI Approach

The crux of pMPI is use of piecewise constant components in the excitation wave, which therefore prevents use of conventional continually time-varying sinusoidal waves. The pMPI approach makes use of two primitive waveform components: 1) periods of temporally-invariant applied field and 2) periods of rapidly varying applied field. The former allows encoding of steady-state information in the raw signal while the latter provides high peak time domain signal-to-noise ratio (SNR) and SNR-efficient excitation as well as temporal separability between the tracer signal and excitation feedthrough. These components can be assembled into arbitrary combinations to form larger periodic excitation waveforms or pulse sequences. The simplest representation of pMPI is a square wave. We will consider square and trapezoidal wave excitation in this paper (mainly because trapezoidal is a more realistic implementation since infinite transmit bandwidth is necessary for a perfect square wave). Exploration of more general pulse sequences are left for future studies.

pMPI requires a new transmit and receive designs for the MPI system due to the untuned, non-monotonal nature of the excitation. As indicated in Fig. 4.3, while some aspects of the typical MPI hardware are reusable such as the shift gradients (**goodwill2012x**), the main transmit receive parts have to be overhauled. We note that as Fig. 4.3 indicates, pMPI can be incorporated into an x-space or system matrix reconstruction paradigm. Here we exploit the flexibility of the arbitrary waveform relaxometer (AWR) system shown in Fig. 4.5(a) to demonstrate square and trapezoidal wave pMPI (Tay et al., 2016). The AWR can be set up as a 1D scanner to measure 1D point-spread functions (PSFs) or modified with additional magnets to generate a field-free line (FFL) system to give 2D images within a limited (small) FOV.

4.4.1 Magnetic Relaxation

Magnetic relaxation in MPI is a very active area of research (Ferguson, Minard, and Krishnan, 2009; Biederer et al., 2009b; Rauwerdink and Weaver, 2010; Goodwill et al., 2011b; Croft, Goodwill, and Conolly, 2012; Croft et al., 2016; Dhavalikar et al., 2016). Relaxation can be leveraged for contrast enhancement, provide avenues for powerful reporting of physiologic state and molecular imaging, and will no doubt be important in the development of pMPI. Multiple relaxation processes may be active simultaneously, including Néel, Brownian, and ferromagnetic processes. All of these processes have different dependencies on applied field conditions, different

processes may be coupled in interesting ways, and nonlinear interactions between particle domains may occur.

In continuous-wave MPI, significant relaxation leads to signal and image degradation in both x-space and system matrix methods (Kuhlmann et al., 2015; Croft, Goodwill, and Conolly, 2012; Tay et al., 2017) . Magnetic relaxation physics act as a time-domain low pass filter during acquisition. From the x-space perspective, there is a direct mapping from the time-domain signal to the image domain such that a secondary spatial blur manifests during reconstruction. From the Fourier domain or system matrix perspective, the higher order harmonics that contain high spatial resolution information are attenuated. Relaxation becomes more prominent, and therefore the negative effect on resolution becomes relatively worse, the larger the tracer. The effect is stark when comparing predictions of Langevin theory with experimental results as shown in Fig. 4.2(c).

While better understanding magnetic relaxation physics is crucial, we leave a more detailed discussion outside the scope of this work. Instead, we focus on how pMPI encoding mitigates the deleterious effect of relaxation on resolution in a general way. pMPI requires only the assumption that magnetic relaxation processes have a finite step response, which is guaranteed for all real physical processes. The experimental data of Fig. 4.5(c) shows the decaying MPI signal elicited after the rapid transitions of a typical square wave excitation. In this context, the basis of pMPI encoding should work *regardless* of the nature of the magnetic relaxation physics.

4.4.2 Square Wave Signal and Imaging Equations

To begin, we first derive the 1D signal and imaging equations for pMPI assuming ideal square waves. Starting from the basic applied field MPI equations from prior work (**goodwill2010x**):

$$H(t,x) = G(x - x_{\mathrm{s}}(t)) \tag{4.1}$$

where $H(t,x)$ is the applied field in $[A\,m^{-1}]$, G is the linear gradient strength in $[T\,m^{-1}]$, and $x_{\mathrm{s}}(t)$ is the center location of the FFP. The steady-state magnetization of a 1D tracer distribution exposed to this field is given by:

$$M_{\mathrm{ss}}(t,x) = m\rho(x)\mathcal{L}(kH(t,x)) \tag{4.2}$$

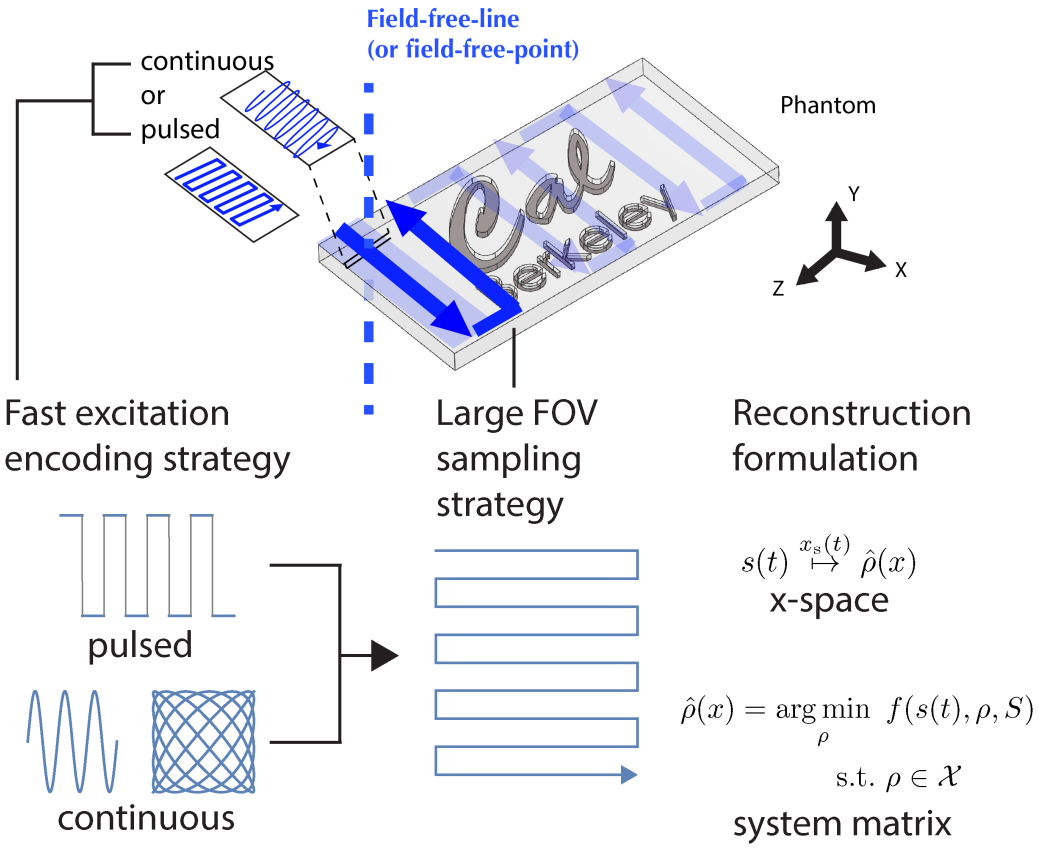

FIGURE 4.3: Pulsed encoding in MPI acquisition. We can describe an MPI acquisition scheme in terms of a choice of fast excitation encoding waveform, FOV sampling strategy, and reconstruction formulation. pMPI replaces the canonical sinusoidal fast excitation encoding with pulsed waveforms. Subsequent aspects of the acquisition scheme such as FOV sampling strategy and reconstruction method may be chosen as desired as long as the pMPI constraints described herein are respected. For example, slew rates involved in FOV sampling cannot compromise steady-state induction. pMPI may be incorporated into the x-space or system matrix paradigm.

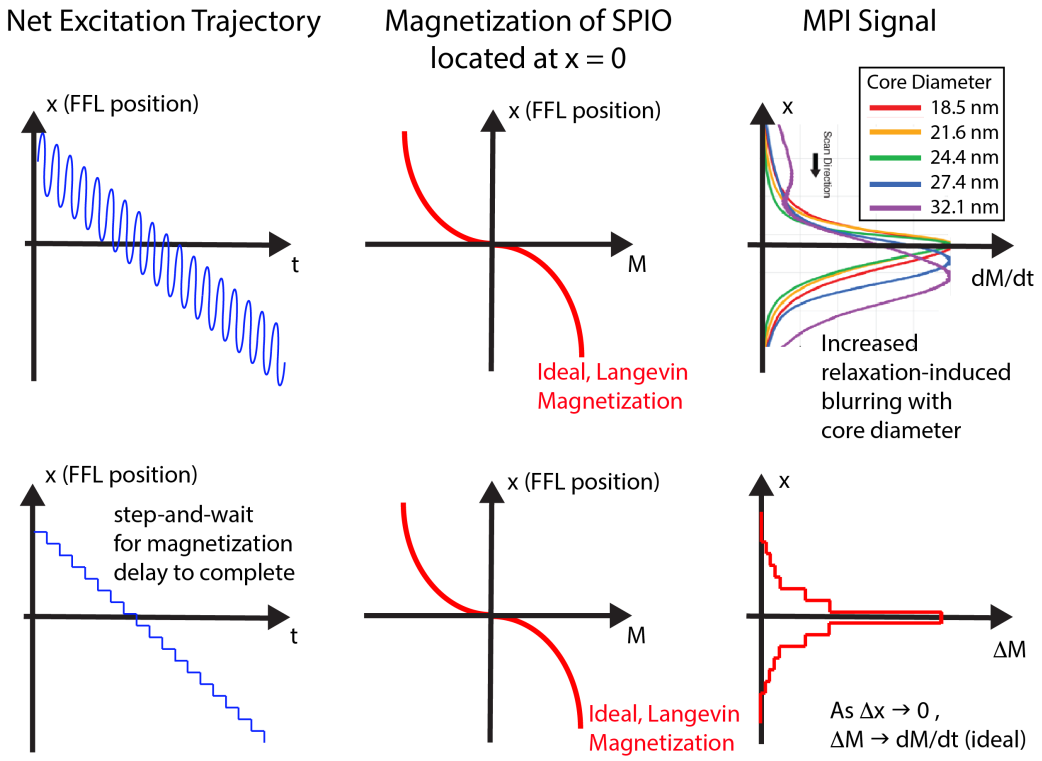

FIGURE 4.4: The strategy behind pulsed MPI explained in 1D. The key principle is a step-and-wait net excitation trajectory (formed from a square wave fast excitation + ramp for large FOV sampling). The wait time must be long enough to allow any delays in magnetization to reach steady-state (the Langevin magnetization). Instead of making the raw received signal (instantaneous dM/dt) as our MPI signal, we integrate the raw signal over the wait time to obtain a ΔM for that step. This measured ΔM is exactly the change in magnetization of the ideal Langevin M-H curve as we step from x to x+Δx. As a result, **pulsed MPI is a discrete sampling of the ideal Langevin dM/dH curve**. With finer and finer sampling ($\Delta x \rightarrow 0$), the 1D image approaches the continuous, ideal dM/dt plot. Because for waiting for steady-state at each step, pulsed MPI completely circumvents any relaxation-induced blurring that is commonly observed in conventional MPI due to the "no-wait" sinusoidal trajectory. This conventional blurring can be understood as delays in magnetization resulting in the dM/dt signal being spread across a larger distance in x.

where m is the magnetic moment of the tracer in $[A\,m^2]$, $\rho(x)$ is the tracer distribution in $[\text{particles}\,m^{-1}]$, $\mathcal{L}$ is the Langevin function, and k is a tracer-specific parameter with units of $[m\,A^{-1}]$ that characterizes the relationship between magnetic and thermal energies:

$$k = \frac{\mu_0 M_{\text{sat}} \pi d^3}{6 k_{\text{B}} T} \tag{4.3}$$

where d is the diameter of the tracer magnetic core in $[m]$ and M_{sat} is the saturation magnetization of the tracer in $[A\,m^{-1}]$.

We now consider excitation with an ideal square wave:

$$x_{\text{s}}(t) = \sum_{n=0}^{k} (-1)^n \, \Delta x \, \sqcap \left(\frac{t - n\Delta t}{\Delta t} \right) \tag{4.4}$$

with x-space displacement $\Delta x = AG^{-1}$ where A is the square wave magnetic field amplitude in $[T]$, Δt is the square wave half-period in $[s]$, and $\sqcap$ is the rectangular function (Gaskill, 1978).

To derive the signal equation, we assume use of an inductive receive coil with homogeneous sensitivity B_1 in $[T\,A^{-1}]$ in the imaging FOV which leads to a volume integral. Considering only the case of 1D, the voltage on the receiver coil is:

$$\begin{aligned} V(t) &= B_1 \frac{\mathrm{d}\Phi(t)}{\mathrm{d}t} = B_1 \frac{\mathrm{d}}{\mathrm{d}t} \iiint_V M(t, \mathbf{u}) \, \mathrm{d}V \\ &= B_1 \frac{\mathrm{d}}{\mathrm{d}t} \iiint_V M(t, u) \delta(v) \delta(w) \, \mathrm{d}u \, \mathrm{d}v \, \mathrm{d}w \\ &= B_1 \frac{\mathrm{d}}{\mathrm{d}t} \int_u M(t, u) \, \mathrm{d}u \end{aligned} \tag{4.5}$$

To continue, we make the assumption of linear time-invariance for magnetic relaxation such that it can be described by a impulse response $h_{\text{m}}(t, x)$ and related step response $r_{\text{m}}(t, x)$. If steady-state magnetization was achieved at the end of the previous square wave half-period, the dynamics of the magnetization over the next half-period should be simply that of a step excitation:

$$\begin{aligned} &M(t \geq t^+, x) = \\ &\quad M_{\text{ss}}(t^-, x) + (M_{\text{ss}}(t^+, x) - M_{\text{ss}}(t^-, x)) r_{\text{m}}(t, x) \end{aligned} \tag{4.6}$$

where the steady-state magnetization immediately prior to and after the step excitation are indicated. Let $t_{n-1} = (n-1)\Delta t^-$, $t_n = n\Delta t^-$, $M_{\text{ss}}(t = t_{n-1}, x) = M_{n-1}(x)$, $M_{\text{ss}}(t = t_n, x) = M_n(x)$, and $\Delta M_n(x) = M_n(x) - M_{n-1}(x)$. We index the signal equation by n, evaluated for each square wave half-period:

$$\begin{aligned} s_n(t) &= V(t)\Big|_{t_{n-1}}^{t_n} \\ &= B_1 \frac{\mathrm{d}}{\mathrm{d}t} \int_u M(t,u)\,\mathrm{d}u \\ &= B_1 \int_u \frac{\mathrm{d}}{\mathrm{d}t} \left(M_{n-1}(u) + \Delta M_n(u) r_{\text{m}}(t,u)\right)\,\mathrm{d}u \\ &= B_1 \int_u \Delta M_n(u) h_{\text{m}}(t,u)\,\mathrm{d}u \end{aligned} \tag{4.7}$$

where the expansion of the magnetization in terms of the steady-state magnetization distributions as shown assumes that the square wave half-period is chosen to be longer than a parameter of merit that quantifies the convergence of $h_{\text{m}}(t,x)$. For example, in the case of a Debye process (Croft et al., 2016), let the half-period be longer than 5 * $\tau_{\max}$ where $\tau_{\max} = \max_x \tau(x)$ is the maximum observable time constant.

Here, we see that the signal associated with each half-period n is a spatial integration of all the steady-state magnetization changes of all the SPIOs in the FOV, but weighted by the ideal Langevin such that SPIOs closest to the FFP give the strongest contribution. This steady-state magnetization change depends on the underlying tracer distribution and start and stop FFP locations corresponding to the excitation step. Thus, for each and every SPIO in the FOV, we are sampling two distinct points on their Langevin curve (where in the curve depends on their relative location to the FFP) as illustrated in Fig. 4.5(c) and therefore we achieve explicit direct encoding (discrete sampling) of the steady-state Langevin magnetization in our scanning strategy.

With this signal equation, we can integrate across a half-period to reverse the time-derivative applied by inductive signal detection in order to directly image the steady-state magnetization change resulting from a discrete step in space, which is effectively a discrete step in the steady-state magnetization of the SPIO:

$$
\begin{aligned}
s(n) &= \int_{t_{n-1}}^{t_n} s_n(t)\,\mathrm{d}t \\
&= B_1 \int_{t_{n-1}}^{t_n} \left(\int_u \Delta M_n(u) h_{\mathrm{m}}(t,u)\,\mathrm{d}u \right) \mathrm{d}t \\
&= B_1 \int_u \Delta M_n(u) \left(\int_{t_{n-1}}^{t_n} h_{\mathrm{m}}(t,u)\,\mathrm{d}t \right) \mathrm{d}u \\
&= B_1 \int_u \left(M_n(u) - M_{n-1}(u) \right) \mathrm{d}u \\
&= B_1 m \rho(x) \overset{x}{*} \left(\mathcal{L}(kGx)|_{x=x_n} - \mathcal{L}(kGx)|_{x=x_{n-1}} \right) \\
&= B_1 m \rho(x) \overset{x}{*} \dot{\mathcal{L}}(kGx) \overset{x}{*} \sqcap \left(\frac{x}{2\Delta x} \right) \Bigg|_{x=x_n-\Delta x}
\end{aligned} \tag{4.8}
$$

where $2\Delta x = x_n - x_{n-1}$ and in the last two lines we invoke the fundamental theorem of calculus and definition of $\sqcap$ to express it as a spatial convolution. Finally, this discrete signal equation can be written as a 1D square wave pMPI imaging equation:

$$
\begin{aligned}
\hat{\rho}(x_n) &= \frac{s(n)}{B_1 m} \\
&= \rho(x) \overset{x}{*} \dot{\mathcal{L}}(kGx) \overset{x}{*} \sqcap \left(\frac{x}{2\Delta x} \right) \Bigg|_{x=x_n-\Delta x} \\
&= \rho(x) \overset{x}{*} h_{\dot{\mathcal{L}}}(x) \overset{x}{*} h_r(x) = \rho(x) \overset{x}{*} h(x)
\end{aligned} \tag{4.9}
$$

Our 1D square wave pMPI point-spread function (PSF), $h(x)$, is then the steady-state Langevin PSF, $h_{\dot{\mathcal{L}}}(x)$, convolved with a rect function, $h_r(x)$, that has a width parameter equal to the "step size" or square wave excitation amplitude Δx. Fig. **??**(a) depicts the effect of this excitation step size on pMPI point-spread-functions. Some key points highlighted by the pMPI imaging equation are:

- The same result applies regardless of the exact model of the relaxation physics, as long as the physics is LTI and the impulse response converges to zero. One common model used is the Debye model (Goodwill et al., 2011b; Croft et al., 2016).

- The results depend on having a long enough "wait time" for magnetization delays to complete, such as $> 2 \cdot \tau_{\max}$ if we assume an exponential response with time constant τ.
- The results of (4.8) and (4.9) hold for non-square waveforms, such as a trapezoidal waveform, as long as there is a flat, constant section longer than the required "wait time".
- pMPI spatial resolution is affected only by two parameters : the steady-state Langevin function and the excitation amplitude which we can pick, thus, we can asymtotically approach the true Langevin resolution in the limit of small excitation amplitudes.
- Adjusting the excitation amplitude enables tradeoff between SNR and resolution (larger amplitudes give more SNR, but less resolution).

4.4.3 Resolution

Since we use the Houston criterion for spatial resolution, we can obtain the full-width-at-half-maximum (FWHM) from equation (4.9) by solving for x in the following equation:

$$\dot{\mathcal{L}}(kG(x+\Delta x)) - \dot{\mathcal{L}}(kG(x-\Delta x)) = \frac{\dot{\mathcal{L}}(kG\Delta x) - \dot{\mathcal{L}}(-kG\Delta x)}{2}$$

While this is difficult to solve, we can approximate the problem by noting the two key components of the PSF: the steady-state derivative of the tracer Langevin function, and the excitation step (peak-to-peak amplitude). The FWHM of the Langevin derivative is noted in (**goodwill2010x**) and the FWHM of a rectangular function is simply the width. Fig. 4.10(a) shows how the PSF changes as a function of the excitation amplitude and Fig. 4.10(b) quantifies the square wave pMPI FWHM resolution as a function of the excitation amplitude. Qualitatively, it can be noted that:

$$\text{FWHM} \approx \begin{cases} \text{FWHM}_{\dot{\mathcal{L}}} & \text{if } \Delta x \ll \text{FWHM}_{\dot{\mathcal{L}}} \\ 2\Delta x & \text{if } \Delta x \gg \text{FWHM}_{\dot{\mathcal{L}}} \\ \text{FWHM}_{\dot{\mathcal{L}}} + \Delta x & \text{otherwise} \end{cases} \tag{4.10}$$

where $\Delta x = AG^{-1}$ is the square wave amplitude in x-space.

Therefore, to significantly realize the gains in resolution that larger tracers promise, we need to approach the steady-state Langevin curve by limiting the square wave excitation amplitudes.

4.4.4 SNR and Bandwidth

In general, the SNR of pMPI is mainly dominated by the SPIO magnetization response characteristics. Similar to conventional MPI, the faster the SPIO can complete the magnetization change, the better the time-normalized SNR because less "wait time" is necessary and pMPI imaging of the FOV can be completed in a shorter time. This leads to similar conclusions as in conventional MPI, where tracers with steeper M-H curves and faster magnetization response perform better.

If the SPIO is kept constant and if conventional MPI (cwMPI) frequency is made slow enough such that the SPIO magnetization is able to "catch up" to the excitation wave, then we can anticipate approximately the same SPIO magnetization change over the same duration between pMPI and cwMPI, therefore generating the same inductive MPI signal since MPI's signal is dM/dt. In fact, pMPI should have better time-normalized SNR because instead of slowly ramping the applied field, pMPI does a rapid initial step and this should enable faster SPIO magnetization since there is a larger average magnetic force applied on SPIO.

Similar to cwMPI, the pMPI excitation parameters exert a large effect on SNR. We assess experimental SNR from varying frequency and amplitude in section 4.6.

Admittedly, the resolution-SNR trade-off may not be always in the favor for resolution. By accepting some blurring, it may be possible to have a significantly higher scan frequency and therefore have a much better time-normalized SNR. Again, this depends critically on the SPIO and optimization of the excitation sequence and whether pMPI or cwMPI works better has to be done on a case-by-case basis.

From section 4.6, the resolution-bandwidth relationship in square wave pMPI is very different than the (relaxation-free) model for sinusoidal MPI (**goodwill2010x**). SPIOs near the FFR is characterized by longer relaxation processes (since there is more magnetization to "rotate through") and tracer farther from the FFR is characterized by shorter relaxation processes. In this context, received signal associated with lower harmonics contains higher spatial resolution information. Coupled with the general desire to use small amplitude excitation, this suggests that narrowband reconstruction can yield improved resolution for a modest loss in SNR.

In general, for optimal SNR and SNR-efficiency, pMPI will benefit from carefully optimized, SPIO-tailored excitation half-period that are no longer than necessary to complete magnetization. Fully establishing steady-state (*e.g.*, in a Debye $5*\tau$ sense) may not be necessary, and resolution-bandwidth tradeoffs could be optimized. In addition, it is beneficial to have the initial step rise as rapid as realistically possible (close as possible to ideal square wave), so as to provide the largest average magnetic force on the SPIOs over a fixed half-period duration. Fig. 4.10(c) quantifies the relationship between peak image domain signal and excitation amplitude and Fig. 4.10 (b) and (c) together illustrate how the choice of excitation amplitude represents a continuous SNR-resolution tradeoff.

4.5 Experimental Methods

We first tested pMPI in a 1-D manner on the AWR system and noted the relationships with various excitation parameters such as frequency and amplitude. A wide range of magnetic core size SPIOs were also used. The experimental results were plotted together with theoretical predictions presented in section 4.4 and compared to validate our abovementioned theory. Finally, we show proof-of-concept 2D pMPI images via a modified small FOV AWR imaging system.

4.5.1 Implementing pMPI Excitation Pulse Sequences

Implementation of a square wave, or more general pMPI pulse sequence, requires transmit and receive systems that differ from that used in standard sinusoidal MPI. Standard MPI typically uses resonant systems in both the transmit and receive electronics. The use of resonance improves available reactive power while relatively attenuating noise and interference. Because the excitation is continuous with reception, direct transmit feedthrough usually necessitates a receive side filter to remove energy at the fundamental harmonic, in addition to broadband common mode interference and feedthrough mitigation strategies such as use of a gradiometer receive coil(s).

pMPI pulse sequences, however, require broadband excitation with relatively high frequency components. Given typical magnetic relaxation times for MPI tracers, we usually desire a square wave rise time of 1–5 μs. As indicated in equation (4.9), smaller excitation amplitudes are desired for high resolution which helps constrain the required slew rates.

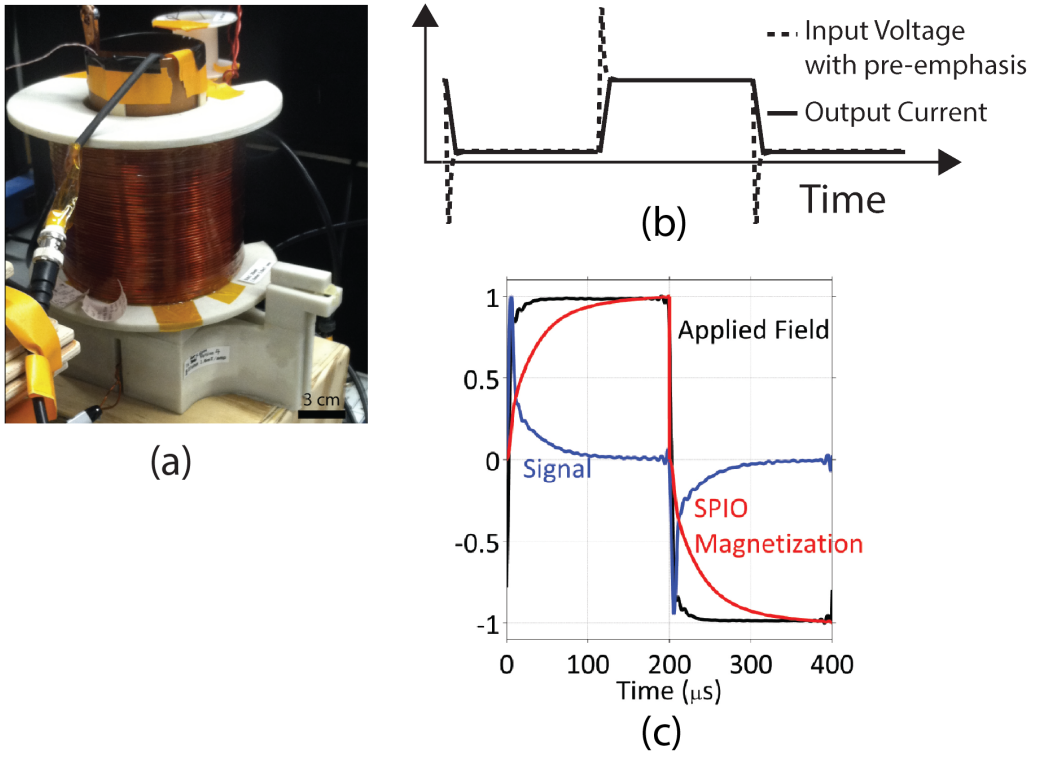

FIGURE 4.5: Hardware implementation of pulsed MPI. (a) Arbitrary waveform relaxometer (AWR) used in this work. The AWR is a benchtop MPI system with a frequency-flexible drive coil that can provide square wave excitation and configurable with or without field-free line (FFL) producing magnets. (b) Pre-emphasized voltage waveforms sent to linear amplifiers in voltage-control mode are used to create square waveforms in the drive coil. (c) Experimental data from implementation of pulsed MPI. Current monitor measurements (AE Techron 7224) verified that a square drive field of 1 mT amplitude was achieved with a rise time of $\sim$ 2 μs. The measured MPI raw inductive signal from the magnetization response of a 32 nm core SPIO is shown in blue. The characteristic peak-and-decay signal expected from SPIOs with significant magnetic relaxation is observed in the raw data. Integrating the blue plot over the wait time of a step gives the net SPIO magnetization change (red plot). We observe that magnetization reaches steady-state as desired (magnetization plateaus)

This type of high power pulse sequence design has been addressed in many previous application spaces (Matter et al., 2006). We have previously reported the construction of our untuned MPI relaxometer system (Tay et al., 2016), which provides high bandwidth excitation by using a low inductance receive coil and benefits from a small sample bore. With this system, we can use a linear amplifier in voltage-controlled mode with pre-emphasized waveforms to achieve the magnetic slew rates we need in pMPI. Other approaches, such as use of timed resonant switcher circuits are also possible.

The low-pass filter effect of an electromagnet system is well understood through Maxwell's equations. To implement pMPI pulse sequences, we can use this knowledge to design an input voltage waveform that will achieve the desired field, subject to our constraints such as the power amplifier maximum output voltage and maximum voltage slew rate. In the context of these contraints, the coil circuit inductance and resistance are important parameters to optimize. For this work, we used square wave and trapezoidal excitation trajectories constructed by solving the following convex optimization:

$$\begin{aligned} &\min_{x} \ ||Ax - y||_2^2 \\ &\text{s.t.} \ \ x \in \mathcal{X} \end{aligned} \tag{4.11}$$

where the matrix A is the physics forward model relating the magnetic field produced by the coil (inductor) in response to an input voltage, x is the voltage waveform, y is the desired or target field waveform, such as a square wave, and $\mathcal{X}$ is the constraint set imposed on x, including the maximum voltage and maximum voltage slew rate.

Solutions to (4.11) are guaranteed optimal in an ℓ_2-norm sense and subject to uncertainty and error in construction of A. This general formulation can be used to build any desired pMPI pulse sequences. To minimize error that did result from imperfect modeling of A, output from the optimization problem was sometimes corrected using a few iterations of a simple online negative feedback control script.

The receive electronics for our system are described in our previous work (Tay et al., 2016). Unlike continuous wave MPI, there is no notch filter associated with a fundamental frequency. Instead the received signal passes through a standard pre-amplifier in a broad band-pass setting. The pre-amplifier begins to attenuate frequencies beyond 1 MHz; we therefore

constrained the received bandwidth to less than 500 kHz.

4.5.2 Nanoparticles

In our experiments, we used a set of monodisperse SPIO tracers all purchased from the same supplier (Imagion Biosystems, Ltd., Albuquerque, NM, USA) with the following core sizes: 18.5 nm, 21.6 nm, 24.4 nm, 27.4 nm, and 32.1 nm. These are single core, crystalline magnetite coated with oleic acid and carboxylic acid outer coating. Detailed characterization and validation of these particles has been performed in previous work (Tay et al., 2017; Vreeland et al., 2015). All experimental samples consisted of 40 μL of stock tracer solution placed in small PCR vials. While stock solutions contained tracer at slightly different concentrations, all data is reported with signal normalized by the mass of iron in the sample for proper comparison.

4.5.3 Testing of 1D pMPI

We subjected samples of each tracer to a number of different encoding and excitation conditions to build parametric data sets. These included excitation amplitude (range: $[1, 20]$mT), steady-state hold time (range: $[25, 750]$ μs), and excitation rise time (range: $[3, 380]$ μs)

Our AWR system shown in Fig. 4.5 is described in detail in our recent work (Tay et al., 2016). Briefly, an inner solenoidal transmit coil is separated from an outer solenoidal bias coil with a cynlindrical copper shield, all arranged coaxially. The transmit and bias coils provide the fast excitation (pMPI or sinusoidal waveforms) and a slowly varying DC offset field, respectively. The biasing field allows us to query the response of a sample across a large magnetic FOV and thus fully characterize the 1D PSF corresponding to the sample. An inductive receive coil wound in a gradiometric fashion is placed coaxial and internal to the transmit coil. A mechanical tuning mechanism allows for on-demand adjustments to the relative geometry between the transmit and receive coils to maximize cancellation of direct feedthrough. MATLAB (Mathworks, Inc., Natick, Massachusetts, USA) scripts were used to drive data acquisition. The raw voltage signal from the receive coil was amplified by an SR560 pre-amplifier (Stanford Research Systems, Inc., California, USA) prior to digitization and sampling at $10\ MHz$ with a PCI-6115 12-bit ADC (National Instruments, TX, USA).

All 1D excitation trajectories consisted of an (approximate) square wave, trapezoidal, or sinusoidal excitation superposed with a linear bias field to cover a magnetic FOV from -40 to 40 mT over a total single acquisition time

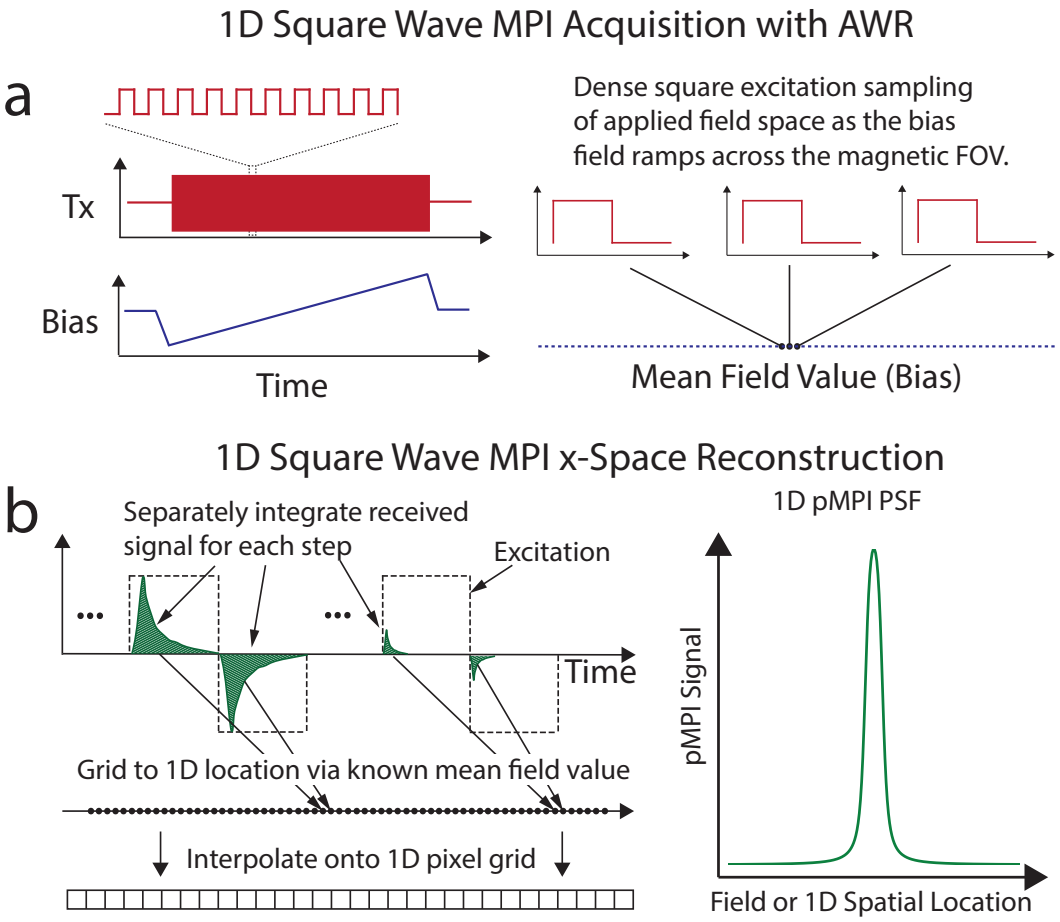

FIGURE 4.6: Square Wave data acquisition and image reconstruction using the AWR. (a) In acquisition, a slowly-varying bias field allows us to sample a large magnetic FOV over time with the faster square wave excitation (Tx). This pulse sequence leads to a dense sampling of points in the applied magnetic field domain. (b) In a simple x-space reconstruction, we can integrate the signal for each square wave half-period and grid this value to the mean field location. In a final step we can interpolate the gridded data onto a desired 1D pixel grid. The result is a 1D square wave PSF. If we divide the applied field by an assumed gradient, we arrive at a 1D spatial PSF.

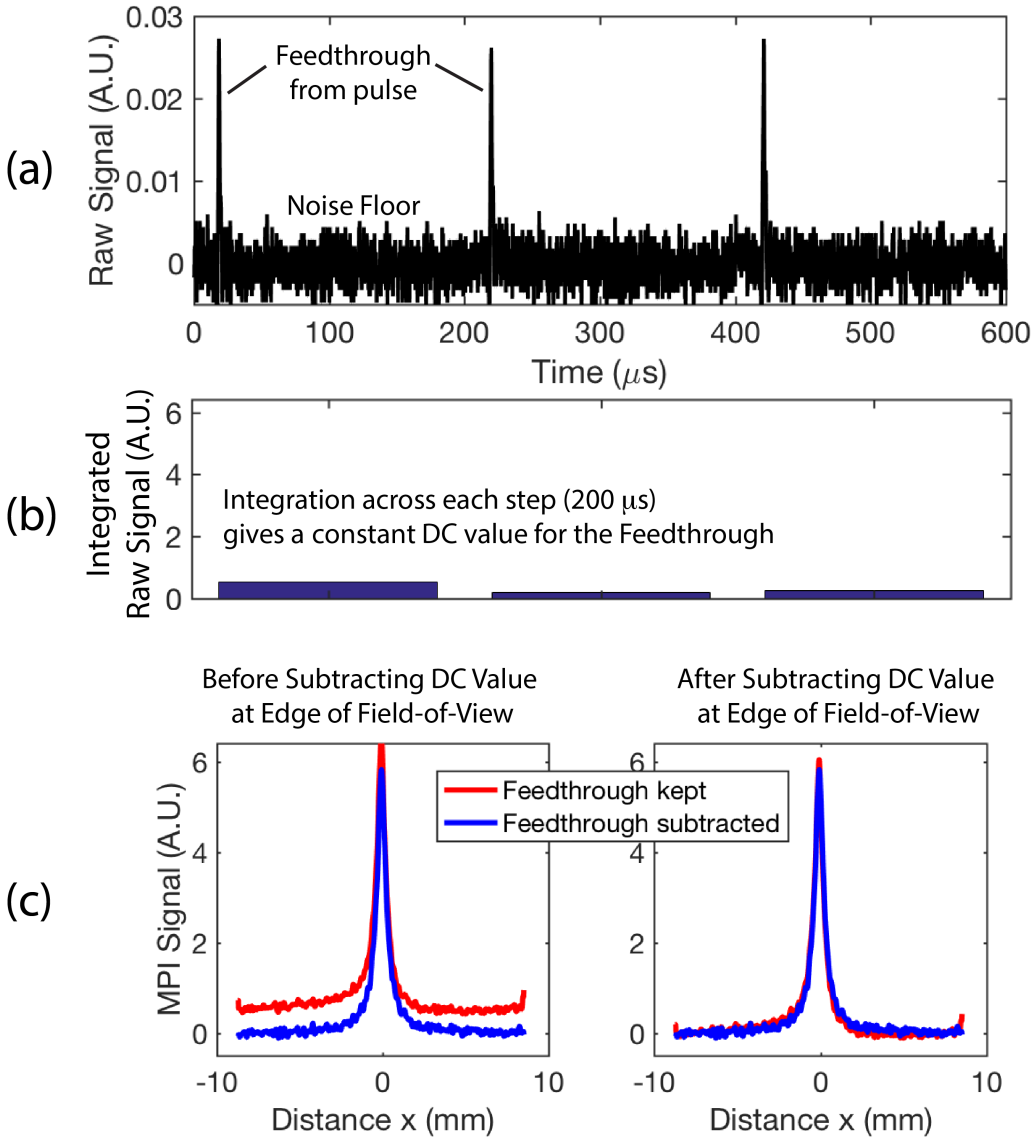

FIGURE 4.7: (a) Feedthrough in pulsed MPI manifests as a narrow spike coinciding with the pulse. The experimentally measured feedthrough is greatly attenuated by fine gradiometer tuning as described in prior work (Tay et al., 2016). (b) Without removal of the feedthrough before reconstruction, this results in a benign, fixed DC value added to each pixel (variation is due to noise). (c) Reconstructed point-spread-functions from experimental data (27nm SPIO, 2.5 kHz 0.5 mT step). Unlike standard MPI that requires a more complex partial FOV DC recovery algorithm (Lu et al., 2013), the feedthrough in pulsed MPI reconstructs as a benign global DC offset that can be removed using robust *a priori* assumptions of zero signal at the edges of the imaging FOV (simple subtraction of the DC value across the entire FOV). Thus, time-domain baseline subtraction is not required in pMPI.

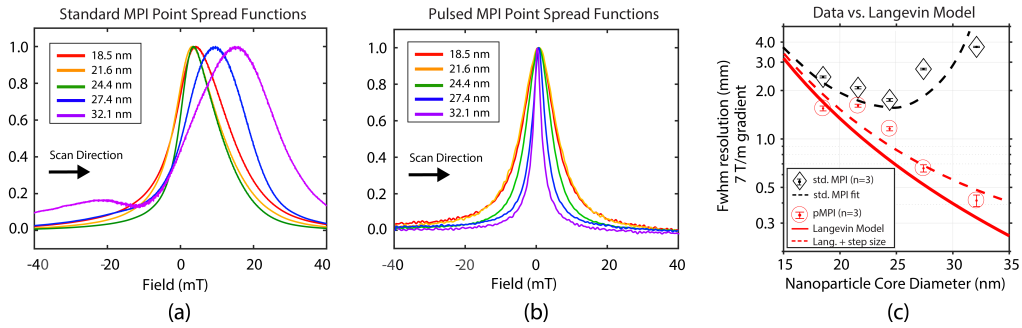

FIGURE 4.8: Experimental comparison between conventional sinusoidal MPI at 25 kHz, 20 mT with square wave pulsed MPI at 2.5 kHz, 1 mT step size.
(a) Standard MPI data shows that resolution stops improving after 24.4 nm (PSF widens) and significant relaxation-induced blurring occurs. (b) Pulsed MPI data for the same range of magnetic core sizes show constant improvement of resolution (PSF narrows) with core size as predicted by the Langevin Model (c) Comparison of experimental sinusoidal MPI FWHM resolution, square wave pMPI FWHM resolution, and theoretical Langevin prediction as a function of tracer core size. Note the inflection point in sinusoidal MPI resolution such that larger tracers have worse resolution while square wave pMPI allows us to realize with Langevin theoretical prediction (solid red line) with a small offset (dashed red line) due to the contribution of the excitation amplitude to FWHM.

of 0.5–0.7 seconds. To improve SNR, up to 25 single acquisitions were taken serially and averaged together, for a maximum of 17.5 seconds total acquisition time per 1D trial or 2D line acquisition. Additionally, void baseline scans, with no sample present, were taken for time domain baseline subtraction in reconstruction. In general, three replicate trials were performed in each experiment to report statistical variation in device performance.

4.5.4 Testing of 2D pMPI

Conventional MPI field-free-line projection scans were obtained on the Berkeley field-free-line preclinical imager that has been validated in previous work (Yu et al., 2017b). In brief, this imager has the drive coil along the z-axis and the field-free-line along the y-axis. x-z projection images are made by shifting the field-free-line along x via electromagnets and shifting the sample through the vertical bore using a robot stage along z. The drive waveform was 20.25 kHz and 20 mT drive waveform and a 3.5 T/m gradient was used.

For 2D projection imaging, a small-bore, miniature replica of the Berkeley field-free-line preclinical imager was implemented on the AWR. While

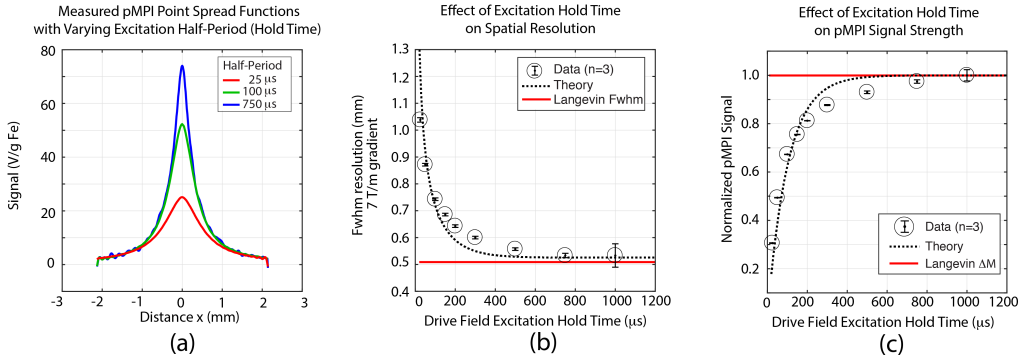

FIGURE 4.9: Square wave MPI experimental results as a function of hold time (half-period of square wave) – the length of time at a constant applied field to establish steady-state – and comparison with theory for 27.4 nm particles. Step size of 1 mT was used. (a) 1D point spread function with varying hold time. Resolution and signal strength worsens with shorter hold times as the SPIO is unable to reach steady-state magnetization, resulting in relaxation-induced blurring and lower peak signal. This is in part due to long relaxation times at low field strength leading to the observed 'peak depression' of the PSF for shorter hold times. (b) Spatial resolution improves and approaches that of the Langevin Model as hold time increases $\rightarrow 3\tau$. The results match our theory that pMPI relies critically on waiting long enough for SPIO magnetization to reach steady-state. (c) pMPI peak signal worsens with shorter hold time as the SPIO does not have enough time to reach steady-state magnetization, resulting in a lower measured ΔM than $M_{\mathrm{steady-state}}$. The results show that long hold times are desirable, but this must be traded-off against longer scan times. Because the resolution and signal strength plots asymptotically approach Langevin values, the optimal hold time should correspond to the start of the asymptotic approach to steady-state because diminishing returns occur thereafter. A good rule-of-thumb for hold time should be 2 – 5 τ where τ is the Debeye relaxation time constant.

the frequency-flexible drive and receive coil was kept, the bias coil was replaced by a NdFeB permanent magnet array that generates a field-free-line with a gradient of 3.5 T/m. This results in the drive coil along z-axis and the field-free-line along the y-axis, which is the same geometry as the preclinical scanner. To shift the field-free-line in x, a helmholtz electromagnet pair was installed. Similar to the preclinical scanner, x-z projection images are made by shifting the field-free-line along x using the helmholtz electromagnets while shifting the field-free-line along z by implementing a slight DC value to the frequency-flexible drive coil for the duration of the scan. A 1 kHz 1 mT step pulsed drive waveform was used.

4.5.5 pMPI reconstruction

In our pMPI x-space implementation, we perform basic digital signal processing (DSP) on the digitized received voltage waveform. This includes application of a digital filter with a $200 - -500\ Hz$ passband around each harmonic of the fundamental frequency (depending on the bias field slew rate), up to a maximum absolute frequency cutoff of $500\ kHz$. With a fast slewing square wave excitation, the transmit feedthrough, in a d/dt sense, is limited to a few μs after each step jump. Due to the significant relaxation of larger core tracers, this can be exceptionally separated from the majority of the tracer signal. In such cases, this allows us to retain most of the tracer signal without need for feedthrough removal or even baseline subtraction. Time-domain baseline subtraction is a robust process with our AWR, and so is generally performed to remove the amount of feedthrough that does overlap along with any remaining sources of interference. However, without time-domain baseline subtraction, feedthrough that remains in the signal translates to a global DC offset in the reconstructed image domain. Using robust *a priori* assumptions of zero signal at the edges of the imaging FOV, we can remove this global DC without requiring a more complex partial FOV DC recovery as employed in sinusoidal x-space MPI (Lu et al., 2013) . We show data for reconstruction with and without time-domain baseline subtraction to demonstrate this property of pMPI.

Fig. 4.6(a) graphically illustrates the relationship between time domain signal and the spatial trajectory in acquisition. This in turn motivates a simple mapping or gridding procedure in reconstruction as illustrated in Fig. 4.6(b). After DSP, we fold the signal into half-period chunks, integrate each chunk, and grid this value to a location in the magnetic field domain: $H_n - \Delta H$ where H_n is value of the total applied field (including the bias field contribution) immediately prior to a step jump and ΔH is the square wave amplitude. The result is a 1D PSF of the MPI signal gridded against applied magnetic field space. ΔH may be positive or negative depending on the slew direction. We also note that the nature of pMPI excitation (abrupt dynamic changes interspersed with quiescent periods) as well as the integration step simplify phase coherence methods required in x-space implementations. Precise identification of the initiation of each half-period excitation is typically easily obtained from the raw data itself. All SNR and signal calculations are normalized to the tracer mass. For 2D image reconstruction, the same procedures is followed. Instead of gridding the signal to a mean magnetic field, however, we grid the value to a mean location.

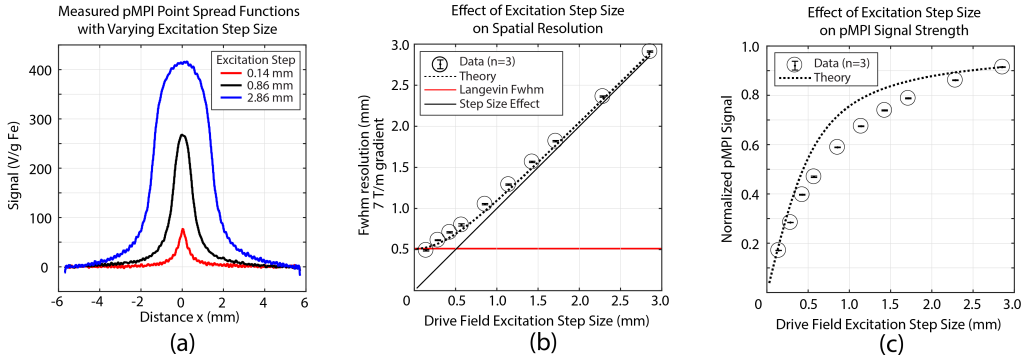

FIGURE 4.10: pMPI experimental results as a function of excitation step size and comparison with theory for 27.4 nm particles. 2.5 kHz square wave with varying amplitudes was used. (a) pMPI 1D point spread functions show higher signal but worse resolution with increasing step size. (b) Spatial resolution improves and approaches that of the Langevin Model as step size decreases $\rightarrow 0$. The results match our theory that pMPI is a discrete sampling of the ideal Langevin dM/dH curve, and the large step sizes equate coarse discrete sampling that incurs a rect convolution blurring effect. (c) pMPI peak signal improves with increasing excitation step size as a larger portion of the SPIO's M-H magnetization curve is covered per step. This implies a spatial resolution and SNR trade-off in optimizing the excitation step size.

Because no gradient fields are present in the 1D scans, the system collapses the sample geometry to a point and the resulting PSF is representative for the sample in aggregate. We have previously described theoretically and shown experimentally (Tay et al., 2016; Croft et al., 2016) that the 1D PSF obtained using an x-space relaxometer corresponds directly to the 1D PSF obtained in an imaging scanner after division by the gradient strength of the scanner. We therefore plot some of our experimental 1D PSFs as a function of position by assuming a $7\ T\,m^{-1}$ gradient, the gradient strength of our highest resolution in house scanner (**goodwill2012x**).

4.6 Experimental Results

4.6.1 Comparison of Pulsed MPI and Standard MPI

Fig. 4.8(a) shows 1D PSFs obtained with the AWR for each of the tracers but using conventional sinusoidal MPI excitation. Here we used the standard $f_0 = 25\ kHz$ and $20\ mT$ excitation amplitude used in our scanning systems. The effects of magnetic relaxation are apparent in the data: blur and translation in the scanning direction. Fig. 4.8(b) shows pMPI PSFs

obtained with the same samples using $1\ mT$ square wave excitation. The steady-state encoding of pMPI leads to PSFs without blurring and translation from magnetic relaxation effects and larger tracers produce narrower PSFs. Finally, Fig. 4.8(c) plots the FWHM resolution for sinusoidal MPI, square wave pMPI, and the theoretical Langevin model. We see the characteristic inflection point around $25\ nm$ for sinusoidal excitation, leading to worse resolution for the larger tracers. In contrast, the square wave pMPI data points follow the theoretical Langevin curve with a slight offset. The effect of the excitation amplitude means we only asymptotically approach the theoretical Langevin resolution, leading to the observed offset. This effect is explained in more detail two subsections below.

4.6.2 Effect of Drive Frequency (Wait Time) on Pulsed MPI

As shown in the Theory Section 4.4, pMPI crucially relies on waiting for SPIO magnetization to complete after each pulse step. An optimal wait time could be defined as the time taken to reach 95% of the steady-state magnetization, which is equal to $\sim 3\tau$ of the Debeye-model relaxation time constant. This time constant varies significantly between SPIOs, therefore, designing an optimal pMPI drive waveform requires prior measurement of the SPIO relaxation behavior. It must be emphasized that pMPI's resolution-enhancing circumvention of relaxation-induced blurring *does not* rely on assuming a Debeye-model of relaxation. In fact, we do not have to assume any relaxation model, and it is only required to measure that the SPIO magnetization reaches (approximately) steady-state after the wait time.

Fig. 4.9 shows the effects of hold time in experimental square wave pMPI. Fig. 4.9(a) shows square wave pMPI PSFs constructed from acquisitions with square wave half-periods of $25\ \mu$ s, $100\ \mu$ s, and $750\ \mu$ s. A phenomenon of 'peak depression' is apparent for shorter half-periods which reduces the FWHM resolution of the PSF as shown in Fig. 4.9(b). The magnetic relaxation is a strong function of the applied field strength. At low field strengths the relaxation time is longest and unable to achieve steady-state conditions at, *e.g.*, 25 or $100\ \mu s$. This results in relaxation-induced blurring as the magnetization signal from one pixel is spread into the next pixel because the magnetization only completes in the next time window. This incomplete magnetization also reduces the signal at low background fields, although steady-state may be achieved at the higher background fields even with short hold times because there is a smaller amount of steady-state magnetization to move through at the near-saturation portions of the ideal Langevin

curve. This results in a 'peak depression' effect where signal at high background fields is relatively unaffected by hold time while the signal at the peak region (low background fields) is attenuated by incomplete magnetization. Fig. 4.9(c) quantifies the peak signal loss as a function of hold time. Due to incomplete magnetization, the peak signal is lower at short hold times. Good agreement of experimental results with theory is observed for both the spatial resolution and peak signal plots.

4.6.3 Effect of Drive Amplitude (Step Size) on Pulsed MPI

Fig. 4.10(a) shows experimental square wave pMPI PSFs for the 27.4 nm tracer excited with different excitation amplitudes. As predicted by the theory, the PSF shape, SNR, and resolution are strongly affected by the choice of excitation amplitude, with the characteristic rectangular blur apparent for the largest excitation. Fig. 4.10(b) experimentally quantifies the relationship between FWHM resolution and excitation amplitude, showing excellent agreement with the theory, and Fig. 4.10(c) quantifies the experimental peak signal as a function of excitation amplitude, also agreeing well with the theory.

4.6.4 Effect of Rise Time (Sharpness of Square Wave) on Pulsed MPI

Fig. 4.11(a) shows experimental pMPI excitation waveforms with varying linear rise times. The shortest duration rise time, 3 μ s is effectively a square wave. Trapezoidal waveforms with rise times of 10, 80, 150, and 380 μ s are also shown. Fig. 4.11(b) shows pMPI PSFs reconstructed from acquisitions using excitation waveforms with the different rise times while Fig. 4.11(c) shows how the peak signal varies with the rise time. There is essentially no effect on PSF shape and FWHM resolution as a function of rise time. PSF shape depends only on steady-state induction with a long enough hold time/half-period. As long as this parameter is chosen to achieve steady-state as indicated in Fig. 4.9, the desired FWHM resolution will be achieved. Longer rise times do lead to a minor decrease in peak image domain signal. This slight change is from longer square wave period (fixed flat top hold time + varying rise time) because the same signal is spread over a larger amount of time. Most importantly, the results here show that perfect square waves are not required to realize the benefits of pMPI, thus the hardware

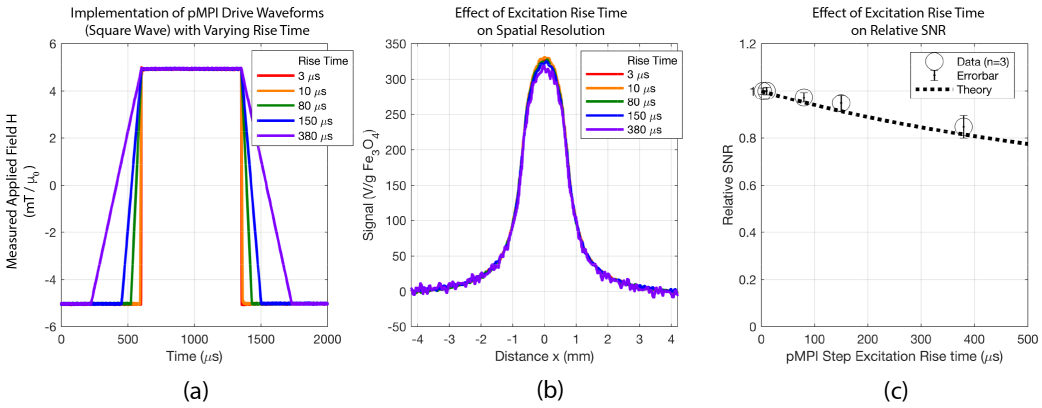

FIGURE 4.11: Experimental analysis of the effect of rise time using trapezoidal excitation waveforms with different rise times. The hold time was kept at 1 ms with a fixed step size of 10 mT. (a) Experimental excitation waveforms measured by the current monitor (AE Techron 7224) and converted to magnetic field by calibration with a gaussmeter probe (Lakeshore Instruments^{TM}). (b) Measured 1D point spread functions show that varying rise time has very little effect on the pMPI performance. (c) Relative SNR changes very little with increasing rise time. The slight change is from longer square wave period (fixed flat top hold time + varying rise time) because the same signal is spread over a larger amount of time. The results here show that perfect square waves are not required to realize the benefits of pMPI, thus the hardware criteria for pMPI is much less stringent as compared to hardware required for near perfect square waves.

criteria for pMPI is much less stringent as compared to hardware required for near perfect square waves.

4.6.5 Harmonic Analysis and Resolution-Bandwidth Relationship

Other than optimizing the pulsed waveform parameters, we also analyzed the effect of receive chain parameters on pMPI performance. One very important parameter is the number of harmonics recorded which directly determines the required receive bandwidth. Here, we reconstructed PSFs from the same experimental dataset but digitally adjusted the received bandwidth used. In Fig.4.12(a), we show reconstructed point spread functions using only 1 (red) or 15 (blue) harmonics of the fundamental square wave excitation frequency. The former corresponds to a narrow receive bandwidth while the latter corresponds to a wide receive bandwidth. In Fig.4.12(b), we plot the PSF FWHM resolution as a function of the number of harmonics used in reconstruction. In Fig.4.12(c), we plot the peak signal

intensity as a function of the number of harmonics used in reconstruction. Unlike in continuous wave MPI, resolution worsens with increasing receive bandwidth and the inclusion of more harmonics. Peak signal does, however, improve. This peculiar resolution-bandwidth relationship is a function of the temporo-spatial encoding of the signal due to the field dependence of the tracer magnetic relaxation. Tracer located far from the FFR is characterized by fast relaxation due to the high field conditions while tracer near the FFR is characterized by slower relaxation. Faster relaxation processes equate to higher harmonic information in the Fourier domain. In this manner, signal from tracer near the FFR center is relatively concentrated at the lower harmonics.

4.7 Discussion

4.7.1 Magnetostimulation Safety Considerations

Time-varying magnetic fields can have two possible effects on the human body - (1) stimulation of nerves through induced electric fields which often manifest as peripheral nerve stimulation (2) tissue heating which is measured by the specific absorption rate (SAR) metric. Because MPI uses strong time-varying magnetic fields, the corresponding safety limits for these two effects are relevant.

In considering magnetostimulation, we note that the fundamental law of electrostimulation (Reilly, 1989) states that a nerve will be stimulated if time-averaged electric field satisfies the following equation for any time period τ :

$$\frac{1}{\tau}\int^{\tau} Edt \geq E_{rheo}\left(1+\frac{\tau_c}{\tau}\right) \tag{4.12}$$

where E_{rheo} is the rheobase which is the minimum E-field required to stimulate a nerve and τ_c is the chronaxie which is a measure of the time needed to depolarize and stimulate a nerve.

For magnetostimulation, the induced electric field can be written as described in (Saritas et al., 2013a):

$$E = c_s \cdot r \cdot \frac{dB}{dt} \tag{4.13}$$

Modeling the human body as concentric rings perpendicular to a uniform B-field applied in the axial direction of the body (as is the case of

MPI preclinical scanners), and substituting a square wave excitation with a ramp-like rise time of τ_{rise}, and obtain:

$$E_{max} = c_s \cdot r \cdot \frac{dB}{dt} \tag{4.14}$$

$$E \approx \begin{cases} c_s \cdot r \cdot 2B_{peak} \div \tau_{\text{rise}} & \text{if } 0 < t <= \tau_{rise} \\ 0 & \text{otherwise} \end{cases} \tag{4.15}$$

We substitute eqn 4.15 into eqn 4.12 to obtain the B-field thresholds above which the nerve is excited :

$$\begin{aligned} B_{pp} \geq B_{min} \left(\frac{\tau_{\text{rise}}}{\tau} + \frac{\tau_{\text{rise}}}{\tau_c} \right) \qquad & \text{if } \tau < \tau_{\text{rise}} \\ B_{\text{pp}} \geq B_{\text{min}} \left(1 + \frac{\tau}{\tau_c} \right) \qquad & otherwise \end{aligned} \tag{4.16}$$

where $B_{\text{min}} = E_{\text{rheo}} \cdot \tau_c / (r \cdot c_s)$.

Because the nerve will be excited if eqn 4.12 holds true for any value of τ, and from eqn 4.16 the worst case occurs when $\tau \to \tau_{\text{rise}}$, we can write the threshold as:

$$B_{\text{pp}} \geq B_{\text{min}} \left(1 + \frac{\tau_{\text{rise}}}{\tau_c} \right) \tag{4.17}$$

Typical values for B_{min} and τ_c for the human torso are $\sim$ 14 mT and 20 – $600\mu s$ respectively (Saritas et al., 2013a). As such, we can avoid magnetostimulation problems if we maintain either of the following: (1) low excitation amplitude where $B_{\text{pp}} < 14mT$ (2) long rise time where $\tau_{\text{rise}} \geq \tau_c$. Although the latter is not favorable for pulsed MPI, fortunately, pulsed MPI uses low amplitudes and our analysis has shown that $B_{pp} \ll \text{FWHM}_{\dot{\mathcal{L}}}$ is necessary for the resolution to approach Langevin predicted resolution. In order to use pulsed MPI to improve upon the current MPI resolution, because the current best tracers are $\sim$ 6 – 12 mT FWHM, $B_{pp} \ll$ 12 mT is necessary and thus pulsed MPI will be safe in terms of magnetostimulation regardless of how short the rise time is. While surprising, this can also be understood as the fact that the larger E-fields generated by shorter rise times is offset by the shorter stimulation duration of the nerve. This is because of

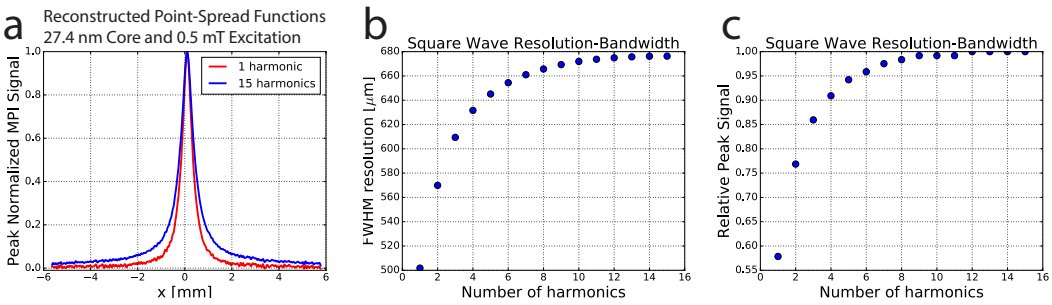

FIGURE 4.12: Experimental signal and resolution bandwidth relationships. (a) PSFs constructed from the same dataset but using only 1 (red) or 15 (blue) harmonics of the fundamental square wave excitation frequency in reconstruction. (b) PSF FWHM resolution as a function of the number of harmonics used in reconstruction. (c) Peak signal intensity as a function of the number of harmonics used in reconstruction. Unlike in continuous wave MPI, resolution worsens with increasing receive bandwidth and the inclusion of more harmonics. Peak signal does, however, improve. This peculiar resolution-bandwidth relationship is a function of the temporo-spatial encoding of the signal due to the field dependence of the tracer magnetic relaxation. Tracer located far from the FFR is characterized by fast relaxation due to the high field conditions while tracer near the FFR is characterized by slower relaxation. Faster relaxation processes equate to higher harmonic information in the Fourier domain. In this manner, signal from tracer near the FFR center is relatively concentrated at the lower harmonics.

the relatively large values of T_c such that for reasonably fast rise times, the E-field threshold $E_{\text{rheo}}(1 + \tau_c/\tau) \rightarrow E_{\text{rheo}}(\tau_c/\tau)$.

4.7.2 SAR Safety Considerations

Using a cylindrical model for the human body, and specifically focusing on the human torso that receives the most heating due to the SAR $\propto r^2$, the volume averaged specific absorption rate can be written as

$$\text{SAR} = \frac{1}{V}\int^{V} \frac{\sigma|\overrightarrow{E}(\overrightarrow{r})|^2}{\rho} dV \tag{4.18}$$

where for sake of simplicity, we assume σ, the tissue electrical conductivity in S/m, and ρ, the tissue density in kg/m^3, are approximately constant everywhere in the body.

Because only the ramping/step portion of the pMPI waveform generates an induced E-field, we can rewrite the equation 4.18 as:

$$\mathrm{SAR}_{\mathrm{ramp}} = \frac{\sigma}{\rho r_0^2} \int_{r=0}^{r_0} \left| \frac{\overrightarrow{E}(\overrightarrow{r})^2}{\rho} \right| r dr \tag{4.19}$$

$$= \frac{\sigma}{4\rho} \left(\frac{B_{\mathrm{ramp}}}{t_{\mathrm{ramp}}} \right)^2 r_0^2 \tag{4.20}$$

where r_0 is the outermost radius corresponding to the human body boundary.

SAR is time-averaged across the duration of the excitation, thus, we must average the generated SAR from the ramp portions with the zero SAR from the flat top regions of the pulsed waveforms, thus obtaining:

$$\mathrm{SAR} = \frac{\sigma r_0^2}{2\rho} \cdot \frac{B_{\mathrm{ramp}}^2}{t_{\mathrm{ramp}}(t_{\mathrm{ramp}} + t_{\mathrm{flat}})} \tag{4.21}$$

where the parameters in the first fraction are constants that are outside our control and the parameters in the second fraction are the pulse drive waveform parameters. We see that we can reduce SAR by using smaller B_{ramp}, longer t_{ramp} and longer t_{flat}. Using the following constants used in a prior MPI safety study (Saritas et al., 2013a): average radius for the human torso r_0 = 20 cm, σ = 0.5 s/m, ρ = 1000 kg/m^3, t_{flat} = 200 μs, and τ_c = 100 μs, B_{min} = 14 mT , we obtain a drive waveform limits plot specific to the pulsed waveforms used in pMPI. This plot is shown in Fig. 4.13. We reference Faes et al., 1999 to consider the effect of different tissue types such as fat, bowel, bone and lossy tissues. The fastest pMPI frequency involved is around 2 MHz, corresponding to a 1μs rise time. The relevant conductivity (σ) calculated from resistivity values (Ωcm) are: Bone 0.1 s/m, Fat 0.05 s/m, Skin 0.5 s/m, Muscle $0.5 - -0.8$ s/m, Lung $0.5 - -0.7$ s/m. The conductivity values at lower frequencies for all tissue types are lower than the 2 MHz values. Even when factoring in the highest conductivity value of 0.8 s/m, which is 1.6-fold higher than assumed, we see from Fig. 4.13 and equation 4.21 that pMPI can still easily maintain safety by using a 1.6-fold longer hold time or a smaller step amplitude. It has been shown that steps less than 2 mT amplitude give the best resolution performance and from Fig. 4.13 we see that safety is easily attained with 2 mT step sizes even at 1 μs rise times.

Because optimal pMPI waveforms use low amplitudes < 5 mTpp and there is negligible effect of rise time on pMPI performance, optimized pMPI

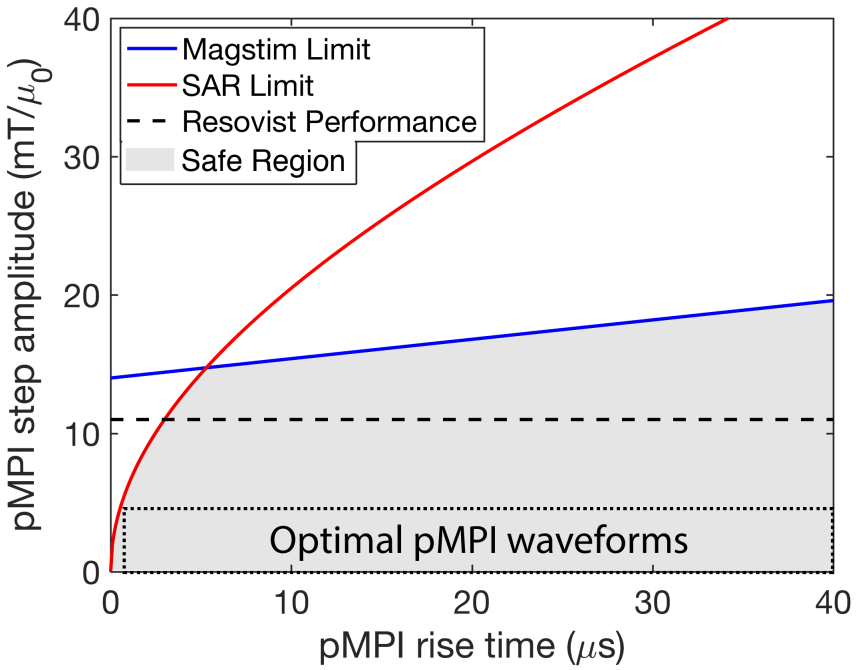

FIGURE 4.13: Safety limits for pMPI waveforms. Because optimal pMPI waveforms use low amplitudes < 5 mTpp and there is negligible effect of rise time on pMPI performance, optimized pMPI waveforms are safe. In general, any pMPI waveform that is designed to improve resolution better than Resovist^{TM}will require < 10 mTpp step size and will be safe as long as the rise time is > 2 μs.

waveforms are safe. In general, any pMPI waveform that is designed to improve resolution better than Resovist^{TM}will require < 10 mTpp step size and will be safe as long as the rise time is > 2 μs.

In conclusion, pulsed MPI with its low amplitude ($\ll 12$ mTpp) waveforms will not run into safety issues with either magnetostimulation or SAR.

4.7.3 Receive Chain Modifications for pMPI

Standard MPI uses a combination of gradiometer attenuation and analog high-order notch filters to remove feedthrough at the fundamental frequency. This is important because feedthrough is many orders of magnitude higher than the SPIO signal and can cause severe dynamic range for the MPI receive system in trying to detect low concentrations of SPIOs. In contrast, the feedthrough for pMPI is not limited to a single frequency f_0 but rather is limited in time-domain to the exact timing of the pulse step. While

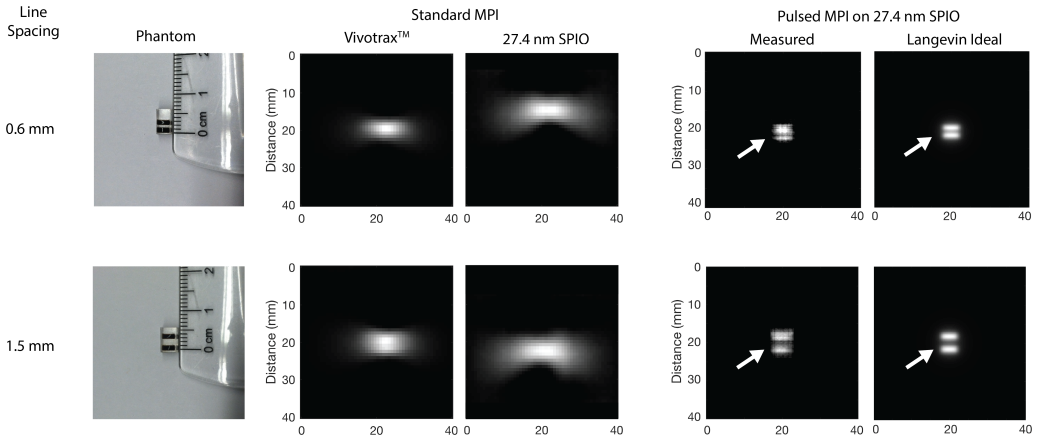

FIGURE 4.14: The resolution gains of pulsed MPI are verified using two-line phantoms with various distances between the lines. The AWR used to obtain 1D point-spread-functions with pulsed waveforms was outfitted with permanent magnets to generate a field-free-line scanner geometry similar to the preclinical scanner described in Fig. 7.3 and in (Yu et al., 2017b). Because the same drive coil is maintained as in the AWR, this small-bore scanner is able to implement pulsed waveforms in a 2D FFL-based scanning trajectory (Fig. 7.3). Projection MPI images are taken of the phantom using standard MPI and pulsed MPI. The results show that while standard MPI has significant blurring and is unable to resolve the two lines, pulsed MPI produces sharp images that are able to resolve the two lines. In addition, the measured images are very similar to the simulated images where the phantom used was 2D convolved with the ideal Langevin point spread function. This verifies that pulsed MPI approaches the spatial resolution predicted by the ideal Langevin model in 2D. The results also show a significant resolution gain of almost 8-fold when comparing standard MPI (27.4 nm SPIO) and pulsed MPI (27.4 nm SPIO). This clearly illustrates the large amount of relaxation-induced blurring present that was circumvented by the pulsed MPI strategy. Comparing to a typical Ferucarbotran tracer (vivotrax^{TM}) commonly used in MPI studies, pulsed MPI still maintains a 5-fold improvement in resolution over standard MPI, achieving 0.6 mm resolution with a 3.5 T/m gradient. This is almost two-fold better better than the 1D scans predict because leaving out a bit more of very initial part of the signal in each half-period improves resolution beyond that achievable by the Langevin model because it removes the "long tails" of the Langevin that cause blur because the signal from these regions completes very quickly and is found almost completely in the initial part. By using only the later parts, we restrict our signal to only the parts of the Langevin curve that have the largest magnetization change *i.e.* when the FFP is just above the SPIO. We name this strategy *tau-weighting* as it exploits the difference in magnetization time constant between the Langevin tails and the Langevin middle section, and we show that it improves resolution at the cost of some SNR. Using a 7 T/m gradient would give a very good 0.3 mm resolution *before deconvolution*. Further resolution improvements could be achieved with deconvolution by trading-off SNR.

gradiometers can also be used for pMPI to attenuate feedthrough, rather than use analog filters for frequency decoupling of signal from feedthrough, we can use a temporal gating system to temporally decouple the signal from the feedthrough. The nature of pMPI is to be used for large core size SPIOs with significant relaxation behavior. Therefore, it is expected that most of the magnetization signal will be delayed to after the initial step / pulse. Thus, with a fast enough rise time, minimal loss of the SPIO magnetization signal will be incurred while the feedthrough that is temporally limited to the pMPI waveform rise time can be *completely* removed.

There are several ways to implement this temporal gating. One method is to have a variable gain preamplifier that very quickly switches the gain of the receive chain from low during the feedthrough spike to high post-feedthrough spike. Another method is to have precision-controlled switches to shunt the voltage feedthrough spike away from the preamplifier during the rise time duration.

4.7.4 Maximum Theoretical Resolution Gain with pMPI

While pMPI has been shown to fully exploit the ideal Langevin theoretical cubic improvement of resolution with core size, it is not possible to continually increase SPIO core size indefinitely. Firstly, the ferromagnetic limit will be hit where the SPIO transitions from superparamagnetic to ferromagnetic. While in theory, pMPI should still be able to image ferromagnetic nanoparticles because the reconstruction algorithm is agnostic to the type of relaxation mechanism, ferromagnetic nanoparticles pose a host of other problems such as aggregation and poor colloidal stability.

Another issue is that the relaxation time constant should continue to increase with core size. This means that scan times will become longer and longer as we use larger core size SPIOs. At some point, there will be diminishing returns and the user may opt to limit the resolution to the maximum acceptable scan time.

Yet another issue is that a finite step size is required for pMPI pulse sequences. As shown in the theory section, the actual spatial resolution is offset from the Langevin value by approximately the step size. As the SPIO Langevin resolution approaches the lowest step size that can be implemented (from an SNR-limited perspective), gains in resolution from using larger SPIOs will have rapidly diminishing returns.

In view of these abovementioned issues, we anticipate that best practical resolution achievable with pMPI will be with 40 nm SPIOs with a net of 0.5

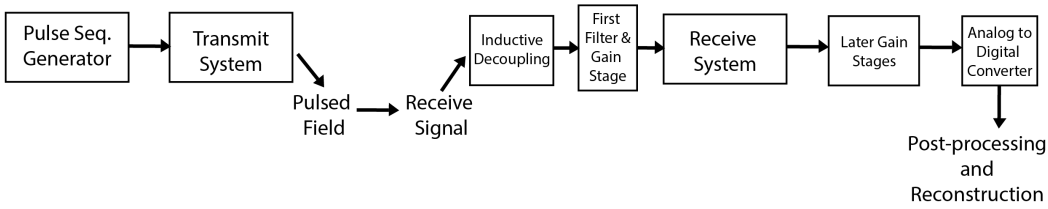

FIGURE 4.15: Block Diagram showing the overall hardware changes necessary to implement pMPI on the existing 3D scanner

mT step + 1 mT Langevin = 1.5 mT fwhm spatial resolution. This translates to approximately 200 micron resolution on a 7 T/m gradient.

4.8 Implementation on the 3D preclinical scanner - Preliminary Data

To implement pMPI on the existing 3D preclinical scanner, we aim to keep the main magnets that generate the MPI gradients, but completely overhaul the transmit and receive systems to incorporate the requisite broadband excitation pMPI entails. Fig. 4.15 shows a block diagram showing the overall changes to the Tx and Rx systems.

In detail, the transmit could utilize a linear circuit design in controlled voltage mode where the requisite voltages needed to produce sharp square waves are pre-calculated in software and sent to the power amplifier. While it is possible to perform this in controlled current mode, practically, it has been difficult to match commercially available power amplifiers with the requisite feedback compensation circuits needed to enable sub-microsecond control of the current by the amplifier (typically power amplifiers for audio systems are the most easily available). Fig. 4.16 details the circuit for such a design.

Alternatively, a switched transmit circuit design similar to Matter et al.'s design for pre-polarized MRI could be used Matter et al., 2006. This design relies on timed switching to connect and disconnect a resonant capacitor to generate the rapid transitions for current and also to maintain constant current for the piecewise-constant portions of the pMPI waveform. These switches need to handle the high power requisite for MPI transmit systems, thus Power Insulated-gate bipolar transistor (Power IGBTs) were a choice candidate due to their high current handling capabilities combined with the simple gate-drive characteristics of MOSFETs. Furthermore, IGBTs are

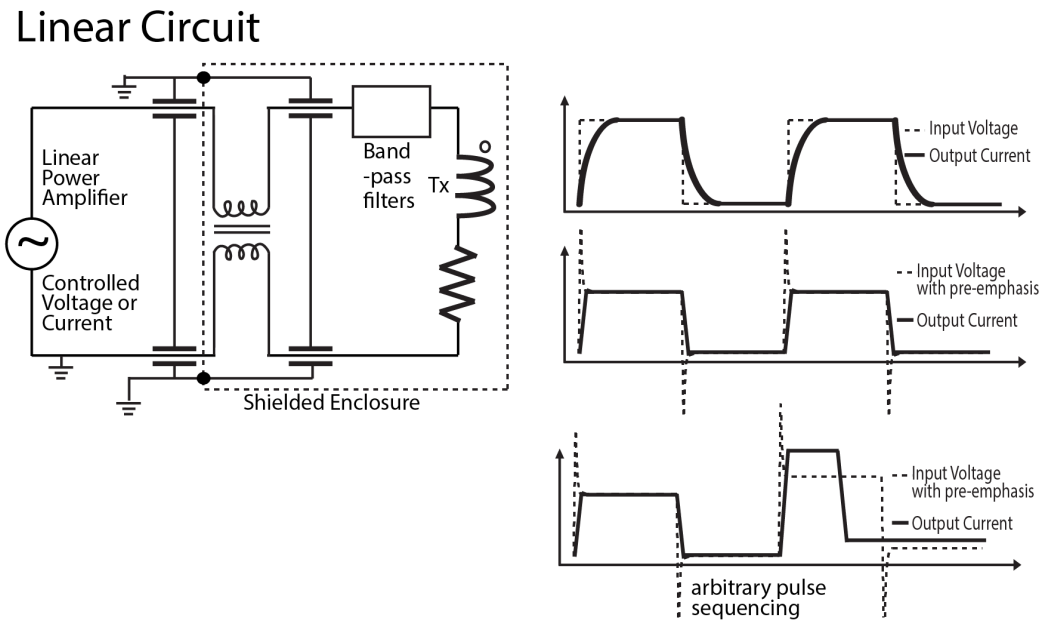

FIGURE 4.16: Linear circuit design for implementation of pMPI

well known to be capable of turning on and off rapidly. The key advantage of the switched circuit design is that much lower amount of power is necessary for pMPI operation since it is essentially a resonant transmit circuit and thus benefits from the power-saving resonant nature. The only power consumption thus comes from the lossy nature of the circuit components and can be "topped up" during each piecewise constant phase by connection to a voltage power source which does not actually need to be high power. Fig. 4.17 details the circuit for such a design.

Finally, a different receive circuit has to be designed to deal with the broadband nature of the excitation. In typical MPI, the excitation can be isolated to the single frequency fundamental and therefore feedthrough can be easily removed by analog filters. For pMPI, the excitation is broadband and overlaps almost exactly with the harmonics of the MPI signal. Furthermore, the feedthrough cannot be simply ignored because the SPIO signal is typically many orders of magnitude lower than the direct feedthrough, since unlike MRI, MPI excites and receives signal simultaneously. Thus, a different strategy is needed to deal with the pMPI feedthrough.

One such strategy is to temporally decouple the feedthrough from the pMPI signal. This relies critically on one key aspect of pMPI which is that the large core tracers that are enabled by pMPI have laggy magnetization.

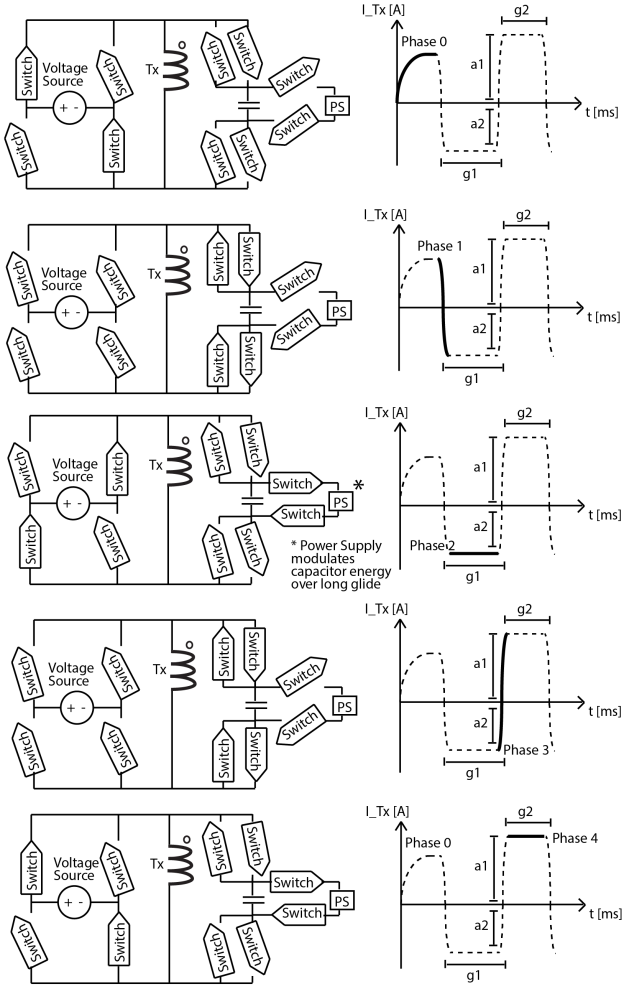

FIGURE 4.17: Switched circuit design for implementation of pMPI. The switches turn the circuit into a resonant one when rapid transitions of current through the inductor transmit is required and switch it back to a linear voltage-powered circuit when piecewise constant pMPI phases are required.

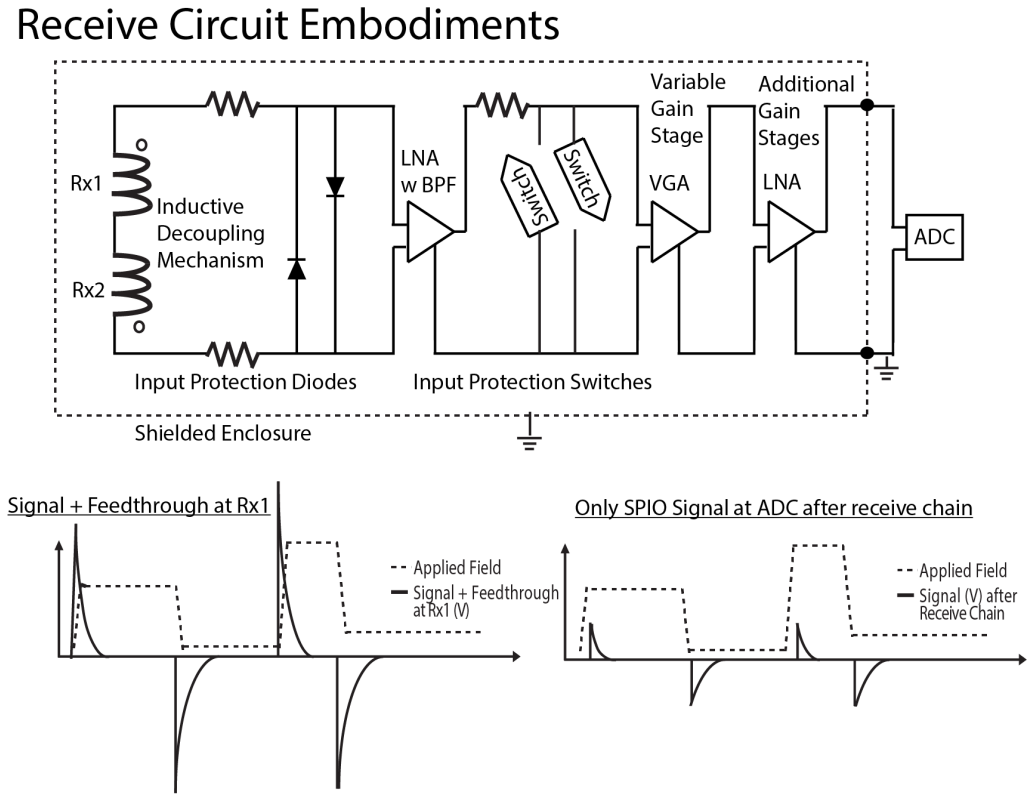

FIGURE 4.18: Receive circuit design for pMPI to deal with the different (pulsed) nature of direct feedthrough.

As such, if the excitation step is rapid and sharp enough, it can be expected that the SPIO magnetization and MPI signal will mostly occur after the excitation step due to the laggy magnetization. As such, almost all the SPIO magnetization, and thus MPI signal, can be preserved because it occurs after the step excitation. The direct feedthrough is restricted only to the step excitation, which we attempt to make as short and sharp as possible. By ”windowing” out this high feedthrough period by both analog and digital strategies, we are able to deal with feedthrough while keeping almost all of the SPIO pMPI signal that comes after the excitation.

There are a few strategies to implement this. First, variable gain amplifiers (VGAs) can be used. VGAs are commonly used in ultrasound circuits to modulate the received signal gain in real-time. Here, we attempt to use them for pMPI to modulate the receive gain to suppress feedthrough while amplifying the weak SPIO signal that comes after. Second, diodes and switchable voltage shunts can be used to protect the pre-amplifier from

overvoltage spikes from the excitation feedthrough. Fig. 4.18 shows a possible implementation of such a receive circuit.

The receive circuit was implemented on a miniature pMPI hardware model to simulate the expected pMPI feedthrough. Key to this preliminary testing is the implementation of the Variable Gain Amplifier setup. AD8331 VGA from Analog Devices ™was installed and tested first on a standard sine wave to show the gain suppression abilities, and then finally on expected pMPI feedthrough spikes. The VGA was able to suppress the spikes while amplifying the subsequent SPIO exponentially delayed (decaying) MPI signal, but further work is needed to further reduce the feedthrough spike, which is still larger than the SPIO signal. Fig. 4.19 shows the initial results on the oscilloscope.

4.9 Conclusion

In this work, we demonstrate a novel, pulsed method of scanning for MPI that we name pulsed MPI (pMPI). This method represents a significant departure from standard sinusoidal drive methods in MPI. We present 1D and 2D experimental results showing significant improvement in MPI spatial resolution with our new pMPI scanning strategy. Most importantly, we demonstrate that we can achieve the ideal Langevin resolution with pMPI, therefore unlocking the potential of the cubic resolution improvement with core size predicted by that model. This is significant because it motivates the development of larger core SPIOs since large SPIOs can now be used for improved resolution MPI scans while in the past relaxation blurring prevented large core SPIOs from effective use, limiting the MPI field to SPIOs with an optimal size of $\sim$ 25 nm. We hope that the novel scanning strategy described here will lead to improvements in MPI performance through development and effective use of larger core MPI tracers.

4.10 Acknowledgments

I would like to thank Daniel Hensley for his close collaboration on this work. I would not have been able to refine the theory this well without critical insights from Daniel. We had approximately equal contributions towards the hardware pulse sequence implementation, theoretical framework and experimental verification of our theory. This is reflected in the

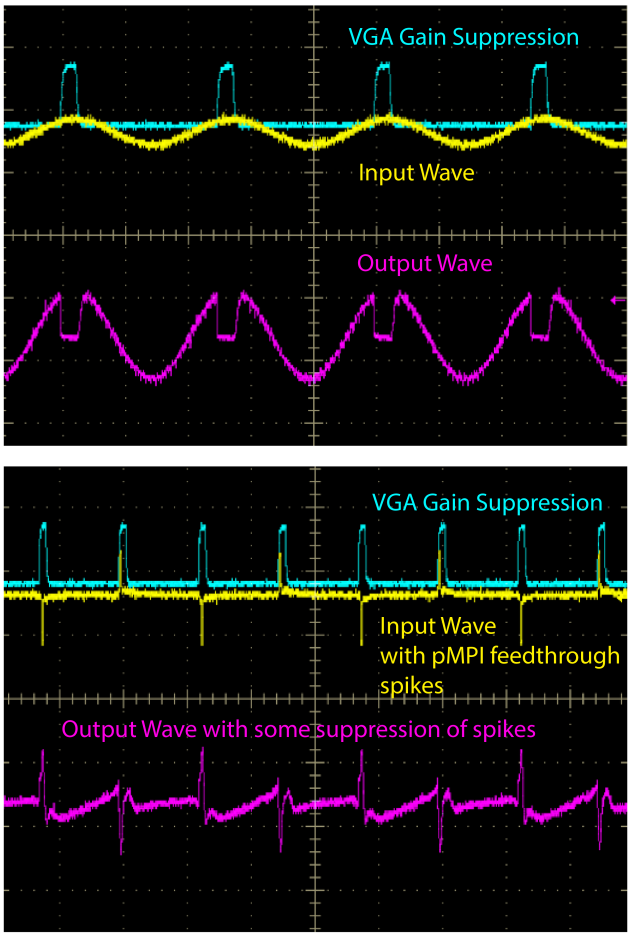

FIGURE 4.19: Preliminary results from testing of a variable gain amplifier (VGA) on the receive chain to mitigate pMPI direct feedthrough.

joint first-author status in our upcoming publication on pMPI. The write-up of this shared work in my dissertation here is original, although Daniel did describe the key ideas of pMPI when he wrote his dissertation a year ago. There is however, significant overlap only in the Methods section of this chapter, since the experiments were performed together with Daniel and these same methods were described in Daniel's dissertation. I would also like to thank Bo Zheng for all his help and advice in the initial attempts of implementing pMPI on the 3D preclinical scanner. I would also like to thank Steven Conolly for providing valuable advice and discussions during the early days of pMPI when the core concepts were still being developed. Special thanks goes out to undergraduates Quincy Huynh, Andrew Hild and Dilveen Goraya for testing some of the pMPI hardware towards implementation on the existing 3D preclinical scanner.

Chapter 5

Optimal Drive Waveforms for High Resolution and High Sensitivity MPI

5.1 Attribution

Reproduced in part from the Journal Publication:
Tay ZW, Hensley DW, Chandrasekharan P, Zheng B, Conolly S. Optimal Drive Waveforms for High Resolution and High Sensitivity MPI. IEEE Transactions of Medical Imaging. 2018. In submission.

5.2 Introduction

In the previous chapter, while we introduced a new MPI scanning method, pMPI, to unlock the benefits of large core size MPI tracers, we note that there are significant hardware changes required to implement pMPI. Most current MPI scanners are monotonal excitation systems at around 20 kHz and 20 mT. In fact, there has not been a study to verify if the use of 20 kHz / 20 mT excitation is the best conventional excitation parameters for MPI. There has been limited work so far to optimize the MPI excitation waveform. In this chapter, we take a step back into conventional MPI to question how to optimize standard excitation waveforms for MPI. The subsequent modifications to the hardware to implement such optimization would be much less than that required by pMPI, since the monotonal excitation strategy is maintained. In short, this chapter aims to provide insights into methods for improvement of MPI with minimal change from the current hardware designs, and provides a facile avenue for MPI optimization and improvement.

Here, we exploit the fact that the AWR is a frequency-flexible device with access to an unprecedented drive waveform parameter space. Prior MPI work has only investigated a handful of drive waveform parameters and while there is recent work showing that the low amplitude or low frequency drive waveforms can improve MPI's spatial resolution, the concomitant decrease of the MPI's tracer sensitivity by more than 10-fold was not addressed. There has yet to be a wide parameter space, multi-objective optimization of the MPI drive waveform for high resolution, high sensitivity and safety. In this first study of its kind, we experimentally optimize the drive waveform across an unprecedented 0.4 kHz – 416 kHz and 0.5 mT – 40 mT amplitude for a wide variety of nanoparticles from Resovist-like clusters to single core nanoparticles of various core sizes to determine optimal waveforms for each nanoparticle. We show that when optimizing for both factors, the trends are no longer monotonic and there are clear optimal drive frequencies and amplitudes. We present novel drive waveforms that show 2-fold improvement in spatial resolution without loss of MPI tracer sensitivity. Lastly, we compare these optimal waveforms to SAR and magnetostimulation safety limits to make recommendations on safe drive waveforms for high resolution and high sensitivity Magnetic Particle Imaging.

5.3 Background

Current preclinical MPI scanners uses drive waveforms of 26 kHz at 16 mT amplitude (Philips-Bruker preclinical demonstrator system) (Rahmer et al., 2015) or 20 kHz at 20 mT amplitude (University of California, Berkeley scanner) (Yu et al., 2017a). While recent work has shown that low amplitude (Croft et al., 2016; Shah, Ferguson, and Krishnan, 2014; Tomitaka et al., 2015) or low frequency drive waveforms (Kuhlmann et al., 2015) can improve MPI's spatial resolution, there is a significant concomitant drop in sensitivity due to the slower magnetic slew rates that was not fully addressed. Furthermore, only two types of particles, Resovist and University of Washington, were investigated and these represent a particle class with relatively small core sizes. There has yet to be a wide parameter space, multi-objective optimization of the MPI drive waveform for high resolution, high sensitivity and safety. Towards this goal, we expand upon prior work by experimentally optimizing the drive waveform across an unprecedented 0.4 kHz – 416 kHz and 0.5 mT – 40 mT amplitude for a wide variety of nanoparticles from Resovist-like clusters to single core nanoparticles of a wide range of core sizes. We show the first imaging data confirming that

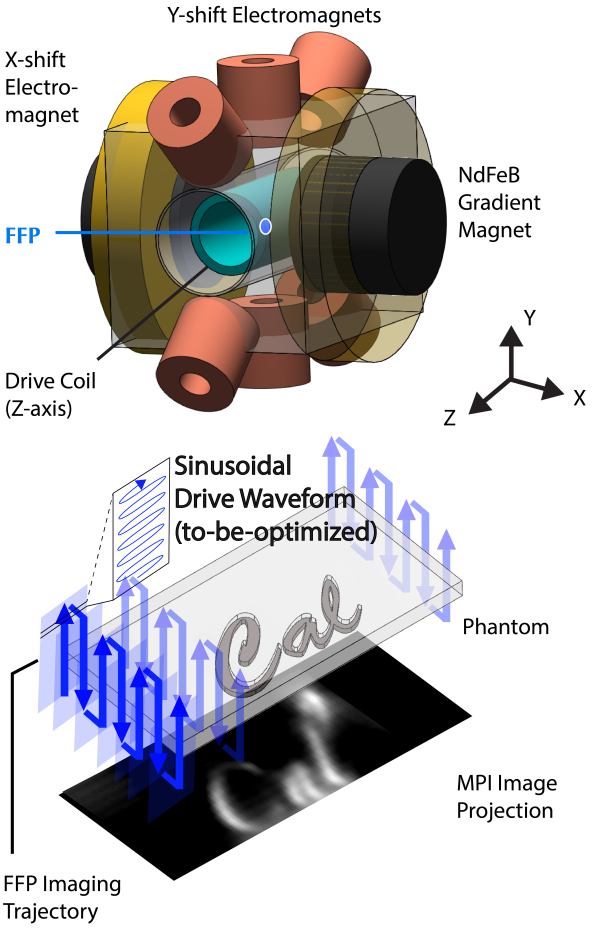

FIGURE 5.1: MPI rasters a sensitive point (the zero-field point or field-free-point) across a 3D volume to form an image of the superparamagnetic iron oxide nanoparticles (SPIONs) present. MPI's inductive signal is generated by the SPION magnetization response to the fast raster from the sinusoidal drive waveform. While the MPI imaging performance is highly dependent on the drive waveform, a comprehensive optimization of the drive waveform has yet to be done. In this work, we optimize the MPI drive waveform across an unprecedented 0.4 kHz - 416 kHz and 0.5 mT - 40 mT for *both* improved resolution and high sensitivity.

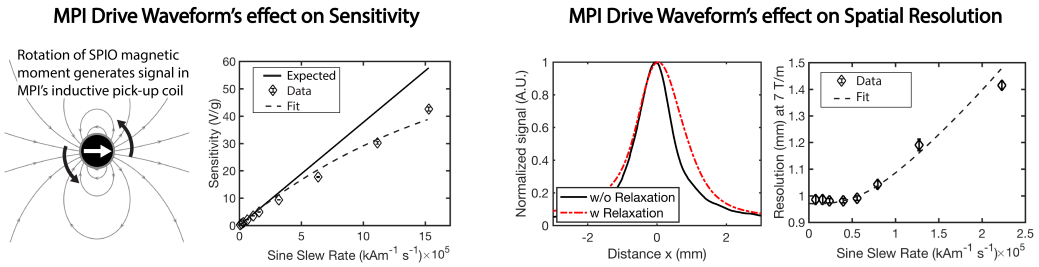

FIGURE 5.2: Because MPI uses inductive pick-up coils to receive the signal, the MPI signal is proportional to drive waveform slew rate by Faraday's law of induction. Thus, high sensitivity MPI needs high slew rate drive waveforms. However, as slew rate increases, we do not observe a perfectly linear gain in sensitivity as the ensemble magnetization of the SPIOs cannot keep up with the drive waveform slew rate due to (ensemble) magnetic relaxation. Magnetic relaxation at high drive waveform slew rates leads to blurring of the MPI signal because of delays in SPIO magnetization. As a result, low slew rates are favorable for resolution, but high slew rates are better for SNR and sensitivity. Because either frequency or amplitude can be adjusted to change the slew rate, and because the trends are not linear, this manifests as a non-trivial optimization problem to find the best trade-off for *both* good resolution and high sensitivity MPI.

our novel optimized waveform is able to significantly improve resolution while maintaining high sensitivity and safety.

To provide context for the experimental results, we will first review the physical theory behind the SPIO response in the time domain. We will then review how changes in the time domain signal translate to image domain effects for both system matrix and x-space reconstruction. Lastly, we will show how the experimental results match the trends predicted by theory.

5.4 Resolution and Sensitivity in MPI

The MPI signal is essentially the changing magnetization of the SPIO that arises when oscillating excitation waveforms induce an ensemble of tracers to rotate their magnetic moments as they attempt to align with the instantaneous magnetic field. Spatial localization in MPI is achieved by superposing a relatively static gradient field on top of these time-varying fields. This generates a sensitive point where the instantaneous applied field is approximately zero. This is known as the field-free-region (FFR). Particles outside of the FFR are saturated and unable to contribute significant time-varying signal, while particles inside the FFR are unsaturated and undergo steep magnetization changes detected by the MPI inductive receive coils.

In an ideal MPI process, the SPIO tracers will respond instantaneously to the applied field and the ensemble response will be accurately described by steady-state Langevin theory (Gleich and Weizenecker, 2005; Goodwill and Conolly, 2010). However, in practice, MPI tracers cannot instantaneously respond to applied fields. The finite *ensemble* temporal response observed by tracers is termed magnetic relaxation. A detailed discussion of the physics first principles governing magnetic relaxation is outside the scope of this paper. The interested reader is referred to the literature. While there are many different models for magnetic relaxation, in general it can be described by the Néel and Brownian mechanisms (**dhavalikar˙2016**; Dieckhoff et al., 2016; Deissler, Wu, and Martens, 2014). The general form for the Néel and Brownian relaxation time constants can be written as:

$$\begin{aligned} \tau_{\mathrm{N}} &= N(H) \cdot \tau_0 \exp\left(\frac{KV_{\mathrm{c}}}{k_{\mathrm{B}}T}\right) \\ \tau_B &= B(H) \cdot \frac{3\eta V_{\mathrm{h}}}{k_{\mathrm{B}}T} \end{aligned} \tag{5.1}$$

where N(H) and B(H) are functions that account for the effect of the applied magnetic field and K is a SPIO-specific anisotropy constant. These equations show that magnetic relaxation depends on the absolute applied field and the SPIO characteristics (Arami et al., 2013; Tay et al., 2017). As a result, the delay in SPIO response is not a constant and varies within a period of the excitation oscillation. This is observed as not only a time-delay but also a widening of the SPIO time-domain response (Croft, Goodwill, and Conolly, 2012). This leads to blurring of the MPI image and reduces both spatial resolution and sensitivity. Magnetic relaxation, when severe, can lead not only to delayed magnetization, but also incomplete magnetization of the SPIO tracer that has a huge impact on MPI sensitivity. While the absolute amount of magnetic relaxation is mostly determined by the properties of the SPIO tracer, its negative effects on the MPI image is modulated by the characteristics of the drive waveform. In the next subsections we will discuss how the drive waveform can be designed to minimize the negative effects of magnetic relaxation on the spatial resolution and sensitivity of the reconstructed MPI image.

5.4.1 Spatial Resolution in X-space Reconstruction

X-space reconstruction of the MPI time-domain signal goes through multiple steps. First, the signal is digitally filtered to keep only frequency components corresponding to the harmonics of the drive frequency. Next, the signal is scaled by a velocity compensation factor that accounts for the varying magnetic slew rate in a single period of the drive waveform. If the signal at the drive frequency (fundamental frequency f_0) is filtered out by a analog filter, the SPIO response at f_0 will also be lost. This information has been shown in prior work to be a unique DC offset for each partial field-of-view (pFOV) which in turn is is defined as the imaging trajectory covered by a single period of the drive waveform (**lu˙2013**). The lost SPIO response at f_0 can thus be recovered by a continuity algorithm that combines overlapping pFOVs. Lastly, the time-domain signal is mapped onto the corresponding instantaneous position of the field-free-region to form an image. In this paper, we use the Houston resolution criterion which approximates a system's resolution is the full-width-half-maximum value of the point spread function (Houston, 1927). It has been shown that the resolution in units of applied field (mT/μ_0) can be robustly converted to spatial resolution (in mm) by simply dividing by the gradient strength G (T/m) (Croft et al., 2016; Tay et al., 2016). For imaging relevance, the data is thus displayed as expected spatial resolution (mm) at a 7 T/m gradient.

The widening of the SPIO temporal response has the most dominant blurring effect in the final step of the reconstruction because the widened temporal signal is spatially mapped onto a wider area in the image, thereby increasing blurring and worsening spatial resolution. Croft et al. (Croft et al., 2016) has shown that a simple first-order Debeye relaxation model is a good phenomenological model for the behavior of Resovist and University of Washington SPIOs. They further show that they can reasonably approximate the spatial resolution by the weighted sum of a base resolution (in terms of full-width-half-maximum) and a drive waveform dependent blurring term.

$$\Delta x \approx \alpha \Delta x_{\text{base}} + \beta \Delta x_{\text{blur}} \tag{5.2}$$

This blurring term has been shown to be a strong function of both the phase lag of the signal, ϕ as well as the drive field amplitude H_{amp}, leading to the trend that lower drive field amplitudes improve spatial resolution. G

denotes the gradient field strength in T/m.

$$\Delta x_{\text{blur}} = \frac{ln(2)\phi(H_{\text{amp}}, f_0)H_{\text{amp}}}{G} \tag{5.3}$$

These equations show that the blurring term can be reduced by reducing the drive amplitude or the phase lag term. Lower drive amplitudes decrease the H_{amp} term but increase ϕ. The net effect on Δx_{blur} depends on the SPIO characteristics defined in (Eqn.5.1) that modulate the ϕ dependence on H_{amp}. Lower drive frequencies decrease phase lag ϕ because the time delays caused by magnetic relaxation are now smaller relative to the longer drive period. It must be emphasized that ϕ is not a linear function of H_{amp} or f_0 due to the field-dependence of the Brownian and Neel time constants and the dependence of dM/dt on the difference between $M_{ss}(H)$ and $M(t)$. The phase lag ϕ can be approximated by weighted sum of time-delays:

$$\phi \approx \int_{t=0}^{0.5/f_0} \frac{M_{ss}(2\pi H_{\text{amp}} f_0 t) - M(t)}{2M_{ss}(H_{\text{amp}})\tau(2\pi H_{\text{amp}} f_0 t)}(t - \frac{0.25}{f_0})dt \div \frac{1}{f_0} \tag{5.4}$$

The phase lag ϕ thus only describes the weighted average of all the instantaneous relaxation time constant as the field changes from $-H_{\text{amp}}$ to $+H_{\text{amp}}$. Regardless, it is clear that lower drive frequencies will improve resolution but lower drive amplitudes improve resolution only if $\phi(H_{\text{amp}}, f_0)$ does not worsen enough to offset the gains from the H_{amp} term.

5.4.2 Signal-to-Noise Ratio (SNR) in Magnetic Particle Imaging

Magnetic Particle Imaging utilizes inductive receiver coils therefore the MPI signal is directly proportional to the rate of change of magnetic flux. The signal equation for MPI (Goodwill and Conolly, 2010) can be written as:

$$\begin{aligned} s(t) &= B_1 \frac{d\phi}{dt} = B_1 m\rho(x) * \dot{\mathcal{L}}[kGx]\,(kG\dot{x}_s(t)) \\ s(t) &\approx B_1 m\rho(x) * \dot{\mathcal{L}}[kGx]\,(k2\pi f_0 H_{\text{amp}}) \end{aligned} \tag{5.5}$$

where B_1 is the receiver coil sensitivity, $\rho(x)$ is the spatial distribution of the magnetic nanoparticles, $\mathcal{L}$ is the langevin function, k is a nanoparticle specific constant defined as the ratio of magnetic to thermal energy ($k = \mu_0 m/k_B T$), G is the magnetic gradient in T/m and $\dot{x}_s(t)$ is the rate of movement of the field-free-point or field-free-line. If we only utilize

the MPI data from the approximately linear region of the drive sinusoid, $G\dot{x}_s(t) \approx 2\pi f_0 H_{\text{amp}}$. When magnetic relaxation is considered as well, the MPI signal equation (Croft, Goodwill, and Conolly, 2012) can be rewritten as :

$$\begin{aligned} s_{relax}(t) &= s(t) * r(t) \\ &\approx B_1 m\rho(x) * \dot{\mathcal{L}}[kGx]\,(k2\pi f_0 H_{\text{amp}}) * r(t) \end{aligned} \tag{5.6}$$

where r(t) is a relaxation convolution kernel describing the magnetic relaxation of the specific nanoparticle used. A common and well-validated model for magnetic relaxation is the Debeye model (Croft, Goodwill, and Conolly, 2012) where $r(t) = (1/\tau)exp(-t/\tau)u(t)$.

Noise in MPI comes from three main sources: (1) body noise (2) resistive receiver coil noise (3) preamplifier noise. The low kHz frequencies used in MPI mean that body noise tends to be negligible. The MPI received signal exists at higher harmonics of the low kHz drive frequency and is higher frequency than the $1/f$ noise present in Si-BJT and Si-JFET transistors used in the preamplifiers. Therefore, we can model the coil noise to be white noise over the noise bandwidth. Assuming AC resistance remains flat, coil noise dominance and that we acquire a fixed number N_{harm} of signal harmonics of the drive (fundamental) frequency f_0, we have:

$$\begin{aligned} < n > &\approx \sqrt{(e_n^2 + 4k_B T_{\text{coil}} R_{\text{coil}})\Delta f} \\ &\approx \sqrt{(e_n^2 + 4k_B T_{\text{coil}} R_{\text{coil}}) N_{\text{harm}} f_0} \end{aligned} \tag{5.7}$$

At first glance, it seems that higher drive frequencies will result in more noise due to a larger requisite receive bandwidth. However, in MPI reconstruction, only a small window around each harmonic in the Fourier signal spectrum is kept after a digital "comb-like" sampling of the Fourier signal spectrum (**lu˙2013**; Goodwill and Conolly, 2010; Croft et al., 2016) . Furthermore, the width of this window is fixed regardless of drive frequency. As a result, although a larger front-end receive bandwidth is required for higher drive frequencies, the effective noise bandwidth post-processing does not increase with f_0. Therefore, the noise post-processing can be rewritten as follows, which emphasizes the invariance of MPI noise with the drive waveform.

$$\begin{aligned} < n_{pp} > &\approx \sqrt{(e_n^2 + 4k_B T_{\text{coil}} R_{\text{coil}}) N_{\text{harm}} f_{\text{window}}} \\ &\approx \sqrt{(e_n^2 + 4k_B T_{\text{coil}} R_{\text{coil}}) \Delta f_{\text{constant}} (N_{\text{harm}})} \end{aligned} \tag{5.8}$$

Overall, the SNR of MPI is therefore directly proportional to the peak signal if we assume a fixed number of signal harmonics is used and that the fourier window around each harmonic is fixed:

$$\begin{aligned} SNR &\approx \frac{s_{\text{peak}}}{< n_{pp} >} \\ SNR &\propto B_1 \dot{\mathcal{L}}(kGx)\,(k2\pi H_{\text{amp}} f_0) \end{aligned} \tag{5.9}$$

This is a powerful statement that shows that the MPI drive waveform is key in determining the SNR of MPI. While the hardware parameters are important in determining the noise properties, they fall out as a constant when investigating the effect of drive waveform on MPI SNR. Because the noise properties are frequency-invariant, SNR is directly proportional to peak signal. This implies that sensitivity S, defined as the peak signal in mV per mg of nanoparticle, is a good metric to compare SNR between different nanoparticles and drive waveforms. Therefore, for the purposes of this paper, we will use sensitivity S as the metric measuring relative SNR between the different nanoparticles and drive waveforms investigated in this paper.

5.4.3 Incomplete Magnetization Significantly Decreases Sensitivity and Further Worsens Blurring

From both equation 5.5 and 5.6, the MPI signal increases with higher drive field slew rate $\dot{x}_s$ according to Faraday's law for an inductive receive coil. When magnetic relaxation is negligible, the MPI signal is approximately proportional to the drive field slew rate. This seems to suggest that the drive field slew rate should be increased to improve signal in MPI. However, as the drive frequency is increased, the ratio of t/τ in the relaxation kernel is smaller on average because each period of the drive waveform is shorter. This implies a greater attenuation of the MPI signal by the relaxation kernel. Therefore, it can be expected that there is a critical drive frequency threshold beyond which there is rapidly diminishing returns for signal in MPI for realistic nanoparticles with non-negligible magnetic relaxation.

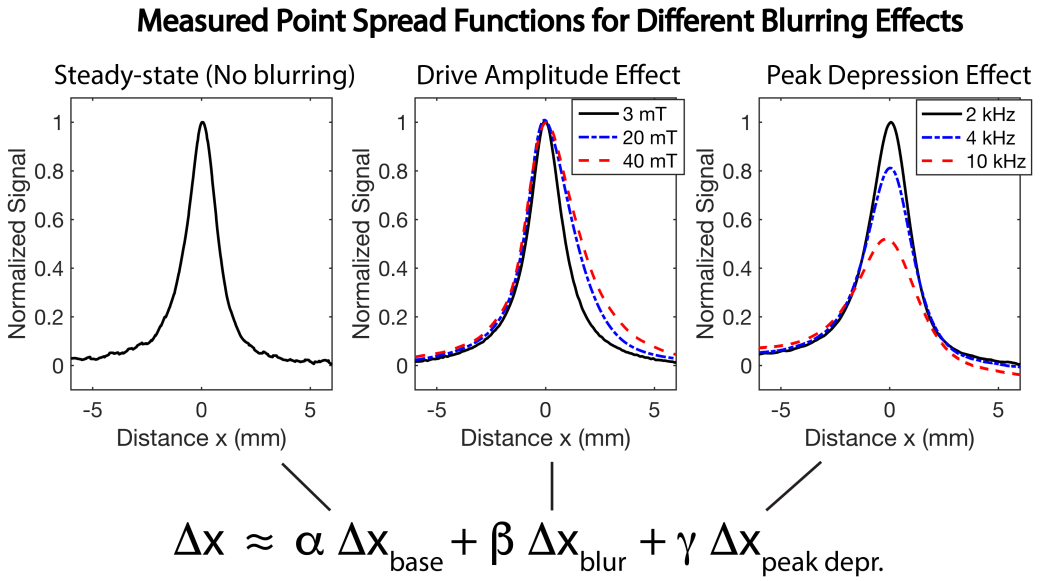

FIGURE 5.3: Our model for MPI resolution expands upon the model from Croft et al. 2016 (Croft et al., 2016) describing the effect of amplitude on MPI resolution. The base model describes the measured resolution as a weighted sum of the base resolution at steady-state (no blurring) and a blurring term that is dependent on the measured SPIO phase lag and drive amplitude applied. To demonstrate drive amplitude blurring, we show experimental point-spread-function of IB 32.1 nm SPIOs with the same drive frequency but varying drive amplitudes. The PSFs are normalized to a peak value set by Faraday's law. The results show increased blurring with higher drive amplitudes with negligible deviation of peak intensity from Faraday's Law. To expand upon the base model, we found that another effect should be added which we term 'peak depression'. This effect is necessary to account for the high frequency sensitivity of larger core size SPIOs as well as for the much larger range of frequencies used in this study. In essence, peak depression highlights the inability of the SPIO to magnetize fully when the applied field drive excursion is centered at the SPIO. This is because the SPIO has to rotate its magnetic moment through the largest angle here (180^o) and rotation is incomplete when the SPIO cannot keep up with the applied drive field. However, when the drive excursion is off-center, the SPIO does not have to rotate through a full 180^o and it keeps up with the drive field better, therefore obtaining magnetization changes closer to that predicted by the ideal Langevin. The result is less-than-expected ΔM / less signal at the peak while full ΔM / normal signal at the sides, giving a point spread function that only has its peak depressed. This effectively worsens resolution as the originally intense signal peak now blends into the background blur. To demonstrate peak depression, we show experimental point-spread-function of IB 32.1 nm SPIOs with the same drive amplitude but varying drive frequency. PSFs are normalized to a peak value set by Faraday's law. The results show that an increasing inability to keep up with higher frequencies, as shown by a deviation of the peak signal from Faraday's law. For instance, doubling the frequency should achieve twice the MPI signal peak, but the measured peak is less than twice.

If we keep the nanoparticle constant and focus only on the drive waveform parameters, equation 5.5 can be rewritten in terms of sensitivity S (mV MPI signal / mg of nanoparticle):

$$\begin{aligned} s(t) &= B_1 m\rho(x) * \dot{\mathcal{L}}[kGx]\,(kG\dot{x}_s(t)) \\ s_{peak} &= B_1 \dot{\mathcal{L}}(kGx)\,(k2\pi H_{\text{amp}} f_0) \\ S &\propto H_{\text{amp}} f_0 \end{aligned} \tag{5.10}$$

However, in cases where magnetic relaxation is large, the MPI signal is significantly attenuated by two effects : (1) the available magnetization change within a half period of the drive waveform is spread out leading to an attenuated peak signal (2) the available magnetization change is decreased because the SPIO is unable to reach its expected magnetization $M_{ss}(H_{\text{amp}}$ when the drive waveform reaches H_{amp} from $-H_{\text{amp}}$. In these cases, the sensitivity equation can be approximated as follows:

$$\begin{aligned} s_{\text{relax}}(t) &= B_1 m\rho(x) * \dot{\mathcal{L}}[kGx]\,(kG\dot{x}_s) * r(t) \\ s_{\text{peak}} &= B_1 \dot{\mathcal{L}}(kGx)\,(k2\pi H_{\text{base}amp} f_0) * (1/\tau) exp(-t/\tau) u(t) \\ S &\propto H_{\text{amp}} f_0 \left(1 - \exp\left(-\frac{1/f_0}{\alpha\tau(H_{\text{amp}})}\right)\right) \end{aligned} \tag{5.11}$$

where k is an SPIO-specific proportionality constant and α modulates $\tau(H_{\text{amp}})$ to provide an averaged, effective τ. As the period of the drive waveform becomes small enough to approach the relaxation time constant at H_{amp}, the MPI sensitivity drops rapidly due to incomplete magnetization of the SPIO. In general, increasing amplitude improves MPI sensitivity because $\tau(H_{\text{amp}})$ decreases with increasing H_{amp}. Increasing frequency only improves MPI sensitivity provided that the drive period is still significantly larger than the relaxation τ.

In addition, incomplete magnetization also increases blurring to worsen the spatial resolution. While the weighted sum approximation of Croft et al. (Eqn.5.2 holds true for lower drive frequencies and for SPIOs with relatively low amounts of magnetic relaxation, we have found that large discrepancies occur when the SPIO has generally large amounts of magnetic relaxation or when high drive frequencies are used. Our experimental results show that these discrepancies are due to incomplete SPIO magnetization within a single pFOV. This incomplete magnetization is most severe for pFOVs centered at the SPIO because there is the largest amount of magnetization change

expected within these pFOVs. As a result of incomplete magnetization at the central pFOV, the peak of the SPIO temporal response is significantly attenuated. However, side pFOVs (with respect to the SPIO position) are attenuated to a lower extent because the average H_{amp} is higher there and results in a much smaller $\tau(H_{\text{amp}})$ for Eqn.5.11. The net result is reshaping of the time domain signal to have attenuated peak height but unaffected side lobes, effectively enhancing the effect of blurring because the blurring signal is increased relative to the central peak signal.

To account for the effect of incomplete magnetization on spatial resolution, we modify the spatial resolution equation (Eqn.5.2) as follows:

$$\begin{aligned} \Delta x &\approx \alpha \Delta x_{\text{base}} + \beta \Delta x_{\text{blur}} + \gamma \Delta x_{\text{peakdepr}} \\ \Delta x &\approx \alpha \Delta x_{\text{base}} + \beta ln(2) \frac{\phi H_{\text{amp}}}{\frac{1}{2}\pi G} + \gamma \frac{\phi}{\frac{1}{2}\pi G} \left(\frac{S_{ss}}{S} - 1 \right) \end{aligned} \tag{5.12}$$

where γ is a new weighting factor for the incomplete magnetization term, S is the measured peak sensitivity, S_{ss} is the expected steady-state peak sensitivity.

The weightings of $\alpha = 1.0, \beta = 1.83, \gamma = 3$ gave the best-fit results.

This changing magnetic flux comes from the drive waveform as direct feedthrough (undesired interference) as well as the ensemble magnetization change of the MPI nanoparticles (desired MPI signal). The direct feedthrough is typically orders of magnitude larger than the tracer signal and indirectly sets the MPI detection limit due to dynamic range limits on the analog-to-digital converter. Various methods can be used to attenuate the direct feedthrough and these are extensively discussed by Graeser et al. (Graeser et al., 2013). Although there are practical limits to feedthrough attenuation, a combination of aggressive analog filtering, precision fabrication of gradiometric receive coils as well as the use of a duplicate system will be capable of very large amounts of feedthrough attenuation. As such, while this factor will set the lower bound for the MPI detection limit, it is usually not the dominant constraint for MPI SNR.

A more important factor to take into account is the noise from various sources such as the receiver coil, patient body as well as preamplifier. Prior work has shown that at the kHz frequencies used in MPI, coil noise (rather than body noise) dominates. The full details of these noise sources in MPI are extensively discussed in prior work (Goodwill and Conolly, 2010; Graeser et al., 2013). Regardless of the noise properties of the system, it is clear that there is better SNR if the raw inductive signal from the MPI

nanoparticles is stronger. To increase the raw inductive signal, the rate of ensemble magnetization change of the nanoparticles must be increased. For ideal nanoparticles that respond instantly to the applied field, this can be achieved by increasing the magnetic slew rate of the applied field via using drive waveforms of a higher frequency or higher amplitude. In practice, due to relaxation effects (delayed response to the applied field due to a minimum magnetic dipole rotation time), there is an upper limit where the rate of magnetization change will not increase further with frequency or amplitude. While one may expect that higher drive frequencies and amplitudes also entail a larger noise bandwidth due to the larger receive bandwidth required to record all the harmonics of the nanoparticle response, in practice this effect is minimal because the MPI signal is limited to a very small frequency band (100 - 1 kHz) centered exactly at each harmonic. Thus, noise from all other parts of the frequency spectrum can be filtered out digitally. For example, at first glance, a 1 kHz drive waveform only requires a 1 - 40 kHz bandwidth to record 40 harmonics. On the other hand, a 100 kHz drive waveform requires a much wider bandwidth of 100 kHz to 4 MHz and therefore in theory should have a lot more noise included. However, if a fixed 1 kHz window is kept around each harmonic for both cases, the former will have a net digital bandwidth of $40 \times 1 = 40kHz$, while the latter will also have the same $40 \times 1 = 40kHz$. If the noise is assumed to be white gaussian, then the noise properties for both cases will be same because most of the high frequency noise not at the harmonic "windows" for the 100 kHz case will be digitally filtered out.

Therefore, in order to have high sensitivity MPI, in conjunction with a low noise receive chain, it is also essential to increase the raw MPI inductive signal by increasing the rate of ensemble magnetization change. This can be done through better nanoparticle design with steeper Langevin curves or by increasing the magnetic slew rate of the drive field. In practice, there is an upper bound on the strategy of increasing magnetic slew rate due to relaxation effects. Furthermore, as the previous sections have shown, MPI resolution is also significantly affected by the drive waveform slew rate. In this study, we focus on optimizing both MPI sensitivity and resolution by investigating the effects of drive frequency and amplitude across an unprecedented 1 kHz to 400 kHz and 0.5 to 40 mT.

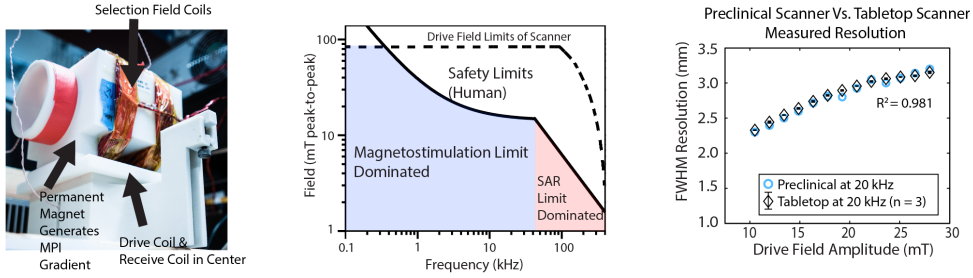

FIGURE 5.4: (A) Photo of the modified Arbitrary Waveform Relaxometer described in previous work (Tay et al., Sci Rep, 2016). While the drive coils are kept the same, permanent magnets and selection field coils were installed to create a small bore scanner. (B) Because the same drive coil and drive transmit chain was maintained, the modified device retains all the frequency flexibility and drive waveform versatility of the previous device. This plot shows that our modified device is able to test a wide variety of drive waveforms. The capability region covers almost all drive waveforms possible within the human safety limits and encompasses a much larger range than the drive waveforms investigated in prior MPI literature. Therefore, using this device, we are able to do a comprehensive optimization of the drive waveform (within safety limits) for MPI by investigating an unprecedented 0.4 – 416 kHz and 0.5 – 40 mT amplitude. (C) We verify the accuracy of resolution measurements from our modified device by comparing the measurements to that obtained from our preclinical scanner that has been extensively validated in prior work. The results show that the resolution measurements are in good agreement.

5.4.4 Multi-objective Optimization for Both Spatial Resolution and Sensitivity Creates Optima Due To Opposing Trends

Spatial Resolution of MPI generally improves with lower drive amplitudes and lower drive frequencies (Croft et al., 2016; Kuhlmann et al., 2015). On the other hand, MPI sensitivity generally improves with higher drive amplitudes and drive frequencies according to Eqn.5.10. These two opposing trends mean that there exists an optimum trade-off of spatial resolution and sensitivity that has not been investigated to-date. In this paper, we consider the complex and interconnected effects determining spatial resolution and sensitivity in order to find an optimum point.

For instance, in Eqn.5.2, it seems on first glance that if phase lag changes negligibly with H_{amp}, MPI spatial resolution should improve monotonically with lower drive amplitudes and approach the ideal resolution predicted by the steady-state Langevin ensemble model. However, considering the blurring effect from incomplete magnetization and the dramatic effect of applied field on relaxation time constants (Eqn.5.12 and 5.1), it is clear that, depending on the SPIO characteristics, at some point the increase in relaxation time constants due to low fields applied and blurring from incomplete magnetization will offset the gains from lower drive amplitudes. Furthermore, the requisite increase in frequency to compensate for the lost sensitivity will increase the phase lag and further offset resolution gains from low drive amplitudes. On the other hand, low drive frequencies reduces phase lag without incurring incomplete magnetization costs and therefore seems to be an attractive strategy. However, the requisite increase in amplitude to compensate for the lost sensitivity will linearly increase phase lag based blurring according to Eqn.5.12. Therefore, there is a need to experimentally optimize the drive waveform (frequency and amplitude) for both spatial resolution and sensitivity to obtain an optimal drive waveform.

5.4.5 Loss of Higher Harmonic Information is Partially Compensated by Decreasing Receive Bandwidth

When low drive amplitudes are used, the signal energy content shifts from the higher harmonics towards the lower harmonics. This is due to changes in the frequency spectrum required to describe the Langevin curve when it is bounded such that the linear region of the curve dominates. Current MPI scanners use an analog filter to remove the direct feedthrough at the

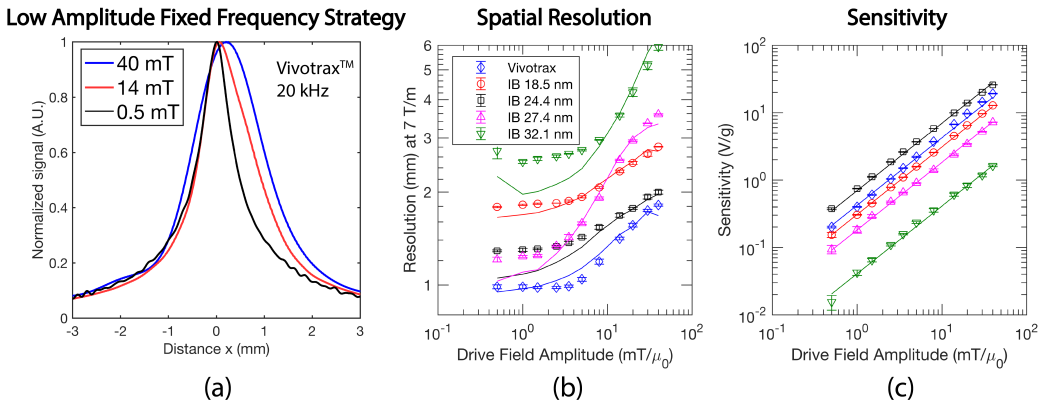

FIGURE 5.5: Experimental results from varying the drive amplitude over a wide range (0.5 mT – 40 mT) while keeping drive frequency constant at 20 kHz. A wide range of nanoparticles with a spread of magnetic core sizes were used (Vivotrax, 18.5 nm, 24.4 nm, 27.4 nm, 32.1 nm ImagionBio SPIOs). (a) Resolution generally improves with lower amplitudes and the trend is similar to the main conclusion reported by Croft et al. (Croft et al., 2016). A near 2-fold improvement was observed for Vivotrax. (b) Similar trends in resolution was observed across the wide range of nanoparticles used. Some SPIOs, such as IB 27.4 nm and IB 32.1 nm had larger improvements in resolution as drive amplitude was lowered. Solid lines represent our theoretical resolution model. (c) However, sensitivity decreases essentially linearly with amplitude, showing that sensitivity has to be sacrificed for resolution improvement for the low amplitude strategy. Solid lines represent the linear trend expected from the SPIO's dM/dt response to the decreased slew rate drive field by Faraday's law. Interestingly, while there is less phase lag (relaxation) at higher amplitudes, the resolution is worse. As Croft et al. 2016 has shown, this is because the blurring effect is amplified for larger amplitudes because the MPI trajectory is correspondingly wider and the blur is mapped onto a larger region in space. This amplification effect outweighs the drop in relaxation.

drive frequency f_0 and therefore the SPIO signal at f_0 is also lost in the raw received signal. Because more of the SPIO signal energy exists at f_0 at low drive amplitudes, this means that there is effectively less raw signal available (on top of the effects of Faraday's law). Although this lost f_0 information can be recovered robustly (**lu˙2013**), SNR is dependent on raw signal received and is still decreased by this effect. To offset this SNR loss, the receive bandwidth can be decreased correspondingly. This is justified because there is very little signal information at the higher harmonics and the resultant image is negligibly distorted by the removal of these harmonics.

5.4.6 Magnetic Slew Rate Alone Cannot Predict MPI Performance

One possibility for simplifying this study is to use magnetic slew rate as opposed to tuning both drive amplitude and drive frequency. However, as shown in Eqn.5.11 and Eqn.5.12, increases in drive frequency does not always offset changes made by decreases in drive amplitude. For instance in Eqn.5.12, while Δx changes linearly with H_{amp}, the phase lag change with frequency is not guaranteed to be linear. Furthermore, there is some dependence of the phase lag on H_{amp} due to the field-dependence of Brownian and Néel time constants in Eqn.5.1. Another example in point is the use of very low amplitude and correspondingly very high frequency drive waveforms. While magnetic slew rate would predict equal MPI performance due to the unchanged slew rate, from a physics viewpoint, the low magnetic torque generated by the very small H_{amp} combined with very short drive periods would result in the incomplete magnetization of the SPIO and the corresponding resolution and sensitivity losses. The typical results seen in AC susceptometry (dynamic susceptometry) support this idea because any nanoparticle will start to show drops in the magnitude of magnetic susceptibility χ that indicate incomplete magnetization at higher frequencies. Therefore, for the wide range of frequencies and amplitudes used in this study, simplifying the optimization to only tune the magnetic slew rate is not feasible.

5.4.7 Similar Conclusions are expected for System Matrix Reconstruction

System matrix reconstruction first calibrates for a system function by individually measuring the spectral response of an SPIO point source positioned at every voxel of the eventual image. This information is encoded in the system matrix S. This matrix can be understood as a spatial sensitivity map describing the spatial sensitivity profile of each harmonic. Reconstruction of the image is then simply a matrix multiplication of S^{-1} with the received response v (**Rahmer2009-tr**).

A widening of the SPIO time-domain response is observed as a steeper decay of the signal strength at higher harmonics. This change in response can be modeled as a convolution-type function on the system function leading to blurring of the high-resolution components (**Rahmer2009-tr**). In terms of sensitivity, because the same SPIO magnetization change is spread out over a larger amount of time, the reconstructed peak height of the SPIO

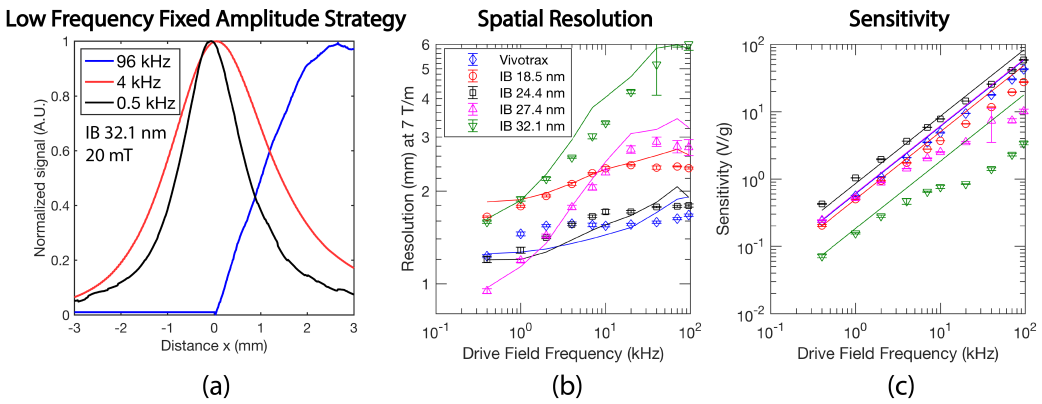

FIGURE 5.6: Experimental results from varying the drive frequency over a wide range (0.5 kHz – 416 kHz) while keeping drive amplitude constant at 20 mT. A wide range of nanoparticles with a spread of magnetic core sizes were used (Vivotrax, 18.5 nm, 24.4 nm, 27.4 nm, 32.1 nm ImagionBio SPIOs). (a) Resolution generally improves with lower frequencies and significant phase lag, where the MPI signal lags behind the applied field resulting in an offset point spread function, is observable at high frequencies of 96 kHz. A 4-fold improvement was observed for IB 32.1 nm going from 96 kHz to 0.5 kHz, showing the high sensitivity of large core SPIOs to drive frequency. (b) For smaller core SPIOs (Vivotrax^{TM}, IB 18.5 nm and IB 24.4 nm), the results show that resolution improves with lower frequencies, although to a lesser extent than an equal change in amplitude as shown in Fig. 5.5. (c) Sensitivity decreases with frequency, showing that low frequency approaches also sacrifice sensitivity for resolution improvement. However, unlike the varying amplitude strategy in Fig. 5.5, at high frequencies sensitivity no longer varies linearly with drive frequency and falls away from Faraday's law. This is because the SPIO rotation cannot keep up with the high drive frequency. This is confirmed by phase lag measurements that show significant increases in phase lag with increasing frequency. This increased phase lag also leads to worse resolution from relaxation-induced blurring.

temporal response is lower and closer to the noise floor. Furthermore, if the dynamics of SPIO magnetization are on a similar order of magnitude as the period of a drive waveform, the SPIO will not fully magnetize even by the end of the period, leading to a lower SPIO magnetization change than expected and overall lower MPI signal throughout the drive period.

5.5 Methods

5.5.1 Berkeley 3D MPI Scanner

The Berkeley 3D MPI Scanner uses a field-free-line configuration at gradient strength of 6.3 T/m. The scanning trajectory uses a combination of

electromagnets and mechanical shifting of the animal/sample to shift the field-free-line within an x-z plane. Full 3D imaging is performed by taking different projection angles via rotating the animal/sample. X-space reconstruction is used to obtain projection images from the data. Subsequently, filtered backprojection (similar to CT) is used for reconstruction. The entire MPI field-free-line reconstruction algorithm is described in detail in prior work (Konkle et al., 2013). For the images used in this work, the field of view is 4 cm $\times$ 4 cm $\times$ 4 cm with a scanning time of 1 minute. The drive waveform used is 20 kHz at 20 mT amplitude.

5.5.2 Berkeley Arbitrary Waveform Relaxometer

The Berkeley Arbitrary Waveform Relaxometer measures the point-spread-function characteristic of MPI tracers with a wide range of MPI drive waveforms. The untuned nature of the device enables the use of drive waveforms between DC – 400 kHz with amplitudes up to 40 mT. We exploit the frequency-flexibility of this device to optimize the MPI drive waveform across a wide parameter space. Like other MPI spectrometers and relaxometers (Behrends, Graeser, and Buzug, 2015; Fidler et al., 2015; Bauer et al., 2016a; Garraud et al., 2017), this device does not utilize magnetic gradients and thus only measures the dynamic magnetization characteristics of the MPI tracer. However, the point-spread-function (PSF) characteristic can predict for imaging performance such as sensitivity and resolution because MPI is an LSI imaging modality (Goodwill and Conolly, 2010) where the MPI image can be described as the convolution of the tracer spatial distribution with the PSF characteristic. Prior work has confirmed this by showing that the resolution predicted by the PSF for this device correlates well with the actual resolution achieved on the 3D MPI scanner (Tay et al., 2016). Because the 3D MPI Scanner uses a fixed frequency of 20 kHz, to accurately confirm the imaging performance predicted by the different drive frequencies (other than 20 kHz) used in this work, we modify the Berkeley Arbitrary Waveform Relaxometer with a permanent magnet array to create a 3.5 T/m field-free-line gradient. Although the field-of-view is small, we are able to obtain 2D projection images of point sources to verify the improved imaging performance predicted by our relaxometer results.

5.5.3 Magnetic Nanoparticles

Imagion Biosystems PrecisionMRX SPIO nanoparticles (Imagion Biosystems, Inc. Albuquerque, NM,USA) with carboxylic acid coated outer shell

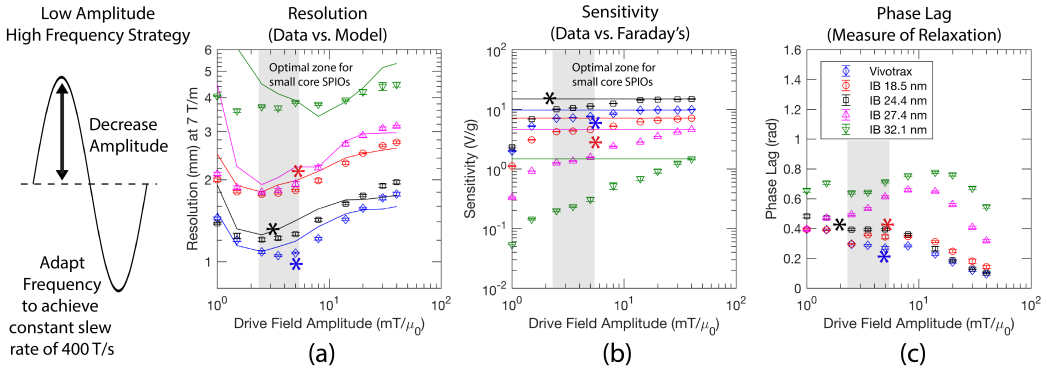

FIGURE 5.7: Experimental Results when using the low amplitude high frequency strategy. This strategy is found to be optimal for small core size SPIOs (Vivotrax^{TM}, IB 18.5 nm, IB 24.4 nm). Optimal points are marked with asterisks and the optimal overall region considering all the 3 SPIOs is shaded in grey. For small SPIOs, decreasing amplitude and adapting the frequency to maintain a fixed slew rate of 400 T/s shows that resolution improves with lower amplitudes. Importantly, we see that sensitivity stays approximately the same following Faraday's law, achieving our objective of improving resolution without trading-off sensitivity. Beyond 160 kHz, the sensitivity starts to drop and depart from Faraday's law while resolution shows no improvement. Thus, we obtain an optimum parameter set of 2.5 mT – 5 mT and 160 kHz – 80 kHz. Similar trends were observed for the IB 18.5 nm and IB 24.4 nm with a very similar optimum parameter set. The phase delay plot shows that the optimal performance parameter set does not correlate well with the minimal phase delay point, again emphasizing that relaxation alone (phase delay) is a limited metric for MPI performance. In contrast, for large core size SPIOs (IB 27.4 nm and IB 32.1 nm), decreasing amplitude and adapting the frequency to maintain a fixed slew rate of 400 T/s shows a significant drop in sensitivity everywhere across the tested parameter range. Unlike the smaller cores, we are unable to maintain high sensitivity by using high frequency to offset lower amplitudes. This is because the larger nanoparticles simply cannot rotate well when pushed to a faster frequency. Thus, the low amplitude high frequency strategy does not work as well for large core sizes.

and varying core diameters were used for this study. The core diameters used are 18.5 nm, 24.4 nm, 27.4 nm and 32.1 nm where the former two are classified as small core tracers and the latter two are classified as large core tracers. Details regarding the performance and characterization of these nanoparticles are detailed in prior work (Tay et al., 2017). In addition, aqueous suspensions of multi-core dextran magnetite nanoparticles (Ferucarbotran, Meito Sangyo, Japan) were used to serve as reference representing the performance of conventional MPI. For all AWR 1D measurements, 30μl of SPIOs at 5 mg/ml was used (0.150 mg Fe total sample).

5.5.4 Calculation of Resolution

We use the Houston criterion for spatial resolution in this study. The metric used is this the full-width-half-maximum (fwhm) of a point source. For relaxometer data, this value is simply the width of the MPI signal peak measured at half of the peak height. Because relaxometers measure the MPI response to a varying applied field (mT/μ_0), the fwhm is converted to spatial resolution in millimeters by simply dividing by the MPI gradient to-be-used. Here, we use 6.3 T/m to match the Berkeley 3D MPI scanner. This method to convert relaxometer data to a spatial resolution metric has been well-validated in prior work and the converted spatial resolution have been shown to correlate well with actual MPI imaging performance on the 3D scanner (Tay et al., 2016).

5.5.5 Calculation of Sensitivity

Sensitivity is measured by the height of the MPI signal peak from relaxometer data divided by the iron mass of the MPI tracer used to give a mV/mg Fe metric. The pre-amplifier gain used was accounted for so the final mV/mg Fe would be the actual MPI signal with a pre-amplifier gain of 1.

5.5.6 Calculation of Phase Lag

The relaxation delay was obtained from cross-correlation of positive and negative signals. This time-delay is simply converted to radians for a phase delay value.

5.6 Results

5.6.1 Small Core SPIOs: Low Amplitude and Low Frequency both improve resolution at the cost of sensitivity

Typical MPI drive waveforms today use 20 – 25 kHz frequency and approximately 20 mT amplitude (Zheng et al., 2017; Yu et al., 2017b; Graeser et al., 2017). Previous work has proposed the use of small amplitude drive waveforms (Croft et al., 2016) or low frequency drive waveforms (Tomitaka et al., 2015; Kuhlmann et al., 2015; Murase et al., 2015) to improve MPI performance. Here we experimentally test these suggestions on two classes

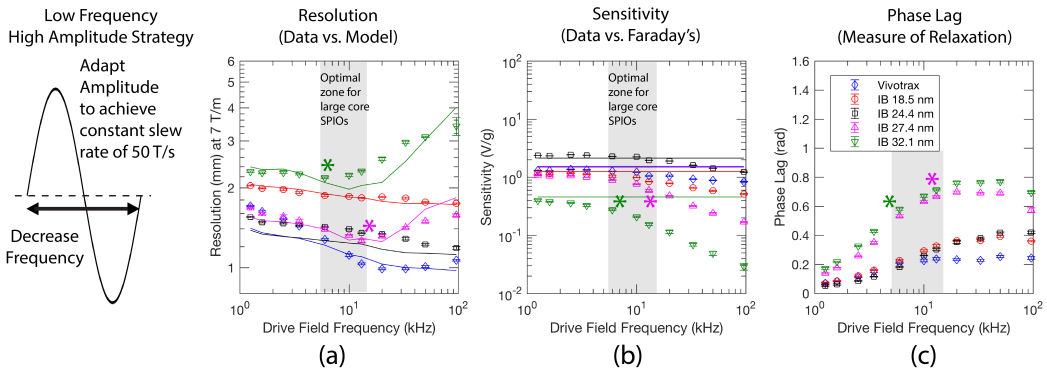

FIGURE 5.8: Experimental Results when using the low frequency high amplitude strategy. This strategy is found to be optimal for large core size SPIOs (IB 27.4 nm and IB 32.1 nm). Optimal points are marked with asterisks and the optimal overall region considering all the 3 SPIOs is shaded in grey. Because large core sizes have increased sensitivity to frequency, we need to use lower frequencies. However, we cannot use too high an amplitude as well, thus we change the slew rate to be lower at 50 T/s so as to enable low frequency and medium amplitudes. We observe that this experimental series works much better for larger cores, obtaining an optimum parameter set of 10 mT and 5 kHz. We see that sensitivity remains constant up to approximately 5 kHz beyond which large deviations from Faraday's law is observed. 5 kHz is optimal because spatial resolution is the best for 32.1 nm and very close to the best resolution for 27.4 nm. For small core sizes, decreasing frequency and adapting the amplitude to maintain a fixed slew rate of 50 T/s does not improve resolution with decreasing frequency, underscoring that for small core sizes, amplitude is the dominant factor affecting resolution. Because sensitivity is lower than the low amplitude high frequency approach while resolution did not improve, this low frequency high amplitude series is not optimal for small cores. This shows that for small core sizes, it is better to ensure small drive amplitudes and to have a very high frequency even if the net slew rate is high.

of nanoparticles - small core sizes (vivotrax, 18.5 and 24.4 nm ImagionBio single core SPIOs) and large core sizes (27.4 and 32.1 nm ImagionBio single core SPIOs).

The results show that in general, lower frequencies and lower amplitudes improve resolution as predicted by prior work. However, a deeper analysis reveals that this comes at a significant cost of decreased sensitivity. Furthermore, the sensitivity decreases almost linearly with lower amplitude or lower frequency, resulting in more than 10-fold drop in sensitivity when implementing the low amplitude and low frequency strategies. This shows that the simple strategy of monotonically decreasing amplitude or frequency to improve MPI performance is not desirable and underscores the importance of finding the optimum parameters so as to minimize sensitivity loss while obtaining as much resolution improvement as possible.

The modified resolution model we described in the theory section shows good agreement with the experimental data. This shows that the combination of the following 4 factors well describes how MPI resolution can be calculated: (1) ideal (base) resolution defined by Langevin theory that is dependent on particle (effective) magnetic core size (2) Relaxation delays of the SPIO magnetization causing blurring (3) Blurring amplification by mapping the MPI signal to a wider region in space due to larger amplitudes / wider MPI trajectories (4) Blurring amplification caused by incomplete magnetization of the SPIO where the corresponding effect of "peak depression" causes effective resolution (full-width-half-maximum) to decrease.

We used Faraday's Law to model the expected (linear) sensitivity increase with amplitude or frequency. Plotting the data against Faraday's predictions helps visualize where the SPIOs are unable to keep up with the expected magnetic moment rotation speed that is set by the drive waveform. For example, at high frequencies, the deviation from Faraday's becomes larger because the SPIOs are unable to rotate fast enough and as a result do not magnetize fully and generate the expected MPI signal. The fixed offset observed of the data from the Faraday's plot for the top row of Figure 4 can be attributed to 20 kHz being slightly too high such that the achieved dM/dt is slightly lower than expected because the SPIO does not rotate as fast as expected. Looking at the bottom row, we see that at low frequencies, the sensitivity measured matches well with Faraday's and only deviates starting from 10 kHz. This delayed and incomplete magnetization also has implications for resolution as described in the earlier theory section.

Notably, when increasing frequency, we get more phase lag (relaxation effects) but less net blurring. In contrast, when increasing amplitude, we get less phase lag but more net blurring than the frequency case. This clearly shows that the MPI drive amplitude is the dominant factor affecting resolution. This is in agreement with the results from (Croft et al., 2016), where it was shown that mapping the relaxation blurring effect to a larger region in space (due to large amplitudes leading to wide trajectories) amplifies the blurring effect on resolution. Because amplitude has a dominant effect of resolution, a possible strategy is to use low amplitudes but high frequencies so as to use the high frequencies to compensate for the sensitivity loss from the low amplitudes.

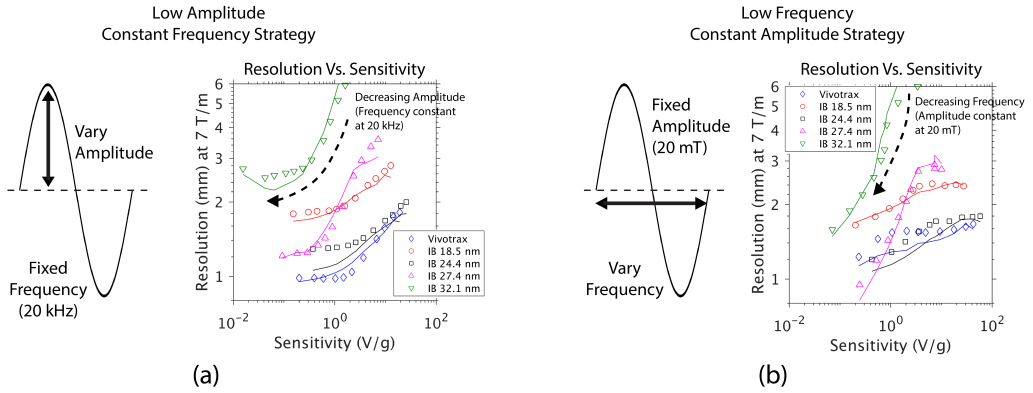

FIGURE 5.9: Experimental data from Fig 4 - 7 are plotted on resolution vs. sensitivity axes for easier visualization of optimal points. (a) Low amplitude only experimental series. The plot shows that decreasing the amplitude while keeping frequency constant results in monotonically better resolution but worse sensitivity. There are no optimal points observed and resolution is traded off for sensitivity. (b) Low frequency only experimental series. Similar to (a), no optimal points are observed and low frequency incurs a significant trading off of sensitivity for resolution.

5.6.2 Large Core SPIOs have higher sensitivity to frequency than small core SPIOs

Keeping frequency constant at 20 kHz and varying amplitude shows that resolution improves with lower amplitudes. A 3-fold improvement was observed. However, sensitivity decreases almost linearly with amplitude, showing that sensitivity has to be sacrificed for resolution improvement for the low amplitude strategy. Phase lag stays approximately constant and only drops at large amplitudes. The slight drop at large amplitudes can help explain the sinusoidal shape of the resolution curve where the resolution does not worsen as much with amplitude after 20 mT.

Keeping amplitude constant at 20 mT and varying frequency shows that resolution improves with lower frequencies with a 3-fold improvement observed. Sensitivity also decreases with frequency, showing that low frequency approaches also sacrifice sensitivity for resolution improvement. Phase lag dramatically increases with high frequencies, and this leads to large deviations from Faraday's for the sensitivity data due to incomplete SPIO magnetization.

In general, mostly similar trends as observed for the large core case with a few notable exceptions. (1) Increasing frequency has a larger blurring effect than that observed for the small core case. As such, in contrast to the

small core case, drive amplitude is no longer the dominant resolution determinant and both frequency and amplitude control the resolution. (2) Sensitivity and phase lag worsens dramatically at high frequencies, therefore, making a high frequency strategy untenable for large core sizes.

5.6.3 Small Core SPIOs: Low amplitude (2.5 – 5.0 mT) and high frequency (80 – 160 kHz) approach is optimal

As described in the previous section, because amplitude has a dominant effect of resolution, a possible strategy is to use low amplitudes but high frequencies so as to use the high frequencies to compensate for the sensitivity loss from the low amplitudes. Here we investigate this strategy by maintaining a constant slew rate while varying amplitude and frequency as a pair (when amplitude goes down, frequency is increased to maintain constant magnetic slew rate). The results in Fig. 5.7 show that for small core SPIOs, improved resolution is achieved without the concomitant loss in sensitivity observed for the simple low amplitude only approach shown in Fig. 5.5.

For small cores, decreasing amplitude and adapting the frequency to maintain a fixed slew rate of 400 T/s shows that resolution improves with lower amplitudes. Beyond 160 kHz, the sensitivity starts to drop while resolution shows no improvement, therefore, we obtain an optimum parameter set of 2.5 mT – 5 mT and 160 kHz – 80 kHz. Comparison to the standard 20 kHz and 20 mT shows negligible change in sensitivity while resolution improves from 1.6 mm to almost 1.0 mm. Similar trends were observed for the ImagionBio SPIOs of 18.5 nm and 24.4 nm with a very similar optimum parameter set. The phase delay plot shows that the optimal performance parameter set does not correlate well with the minimal phase delay point, again emphasizing that relaxation alone (phase delay) is a limited metric for MPI performance.

In contrast, in Fig. 5.8, decreasing frequency and adapting the amplitude to maintain a fixed slew rate of 50 T/s shows that resolution does not improve with decreasing frequency, underscoring that for small core sizes, amplitude is the dominant factor affecting resolution. Because sensitivity is lower than the top row data while resolution did not improve, we see that the series where amplitude is varied and slew rate is fixed at 400 T/s is the optimal series. This shows that for small core sizes, it is better to ensure small drive amplitudes and to have a very high frequency even if the net slew rate is high.

5.6.4 Large Core SPIOs: Low amplitude ($\sim$ 8 mT) and medium frequency ($\sim$ 6 kHz) approach is optimal

Because large core SPIOs have a much larger sensitivity to frequency than small core SPIOs, we cannot use the low amplitude high frequency strategy. To maintain the resolution gains from low amplitude while maximizing sensitivity requires titrating the increase in frequency before a critical threshold where frequency sensitivity increases. As such, we change the slew rate to be lower at 50 T/s so as to enable low frequency and medium amplitudes. We observe that this experimental series works much better. This is because for large core sizes, their magnetic moment rotation is dominated by Brownian relaxation and requires the entire nanoparticle to physically rotate. Due to viscous drag forces, it is difficult to achieve high rotation frequencies and our experimental results show that performance starts to decrease dramatically above 5 kHz. As such, the optimal parameter set for both resolution and sensitivity is around 10 mT and 5 kHz for large core sizes between 27.4 – 32.1 nm as shown in Fig. 5.8. Comparison to the standard 20 kHz and 20 mT shows > 2.5-fold improvement in resolution for 27.4 nm SPIOs while sensitivity does not deviate much from the expected Faraday value. Similar results are obtained for 32.1 nm SPIOs. Despite the fact that the net drive waveform slew rate is lower by a factor of 8 than the typical 20 kHz, 20 mT drive waveform, the loss in sensitivity is only 3 – 5 fold.

When using the low amplitude high frequency strategy for large core sizes, we observe non-optimal results as expected. In essence, while resolution improves with lower amplitudes, despite a constant slew rate, the sensitivity drops consistently with the compensate increase in frequency. This emphasizes the high sensitivity to frequency for large core size particles. Because larger cores have high relaxation and are unable to catch up to higher drive frequencies, this results in incomplete magnetization, lower dM/dt and thus lower MPI signal and sensitivity. Therefore, unlike smaller cores, we are unable to compensate for the loss in sensitivity from low amplitude by increasing frequency since the nanoparticle simply cannot rotate well when pushed to a faster frequency.

Again, similar to the small core size SPIOs, we observe here that the phase lag plot does not correlate well with the optimal MPI performance. The point of minimum phase lag (minimum relaxation effect) does not have the best MPI performance (whether resolution or sensitivity). This

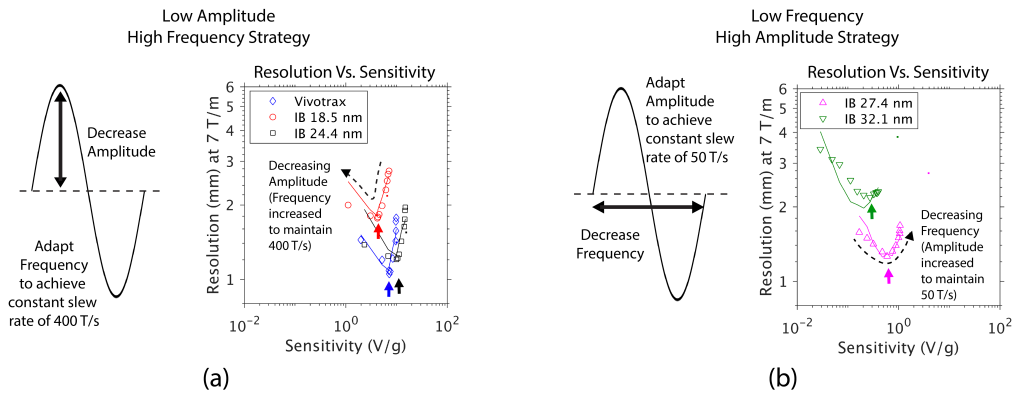

FIGURE 5.10: Experimental data from Fig 4 - 7 are plotted on resolution vs. sensitivity axes for easier visualization of optimal points. (a) In contrast with Fig 5.9, with a low amplitude high frequency approach (constant slew rate of 400 T/s), we observe optimal points in the plot. The steep valley like plots show that good resolution can be obtained at a optimal parameter set with a minimal cost in sensitivity. Comparison to the 20 kHz 20 mT standard MPI parameters (*Typ marking) show that resolution is significantly improved and sensitivity is negligibly affected. (b) Similar results are observed for large SPIOs when a constant slew rate of 50 T/s is used. Optimal points are easily identified on the plots. Very significant improvements in resolution are achieved over standard MPI but at some cost of sensitivity. This is mainly because a 8-fold lower slew rate is used to match the large core SPIOs that are not normally suitable for conventional MPI at 400 T/s slew rate.

emphasizes that regardless of the nanoparticle behavior or size, the relaxation delay alone does not predict well for MPI performance. MPI performance requires consideration of more factors and is more complex as described in our theory section. The drive waveform parameters and mapping/gridding process, as shown by all the results up to this point, is a critical factor in determining MPI performance.

5.6.5 Expanded MPI resolution model matches well with measured data

Fig.6 – 9 show good agreement of measured resolution values with our expanded MPI resolution model described in the theory section. Generally, large deviations from the model only occur at very poor resolutions ($>$ 4mm) where the MPI reconstruction algorithm may not work well at obtaining an accurate point spread function or image. This validates our model that MPI resolution is affected by peak depression blurring effects in addition to previously characterized amplitude and relaxation phase delay blurring effects.

5.6.6 Small Particles: Proof of global bound on error

Placeholder now: showing two time-domain signals on same plot (same slew rate at zero-crossing but different amplitude) - show that larger amplitude has spill-over as opposed to low amplitude. Panel of 1 x 2. Also show windowing helps but not by much.

5.6.7 Large Particles: LAHF failure due to incomplete magnetization of the SPIO at pFOVs centered at or near the SPIO particle

For pFOVs near the particle, Tau(H) is extremely long due to the low amplitudes. As a result, the particle magnetizes to a significant lower extent than the steady-state M-H curve predicts. This means there is much lower signal energy in this pFOV. However, at pFOVs farther from the particle, Tau(H) is much shorter and particle is able to magnetize to the steady-state M-H curve, and signal energy matches that predicted by the Langevin. As a result, because we get significantly lower MPI signal when scanning at the particle but still receive unaffected blurring from the Langevin "tails" when further from the particle, the spatial resolution is worsened. This is equivalent in effect to a peak depression of the steady-state Langevin PSF. This is illustrated in Fig. 5.3.

HALF works better due to the dependence of Tau on applied field. For small particles, the effective Tau very quickly reaches negligible levels with applied field. However, this is not the case for larger particles that have Brownian-dominant relaxation. Large amplitude excitation fields enable these particles to rotate faster by Brownian mechanisms or may even enable a switch from Brownian to Neel mechanisms. The low frequency significantly reduces the impact of the peak depression phenomenon described in the last section as the particle now has enough time to rotate.

5.7 Discussion

5.7.1 Low Amplitude, High Frequency Drive Waveforms are Optimal

As shown from the results, we obtained optimal drive waveform of 2.5 – 5 mT and 80 – 160 kHz for the most commonly used small core size SPIOs in MPI. This is starkly different from the typical 20 kHz and 20 mT used

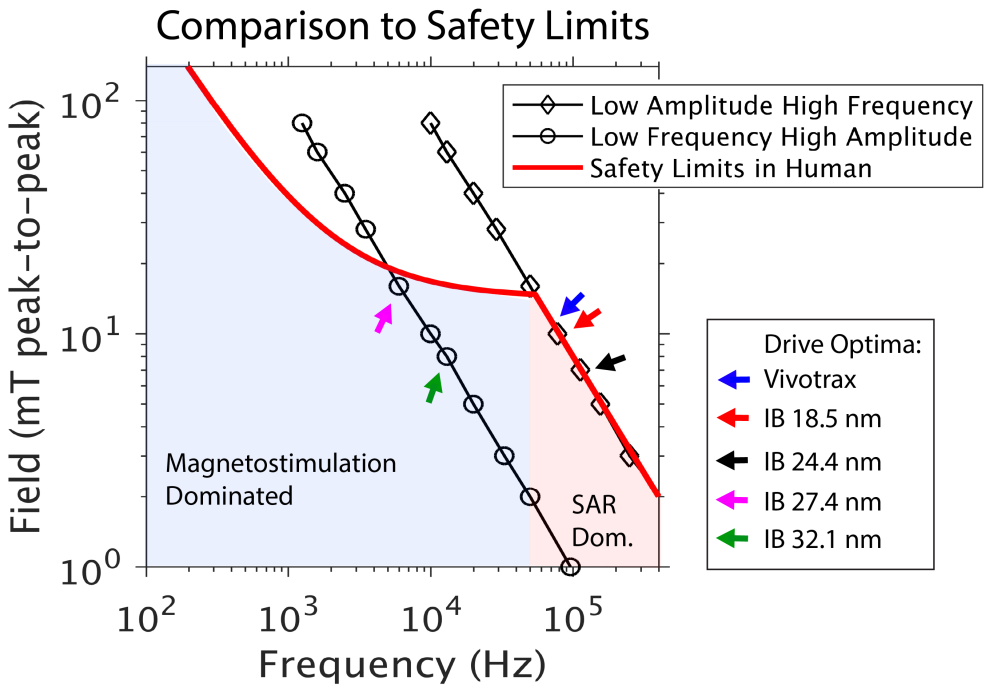

FIGURE 5.11: MPI drive waveform safety limits in a human compared to the optimal drive waveforms obtained in this study. The experimental series of the low amplitude high frequency series and the high amplitude low frequency series are plotted, showing that the optimal points obtained for the respective series fall within safety limits. The optima for low amplitude high frequency are on the edge of the safety limits but because this is in the SAR dominated regime and the 4 W/kg SAR limit used for this plot is relatively conservative, the optimal waveform here can be considered to be safe.

in most of MPI literature and presents a significant break from the status quo. The gains afforded from changing to this optimal parameter set are significant, with $1.5 - -2$-fold improvement in resolution while sensitivity is negligibly affected. Our work has therefore demonstrated a novel way to image in MPI by changing significantly the drive waveform parameters in order to achieve a significant improvement in imaging performance over the current imaging procedure.

5.7.2 Magnetostimulation and SAR Safety Considerations

From prior work by Saritas et al. (Saritas et al., 2013a), the magnetostimulation and SAR safety limits have been calculated for a human torso in terms of drive amplitude and frequency. Referencing this work, we plot our optimal experimental series on the same axes (see Fig. 5.11). The calculation constants used are $r_0 = 15$ cm, $\sigma = 0.3$ s/m, $\rho = 1000 kg/m^3$, $B_{\min} = 14$ mTpp, $T_c = 100\mu$s. From the figure, we see that the optimal waveforms that resulted from our optimization are within safety limits of both magnetostimulation and SAR. While one of the experimental series (high freq series) is very close to the limit, because this is in the SAR dominated regime and the 4 W/kg limit used for this plot is relatively conservative, the optimal waveform here can be considered to be safe. Furthermore, a slightly lower duty cycle during imaging (brief pauses during the imaging sequence) can be implemented to ensure that the average SAR is within 4 W/kg. The slightly lower duty cycle should have a negligible effect on scan time, but make sure that the drive waveform falls well within safety limits. For instance a 90% duty cycle only increases scan time by about 10%.

5.7.3 Relationship to System Matrix Reconstruction

Although the x-space method: point spread functions and full-width-half-maximum was used to analyze the resolution and sensitivity in this paper, we expect similar conclusions for system matrix reconstruction. The harmonic spectra of our experimental data show steeper slopes when resolution is worse, matching conventional methods in prior work on use of harmonic spectra to predict resolution or well-posedness of the inverse reconstruction problem. Notably, with system matrix reconstruction, it is possible to tradeoff sensitivity for resolution due to the deconvolution procedure. Regardless, optimizing the drive waveform to obtain a good harmonic spectra (which corresponds to a sharp and narrow point spread function), prior

to deconvolution, is still very important. In Figure X, we compare the harmonic spectra of conventional MPI to that of our optimal drive parameters and show an improved harmonic spectra, therefore confirming that our results are still relevant to system matrix method of reconstruction.

Interestingly, with lower amplitudes, because each half-period only traverses a very small portion of the SPIO magnetization curve, only a few harmonics are obtained because each small region of the magnetization curve is closer to being linear the lower the amplitude of the drive waveform. However, improved resolution is still able to be achieved. We attribute this to the fact that these higher harmonics are not stored in harmonics of the fundamental of the drive waveform, but rather in the intermodulation harmonics (sidebands) that result from the selection field coils slowly shifting across the field-of-view. This selection field shift frequency is much lower at about 10 Hz, and therefore all the high resolution harmonic data is stored in the intermodulation sidebands. As such, paradoxically, even when we excite at 80 – 160 kHz, we do not require a 10 MHz bandwidth to collect enough harmonics, but have our high resolution harmonic data in the intermodulation sidebands of the first few fundamental frequency harmonics.

5.7.4 Implementation on Preclinical Scanners and Path to Clinical Application

As shown in Fig. 5.11, the new optimal drive waveform proposed is safe for humans (mainly due to the low amplitudes). The main implementation challenge will be shifting the transmit and receive bandwidth to higher frequencies. At higher frequencies, the transmit chain could potentially consume more power due to thermal losses from the enhanced skin effect. However, with appropriate choice of litz wire, this problem can be mitigated. For the receive chain, it may be difficult to capture 40 – 50 harmonics if the fundamental frequency is increased to 100 kHz. Digital-to-analog converters typically trade-off dynamic range and receive bandwidth and therefore it may be challenging to have affordability that maintains a large dynamic range while acquiring up to 10 MHz of bandwidth. Fortunately, due to the small amplitudes, only a small region of the SPIO magnetization curve is traversed, and this means that it may not be required to record that many harmonics to accurately reproduce the SPIO response. The selection field (at much lower frequency), helps cover the entire (saturation) magnetization response range and therefore we expect to see a transfer of energy from the fundamental harmonics to the intermodulation sidebands.

Therefore, it may be possible to keep the conventional receive bandwidth of 1 MHz even at a larger fundamental frequency because the high resolution information is transferred to the intermodulation sidebands due to the low drive amplitudes.

5.8 Conclusion

In this first study of its kind, we experimentally optimize the drive waveform across an unprecedented 0.4 kHz – 416 kHz and 0.5 mT – 40 mT amplitude for a wide variety of nanoparticles from Resovist-like clusters to single core nanoparticles of various core sizes to determine optimal waveforms for each nanoparticle. We show that when optimizing for both factors, the trends are no longer monotonic and there are clear optimal drive frequencies and amplitudes. We present novel drive waveforms that show 2-fold improvement in spatial resolution without loss of MPI tracer sensitivity. Lastly, we compare these optimal waveforms to SAR and magnetostimulation safety limits and show that our optimal parameters (2.5 – 5 mT and 80 – 160 kHz) for high resolution and high sensitivity Magnetic Particle Imaging are safe for human imaging. The new waveforms are significantly different from conventional MPI with approximately an order of magnitude change in both amplitude and frequency. The optimization findings are also robust across nanoparticles within the same size class (only two classes - large and small). Thus, we have optimized and discovered a novel drive waveform for MPI with significant improvements in resolution while maintaining the high sensitivity of conventional MPI. We hope our findings will help advise future MPI scanner design for improved performance.

5.9 Acknowledgments

I would like to thank Daniel Hensley for discussions regarding experimental planning and theoretical discussions about the various blurring mechanisms discovered and explained in this study.

Chapter 6

Strongly Interacting Magnetic Particle Imaging (SiMPI)

6.1 Introduction

Conventionally, Magnetic Particle Imaging likes to think about each nanoparticle as an independent, non-interacting magnetic domain. This allows the ensemble of nanoparticles to be well-modeled by the Langevin model of superparamagnetism. Here, we explore the possibility of having nanoparticles close enough to strongly interact. We demonstrate a new method in Magnetic Particle Imaging to exploit these strong inter-particle interactions to achieve (in theory) the ideal step-like magnetization. This would enable very large resolution improvements in theory due to the delta-like point spread function achieved. In addition, the signal strength is also improved by a few orders of magnitude as the magnetization goes from positive saturation to negative saturation very quickly. In practice, without any deconvolution, we observe 100-micron spatial resolution in 2D imaging and more than 100-fold improved sensitivity compared to the current MPI *de facto* standard, Resovist. In this work, we outline a theoretical model for how inter-particle interactions can dramatically improve MPI performance and show experimental data demonstrating achieved MPI performance improvements. We also discuss practical challenges remaining as well as potential strategies to tackle them.

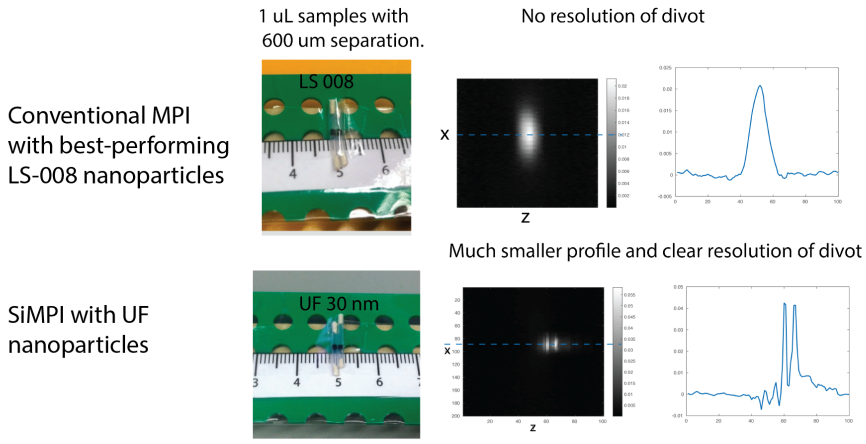

FIGURE 6.1: Initial results showing the large improvement in resolution with SiMPI over the best-performing nanoparticles with conventional MPI. This is the main motivation of developing SiMPI.

6.2 Theory

6.2.1 Conventional Magnetic Particle Imaging vs Strongly Interacting Magnetic Particle Imaging

In conventional magnetic particle imaging, the nanoparticles are considered to be independent single-domain magnetic dipoles that have negligible interactions with each other and are only affected by the external MPI gradient and excitation (drive) fields. As such, models such as the Langevin model look at the ensemble behavior of many individual magnetic dipoles and provide a means to look at the net magnetic behavior from an external observer by summing the (probabilistic) thermal and applied magnetic field effect on each nanoparticle.

In this new variant of magnetic particle imaging, we depart from conventional assumptions and in fact, seek to exploit the effects of inter-particle interactions. We seek to make these interactions very strong in order to reap the many benefits that we will explain in more detail later on. As a result of this objective, we name this new way for imaging Strongly Interacting Magnetic Particle Imaging.

6.2.2 Requirements for SiMPI, Challenges and Initial Solutions

The key aspect of SiMPI is that the nanoparticles are close enough to interact. This requires a few things: (1) The concentration is high enough that nanoparticles have a significant chance to collide in a way that they will "magnetically capture" each other and start forming a nucleus where more and more nanoparticles join, and each of them are close enough to each other to have their magnetic dipoles strongly interact across particles, (2) The outer (non-magnetic) coating or shell of the nanoparticles cannot be too thick such that it prevents close enough proximity between the magnetic cores to strongly interacting, (3) ensuring that all the nanoparticles exist within strongly-interacting multi-particle structures as described above. This is essential since the single, non-interacting, nanoparticle is also able to contribute to the MPI signal but with less desirable imaging characteristics (as will be explained later), and as such, it is to our interest to ensure that all nanoparticles exist within multi-particle structures.

As a result of the three conditions above, some challenges are immediately evident. Firstly, MPI is only a linear and shift-invariant (LSI) system if we can assume that each nanoparticle behaves in the same way and contributes the same way to the MPI signal. Critically, linearity is depend on the MPI signal being proportional to the mass of the nanoparticle in the voxel. In point (1) explained above, we see that the nanoparticles can contribute to the MPI signal as individual entities or as part of the multi-particle structure. The ratio of these two states is dependent on the nanoparticle concentration in a non-linear fashion, therefore, in its natural state, SiMPI would be not LSI due to a concentration latching effect, where SiMPI dominates over a critical concentration and conventional MPI dominates below that threshold. Second, in order for nanoparticles to be colloidally stable in water, the magnetic core needs to be coated with a hydrophilic coating which is often rather thick. As a result, current SiMPI has only been observed in nanoparticles in organic solvents where there is no hydrophilic coating and magnetic cores are able to approach very close to each other without having a minimum distance set by the hydrophilic coating thickness. Work is currently being conducted to search for a suitable coating that allows phase transfer of nanoparticles to water while maintaining SiMPI properties.

To address these two challenges, I developed a initial solution where the nanoparticles are held within a emulsion of oil droplets inside water. This solves both problems because we achieve high local concentrations of

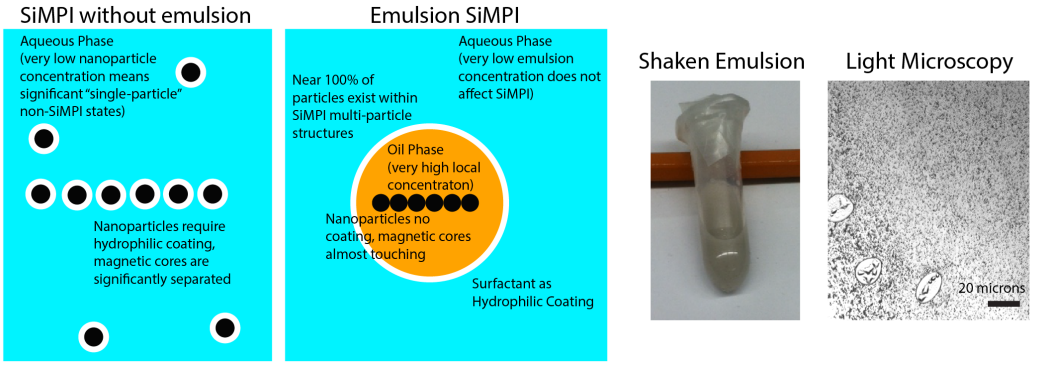

FIGURE 6.2: (left) Illustration showing the advantage of an emulsion formulation for SiMPI. This is just an initial solution, more robust solutions could potentially have the oil phase replaced by some other (more solid) matrix that sets the nanoparticles in a chain geometry. (middle) Photo of the shaken emulsion (right) Light microscopy (100x) of the shaken emulsion.

nanoparticles within each emulsion droplet even if the emulsion itself becomes very dilute (for instance, diluted by blood volume after intravenous injection). With high local concentrations, we can ensure that essentially all nanoparticles exist within the multi-particle structure when contributing to the MPI signal, solving the concentration latching problem and ensuring maximal benefit since every particle is performing SiMPI rather than being "wasted" as a conventional particle. Also, there is no need for a hydrophilic coating on each magnetic core since the hydrophilic coating is addressed by the surfactant that forms the shell of each emulsion droplet, and therefore, the magnetic nanoparticle cores can almost touch, enhancing the beneficial effects of very strong magnetic interactions between particles. The initial proof-of-concept was performed with a shaken emulsion of 0.2 mg/ml UF RL3 nanoparticles in toluene with DI water. The volume ratio is 1:3, with 1% v/v of Tween-20 or Triton-X as surfactant. Vortexing was done on maximum intensity for 30 seconds, upon which the initial solution forms a emulsion that has the visual appearance of a very light-gray cream/milk.

6.2.3 Model for Inter-Particle Magnetic Interactions when Particles are in Close Proximity

Magnetic Particle Imaging utilizes superparamagnetic iron oxide nanoparticles (SPIONS) that are essentially ferromagnetic single-domain crystal that have a permanent magnetization. However, these behave like a paramagnet

when observed as an ensemble due to thermal agitation forces randomizing the directions of the dipole moments of individual crystals. Because each nanoparticle has a permanent dipole moment, they always exert interparticle forces on neighboring particles. In most cases when the suspension is dilute and the particles are far enough apart, these interactions are negligibly weak. The magnitude of the dipole field from a single superparamagnetic iron oxide nanoparticle falls off with distance as follows:

$$\begin{aligned} \mathbf{B(r)} &= \frac{\mu_0}{4\pi}\left(\frac{3\mathbf{r}(\mathbf{m}\cdot\mathbf{r})}{r^5} - \frac{\mathbf{m}}{r^3}\right) \\ B_{max}(r) &= \frac{\mu_0 m}{2\pi r^3} \end{aligned} \tag{6.1}$$

Assuming that the nanoparticles are small enough and sufficiently distant that their shape and size is not important such that both magnets can be modeled as being magnetic dipoles, the interparticle force can be described as:

$$F(m,r) = \frac{-3\mu_0 m^2}{2\pi r^4} \tag{6.2}$$

where the simplification occurs if $\mathbf{r}$,$\mathbf{m}_1$,$\mathbf{m}_2$ are all along the same axis. Thus, it can be seen that the interparticle force varies to the fourth-power of the interparticle distance.

For typical SPIOs with core sizes of $15-35$ nm and coating thickness of $7-50$ nm (**Ferguson2015-yj**; Tay et al., 2017), interparticle dipole-dipole interactions can be considered negligible for typical *in-vivo* concentrations. While recent work has shown that for very concentrated SPIO dispersions ($>$ 39 mM Fe), magnetic dipole-dipole interactions significantly influence the MPI signal (**Them2017-kj**), most in-vivo concentrations are relatively dilute.

Let us consider a magnetite nanoparticle of 20 nm diameter with a typical magnetic dipole moment m ranging from 10^{-18} to 10^{-17}. For an interparticle distance of 200 nm, the maximum dipole field magnitude at the position of a neighboring particle positioned along the dipole field is approximately 0.25 mT and the maximum inter-particle force is 37.5 fN. This is comparable to typical particle collision forces involved in random thermal Brownian motion that are on the order of 10 fN (Finer, Simmons, and Spudich, 1994). For this case thermal agitation completely randomizes the dipole moment directions and thus, we can assume that inter-particle forces are unable to hold particles in a fixed geometry so that particles experience

a net local field in one direction from neighboring particles. However, for an inter-particle distance of 20 nm, the dipole field magnitude increases to 250 mT and the inter-particle force is about 37.5 pN. This is orders of magnitude larger than typical Brownian forces that are approximately 0.01 pN and one order of magnitude higher than hydrogen bonds (4 pN) and molecular stepper (kinesin on microtubule) bonds (5 pN) (Finer, Simmons, and Spudich, 1994). Furthermore, this has a positive feedback tendency where the net dipole moment of a chain of two nanoparticles is larger than that of one nanoparticle and is therefore stronger at attracting more nanoparticles to form an even longer chain. As such, it is possible for inter-particle forces to dominate over thermal agitation forces and hold particles in a favorable and stable geometry such as a chain.

6.2.4 Theoretical Conditions Necessary for Local Clustering of Nanoparticles

To evaluate the conditions necessary for local clustering, we perform a simplified 1D analysis of magnetic nanoparticles initially spaced far apart and at random orientations such that the net ensemble magnetization is zero. In this case, the average inter-particle force is zero. Upon application of a homogeneous magnetic field in one direction, the magnetic dipoles align to face the same direction such that the average inter-particle force is at a (angular) maximum. We can model the simple 1D case of particle motion by three factors: (1) an attractive magnetic force between particles (2) viscous drag resisting the motion using Stokes' law for a small sphere (3) thermal disordering forces tending to disorder or push apart particles coming together:

$$F_{net}(r) \approx \frac{-3\mu_0 m^2}{2\pi r^4} + 6\pi\eta r_h v + F_{disorder} \tag{6.3}$$

Given an infinite amount of time to aggregate, the viscous drag term can be neglected and thus the "capture radius" can be calculated as:

$$\begin{aligned} \frac{3\mu_0 m^2}{2\pi r^4} &> F_{disorder} \\ r &< \left(\frac{3\mu_0 m^2}{2\pi F_{disorder}}\right)^{1/4} \end{aligned} \tag{6.4}$$

For a typical magnetite nanoparticle of 20 nm with typical magnetic dipole moment m of 10^{-17} to 10^{-18} and assuming $F_{disorder} = 0.01pN$, the

capture radius is between 88 nm and 278 nm. This means that the critical concentration (v/v) is between $0.64 to 0.03\%$. In mg/ml for magnetite, this is about 1.5 mg/ml. Experimentally, this concentration is much higher than the critical concentration of 0.04 mg/ml where the transition occurs between SIMPI behavior and conventional SPIO behavior. Modifying the approximate 0.01 pN value in literature to 0.001 pN and 0.1 fN gives a capture concentration of 0.25 mg/ml and 0.05 mg/ml. A value of 0.1 fN makes sense because the force of a single brownian collision is 0.01 pN, therefore, the averaged net disordering force from many collisions from different directions will be much lower especially when evaluated only in the direction of the attraction axis.

Another indirect modeling method to calculate this averaged $F_{disorder}$ will be to calculate the diffusion time of a nanoparticle in a viscous media. The time will allow the calculation of diffusion velocity and therefore the viscous drag force. This should approximately be equal to the $F_{disorder}$ value.

6.2.5 Close Proximity and Stable Relative Geometry of Particles Generates Large Local Fields Requiring A Coercive External Field to Overcome

Because the magnetically associated particle ensembles have a stable relative geometry, any one particle in the ensemble will feel a large local field caused by its neighbors that are locked in a specific relative geometry to itself. The most stable geometry is that of a chain, where the magnetic dipoles of each particle lines up with the others along a common axis. To evaluate the relative energy of the applied external field versus the internal local field, we reference prior work from Kornig et al. (Körnig et al., 2014). The energy from the external applied field can be determined as follows:

$$\begin{aligned} E_{ext} &= -\sum_{i=1}^{n} \mathbf{m}_i \cdot \mathbf{B}_{ext} \\ E_{ext} &\approx -nmB_{ext}cos(\Omega - \alpha) \end{aligned} \tag{6.5}$$

assuming that all crystals in the chain have the same angle α to the chain axis and have approximately the same magnetic moment m. Ω is the angle of applied field to the chain axis.

Now we consider the energy from the local field generated by dipole-dipole interactions that we term as E_{loc} assuming that the neighboring particles have the same angle ($\alpha_i = \alpha_j = \alpha$) to the chain axis as the central particle as laid out in (Körnig et al., 2014):

$$\begin{aligned} E_{loc} &= \frac{\mu_0}{4\pi}\sum_{i=2}^{n}\sum_{j=1}^{i-1}\left(\frac{3(\mathbf{m}_i\mathbf{r}_{ij})(\mathbf{m}_j\mathbf{r}_{ij})}{r_{ij}^5} - \frac{\mathbf{m}_i\cdot\mathbf{m}_j}{r_{ij}^3}\right) \\ E_{loc} &= -\frac{\mu_0}{4\pi}\sum_{i=2}^{n}\sum_{j=1}^{i-1}\frac{m_i m_j}{r_{ij}^3}\left(3cos\alpha_i cos\alpha_j - cos(\alpha_i-\alpha_j)\right) \\ E_{loc} &\approx -\frac{2(n-1)\mu_0 m^2}{4\pi r^3}\left(3cos^2\alpha - 1\right) \\ E_{loc} &\approx -\frac{2(n-1)\mu_0 m^2}{4\pi c^3}\left(3cos^2\alpha - 1\right) \end{aligned} \tag{6.6}$$

where the approximation occurs because only the interactions between neighboring particles are significant and interactions between particles spaced farther apart can be considered negligible. c is the center-to-center distance between adjacent particles. The local B_{loc} **along the chain axis in the 1D case** where $\hat{\mathbf{u}}$ is a unit vector along the chain axis, can thus be expressed as follows:

$$\begin{aligned} E_{loc} &\approx (n-1)\mathbf{m}\cdot\mathbf{B}_{loc} \\ B_{loc} &= \frac{\mu_0}{4\pi}\sum_{i=2}^{n}\sum_{j=1}^{i-1}\left(\frac{3(\mathbf{m}_i\mathbf{r}_{ij})(\hat{\mathbf{u}}_j\mathbf{r}_{ij})}{r_{ij}^5} - \frac{\mathbf{m}_i\cdot\hat{\mathbf{u}}_j}{r_{ij}^3}\right) \\ B_{loc} &\approx \frac{2(n-1)\mu_0 m}{4\pi r^3}\left(2cos\alpha\right) \end{aligned} \tag{6.7}$$

The H-field that is observed locally by any nanoparticle in the chain can be written as:

$$H_{loc} = H_{ext} + \frac{B_{loc}}{\mu_0} \tag{6.8}$$

As calculated in the previous subsection, B_{loc} can be as high as 200 mT. Since B_{loc} is much higher than B_{ext} and is aligned with the chain axis, the magnetic moment of the particles remains aligned with the chain axis. This basically acts like a coercive offset in H_{loc}. Because B_{loc} is a function of α which in turn is a function of the stability of the chain and the magnitude

and direction of the 3D applied field vector H (less and less stable as it approaches the coercive threshold), B_{loc} decreases as H_{ext} approaches the coercive threshold, therefore instantaneously decreasing the coercive threshold. This triggers a positive feedback cascade where H_{loc} is rapidly diminished and the particles align rapidly to H_{ext}, effectively causing a large change in H_{loc} locally although there is only a small change in H_{ext}. This **amplification** of the rate of change of H_{loc} is modulated by the time constant of the change in nanoparticle angle α.

The average angle α is related to the ensemble magnetization assuming single-domain particles with constant magnetic moment, m, as follows:

$$M_{loc}(t) = Nmcos\alpha(t) \tag{6.9}$$

The local magnetization is also described by the Langevin function but modulated by a time constant to account for the finite delays in the change of the ensemble magnetization. We can substitute Eqn.6.9 in to form a complete equation:

$$\begin{aligned}
M_{loc}(t) &= Nm \cdot e^{-t/\tau} * \mathcal{L}(kH_{loc}) \\
M_{loc}(t) &= Nm \cdot e^{-t/\tau} * \mathcal{L}\left(k(H_{ext} + \frac{2(n-1)m}{4\pi r^3}(2cos\alpha(t))\right) \\
M_{loc}(t) &= Nm \cdot e^{-t/\tau} * \mathcal{L}\left(k(H_{ext} + \frac{2(n-1)m}{4\pi r^3}(2M_{loc}/(Nm))\right) \\
M_{loc}(t) &= Nm \cdot e^{-t/\tau} * \mathcal{L}\left(k(H_{ext} + \frac{(n-1)M_{loc}}{N\pi r^3}\right) \\
M_{loc}(t) &= Nm \cdot e^{-t/\tau} * \mathcal{L}\left(k(H_{ext} + \frac{F}{N}M_{loc}\right)
\end{aligned} \tag{6.10}$$

where F/N is the ratio of the constant describing the field fall-off to the number density

Prior work with magnetosome chains has shown that the coercive field is much larger in the geometry of linear chains as opposed to clusters of nanoparticles (Körnig et al., 2014) where the coercive threshold is lower than 10 mT. This suggests that chains are responsible for the effect we observe here since the observed coercive threshold is higher than 10 mT.

6.2.6 Implications and Re-modeling as a Positive Feedback System - Schmidtt Trigger

In the previous subsection, we showed that from an energetics perspective, SPIO chains can be stable and can provide stronger local magnetic fields than possible with the external applied field alone. We also see that the local inter-particle fields are strong and provide a form of "remanent magnetization" that opposes changing of each particle's magnetization.

In this subsection, we show how we can re-model this phenomenon as a positive feedback system and we draw upon the Schmidtt trigger analogy to provide a reference model. First, we can rewrite the field felt by each nanoparticle as the sum of the external applied field and the "neighbor" field.

$$H_{\text{net}}(t) = H_{\text{external}}(t) + \alpha M_{\text{neighbor}}(t) \tag{6.11}$$

Here, the dimensionless alpha term modulates the effect of the SPIOs closeby and depends mostly on the inter-particle distance. Since the magnetic fields of the SPIO (modeled as a single-domain dipole) fall off as r^3, the dominant fields are the two adjacent neighbors in the chain. As discussed in an earlier section, for a small inter-particle distance of 20 nm, the felt-neighbor-field is approximately 250 mT which is an order of magnitude higher than typical MPI excitation amplitudes. However, this falls off quickly with distance and at 200 nm, the field is only 0.25 mT. Clearly, if SPIOs are almost touching each other, the neighbor-field cannot be neglected and strongly-interacting MPI behavior will manifest.

Substituting this into our magnetization equation, we get:

$$M(t) = Nm \cdot \mathrm{e}^{-t/\tau} * \mathcal{L}(k(H + \alpha M_{\text{neighbor}}(t))) \tag{6.12}$$

where $N[\text{particles}\, m^{-3}]$ is the local number density of magnetic particles at the scale of the interacting chain/crystal, α is a dimensionless coefficient that depends on inter-particle distance and core size, and $M_{\text{loc}}(t)$ is the local magnetization at the scale of interacting chain/crystals. We have also included finite relaxation dynamics by convolution of the energy-only relationships with a Debeye relaxation kernel, $\mathrm{e}^{t/\tau}$.

To further simplify the equation, we rewrite it with normalized dimensionless terms where we are simply concerned with the (dimensionless) polarization of the SPIO (normalized to the maximum (saturated) ensemble magnetization $Nm = M_{\text{sat}}$). We also make the applied field dimensionless by normalizing to H_{sat}, which is the applied field needed to achieve

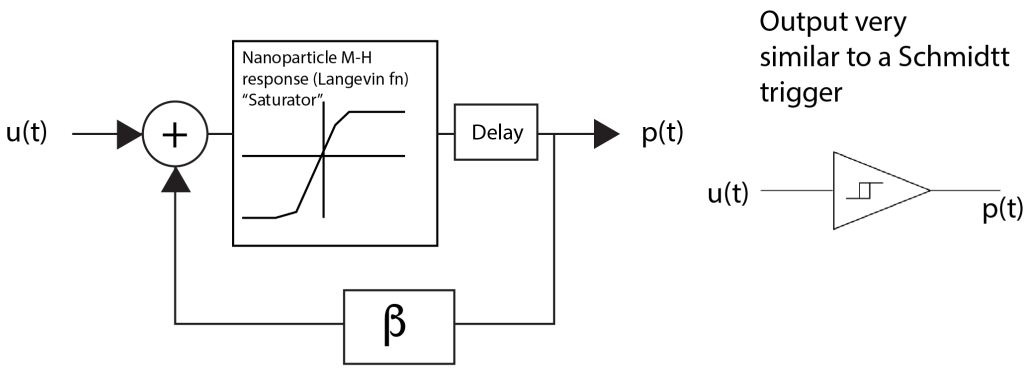

FIGURE 6.3: (left) Block diagram showing how our model works. (right) Since the Langevin function saturates and the delay term introduces hysteresis, we see that the output will be very similar to a Schmidtt trigger, whose symbol is an op-amp with a hysteresis curve. Essentially, like a Schmidtt trigger which is a comparator circuit with hysteresis that occurs via applying positive feedback to the noninverting input of the amplifier, our SiMPI multi-particle structure applies positive feedback via local fields to the input field felt by each particle, and the Langevin behavior of each individual particle gives us the saturator component. Experimental data showing hysteresis curves from our nanoparticles that look a lot like Schmidtt trigger input-output curves is shown in Fig. 6.8

M_{sat}. We therefore make the following definitions: $u(t) = H(t)/H_{sat}$, $p(t) = M(t)/M_{\text{sat}}$, and $\beta = \alpha M_{sat}/H_{sat} = \alpha\chi_{\text{SPIO}}$

Our magnetization equation thus becomes:

$$M(t) = Nm \cdot \mathrm{e}^{-t/\tau} * \mathcal{L}((H + \alpha M_{\text{loc}}(t))\frac{1}{H_{sat}}) \tag{6.13}$$

$$p(t) = \mathrm{e}^{-t/\tau} * \mathcal{L}(k(u(t) + \beta p(t))) \tag{6.14}$$

where k is a constant to adjust the input argument of the Langevin to achieve Langevin saturation.

This is clearly a positive feedback system and as β increases, the positive feedback becomes stronger and results in a smaller applied field required to cause ensemble saturation of magnetization. From the equations governing MPI performance shown in the beginning of the dissertation in Chapter 1, MPI SNR improves linearly with $M_{\text{sat}}/H_{\text{sat}}$ and spatial resolution improves approximately linearly with smaller H_{sat}. Thus, using positive feedback to force ensemble magnetization to saturation allows H_{sat} to become smaller with linear improvements to both SNR and spatial resolution. With good values for β, in theory, H_{sat} approaches zero and therefore both SNR and spatial resolution can be improved near infinitely. This can be understood

from the fact that the ideal MPI magnetization response of the SPIO is a step function with step at $H = 0$ since dM/dH which is the MPI point-spread-function would be an (near) infinitely tall delta function which gives infinitely good SNR and spatial resolution. In reality however, this feedback circuit has a "delay term" as magnetization does not occur instantaneously. Therefore, for realistic scanning times, the ensemble magnetization may not be able fully polarize and therefore infinitely good MPI performance will not be achieved. Continuous rastering of the FFP also imply that there will be some blurring of signal between voxels since by the time positive feedback finishes polarizing the SPIOs in a voxel, the FFP may have moved through several voxels, thus "smearing" signal between voxels and causing some inevitable blurring (rather than delta-function-like perfect spatial resolution). Nevertheless, this method of exploiting positive feedback is a very powerful method to improve MPI performance and should still give dramatic improvements in MPI performance.

To analytically solve this positive feedback equation, we first need to approximate the Langevin operator as $\mathcal{L}(x) \approx x\partial\mathcal{L}/\partial x$ and that the relaxation time constant is small enough such that near-infinite feedback loops can occur within the scan time. Our equation can thus be approximated as a power series:

$$p(t) \approx u(t)\partial\mathcal{L}/\partial x \left(1 + \partial\mathcal{L}/\partial x\beta + (\partial\mathcal{L}/\partial x)^2\beta^2 + (\partial\mathcal{L}/\partial x)^3\beta^3 + \cdots\right) \quad (6.15)$$

If $|(\partial\mathcal{L}/\partial x)\beta| < 1$, this infinite series converges (since $1/(1-x) = 1 + x + x^2 + \cdots$) to :

$$p(t) \approx u(t) \cdot \frac{\partial\mathcal{L}/\partial x}{1 - (\partial\mathcal{L}/\partial x)\beta} \quad (6.16)$$

If $|\beta| > 1$, this infinite series simply "hits the rails":

$$p(t) \approx \text{sign}(u(t)) \quad (6.17)$$

Again, we note the potential of strongly-interacting SPIOs to vastly improve MPI performance as we again observe that when $\beta > 1$, the output of the system is simply $\text{sign}(u(t))$ which means that the SPIO magnetization response is a perfect step function. This translates to, in theory, **infinitely good SNR and spatial resolution.** We plot the theoretical input-output of the SiMPI positive feedback system in Fig. 6.4 for various values of β.

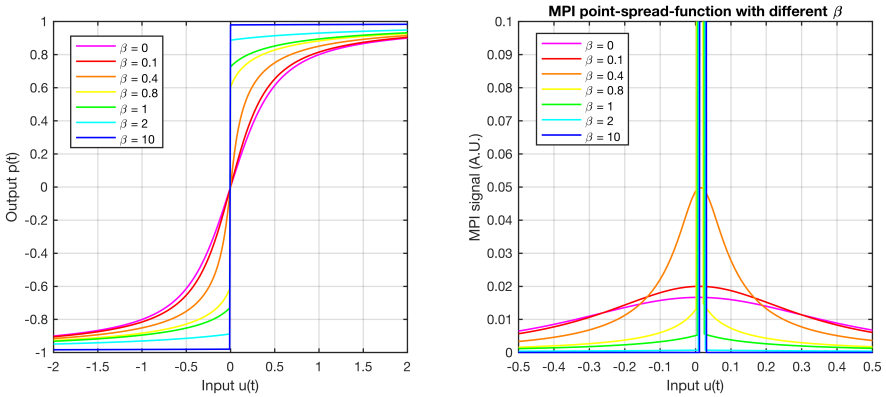

FIGURE 6.4: Simulated plots of the input u(t) and output p(t) of the SiMPI positive feedback system without considering relaxation delays (the Debeye relaxation term is ignored). 100 recursions of the positive feedback loops was used in the simulation. As β approaches and goes above unity, the SiMPI system becomes more and more like a step function, which promises near infinitely good SNR and spatial resolution for MPI in theory. In practice however, relaxation delays limit the number of recursions through the feedback loop and therefore limit the output of the positive feedback since scanning times must be realistic and cannot afford to "wait" forever for near infinite feedback loops to occur.

6.2.7 Analysis involving SPIO relaxation

From the previous subsection, we note that one important caveat is that we need to account for the relaxation term, as the positive feedback has a delay term. This will set an effective limit and therefore the M-H curve will not be a perfect step function. This also implies that there will be some (dynamic) hysteresis as for a continually changing applied H field, by the time the delay is factored in, the applied field would have moved significantly from the zero crossing and thus the delayed positive feedback magnetization change will not be located at the zero point (or the sign-change point). The stronger the relaxation term, the greater the width of the hysteresis as shown in the simulated plots from Fig. 6.5. This is the theoretical basis for the minimum threshold drive amplitude for SiMPI, and also explains why at lower excitation frequencies, the minimum threshold drive amplitude further decreases. In theory, at very low excitation frequencies, there should be no hysteresis and no excitation amplitude threshold. In practice however, we still observe a minimum threshold as seen in Fig. 6.7. We believe that this is the result of the stability of the chain, since the Langevin equation depends on thermal-magnetic equilibrium to describe the change in ensemble magnetization. Because the chain is exceptionally stable once formed, at zero applied field, it may take a much longer time than predicted by the Langevin model for

the chain to "fall apart" and have the net magnetization randomize to zero. As such, there is a necessary minimum coercive energy input threshold to force the SPIO chain to reverse magnetization polarity and give SiMPI signal.

Another factor to take note here is that the time constant for relaxation has a strong applied field dependence (Deissler, Wu, and Martens, 2014). For example, the Néel time constant changes by more than 3 orders of magnitude going from zero applied field to 20 mT. The Brownian time constant changes by more than 10-fold as well for the same range of applied fields. As such, it may also be the case that positive feedback loops are occurring at very low drive amplitudes, but because the time constant for relaxation is so long, the rate of change of magnetization from one polarity to the other polarity (even if $\beta > 1$) takes a very long time. Since the MPI signal is proportional to dM/dt, this results in very low signal strength and SiMPI-like peaks are hard to observe. On the other hand, if the drive amplitude is higher, even if the frequency is very low, the time constant decreases significantly as the drive amplitude increases from zero to the peak amplitude. As a result, the magnetization change occurs most rapidly close to the peak of the drive waveform, and since MPI signal is proportional to dM/dt, this rapid magnetization change is observed as an offset (hysteretic) peak characteristic of the sharp signal peaks expected of SiMPI. Therefore, the "minimum" drive amplitude may be caused in part by the reduction in relaxation time constant with applied field.

6.2.8 Parameters governing SiMPI

From the previous subsection we see that the value of β and thus α are key to SiMPI performance. These parameters are dominated by the inter-particle spacing. In this subsection, we provide a in-depth definition of these important parameters.

We can calculate the dimensionless interaction factor α as follows, using the geometry of the dipolar field and assuming the ideal linear chain:

$$\alpha = 2k\left(\frac{r}{c}\right)^3 \tag{6.18}$$

where $c[m]$ is the center-to-center distance between adjacent particles and $r[m]$ is the core radius. We assume only the effect of the two neighboring particles are dominant and particles further away exert negligible effect due to the r/c term since c = 2c. $k < 1$ is a lossy factor to account for the fact that

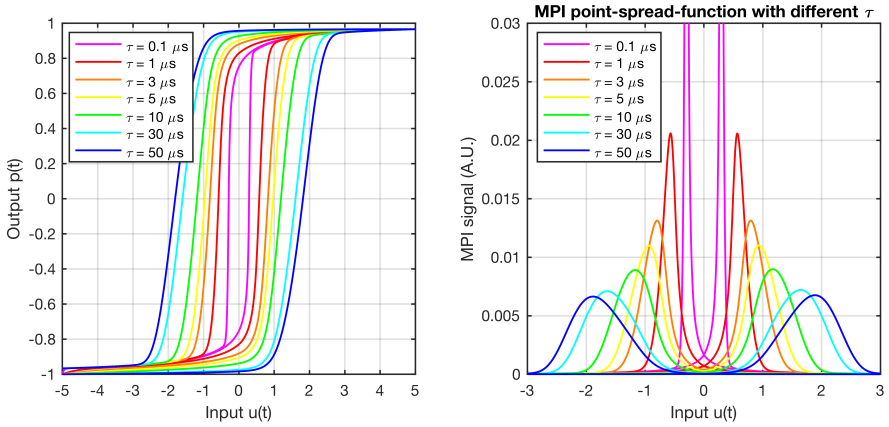

FIGURE 6.5: Plots of the input u(t) and output p(t) of the SiMPI positive feedback system with relaxation taken into account. Upon taking into account relaxation, hysteretic behavior is observed which is similar in appearance to experimentally obtained data and point-spread-function. Simulation parameters use a linear $u(t)$ slew from -5 to 5 over a duration of 25μs which is a half-period of the typical 20 kHz MPI excitation. The reverse slew is then performed to complete the slew in the other direction and finish off a full period, forming complete hysteretic loops. $\beta = 1$ was assumed and strong field dependence of the time constant was assumed: $\tau(u(t)) = \tau_{\text{base}} exp(-10u(t)/u_{\max}$ if $u(t)$ is opposite sign of $p(t)$, otherwise $\tau(u(t)) = \tau_{\text{base}}$. Various (Debeye) relaxation time constant τ_{base} was used, showing the dependence of the hysteresis width on relaxation time constant. The shorter the relaxation time constant, the better the SiMPI performance.

magnetization at the surface of the single-domain nanoparticle is less than the particle magnetization.

This leads to β being :

$$\beta = 2k \left(\frac{r}{c}\right)^3 \frac{M_{sat}}{H_{sat}} \tag{6.19}$$

and since M_{sat} is usually about $0.6T/\mu_0$ for bulk magnetite and H_{sat} is usually about 6 mT, we get an approximate equation:

$$\beta \approx 200k \left(\frac{r}{c}\right)^3 \tag{6.20}$$

therefore showing that as long as the distance between particles is not too big, we get $\beta > 1$ which leads to saturating positive feedback (the magnetization "hits the rails" as soon as sign changes from positive to negative).

6.2.9 Recommended Modifications to X-Space Scanning

Because the time delay may not be trivial, in order to implement SiMPI robustly, we recommend that either the excitation frequency is lowered significantly from the standard 20 kHz in order to allow time for positive feedback loops to saturate the magnetization, or that the excitation amplitude is maintained to be high such that it counteracts the saturating term to allow the net input to change sign. However, this results in "dynamic hysteresis" and requires changes to the x-space reconstruction since the point spread function will now be offset from the zero applied field point. The former recommendation is better in that there will be no offset from the zero point, but the very low frequency will result in much lower SNR since MPI's signal is proportional to the rate of change of magnetization.

6.2.10 Recommended Modifications to X-Space Reconstruction

To reconstruct the MPI image properly when a hysteretic point spread function is observed, we need to throw out all data and use only data after the coercive threshold. This prevents the MPI gridding algorithm from averaging zero signal with the SiMPI signal and resulting in non-linearity due to the two states of the nanoparticle. Next, since the point-spread-function is offset, this needs to be accounted for since the position of the point source is offset in the image. To address this, we recommend taking the average of

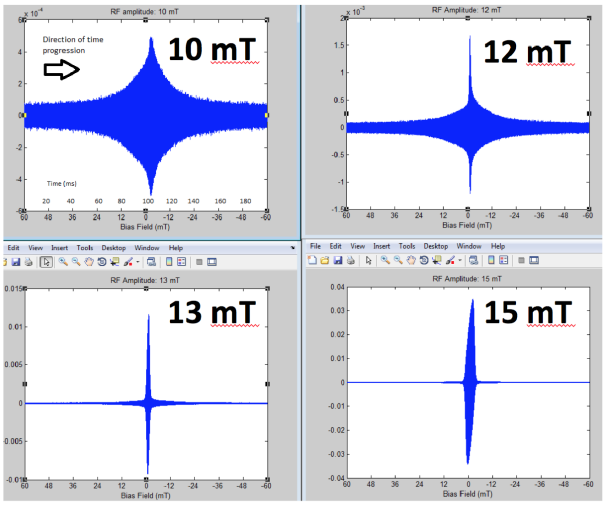

Drive Ampl	FWHM	Peak Str
10	16.4 mT	0.52
12	3.0 mT	1.71
13	0.65 mT	12.2
15	0.75 mT	36.1

FIGURE 6.6: Effect of drive/excitation amplitude on SiMPI. If drive amplitude is below the threshold, SiMPI behavior is lost and the conventional MPI response is seen, which is a few orders of magnitude weaker in SNR and almost an order of magnitude poorer in resolution. To show that SiMPI is not merely a reconstruction artifact or trick, we show raw time-domain data from the MPI receiver coil as drive amplitude is changed. As time passes, the background near-DC field is very slowly ramped down and passes zero. The zero point of the background field corresponds to center of the time course. We observe broad envelopes and then a very sharp peak as the drive amplitude reaches the threshold, showing the switch from conventional MPI to SiMPI behavior. The strength of the raw signal changes by orders of magnitude as well. The slight broadening of the envelope in 15 mT plot is due to the envelope widening since there is more leeway above the coercive threshold of 14 mT and thus MPI signal is seen when the the background field is at zero and when it is near zero ($< 1mT$ away as well, hence, the broadening of the envelope. Critically, this suggests that with a drive amplitude equal to the SiMPI amplitude threshold, we can directly form an image from the raw time domain envelope, opening opportunities to reduce reconstruction computational load and time as well as possibility of demodulation of our AM signal (the envelope) and thus using a much lower receive bandwidth.

the two positions in the positive and negative slew direction images, since the offset will be in different directions. Basically, a cross-correlation algorithm can calculate the offset between the two images, and the final image can simply be one of the images with axis offset by a half of the calculated offset from the algorithm.

6.3 Experimental Results

6.3.1 Drive Amplitude Needs to Be Higher Than Coercive Threshold

In Fig. 6.6 we show that drive amplitude needs to be higher than a threshold to generate SiMPI behavior. This ties in with the model where the input argument to the Langevin saturator has to be made to change sign by a ”coercive” external input term to cancel the remanent magnetization term from neighboring particles. This is a dynamic ”coercive” threshold, because of the relaxation/delay term, the SiMPI system cannot instantly respond to changes in applied field, and thus there is large remanent fields from neighboring particles. If a long time is given for the SiMPI system to respond to changes in the externally applied field, we expect very little or no coercive offsets / threshold.

6.3.2 Lower Drive Frequencies Decrease The Coercive Threshold

In Fig. 6.7, we investigate the effect of frequency on SiMPI. Lower frequencies lower the coercive threshold, and this is likely due to there being more time to deal with the delay in the positive feedback loop, therefore less applied field is needed for the input argument to switch sign and saturate in the other direction (thus generating the step response and the sharp dM/dt peak we receive in MPI). However, the spatial resolution also worsens, possibly because there is more time spent near zero field where thermal forces are able to break apart the chain structure, therefore resulting in a mix of SiMPI and non-SiMPI behavior.

6.3.3 Requirement of A Minimum Particle Concentration

The data in Fig. 6.8 shows that a minimum concentration is required for robust SiMPI behavior, below which, the point-spread-function worsens

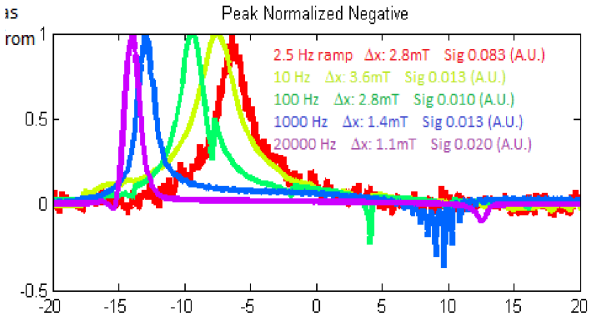

Freq (Hz)	Spatial Resolution	Normalized SNR	Coercive Threshold
2.5 (no RF)	2.8 mT	8.3	6.0 mT
10	3.6 mT	1.3	7.5 mT
100	2.8 mT	1.0	9.5 mT
1000	1.4 mT	1.3	13.0 mT
20000	1.1 mT	2.0	14.0 mT

FIGURE 6.7: Effect of drive/excitation frequency on SiMPI. Lower frequencies lower the coercive threshold, and this is likely due to there being more time to deal with the delay in the positive feedback loop, therefore less applied field is needed for the input argument to switch sign and saturate in the other direction (thus generating the step response and the sharp dM/dt peak we receive in MPI). However, the spatial resolution also worsens, possibly because there is more time spent near zero field where thermal forces are able to break apart the chain structure, therefore resulting in a mix of SiMPI and non-SiMPI behavior.

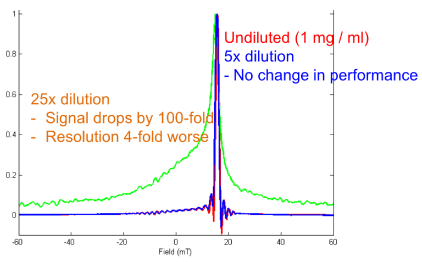

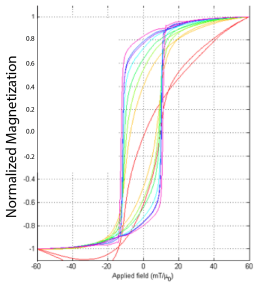

Dilution	Hysteresis Loop	SiMPI ?
0	Square-like	✓
2	Square-like	✓
4	Square-like	✓
8	Square-like	✓
16	Square-like	✓
32	Elliptic	×
64	Elliptic	×
128	Elliptic	×

SiMPI occurs when the hysteresis loop has step-like, square edges

FIGURE 6.8: Concentration latching in SiMPI. Below a certain threshold concentration, the dynamic hysteresis curves no longer show "step-like" behavior and the point spread functions become broader. SiMPI behavior is lost and MPI performance degrades to conventional levels. Note the dynamic hysteresis curves at high concentrations look very similar to the input-output function of a Schmidtt trigger.

significantly and SNR drops. This can be understood as the point-spread-function being a weighted combination of two SPIO states: where one state is the high SNR, high resolution but offset peak SiMPI state and the other state is the centered, low SNR, low resolution conventional MPI peak. The fact that the worsening of the point-spread-function always "blurs" more towards the center than the edges suggests that the blurring is actually simply the conventional (centered peak) MPI state becoming more and more dominant in the mixed SiMPI and cwMPI signal. To ensure LSI properties, it is thus critical to operate above this threshold concentration to avoid having a combination of two states (SiMPI and non-SiMPI) of the nanoparticle and being unable to linearly quantify nanoparticle mass.

Also, experiments in solid-at-room-temperature dodecane solvent show that coercive effect is suppressed, suggested that close proximity is required for the observed effect.

6.3.4 2D Imaging

Fig. 6.9 shows the 2D Imaging results that clearly show large improvements in spatial resolution and SNR with SiMPI. Clear images are still obtained even though concentrations were almost 2 orders of magnitude lower than standard MPI tracers and cwMPI scanning.

6.3.5 TEM images prove chain formation

To verify our model's premise that magnetic chains of nanoparticles are formed, TEM images of the RL3 nanoparticles were taken at different polarizing fields. The results are shown in Fig. 6.10.

6.3.6 Prepolarizing pulse can help ensure SiMPI behavior by giving time for chain formation

First, we show here that viscosity does affect SiMPI behavior because the more viscous the media, the longer the time is required for chain formation to enable SiMPI. See Fig. 6.11. To address this, we show that we can use a prepolarizing pulse to form the SiMPI chain before performing the MPI scanning and readout. The results of this strategy is shown in Fig. 6.12. This allows us to robustify SiMPI to concentration latching effects by using a prepolarizing pulse to ensure almost all nanoparticles exist within SiMPI structures / chains.

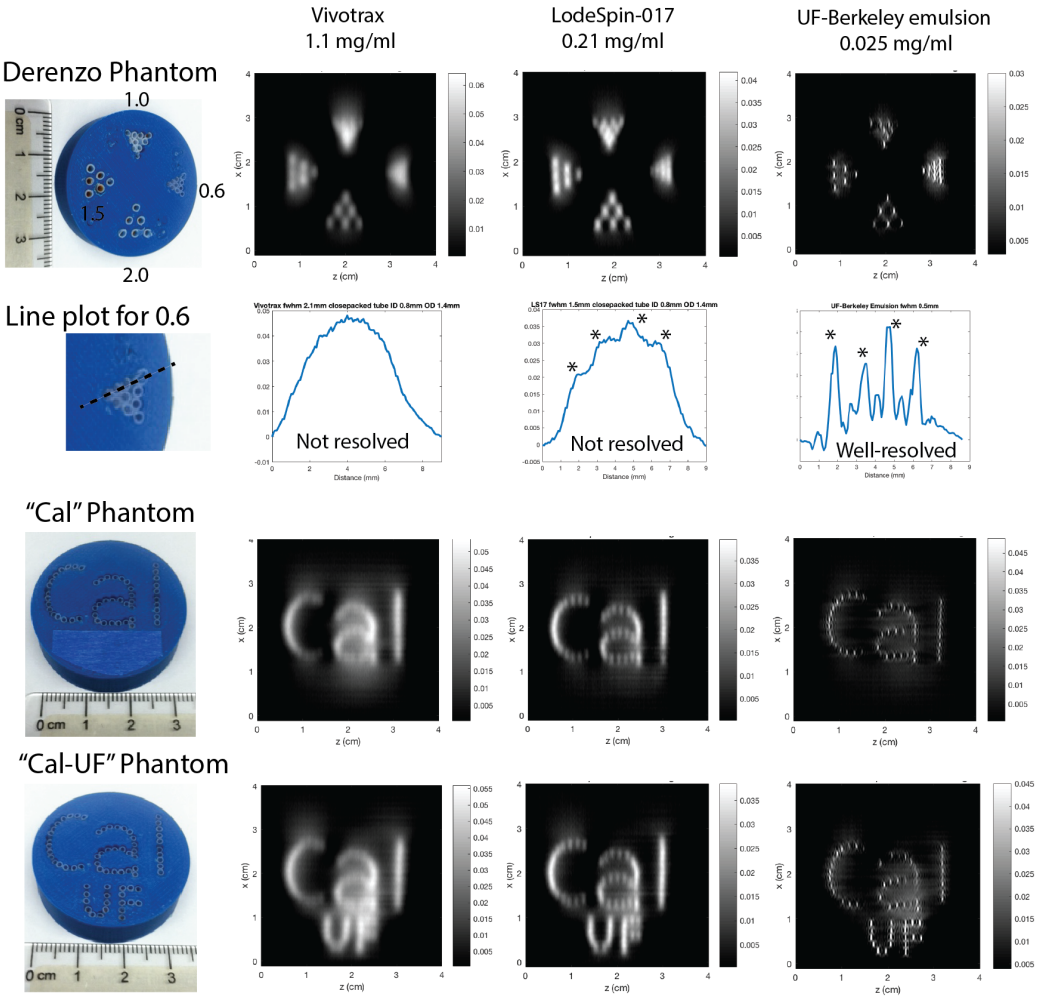

Sensitivity:	54.5 mV/mg Fe	190 mV/mg Fe	2000 mV/mg Fe
Resolution:	1.7 mm	1.0 mm	0.3 mm

FIGURE 6.9: Various 2D Phantoms show dramatic improvement in imaging performance with SiMPI

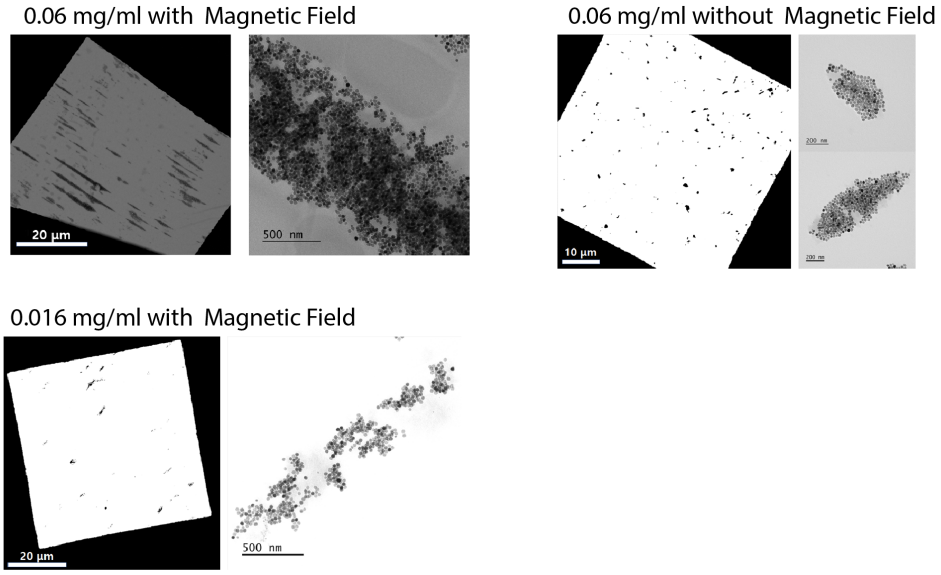

FIGURE 6.10: TEM imaging show clear chain formation when magnetic field is applied. At low concentrations, chains barely form due to abovementioned concentration latching effects.

Effect of viscosity on SiMPI
Toluene at -60 is 3.11 mPa s
Toluene at -7 is 0.87 mPa s

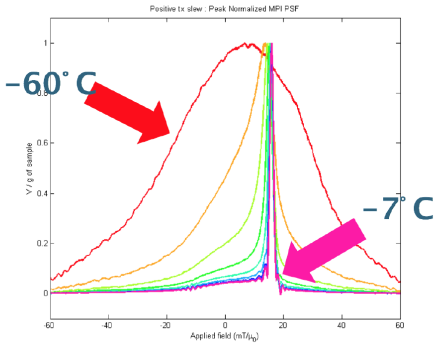

FIGURE 6.11: Temperature was used to change the toluene viscosity to affect the SiMPI nanoparticles. Higher viscosity shows poorer SiMPI performance as the nanoparticles have greater difficulty coming together to form chains needed for SiMPI.

6.3.7 SiMPI behavior requires nanoparticle chain to have its axis parallel to RF excitation axis

Interestingly, when the nanoparticle chain has its axis perpendicular to the drive field excitation axis, SiMPI does not occur at all. This makes sense because the initially formed long chain of particles is unable to quickly reorient to match the drive field excitation axis. Furthermore, from the geometry, the neighboring particles now actually provide a de-magnetizing field when they get polarized in the (perpendicular) direction by the drive field, and rather than positive feedback, negative feedback is observed and very poor MPI signal / performance is observed.

This is good for SiMPI images however, since the typical EPI raster trajectory used means that in conventional MPI the field-free-point passing just above or below the nanoparticle generates blurring MPI signal by inducing some rotation of the nanoparticle magnetic moment to point in the other direction from the field-free-point. This is known as the tangential envelope in prior MPI work Lu et al., 2017 and creates a wispy haze that reduces perspicuity and effective resolution of the MPI images. If instead of conventional MPI, SiMPI is used, the fact that parallel background and drive axes is required mean that there will only be SiMPI when the field-free-point rasters through the nanoparticle, and there will be no SiMPI signal when the field-free-point passes just above or below (effectively the background field direction is perpendicular to the drive axis). This acts as natural suppression of the tangential envelope, and therefore non-hazy MPI images can be obtained even without multi-channel acquisition as required in Lu et al., 2017.

6.4 Conclusion

The results shown here show the great promise of SiMPI to very significantly improve MPI spatial resolution and SNR. However, much work remains to be done to robustify the chemical formulation in order to maintain SiMPI behavior under all circumstances (in vivo, at different polarizing fields etc). Especially with regards to a safe (the toluene used in this initial work is not considered to be a desirable compound to be injected), colloidally stable formulation, this chemistry work into a nanocarrier or appropriate ”shell” for SiMPI multi-particle structures will be vital to enable in vivo scans with SiMPI.

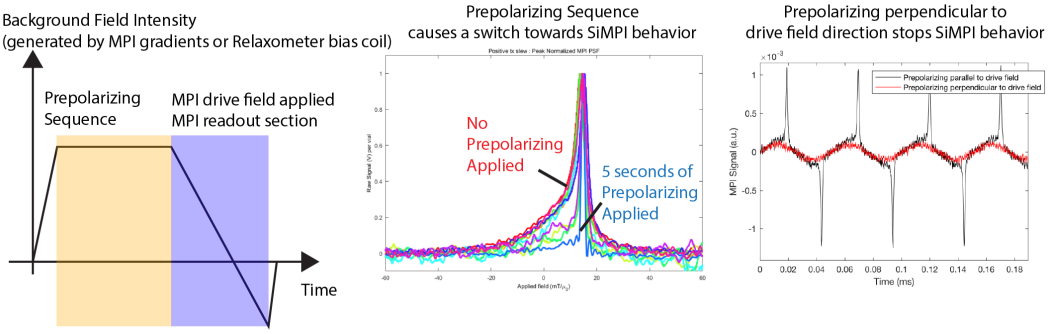

FIGURE 6.12: (left) prepolarizing pulse to form the SiMPI chain before performing the MPI scanning and readout. (middle) The prepolarizing pulse generates SiMPI behavior where there was no SiMPI before due to lack of a pre-existing chain. (right) The prepolarizing pulse has to be parallel to the drive field direction to work. The perpendicular case actually suppresses SiMPI behavior completely.

6.5 Acknowledgment

I would like to thank Daniel for all the theoretical discussions behind the mechanism of SiMPI. Daniel and I initially noticed the sharp peaks characteristic of SiMPI on a relaxometer (AWR) scan of the RL3 particles, and we worked together to characterize and develop the SiMPI concept from the first AWR discovery of this phenomena. Bo Zheng suggested the Schmidtt trigger model for the phenomenon and Steve Conolly helped formalize the math and parameterize the physical relation its current intuitive form. The theory section written here is my own work and derivation, but based on Steve's initial model of a saturating positive feedback system. Special thanks goes out to rotation students Barry Fung and Soo-Hyun Shin for the TEM experiments and Caylin VanHook for prepolarization experiments. Lastly, and most importantly, we would like to thank our collaborators the Rinaldi group at University of Florida who kindly provided us with the nanoparticles that enabled this work.

Part II

Theranostics and Therapeutic Tracking Applications of MPI

Part 2 Preface

The second part of the dissertation aims to showcase some of the MPI applications I helped developed during my graduate school career.

In Chapter 7, I explore the potential of MPI for theranostics. MPI is rather unique in this aspect because the physics underlying MPI signal generation is almost exactly the same as that underlying magnetic hyperthermia. Furthermore, the same magnetic core generates MPI signal and hyperthermia heat, ensuring robustness in the theranostics process and avoiding any label—therapeutic agent separation issues. As a result, MPI hardware can be exploited to provide not only image-guidance for therapy, but also localize therapy to user-defined location with similar spatial precision as MPI's spatial resolution, therefore potentially achieving < 2 mm margins with strong gradients of 7 T/m. With high contrast, high sensitivity and linearity quantitative images and precise control of location and dosage (through robust SAR predictions based on MPI image intensity), MPI is compelling for theranostics. By performing the first MPI image-guided *in vivo* cancer theranostics workflow here, I demonstrate that MPI is a powerful platform for magnetic-based theranostics. Furthermore, the same image-guided localization mechanism can be used to localize drug release via localization for actuation energy for temperature-sensitive release or mechanical disruption of nanocarrier membrane.

In Chapter 8, I explore a new application for MPI which is lung imaging by nebulized or aerosolized SPIOs. Unlike MRI, MPI works well in the lungs because it works by a different mechanism and thus does not suffer the same air-tissue susceptibility problems as MRI. Traditionally, aerosol imaging is performed with nuclear medicine via radioaerosol studies. I demonstrate that MPI is a viable non-radioactive complement to assess delivery efficiency of the aerosol and quantify important metrics such as mucociliary clearance.

Chapter 7

Magnetic Particle Imaging Theranostics: *In Vivo* Proof-of-concept using Gradient Fields For Arbitrary Localization of Therapy

7.1 Attribution

7.2 Introduction

Image guided treatment of cancer enables physicians to localize and treat tumors with great precision. Here, we present *in vivo* results showing that an emerging imaging modality, Magnetic Particle Imaging (MPI), can be combined with Magnetic Hyperthermia into a image-guided theranostic platform. MPI is a noninvasive 3D tomographic imaging method with high sensitivity and contrast, zero ionizing radiation, and is linearly quantitative at any depth with no view limitations. The same superparamagnetic iron oxide nanoparticle (SPIONs) tracers imaged in MPI can also be excited to generate heat for magnetic hyperthermia. In this study, we demonstrate a

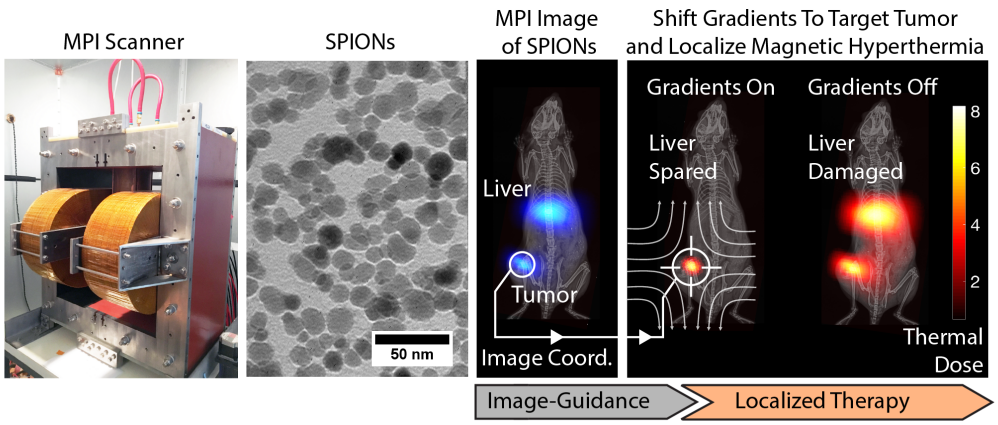

FIGURE 7.1: Simple Pictorial Representation of how theranostic MPI uses MPI gradients to selectively treat the tumor while avoiding potential damage to healthy organs like the liver.

theranostic platform, with quantitative MPI image-guidance for treatment planning and use of the MPI gradients for spatial localization of magnetic hyperthermia to arbitrarily selected regions. This addresses a key challenge of conventional magnetic hyperthermia - SPIONs delivered systemically accumulate in off-target organs (*e.g.*, liver and spleen), and difficulty in localizing hyperthermia results in collateral heat damage to these organs. Using a MPI-magnetic hyperthermia workflow, we demonstrate image-guided, spatial localization of hyperthermia to the tumor while minimizing collateral damage to the nearby liver (1 – 2 cm distant). Localization of thermal damage and therapy was validated with luciferase activity and histological assessment. Apart from localizing thermal therapy, the technique presented here can also be extended to localize actuation of drug release and other biomechanical-based therapies. With high contrast and high sensitivity imaging combined with precise control and localization of the actuated therapy, MPI is a powerful platform for magnetic-based theranostics.

7.3 Background

The ideal image-guided treatment of tumors aims to treat only the cancer cells while minimizing damage to surrounding tissue. Current image-guided therapies such as Cyberknife / Gamma Knife and radiofrequency (RF) ablation (Day, Morton, and West, 2009) have their own limitations.

Cyberknife relies on a weeks-old landmark CT / PET-CT study for image-guidance while RF ablation cannot be applied in deep tissues without invasive catheters which can cause complications such as lung pneumothorax.

Magnetic hyperthermia is a promising approach that has the potential for real-time image-guidance while reaching deep tissues without invasive catheters. This approach relies on delivery of magnetic nanoparticles to tumors, followed by application of alternating magnetic fields (AMF) that cause the SPIONs to generate and release heat to their environment (Jordan et al., 1999; Rosensweig, 2002b; Jordan et al., 2006; Thiesen and Jordan, 2008). Magnetic hyperthermia can be achieved deep in the body since the alternating magnetic fields (AMF) used can fully penetrate the human body and actuate heating of nanoparticles without tissue depth limitations (Hensley et al., 2016; Rodrigues et al., 2017). This approach has many advantages: First, SPIONs are regarded as biocompatible and biodegradable (Weissleder et al., 1989; Pouliquen et al., 1991) *in vivo*. Second, heating is localized to the SPION biodistribution. Third, magnetic hyperthermia has greater synergy with chemical therapies (Alvarez-Berrios et al., 2015; Alvarez-Berríos et al., 2014; Alvarez-Berríos et al., 2013; Lee et al., 2011; Torres-Lugo and Rinaldi, 2013) than other forms of hyperthermia. Fourth, magnetic hyperthermia has also been shown to induce anti-tumor immunity (Ito, Honda, and Kobayashi, 2006; Toraya-Brown et al., 2014) and can kill cancer cells without a macroscopic temperature rise. Lastly, instrumentation already exists (Jordan et al., 2001) to generate AMFs suitable for SPION-based thermal therapy in patients.

However, magnetic hyperthermia has several challenges to address. First and foremost, SPIONs delivered systemically accumulate in off-target organs (e.g., liver and spleen), resulting in collateral damage (Kut et al., 2012) to these organs. Current approaches to actuate SPION heating do not permit spatial control with precision required to spare healthy organs while treating tumors. More specifically, while magnetic hyperthermia is inherently localized to the SPION distribution, which is limited to imperfect SPION surface-ligand based targeting of the tumor, arbitrary localization inside this distribution is not currently possible. Strategies to focus the excitation wave (100 – 1000 kHz) are fundamentally limited by diffraction, regardless of the number of external coils employed, to a spot size of about half the *in vivo* wavelength (17 – 150 m) and is thus untenable for clinical applications. Other strategies to localize the excitation using surface coils work poorly at depth due to field amplitude fall-off of the excitation wave.

In addition, some other challenges are quantitative imaging of SPION mass for hyperthermia treatment planning. Due to relatively high SPION

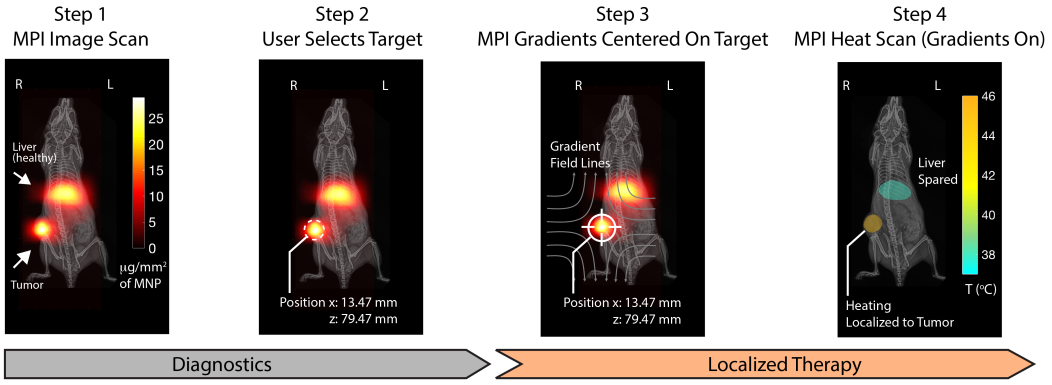

FIGURE 7.2: Theranostic Workflow demonstrated experimentally on a U87MG xenograft mouse model with SPIONs present in the liver and tumor. Step 1: an MPI image scan at 20 kHz, 20 mT enables clear visualization with high contrast of the SPION biodistribution in regions of pathology (tumor) and also in healthy clearance organs (liver). Imaging parameters are such that SPIONs do not heat. Step 2: the user selects a region, in this case the tumor, to localize the magnetic hyperthermia to. Step 3: The MPI gradients are shifted to center the field-free region (FFR) on the target. This magnetically saturates SPIONs away from the FFR to prevent heating. Step 4: Heat scan at 354 kHz, 13 mT is performed while the MPI gradients are on and held in position. Heating is experimentally localized in the FFR (centered at tumor) while minimizing collateral heat damage to the liver.

doses required for heating, for this case, quantification with MRI is difficult since the SPION effect on MRI T2* saturates. We currently lack non-invasive methods of monitoring temperature rise around the SPION for deep tumors, and it is difficult to use MR Thermometry in regions close to the SPIONs (Rieke and Butts Pauly, 2008).

To address these challenges, we propose the use of Magnetic Particle Imaging (MPI) for image-guidance and the use of strong magnetic gradient fields inherent in MPI systems to provide user-defined, arbitrary localization of magnetic hyperthermia. Fig. 7.2 uses experimental data to depict the theranostic workflow proposed.

First developed in 2005 by Gleich and Weizenecker (Gleich and Weizenecker, 2005), MPI is a new tracer-based molecular imaging technique that directly detects and quantifies the non-linear magnetization of superparamagnetic iron oxide (SPION) tracers (Knopp et al., 2011; Rahmer et al., 2009; Franke et al., 2016; Vogel et al., 2015a; Saritas et al., 2013b). As in other molecular imaging techniques, like nuclear medicine, there is no signal from background tissue in MPI, giving MPI images high image contrast for SPION tracers. This unique contrast mechanism, combined with the use of low-frequency magnetic fields and clinically safe magnetic tracers,

enables MPI to produce clinical-grade images with zero tissue signal attenuation and high image sensitivity (Gleich and Weizenecker, 2005; Goodwill and Conolly, 2010). Unlike MRI, safety in MPI is bound by magnetostimulation and specific absorption rate (SAR) safety limitations (Saritas et al., 2013a). MPI is best compared to gold-standard tracer imaging techniques, such as nuclear medicine, but without the limitations of radiation safety or radionuclide half-life for longitudinal imaging. As such, MPI shows excellent promise for clinical applications such as angiography (Haegele et al., 2012), stem cell tracking and vitality assessment (Zheng et al., 2015; Zheng et al., 2016; Fidler et al., 2015), brain perfusion (Orendorff et al., 2016), lung perfusion (Zhou et al., 2017),lung ventilation (Nishimoto et al., 2015), cancer imaging (Yu et al., 2017a), gut bleed detection (Yu et al., 2017b) and hyperthermia (Hensley et al., 2016; Murase et al., 2015; Banura et al., 2016).

Magnetic Particle Imaging works by exploiting the nonlinear magnetization of the SPION tracers used. Strong magnetic field gradients magnetically saturate the SPIONs everywhere except the SPIONs within the field-free-region (FFR). Only these unsaturated tracers are able to respond to a small excitation magnetic field (20 kHz 20 mT). MPI uses an inductive pick-up coil to pick up the dynamic magnetization response of these SPIONs and this MPI signal is associated with the FFR spatial location. MPI can be considered a (magnetic) sensitive point method, and scans a 3D volume by rastering the sensitive FFR point around (Fig. 7.3). Image reconstruction can be performed by the x-space approach by gridding the MPI signal to the instantaneous location of the FFR (Goodwill and Conolly, 2010) or by a frequency domain approach by solving the inverse problem with a calibrated system function (Rahmer et al., 2009). Hardware details of the Philips-Bruker 3D Fast MPI demonstrator scanner and the Berkeley x-space scanners were previously described (Rahmer et al., 2015; Goodwill et al., 2012b; Goodwill et al., 2012c).

MPI has several intrinsic advantages. First, MPI has been shown to be a highly sensitive tracer modality with near picogram sensitivity (Graeser et al., 2017; Them et al., 2016a; Them et al., 2016b). MPI has high temporal resolution, with real-time MPI image-guidance of catheters demonstrated (Salamon et al., 2016; Rahmer et al., 2017). Temporal resolutions of 46 frames per second have been shown in recent state-of-the-art scanners (Ludewig et al., 2017). Next, MPI has been demonstrated to be high-contrast (no tissue signal unlike MRI) and quantitative for the SPION mass (Zheng et al., 2015; Zheng et al., 2016; Yu et al., 2016; Ludewig et al., 2017; Tay et al., 2016) therefore allowing robust prediction of SAR dose from an image of the SPIONs.

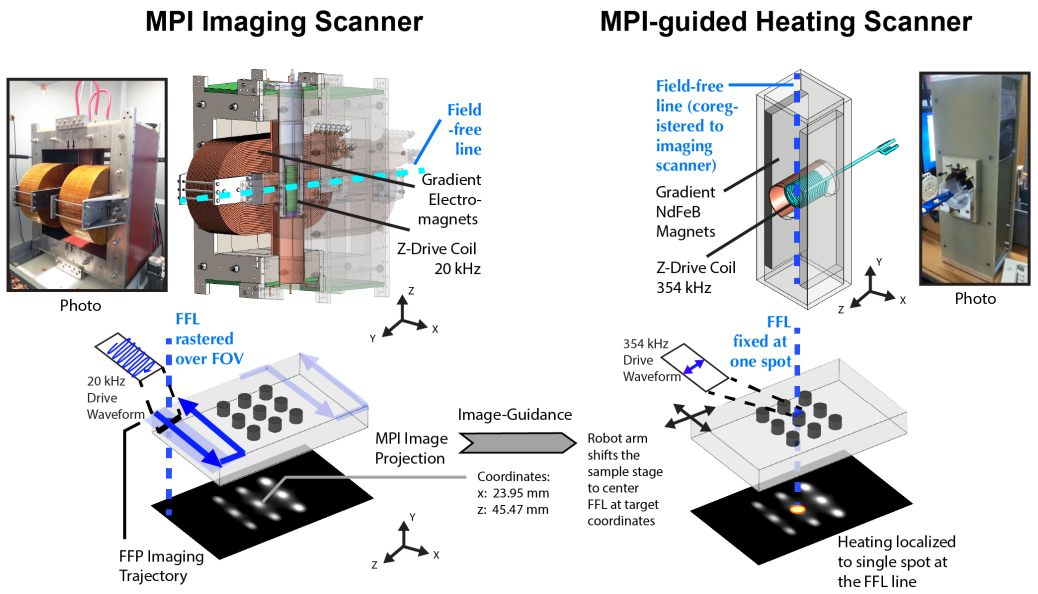

FIGURE 7.3: Hardware setup of the MPI scanner and the image-guided magnetic hyperthermia scanner. Images are first obtained on our Berkeley MPI Scanner (validated in prior work (Yu et al., 2017b)). To obtain an image, the sensitive field-free-region (FFR) is rastered through a volume. In this study, a field-free-line geometry is used, and images obtained are similar to projection scintigraphy. A separate higher-frequency MPI scanner is used for application of magnetic hyperthermia but has the same geometry, field-free-line. The coordinates are matched to the coordinates of the field-free-line (FFL) of the imaging scanner so as to enable image-guidance from the first scanner. The user is able to pick a target from the image, and the corresponding coordinates on the image is sent to the MPI heating scanner. The robot arm shifts the co-registered animal bed to center the FFL of the heating scanner to the requested coordinates. To locally heat only the target spot, the field-free-line is held in place over the spot while a higher frequency (354kHz) excitation is performed.

The physics underlying MPI is very similar to the physics underlying magnetic hyperthermia, which makes MPI an ideal candidate for resolving some of the challenges mentioned above. For example, the exact same nanoparticle core generates the MPI signal as well as the heat for magnetic hyperthermia (Dhavalikar and Rinaldi, 2016). The issue of the imaging label separating from the therapeutic core is thus non-existent. Furthermore, the same physical mechanism (rotation of magnetic moment) that generates signal in MPI generates heating in magnetic hyperthermia, thus giving the MPI-predicted heating strong predictive power and extraordinary robustness (Murase et al., 2015; Banura et al., 2016).

Limitations of Current Magnetic Hyperthermia Methods

One serious clinical challenge for magnetic hyperthermia is the difficulty of targeting heating deep within the body. Since the non-specific uptake of even targeted SPIONs is far higher in the excretory organs (liver, spleen, or kidneys) than in the targeted region such as the tumor (Wilhelm et al., 2016), indiscriminate magnetic heating of all the nanoparticles in the body will result in significant collateral damage to healthy tissues. There is currently no way in magnetic hyperthermia to target magnetic energy to specific regions of magnetic nanoparticles arbitrarily deep in the body. This is because our ability to focus electromagnetic fields at the frequencies used in magnetic hyperthermia (around 300 kHz) is fundamentally limited by diffraction, regardless of the number of external coils employed, to about half the *in vivo* wavelength. Unfortunately, at the high frequencies used in magnetic hyperthermia (typically ~ 300 kHz), this value is roughly 50 meters and much larger than the subject (Hensley et al., 2016; Hensleya et al., 2017). Many magnetic hyperthermia methods use large homogeneous field-producing coils. This leads to significant heat deposition at all sites where the SPION concentration is high, including healthy sites of accumulation. Alternatively, surface coils which do not provide a homogeneous excitation field can be used to target the heating, as depicted in Fig. 7.4. Due to the rapid spreading of the magnetic field with distance from the coil, this approach can selectively target lesions near the surface of the subject, but it cannot deliver energy to particle distributions deeper in the body.

Signal Localization in MPI can also be used to Localize Heating in Magnetic Hyperthermia

To address this issue, we exploit the similarity of working mechanism between MPI and magnetic hyperthermia. Unlike prior strategies for localizing heating in magnetic hyperthermia, rather than shaping the excitation field for heat localization we use a completely different mechanism of gradient magnetic fields to magnetically saturate and render almost all but a few SPIONs unresponsive to excitation. This is essentially the same concept used for MPI imaging described above. Because the signal generation mechanism in MPI and the heat generation mechanism of magnetic hyperthermia are the same - both rely on nanoparticle rotation, either physically or the internal rotation of the magnetic dipole moment, the MPI gradients (hardware) that are used to localize MPI signal by rendering all but one location unresponsive to MPI excitation, can also be used for localization of

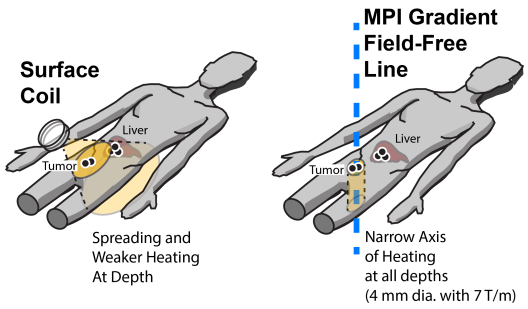

FIGURE 7.4: Illustration of MPI-localized heating in the tumor while sparing the liver. This is compared to a surface coil method that can localize excitation near the body surface, but is unable to maintain narrow excitation deep within the body due to the field spreading and drop-off with distance. Furthermore, since $\lambda/2 \approx 50$ m for typical heating frequencies, the excitation field cannot be focused into a narrow spot. Collateral damage may done to healthy tissues with non-specific SPION accumulations i.e. clearance organs. In contrast, MPI gradients localizes heating by a completely different mechanism, which is to suppress nanoparticle rotation rather than shaping the excitation wave. Like MPI which can image at depth, heating is localized to the field-free-line (narrow axis) without spreading or attenuation with depth. With a 7 T/m gradient, localization to within a 4 mm diameter cylinder is expected.

magnetic hyperthermia heating. This gradient-based mechanism can also be understood as magnetically locking the nanoparticles in place (magnetic saturation) and preventing rotation to generate heat or MPI signal. Only the central region of the gradient field with zero magnitude lacks this suppression, therefore localizing the MPI signal or magnetic hyperthermia heating. This can also be understood by SPION hysteresis curves at different positions in the gradient. Hysteresis in the dynamic magnetization curves occur due to relaxation effects (Tay et al., 2017; Dhavalikar and Rinaldi, 2016) and heating is related to the area in the M-H plot bounded by this curve. The spatially-variable saturating effect is observed by the hysteresis curves becoming narrower as the SPION is moved away from the field-free-region (see Fig. 7.5). The hardware to shift and control the location of this zero field point (field-free-line) is already present in MPI scanners (Yu et al., 2017b; Ludewig et al., 2017; Zheng et al., 2015; Rahmer et al., 2015). The same imaging hardware for MPI which rasters the signal localization spot about the field-of-view to generate an image, can be utilized in magnetic hyperthermia to localize heat to user-selected regions by designing a shift-and-park trajectory to visit and heat selected thermal therapy targets in turn.

This proposed method enables precise thermal dose localization with high spatial resolution. Precision of the localization improves with

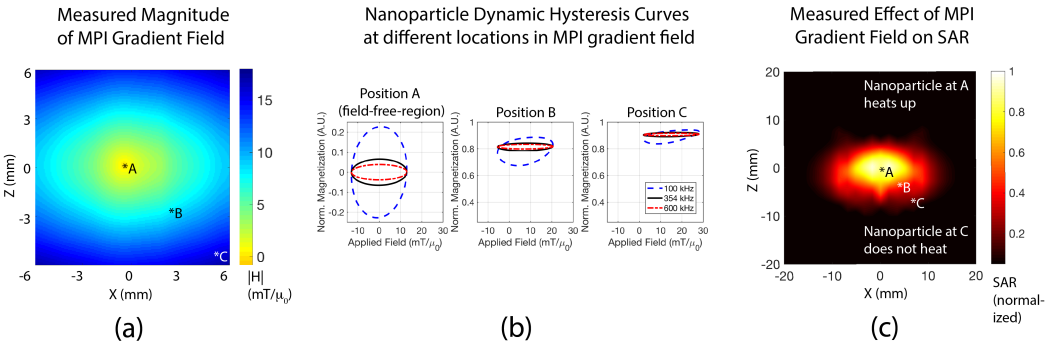

FIGURE 7.5: Experimental results demonstrating the mechanism behind MPI gradient-based localization of heating.(a) Magnitude of the MPI gradient in the x-z plane (Lakeshore^{TM}Gaussmeter). The gradient field has zero magnetic field at the center and a high magnitude everywhere else. Due to the field-free-line geometry along the y-axis, each x-z slice along y has the same magnetic field profile. (b) SPION dynamic hysteresis loops was simulated at different positions in the gradient field. The hysteresis loops are most open at position A ($|H| = 0$) while the hysteresis loops are closed at other positions. Because heating depends on the area bounded by the hysteresis loop, the gradient field localizes heating to the field-free-line where $|H| \approx 0$. Different drive frequencies have the same trend, showing that this localization method is flexible and works for a range of MPI drive fields. (c) Nanoparticles were put at different locations in the gradient field and heated with 354 kHz, 13 mT excitation. The measured temperature rise and SAR (Neoptix^{TM}probes) is observed to be highest when the nanoparticle is located at position A (field-free-line), in line with simulations in (b). Heating was suppressed at other positions due to the large $|H|$ away from the field-free-line. The 2.35 T/m gradient used here localizes heating to within a 7 mm radius region, but doubling the gradient to 7 T/m will improve localization to 2.3 mm radius.

higher MPI gradient strength, thus offering an avenue towards high-spatial-precision thermal therapy. We achieved $\sim$ 7 mm (full-width-half-maximum) spatio-thermal resolution with a 2.35 T/m MPI gradient and expect $\sim$ 2.35 mm with a 7 T/m MPI gradient based on previous imaging and theory results (Yu, Goodwill, and Conolly, 2015)).

As such, we can envision a theranostic workflow where an MPI image is first taken and the same MPI gradients are subsequently used to target and localize SPION heating in the therapy stage. Notably, image-guidance for targeting of the heat dose is particularly robust due to the common dependence on the field-free-line for both imaging and heat localization. MPI signal occurs when field-free-line is just rastered across the SPION location. Similarly, magnetic hyperthermia heating is restricted to the field-free-line location. Thus, localizing heating to a selected SPION location can be as

simple and robust as applying the coordinates of the field-free-line at the instantaneous point in time when the selected SPION gave signal. To ensure heating only in the magnetic hyperthermia stage and not in the diagnostic/imaging stage, a very low frequency (20 kHz) is used for MPI imaging. The strong frequency dependence of magnetic hyperthermia (Dhavalikar and Rinaldi, 2016) means that SPIONs do not heat during MPI imaging. During the magnetic hyperthermia stage, a much higher frequency of 354 kHz is used to ensure heating. In addition, the trajectory of the FFR can be designed to help. During imaging, a raster trajectory is used thus each nanoparticle is only very briefly interrogated (few milliseconds), and thus the energy deposited at each location is negligible. In contrast, to heat up a target location, the FFR is parked there for minutes.

The MPI-magnetic hyperthermia theranostic platform can be real-time and closed-loop. The former is evidenced by the 46 frames-per-second achieved in the Philips-Bruker 3D Fast MPI demonstrator scanner (Ludewig et al., 2017). In a combined MPI-Hyperthermia scanner, seamless switching between imaging mode and heating mode should be possible without moving the subject, enabling real-time image-guidance of heating. This idea is discussed in prior work (Hensley et al., 2016). MPI can also provide closed-loop temperature monitoring and feedback. This relies on using the SPIONs as temperature sensors and communicating the temperature through the MPI signal. Prior work on MPI thermometry demonstrates a 0.4% change in the signal per ^{o}C (Weaver, Rauwerdink, and Hansen, 2009) as compared to 10 parts per billion for MR thermometry (Rieke and Butts Pauly, 2008). MPI relaxation has also been shown to be promising as a temperature sensor (Perreard et al., 2014a).

Prior studies have investigated the effect of frequency on magnetic hyperthermia heating (Dhavalikar and Rinaldi, 2016) as well as the use of gradients to localize heating*in vitro* (Hensley et al., 2016; Hensleya et al., 2017) and *in vivo* (Tasci et al., 2009). We expand upon prior work and combine all the elements to perform the first in-vivo demonstration of MPI image-guidance for localization heating *and therapy* in the context of a rodent cancer model. In this study, we demonstrate MPI image-guided heating in-vivo with a single nanoparticle agent as per the concept of theranostics. Fig. 7.2 showcases *in vivo* experimental data that demonstrates the theranostics workflow applied in this work. Second, we show prediction of the in-vivo heat dose, and by extension therapeutic outcome, of solid tumors through the quantitative MPI images. Third, based on the MPI image, a target region can be arbitrarily chosen and the heat dose localized in-vivo with MPI gradients, thus avoiding damage to the liver or, in the case of a double

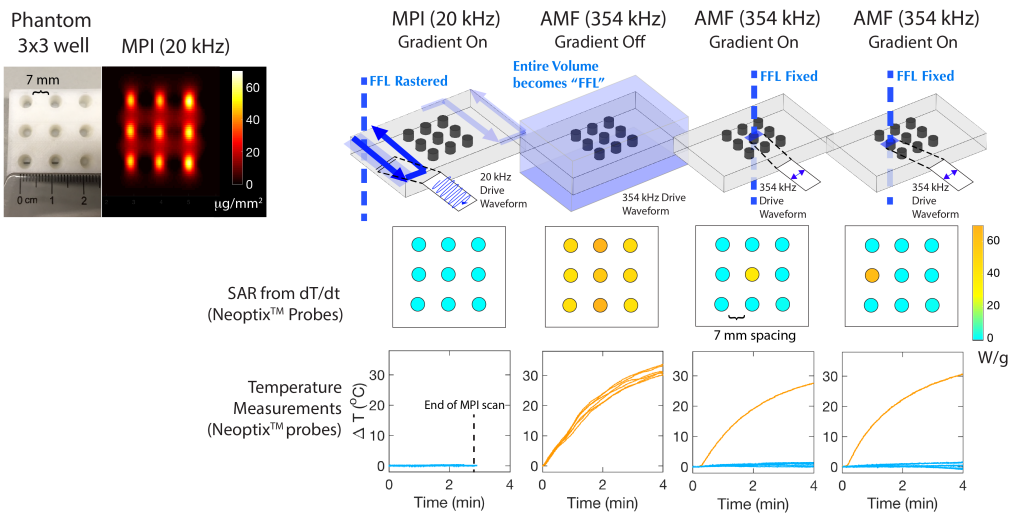

FIGURE 7.6: *in vitro* experimental demonstration of localization of magnetic hyperthermia. A 3 x 3 grid phantom was used where each well was filled with 100 μl of 25 mg/ml SPIONs. The temperature of each well was measured by Neoptix^{TM}fiber optic temperature sensors under different imaging or heating conditions. During a standard MPI scan, no heating was observed due to the low frequency (20 kHz) and raster trajectory. During a high frequency (354 kHz) heating scan without MPI gradients, all the wells heat up. When the MPI gradients are used, the user is able to selectively heat up only the well where the field-free-line is located, with negligible heating in all neighboring wells. Because the wells are spaced 7 mm apart, we demonstrated that heating is localized to within 7 mm for a 2.35 T/m MPI gradient. Higher gradients at 7 T/m can improve this value to 2.35 mm.

tumor mouse, selectively sparing one of the tumors. Lastly, we use histological assessment as well as luciferin bioluminescent imaging of a luciferase-competent xenograft of MDA-MB-231 cells to confirm that thermal damage is also localized to the target point defined by the MPI gradients.

With high contrast and high sensitivity imaging combined with precise localization of the actuated therapy, we believe MPI is a powerful platform for magnetic-based theranostics.

7.4 Methods

7.5 Superparamagnetic Iron Oxide Nanoparticles (SPIONs)

7.5.1 SPION Synthesis

SPIONs were synthesized by the co-precipitation method optimized for high energy dissipation rates described by Mrida et al. (Mérida et al., 2015) .Briefly, deionized water was degassed with nitrogen and used to prepare solutions of iron (II) chloride tetrahydrate (99%, Sigma-Aldrich) and iron (III) chloride hexahydrate (99%, Sigma-Aldrich) at a 1:2 molar ratio respectively, with a total iron concentration of 0.30 M. The iron salt solutions were sonicated, degassed, and mixed in a glass reactor. The reaction mixture was heated to 75^oC and ammonium hydroxide (29% vol/vol, Fisher Scientific) was added to the mixture to raise pH to 8.0-9.0. The reaction temperature was increased to 85^oC and allowed to react for one-hour. The pH was maintained around 8.0-9.0 by periodic addition of ammonium hydroxide. The resulting iron oxide nanoparticles were peptized using tetramethylammonium hydroxide (TMAOH, 1 M, Sigma-Aldrich) at a volume ratio 1:2 SPION/TMAOH twice. Peptized nanoparticles were suspended in water.

To coat the particles with polyethylene glycol (PEG), oleic acid (OA, 90%, Sigma-Aldrich) was adsorbed onto the particles. OA was added to SPIONs solution at 15 g OA/g SPIONs and ultrasonicated (Q700, Qsonica Sonicators) for 15 minutes. The mixture was transferred to a glass reactor, heated to 50^oC and allowed to react for 2 hours. SPIONs were precipitated using twice the volume of ethanol (200 proof, Decon Labs) and magnetically decanted to recover the particles, following which they were suspended in toluene ($> 98\%$, Sigma-Aldrich).

7.5.2 SPION Surface Modification with PEGsilane

PEGsilane was synthesized by a two-step process. First, mono-methoxy PEG (mPEG, 99.999%, Sigma-Aldrich) of 5 kDa molecular weight was converted to mPEG-COOH as described by Lele et al. (Lele and Kulkarni, 1998). Briefly, 0.05 mol of mPEG suspended in 400 mL of acetone (99.8%, Fisher Chemicals), was oxidized by adding 16.1 mL of Jones reagent and allowed to react for 24 hours. The reaction was stopped by adding excess isopropanol (70%, Sigma-Aldrich), and impurities from the reaction removed

with activated charcoal (12-40 mesh, ACROS Organics). Chromium salts and activated charcoal were removed through vacuum filtration, then the acetone solution was concentrated using a rotary evaporator. The mixture of mPEG-COOH was re-dissolved in 1M hydrochloric acid (37% vol/vol, Fisher Chemicals). Liquid-liquid extraction was performed using 75 mL of dichloromethane ($> 99.5\%$, Sigma-Aldrich) to extract the polymer to the organic phase. The solution was concentrated by rotary evaporation and the mPEG-COOH precipitated using cold ethyl ether ($> 99.8\%$, Fisher Chemicals).

To obtain PEGsilane, amidation of mPEG-COOH with 3-aminopropyl triethoxysilane (APS, TCI America) was performed. Briefly, a 1:1 molar ratio of mPEG-COOH:APS was mixed together for 2 hours at 120^oC and 500mbar. At the end, the PEGsilane was allowed to cool to room temperature and hardened. The SPIONs were coated with PEGsilane by ligand exchange, replacing the oleic acid molecules for PEGsilane, following a previously described procedure (Barrera, Herrera, and Rinaldi, 2009). In brief, 3.5 g of PEGsilane dissolved in 250 mL of dry toluene was mixed with 250 mL of OA adsorbed SPIONs at 0.8 mg/mL, then 40μL of acetic acid (99.8%, ACROS Organics) was added to catalyze the hydrolysis and condensation of the silane groups onto the SPION surface. The solution was placed in a shaker for 72 hours, after which PEGsilance coated SPIONs were precipitated using cold ethyl ether. The precipitate was dried and resuspended in water. SPIONs were then dialyzed to remove excess PEGsilane and further sterilized by filtration for animal experiments.

7.5.3 SPION Characterization

SPION's magnetic, physical, and hydrodynamic diameters were determined and the results shown in Fig. 7.7. Magnetic size distribution was determined using a Quantum Design Magnetic Property Measurement System 3 (MPMS3) Superconducting Quantum Inference Device (SQUID) magnetometer. Magnetization curves at room temperature were obtained for liquid samples in a PTFE sample holder with 100 μL of SPIONs suspended in water. Physical diameters were obtained using a Hitachi H 7000 Transmission Electron Microscope (TEM). Images of SPIONs at 1 mg/mL sampled on an Ultrathin Carbon Type A (3-4nm) with removable formvar grid from TedPella were acquired using a Veleta CCD side mount camera and were analyzed using ImageJ. Hydrodynamic diameters were determined

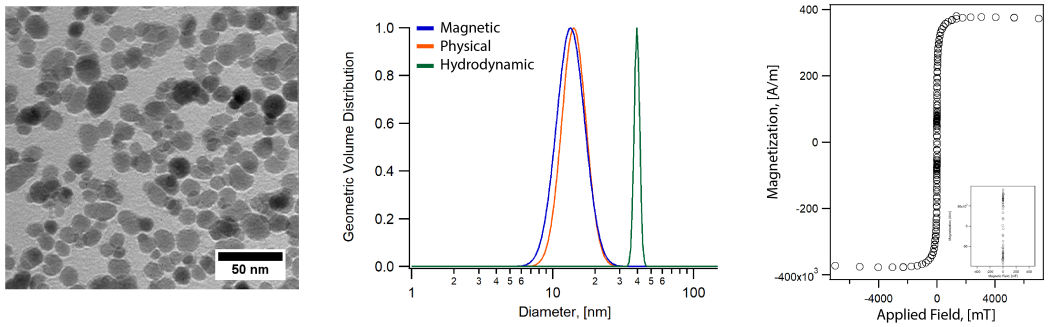

FIGURE 7.7: Experimental characterization of the magnetic nanoparticles used in this study. The nanoparticles are PEG coated, single crystalline core, superparamagnetic iron oxide. (a) TEM of the nanoparticles. (b) Histogram of the core size distribution gives a nominal core size of 13 nm with effective magnetic core size of 11.7 nm. DLS analysis of the hydrodynamic diameter with number weighted distribution gives a value of ~ 40 nm. (c) Magnetization response of the SPIONs. Inset shows a zoom in of the region close to zero field.

through room temperature dynamic light scattering (DLS), using a particle size analyzer (Zeta PALS, Brookhaven Instruments). For DLS, aqueous nanoparticle samples (500 μL) with concentration between 0.1 and 1 mg/mL were filtered using a 0.2 μm syringe filter prior to measurements.

7.5.4 Dynamic Magnetization Response in Different Locations in the MPI Gradient

Experimental measurements of the magnitude of the gradient field was taken with a Lakeshore^{TM}475 DSP Gaussmeter (Lake Shore Cryotronics, Ohio, USA) and plotted in Fig. 7.5a. Subsequently, the 2D spatial localization of SAR was experimentally measured by shifting a point source tube to different positions in the gradient field. The normalized SAR value was calculated by taking the initial rate of temperature rise at each position and plotted in Fig. 7.5c. For Fig. 7.5b, simulations were performed to obtain the dynamic magnetization response of the SPIONs to an applied alternating field in the presence of a field gradient. The results was obtained from the numerical solution of the MRSh magnetization relaxation equation as outlined in (Dhavalikar et al., 2016). The dynamic magnetization was normalized to the saturation magnetization to facilitate visualization and understanding of the effect of field gradient on the dynamic hysteresis

loop. Here, the value of unity indicates that particles are in a state of saturation. The SPIONs synthesized by the co-precipitation method and coated with PEG typically form small clusters. Thus, assuming a two particle cluster containing particles of diameter equal to 11.7 nm, an effective magnetic core diameter of 23.4 nm was used in the simulations. Interparticle interactions are not included in the model. The hydrodynamic diameter of the SPIONs was assumed to be approximately 40 nm as determined from DLS measurements. The suspension medium being water was assumed to have a viscosity of 0.89 mPa·s at 298 K. Simulations were executed using a bias field value corresponding to the magnitude of the gradient field measured at various positions (A, B, and C) in the setup. Excitation field frequency of 354 kHz and 13 mT amplitude was used to match the experimental conditions. Simulations were also executed at 100 kHz and 600 kHz excitation field frequencies to show that the strategy of localizing heat using a field gradient is flexible and also viable with a different setup.

7.6 Animal Procedures

7.6.1 Development of Tumor Xenograft

All animal procedures were approved by the Animal Care and Use Committee at UC Berkeley and conducted according to the National Research Council's Guide for the Care and Use of Laboratory Animals. Nude athymic mice between 7 – 9 weeks old (Charles River Laboratories) weighing approximately 23 g were used in this study. After one week habituation, tumor xenografts were developed by subcutaneous injection of 2 million cancer cells in 100μl of sterile 1X PBS into the flank. U87MG and MDA-MB-231-Luc cell lines were serum starved for four hours before use (UC Berkeley Cell Culture Facility). Tumor volumes in all mice were measured thrice a week using a vernier caliper. When the tumor volume reached approximately 100-150 mm^3, the mice were divided into control and experimental groups. For our controlled heating experiment a dual tumor model was developed in the same mice by implanting tumor cells subcutaneously in the shoulder and flank.

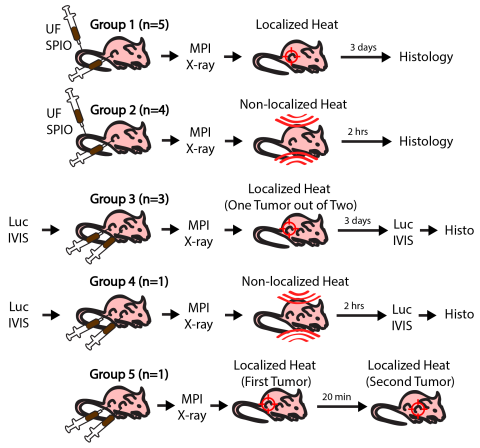

FIGURE 7.8: This study used 5 groups of athymic nude mice. Groups 1 and 2 had a single U87MG xenograft and received tail vein injections and intratumoral injection of 1.25 mg Fe SPION each. Bioluminescence imaging was performed for groups 3 and 4 that had luciferin-competent dual MDA-MB-231-luc xenografts (each intratumorally injected with 1.25 mg Fe SPION). Group 5 had a double U87MG xenograft and received intratumoral injection of 1.25 mg Fe SPION in each tumor. MPI and projection X-ray was performed for all groups. Groups 1 & 3 had gradient-localized heating while Groups 2 & 4 had gradient-localization off during heating. Group 5 had gradient-localized heating that sequentially targeted one tumor then another. For all groups, post-euthanasia, the liver and tumor were excised for histology.

7.6.2 Animal Preparation for MPI-magnetic hyperthermia Procedure

MPI-magnetic hyperthermia experiments were carried out as outlined in Fig. 8.1. Experimental group 1 (n=5) and group 2 (n=4) with single U87MG xenografts received 1.25 mg Fe of SPION by intratumoral injection and 50 μl of 25 mg/ml SPION as a tail vein injection for a total of 2.5 mg Fe per mouse. All MPI/magnetic hyperthermia were carried out on murine models under anesthesia. The mice were maintained at 1-2% isoflurane (60-80 breaths-per minutes) mixed with medical oxygen (1 lpm) supplied via nose cone. The core body temperature was constantly monitored by an optical fiber thermal probe (Neoptix^{TM}) inserted into the rectum. The core body temperature was maintained at 36-37 ^{o}C before starting magnetic hyperthermia with the help of controlled warm air delivered into the imaging bore from an external heater. The systemically administered SPIONs were allowed to completely clear from circulation to the liver before MPI imaging and heating was performed (approximately 24 hours).

Experimental group 3 (n=3) and group 4 (n=1) with MDA-MB-231-Luc

had two tumors per mouse, and each tumor received 1.25 mg Fe of SPION by intratumoral injection. Luciferase activity was measured after intraperitoneal injection of D-Luciferin Monosodium salt at a dose of 150 mg/kg reconstituted in 1X PBS (Pierce^{TM} ThermoFisher Scientific). Bioluminescent signal were obtained using an IVIS Lumina system with auto exposure time and medium binning. The bioluminescent image were exported as DICOM and processed off-line. The bioluminescent imaging was performed before and after the MPI-magnetic hyperthermia imaging and heating procedure.

Localization of heating via MPI gradients was performed in groups 1 and 3 while non-localized heating (where MPI gradients were turned off) was performed in groups 2 and 4. In experimental group 5 (n=2) with one dual U87MG tumor mouse and one dual MDA-MB-231-luc tumor mouse, each tumor received 1.25 mg Fe of SPION by intratumoral injection and sequential localized heating was performed by heating one tumor first then heating the other tumor to demonstrate arbitrary control of the heat localization within a single scan. For the control group (n=1, Control 1, sham) saline was injected intratumorally and had 50μl of 25 mg/ml SPION as a tail vein injection for a total of 1.25 mg Fe per mouse. Localized heating via MPI gradients was targeted at the (saline-injected) tumor to assess thermal resolution via measuring heating of the liver when targeting of a non-spio tumor was performed. Control 2 (n=1) received both an intratumor and tail vein injection of saline (volumes and procedure same as Experimental Group 1) and non-localized heating was performed to assess non-specific tissue-based SAR from the 354 kHz 13 mT magnetic field. Control 3 (n=1) received both an intratumor and tail vein injection of SPIONs (volumes and concentration same as Experimental Group 1) but received no heating from magnetic fields. After treatment with magnetic hyperthermia, all mice were observed for signs of superficial skin burns, signs of distress and discomfort, hunched posture, respiratory difficulties, or reticence to move. The hyperthermia procedure was immediately terminated if the core body temperature reached 40^{o}C in accordance with prior literature on the response of mice to changes in their core body temperature (Duhan et al., 2012) as well as prior work on minimal thermal damage thresholds required to cause damage to tissue (Yarmolenko et al., 2011; Rhoon, 2016).

7.6.3 Histological Assessment

Animals in group 2, 4 and 5 were euthanized 2 hours after hyperthermia treatment (kept under isoflurane) while animals in group 1 and 3 were monitored for up to 3 days post treatment before euthanasia. Animals were

first put under isoflurane anesthesia, then euthanized by carbon dioxide asphyxiation and cervical dislocation. After euthanasia, the tumor, liver, spleen and muscle surrounding the tumor was immediately excised and preserved in 10% formalin as preparation for histological sectioning. Hematoxylin and eosin (H & E) staining was done to assess tissue damage and Prussian Blue staining was done to assess SPION distribution within the tissue. In Situ Cell Death Detection Kit (TUNEL stain, TMR Red, Roche Diagnostics GmbH, Mannheim Germany) with nucleus counter-stained with DAPI was used to assess for apoptotic cells resulting from thermal damage. The slides were observed using appropriate color filters (ZEISS AX10 Observer D1 with a ZEISS Axiocam ERc 5s). FIJI software and its standard cell counting algorithm (Rueden et al., 2017; Schindelin et al., 2012) was used in calculating the percentage of cells that underwent apoptosis.

7.6.4 Imaging and Magnetic Hyperthermia

After administration of the SPIONs, the mice were imaged in the custom-built Berkeley 3D MPI scanner described in prior work (Yu et al., 2017b). The 3D MPI scanner has a 6.3 T/m MPI gradient generated by water-cooled electromagnets with a field-free-line configuration and has a drive field at 20.25 kHz and 20 mT amplitude. The field-free-line was rastered through the field-of-view of 12.35 cm x 4.75 cm x 4.75 cm and 2D projection images were acquired. The scan time was approximately 2 minutes excluding robot arm motion time. The FFL with axis along the y-direction was electromagnetically shifted along the x-axis as shown in Fig. 7.3. The animal bed was mechanically translated by a robot arm in the z-direction at 1 mm increments to complete projection imaging of the x-z plane. All images were reconstructed using x-space MPI reconstruction algorithm described in prior work (Yu et al., 2016). To obtain a 3D volume, the field-free-line was taken at different angles through the mice and the 3D volume is reconstructed with projection recon algorithms as described in our prior work on MPI tomography (Konkle et al., 2013). To provide an anatomic reference, projection X-ray was taken after the MPI scan when the mice were alive and at the end of treatment, a post-mortem CT was taken to provide a 3D anatomic reference.

After an MPI image is obtained of the biodistribution of the SPIONs within the mice, localized heating of the SPIONs was performed at a 2.35 T/m gradient with field-free-line configuration created with NdFeB permanent magnets and a drive field of 354 kHz and 13 mT. The heating duration

is between 30 minutes - 60 minutes depending on the real-time *in vivo* temperature measurements from which real-time updates on the total thermal dose could be obtained in order to achieve CEM43 of $\sim$ 60 – 90 minutes. The equation (Rhoon et al., 2013) for CEM43 used is :

$$\text{CEM43} = \sum_{i=1}^{n} t_i \cdot R^{(43-T_i)} \tag{7.1}$$

where R is 0.5 when above 43^{o}C and R is 0.25 when below 43^{o}C.

To perform image-guided localization of heating, the home field-free-line coordinates of both scans were aligned. From the obtained MPI image, the required displacement of the field-free-line from the home position to the desired target location was calculated. This value is used by the robot arm to shift the animal bed relative to the field-free-line. This is to align the field-free-line to the *in vivo* target location in order to localize the heating to the desired location. A detailed pictorial representation of the hardware used and the image-guidance workflow is presented in Fig. 7.3.

7.6.5 *In Vivo* Temperature Measurement

Neoptix^{TM}fiber optic temperature sensors were placed on the surface of the flank tumor and inserted into the intraperitoneal cavity and placed close to the liver to obtain real-time tumor and liver temperature measurements. One sensor was inserted into the rectum to measure the core body temperature as typically performed in prior hyperthermia studies (**Murase2015**). The fiber optic probes interfaced with the Neoptix Reflex^{TM}that has a measurement accuracy of $\pm 0.8^o$C and sampling rate of approximately 1 sample per second.

7.6.6 Predictive Algorithm for Thermal Dose Planning

Because MPI is quantitative for the mass of SPION, and since SAR is proportional to the SPION mass, we can obtain a SAR image from the MPI image. To predict the localization effect of the MPI gradients, we dot multiply the SAR image with suppression effect of the MPI gradient which is in essence a SAR spatial filter. We thus obtain a prediction of the SAR dose after gradient localization. Finally, to account for heat spreading through tissue from the SPION mass, we convolve the previous image with a temperature spatial point spread function (PSF).

To measure the SAR suppression effect of the MPI gradient, we measured the temperature rise (Neoptix^{TM}probe) of a point source of SPIONs (1.4 mm ID tube, 354 kHz, 13 mT excitation) as it is moved to different positions (x-z plane) in the background gradient field. To measure the temperature spatial point spread function (PSF), we created a 2 mm ID well in an 2% agarose gel phantom and filled it with 50μl of 25 mg/ml SPIONs. Constant heating was performed at 354 kHz, 13 mT and temperature of the agarose at various distances from the central well was measured (Neoptix^{TM}probe). When the temperature reaches steady-state, the spatial temperature profile of the agarose was recorded.

7.7 Results and Discussion

7.7.1 User-defined, Arbitrary Localization of Heating *In Vitro*

A potential theranostic workflow is as follows: (1) MPI image scan is taken. (2) User selects which nanoparticle cluster to heat (3) Field-free-point is shifted to selected spatial location either through mechanical movement of the sample through a robot arm or electromagnetic shifting of the gradients. (4) Heat scan at high frequency is performed where only the selected region experiences heating because nanoparticles elsewhere are prevented from rotating/heating up by the MPI gradients which remain on throughout the heat scan. A pictorial representation of this workflow is shown for experimental *in vivo* data in Fig. 7.2.

Fig. 7.6 shows the*in vitro* results obtained from a 3 x 3 phantom undergoing the described theranostic workflow. During the initial MPI imaging scan, negligible heating is observed. This is because each nanoparticle is interrogated / excited very briefly due to the raster imaging trajectory. In addition, a low frequency of 20 kHz is used. In contrast, the heating mode of the MPI-magnetic hyperthermia system generates significant heating over the same time of the MPI scan. Without the MPI gradients, all the wells in the phantom are heated up equally. This is also different from the MPI scan because the entire region of nanoparticles is continuously excited for the entire duration and a higher excitation frequency is used. Finally, by putting the MPI gradients in place, a field-free-line is generated and heating can be localized to that line. From the MPI image, one of the 9 vials is chosen. We chose the central vial to demonstrate that all other neighboring vials do not heat up. As shown in the results, negligible heating is observed in all wells

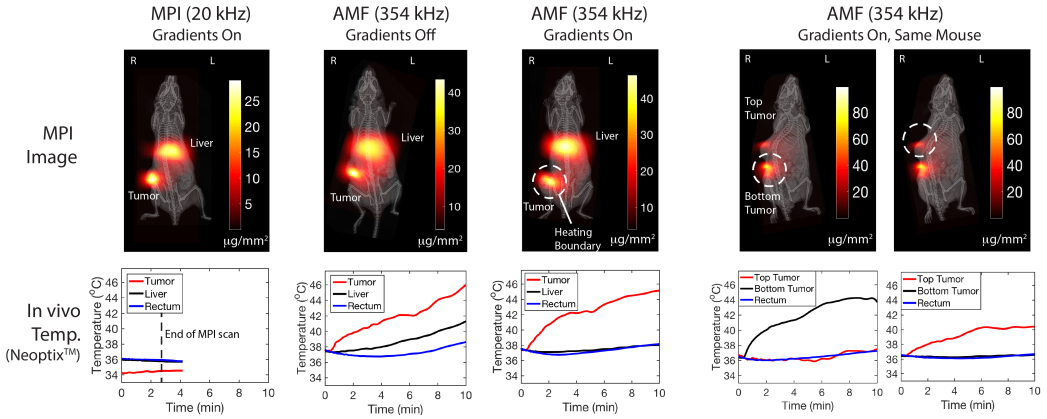

FIGURE 7.9: *In vivo* experimental demonstration of localization of magnetic hyperthermia. The tumor was heated while sparing the liver. All *in vivo* local temperatures were measured by Neoptix™ fiber optic temperature sensors. During a standard MPI scan, negligible heating was observed in the mouse to the low frequency (20 kHz) and raster trajectory. During a high frequency (354 kHz) heating scan without MPI gradients, all *in vivo* locations with nanoparticles heat up (thus damaging the healthy liver). When the MPI gradients are used, only the tumor is heated while the liver is spared. Lastly, we used a dual tumor mouse to demonstrate arbitrary user control of which tumor to heat. We first centered the field-free-line over the bottom tumor. Only the bottom tumor heated up while the top tumor was spared. Subsequently, without removing the mouse, we shifted the field-free-line over the top tumor. Only the top tumor heated up while the bottom tumor was spared, demonstrating arbitrary control of the site of heating just by shifting the MPI field-free-line.

except the targeted well. In addition, this heating location can be arbitrarily moved to another well simply by shifting the location of the field-free-line that is under the control of the MPI gradients. This demonstrates arbitrary control of heating location. Lastly, the 3 x 3 phantom has the wells spaced 7 mm apart. The results demonstrate that for a 2.35 T/m gradient used, heating can be localized to within a 7 mm radius. Stronger MPI gradients narrow the 'heating spot size' linearly with the gradient strength. If higher MPI gradients such as the 7 T/m gradient reported in a recent MPI on small animals (Yu et al., 2017b) are used, heat localization is expected to improve to $<$ 2.35 mm.

7.7.2 Image-guided, Arbitrary Localization of Heating *In Vivo*

In Fig. 7.2, we show experimental *in vivo* data in a xenograft athymic mouse model outlining the ideal theranostics workflow *in vivo* or in the clinic. In

this experiment, we show that we are able to image the biodistribution of the SPIONs in an animal, segment the regions that we wish to heat, estimate the thermal dose required due to the quantitative nature of MPI imaging *in vivo*, and then apply a highly localized heat dose only to locations in a tumor. This is done while sparing nearby healthy tissues that may have non-specific accumulations of nanoparticles, or the body's natural clearance organs for these SPIONs, such as the liver or spleen. These clearance organs are sensitive to heat damage and can be significantly affected from alternating magnetic field (AMF) heating as evidenced in prior workKut et al., 2012; King et al., 2015.

The results shown in Fig. 7.9 for the experimental group 1 confirm that the *in vitro* localization can be replicated *in vivo* and also underscored the importance of MPI gradients in localizing AMF heating. Similar to the*in vitro* experimental series, first, we verify that there is negligible heating during the MPI scan. Second, when the MPI gradients are turned off and the entire volume is excited at 354 kHz, indiscriminate heating occurs at all locations with SPIONs. Heating of the SPIONs cleared to the liver is observed at the same time as the heating of the tumor. Tumor and liver temperatures of 43^oC were reached in only 12 minutes. A control mouse with saline instead of SPIONs was also subject to the same uniform AMF but showed no increase in tumor and liver temperatures, verifying that this indiscriminate heating is not a result of non-specific SAR from AMF interacting with biological tissue. Next, the MPI gradients are turned on and we observe that the liver is spared from heating while only the tumor is heated. Lastly, we use a dual tumor mouse to demonstrate arbitrary control of the heating location. Initially, the bottom tumor is targeted and the results show localized heating in the bottom tumor but not the top tumor. Then, the field-free-line is shifted to the top tumor and the results show heating in the top tumor but not the bottom. These results show that with MPI gradients, the user can arbitrary control the location of heating. With guidance from the initial MPI image, the treatment planning can design a "heating trajectory" for the field-free-line or field-free-point and therefore spare healthy organs from collateral damage.

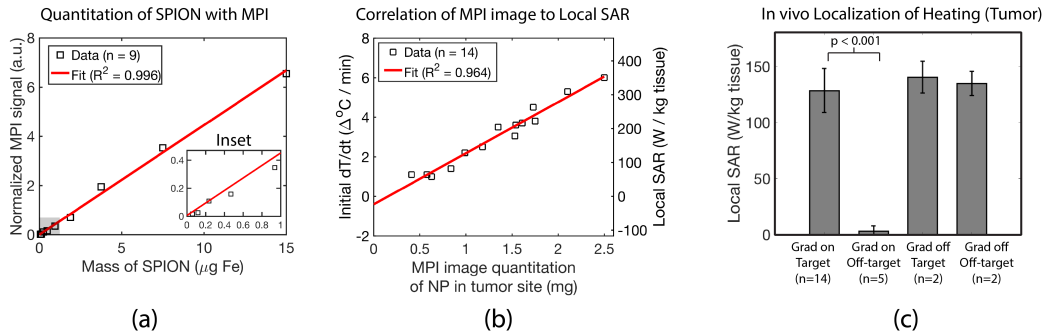

FIGURE 7.10: Experimental demonstration of MPI's potential for dose planning, image guidance and actuation localization. (a) The MPI image is linearly quantitative (R^2 = 0.996) for the amount of SPION. (b) The MPI image intensity is well correlated (R^2 = 0.964) with the deposited SAR measured *in vivo*, demonstrating robustness for dose planning and image guidance. (c) Robust localization of the heating to the targeted location is demonstrated (n = 14, p-value of < 0.001 with Welch's t-test). Localization is clearly attributed to the MPI gradient, since there is no localization of heating when the gradients are off. This implies that MPI gradients can robustly spare the liver while treating the tumor 1 – 2 cm away.

7.7.3 Robustness of Dose Planning and Heat Localization *In Vivo*

MPI has a few unique characteristics that allow for robust thermal dose planning. First, MPI is a quantitative imaging modality and is able to accurately image the amount of the iron or SPION *in vivo*. This has been extensively validated by prior work (Zheng et al., 2016; Tay et al., 2016; Yu et al., 2016). Second, because the exact same nanoparticle core generates the MPI signal as well as the magnetic hyperthermia heat, the MPI signal is robustly predictive for thermal energy deposition. Issues of the imaging label separating from the therapeutic core are thus non-existent. Because the thermal energy deposited is linearly related to the amount of SPIONs, by accurately quantifying the amount of SPIONs *in vivo*, the expected thermal energy deposited can be directly calculated. This can be clearly seen by the fact that thermal efficiency is often calculated by the SAR of the magnetic particles used in units of W/g of particles.

In Fig 7.10, we experimentally validate these unique characteristics of MPI. In Fig 7.10.a, we verify that with our field-free-line scanner, MPI is quantitative for the amount of iron even when projection images are taken. In Fig 7.10.b, we correlate the SAR deposited (proportional to the initial temperature rise measured when the 354 kHz excitation is initiated) to the MPI image intensity. Our results show that MPI pixel intensity (linear with

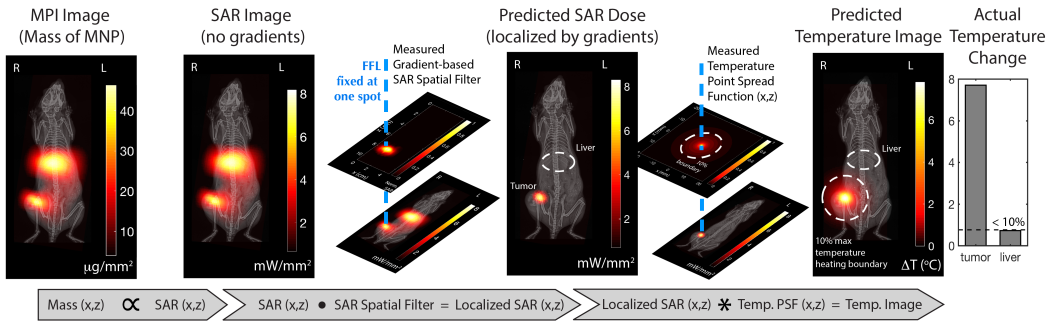

FIGURE 7.11: Experimental demonstration that MPI can predict the spatial distribution of heating for image-guided, gradient-localized magnetic hyperthermia. Because MPI is quantitative for the mass of SPION, and since SAR is proportional to the SPION mass, we can obtain a SAR image from the MPI image (no gradients and localization yet). To predict the localization effect of the MPI gradients, we dot multiply the SAR image with suppression effect of the MPI gradient which is in essence a SAR spatial filter. We thus obtain a prediction of the SAR dose after gradient localization. Finally, to account for heat spreading through tissue from the SPION mass, we convolve the previous image with a temperature spatial point spread function (PSF). Our predicted spatial distribution of heating matches experimental data in that the liver was heated by less than $0.8\%^oC$ as predicted by the calculated temperature map.

mass of SPION) is well correlated with the initial dT/dt and local SAR (R^2 = 0.964). The MPI image is thus invaluable for thermal dose planning, underscoring the theranostics potential of MPI for image guided thermal therapy.

Lastly, in Fig 7.10.c, we demonstrate statistics showing that robust localization of heating to the target location (n = 14) and that minimal heating is observed at non-target locations even if SPIONs are present. This is clearly attributed to the presence of the MPI gradient and field-free-line as no heat localization is observed when the MPI gradient is absent.

These results taken together shows that MPI can be very useful in clinical situations where non-specific uptake of therapeutics is an issue. With gradient-based localization of actuation (heat), MPI enables extremely localized and precise treatment even when the biological specificity of the therapeutic is not high and collateral damage to healthy parts of the body needs to be avoided. This relaxes the requirements for biological specificity and enables higher doses because actuation of therapy can be specific rather than indiscriminate.

7.7.4 Predictive Algorithm for the *In Vivo* Distribution of Heating

Here, we demonstrate the process behind estimating the thermal dose required as well as predicting the effectiveness of MPI-gradient spatial localization to verify if sensitive organs will be affected by the designed magnetic hyperthermia scan. Using this method, we can potentially simulate different target locations for the best region to target the MPI gradients to maximize tumor heating while avoiding nearby sensitive organs such as the liver.

To develop a predictive algorithm, we first calibrate the localization point-spread-function for heating due to the MPI gradient as well as the heat spread point-spread-function at steady-state (for a small point-source of heated SPIONs in an agarose gel phantom). This needs only be done once per MPI device. Mathematically as shown in Fig. 7.11, we would take the SAR image measured from the MPI SPION biodistribution image, then dot multiply it with the MPI gradient localization point-spread-function (centered at the target heating location). Subsequently, the gradient-narrowed SAR image is then convolved with the temperature spatial-point-spread-function to obtain a temperature rise image. This PSF was measured at temperature steady-state in an agarose phantom (no convective cooling) with constant heating of the point source. This PSF represents the worst-case spread of temperature rise (agarose is similar to a dead tissue phantom). The convective cooling from the blood perfusion in *vivo* will narrow this spread (assuming the blood pool represents a thermal sink). As such, the 10% boundary marked represents the worst case temperature spatial profile and in reality, the temperature rise *in vivo* should be constrained to a smaller region. The results from the forward model shown in the diagram match the experimental results in that no temperature rise was observed in the liver, which is outside the predicted temperature rise boundary. As such, this forward model based on worst-case heat-spread will be useful, albeit being quite conservative, for clinicians whose main aim is to avoid any damage to healthy organs and therefore would like to leave a large buffer region for safety.

7.7.5 Luciferase Assay shows Localized Therapy *In Vivo*

Assessment of treatment response was carried out on experimental groups 3 and 4 that have dual tumors of human triple negative breast cancer, MDA-MB-231-Luc. The luciferase expression in the tumors was measured before

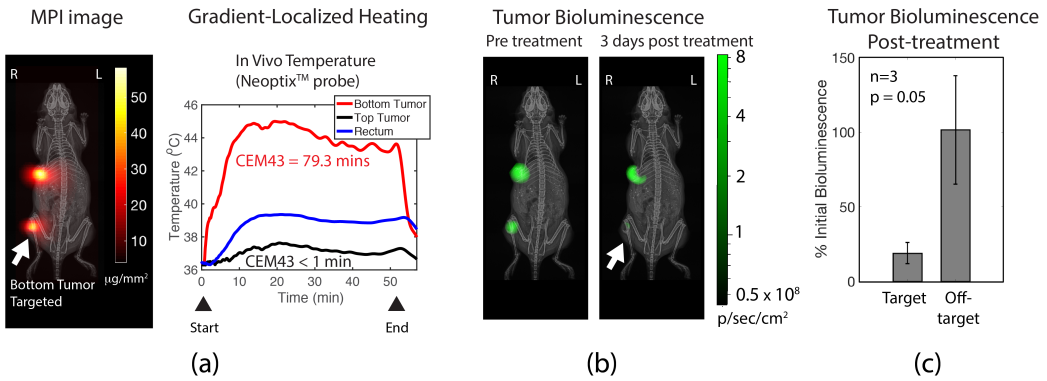

FIGURE 7.12: Experimental assessment of localized heat therapy using a bioluminescence-competent MDA-MB-231-luc xenograft model. (a) MPI image of the dual tumor MDA-MB-231-luc xenograft mice. The bottom tumor is targeted during gradient-localized heating. *in vivo* temperature at both tumors and the rectum measured by NeoptixTM fiber optic temperature probes. The greatest heating occurred in the targeted bottom tumor, while the upper tumor received negligible heating. The total CEM43 achieved was 79.3 minutes in the targeted bottom tumor. The core body temperature, however, was slightly elevated and likely due to the homeostatic response distributing heat from the heated bottom tumor to the rest of the body. (b) Luciferase bioluminescence activity of the tumor was measured before and after treatment. The results show significant decrease in activity for the treated bottom tumor, while the untreated tumor had almost no change in bioluminescence activity. Thus, this demonstrates the utility of MPI gradients in localizing tumor therapy. (c) Statistics (n = 3, p-value = 0.05 with Welch's t-test) show that localization of therapy is robust.

and after treatment, and used to evaluate the treatment response. The *in vivo* experimental results show significant heating of the targeted tumor while the other tumor experienced negligible heating (Fig. 7.12). Heating was maintained to achieve a CEM43 of greater than 70 minutes in order to observe any discernible treatment response (Rhoon et al., 2013; Rhoon, 2016; Yarmolenko et al., 2011). The luciferase activity reduced considerably ($\sim$ 10-fold) in the treated tumor compared to the non-treated tumor. The luciferase activity confirms the thermal dose was selectively deposited on the tumor and resulted in significant thermal damage.

7.7.6 Histological Assessment Verifies Localization of Thermal Damage to Target Region Only

Apoptosis in organs as a result of thermal damage was measured by quantification of the single and double stranded DNA breaks (TUNEL staining). Percentage apoptosis was calculated by dividing the number of TUNEL

stained cells by the total number of cells (DAPI stain). From the histology images, significant numbers of cells undergoing apoptosis can be observed in the tumors targeted with magnetic hyperthermia while no tissue damage was observed in off-target tumors (Fig. 7.13.a). Experimental replicates (n=3) show robust localization of damage to the target region and protection of the off-target regions (Fig. 7.13.b). To evaluate the protective effect of gradient-based heat localization on minimizing collateral damage to the liver, we compared the liver from a mouse subject to uniform heating (no MPI gradients) as opposed to a mouse subject to gradient-localized heating (heating targeted at tumor and away from the liver). The results (Fig. 7.13.a) show visible damage to the liver when MPI gradients are absent while there is negligible damage when MPI gradients are present, confirming that MPI gradient-based localization of heating can indeed minimize collateral damage to clearance organs such as the liver. Presence of SPIONs in both the liver and tumor was verified by Prussian Blue staining (Fig. 7.13.c). SPIONs were directly injected into the tumor, but not for the liver which accumulated SPIONs naturally after a tail vein injection. Distribution is relatively even throughout the tumor and liver. This verifies that there is indeed clearance of SPIONs to the liver and that it can potentially be damaged by magnetic hyperthermia in the absence of the spatial localization gradients.

7.7.7 Discussion

Precision of Localization Linearly Improves with Gradient Strength

Image guided tumor ablation aims to kill 100% of tumor cells with minimal destruction of adjacent healthy tissue. The unavoidable dead region at the tumor periphery is termed the tumor margins and 2-mm margins are considered standard in clinical practice. In this work, we experimentally demonstrated a radial margin of ~ 7 mm on a 2.35 T/m gradient. Because spatial precision improves linearly with gradient strength, increasing the magnetic hyperthermia gradient strength to 7 T/m will improve precision to 2.35 mm which is very close to the 2 mm objective. This level of precision should be more than adequate to avoid heating healthy sites such as the liver while targeting various lesions. With electromagnet gradients, the gradient strength can be adapted to the clinical situation. Lower gradients allows more efficient heating of larger lesions while higher gradients can improve precision when a nearby organ is close and at risk of collateral heat damage.

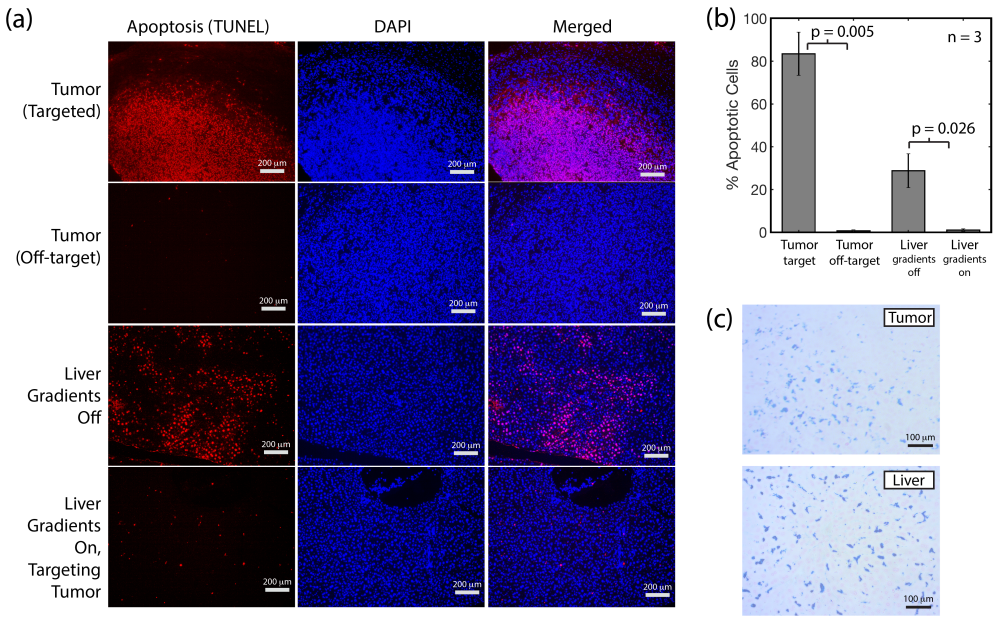

FIGURE 7.13: Histological assessment of MPI localization of thermal damage. (a) Apoptosis assay (red) and DAPI stain (blue) shows apoptosis only occurs in the targeted tumor but not in the neighboring off-target tumor, verifying localization of heat damage by the MPI gradients. The liver is also damaged when MPI gradients are turned off and uniform heating of the tumor and all other locations occurs. In contrast, no damage is observed in the liver when the MPI gradient is turned on and targeted at the tumor. (b) Statistics (n = 3, p-value = 0.005 with Welch's t-test) show that localization of thermal damage by MPI gradients is robust. The liver sustains significant damage if MPI gradients are off due to collateral heating of the SPIONs cleared to the liver. In contrast, the liver is negligibly damaged if MPI gradients are on (p-value = 0.026). These results validate the ability of MPI gradients to robustly localize thermal damage to the tumor while sparing the liver 1 – 2 cm away. (c) Prussian Blue stain confirms that SPIONs are successfully delivered to both the tumor and liver (clearance organ).

Implementation of Real-time MPI-magnetic hyperthermia

An ideal real-time theranostic platform will allow real-time visualization of the pathology and the treatment region such that imaging is simultaneous with the therapy. Because the SPIONs also generate MPI signal during heating, real-time simultaneous MPI-therapy should be possible. To achieve this, the currently separate MPI imaging and MPI heating drive coils should be combined in one scanner with the addition of a receive coil optimized to pick up the MPI signal at $f_0 = 354$ kHz. Because the field-free-line needs to be constantly parked at a fixed location to maintain heat localization, one practical limitation is that the field-of-view is limited to the vicinity of the

hyperthermia target location. However, this should not be a problem once the radiologist uses the initial MPI image to restrict the region-of-interest to the tumor vicinity.

If real-time imaging of a wider field-of-view is required, fast switching between imaging and heating modes could be designed such that heating is performed $> 95\%$ of the time and wide-view imaging in the other 5% (field-free-line is freed from its locked position to raster around). After the image, the FFL is immediately shifted back to focus heating on the desired spot again. This strategy is reasonable because MPI scans are relatively fast (3D Lissajous trajectory at 46 frames per second (Ludewig et al., 2017)) and because movement of the SPIONs into and away from the tumor takes much longer than the time interval between imaging updates. For example, the enhanced permeability and retention wash-in and wash-out of SPIONs from the tumor as studied by MPI is shown to be on the time-scale of hours (Yu et al., 2017a).

Real-time Temperature Feedback with MPI Thermometry

Because assessment of thermal therapy and dosage is most accurate with *in vivo* temperature feedback, it is desirable to have some form of non-invasive measurement of the temperature of the treated site to act as feedback for a closed loop thermal therapy system. Optical temperature probes are limited to the skin surface, while IR cameras must deal with thermal background, depth attenuation and reflectance. MR thermometry (Rieke and Butts Pauly, 2008), while non-invasive and effective at depth, is difficult to implement in the vicinity of SPIONs because it is based on a 10 parts per billion per ^{o}C effect. SPIONs are known to induce larger variations in the MR signal than that.

In contrast, MPI thermometry benefits from the good attributes of MPI - being able to image at depth and having high sensitivity and contrast (no tissue signal). In essence, MPI thermometry uses the SPIONs as sensors of the *in vivo* microenvironment temperature. Prior work on*in vitro* MPI thermometry has been shown to be promising (Weaver, Rauwerdink, and Hansen, 2009; Perreard et al., 2014a). In brief, these methods rely on (1) using the SPIONs to measure the microenvironment viscosity which changes with temperature or (2) changes in the SPION magnetization response due to temperature dependence of the Langevin function for SPIONs. Using the latter method, MPI thermometry achieves a 0.4% change in the signal per ^{o}C (Weaver, Rauwerdink, and Hansen, 2009). This is more sensitive than MR thermometry (water signal changes by 10 parts per billion per

^{o}C) (Rieke and Butts Pauly, 2008). Similar to the mode switching strategy of real-time MPI-magnetic hyperthermia, one can envision seamless fast switching from heating mode to temperature measurement mode. Because heating is expected to be slow, a temporal resolution of seconds to minutes should be acceptable. Furthermore, because only the temperature of the treatment region is of interest, time-consuming coverage of the entire field-of-view is not needed.

SAR and Magnetostimulation Safety Considerations

Time-varying magnetic fields can have two possible effects on the human body - (1) stimulation of nerves through induced electric fields, which often manifest as peripheral nerve stimulation, and (2) tissue heating via induced eddy currents in the body, which is measured by the specific absorption rate (SAR) metric. Because MPI and magnetic hyperthermia uses strong time-varying magnetic fields, the corresponding safety limits for these two effects are relevant.

From prior work, we note that below 42 kHz, safety is dominated by magnetostimulation limits while above 42 kHz, (induced eddy-current) SAR limits dominate (Saritas et al., 2013b). Thus, the MPI imaging scan at 20 kHz has to address magnetostimulation. We note that while the 20 mT used in this work is safe for rodents, it is about 2-fold higher than the 8 mT limit for humans at 20 kHz (Saritas et al., 2013b). To address this, MPI should use lower amplitudes of < 8 mT for clinical scans and this has been shown to be feasible and actually improve MPI performance especially in terms of spatial resolution (Croft et al., 2016).

Next, the magnetic hyperthermia heating scan has to address SAR limits. While the 354 kHz and 13 mT used in this study is higher than the ~ 2 mT reported at 354 kHz, it must be noted that the reported values use a conservative SAR limit of 4 W/kg and a large torso radius of 20 cm. FDA SAR limits for localized heating of the torso is 10 W/kg (Zaremba, 2001). Using 10W/kg and a 15 cm (average size) torso radius, and because SAR is proportional to $r^2 f^2 B_{pp}^2$, the limit is calculated to be 4.3 mT and is lower than the 13 mT used in this study.

One possible strategy to address SAR limits, depending on the particle, is to use a lower frequency but higher amplitude. In essence, one could

further optimize and tailor the heating waveform to the nanoparticle characteristics. From the Rosensweig equation (Rosensweig, 2002a),

$$P = \pi \mu_0 \chi_0 H^2 f \frac{2\pi f \tau}{1 + (2\pi f \tau)^2} \tag{7.2}$$

where τ is the relaxation time for reorientation of magnetic moments in SPION, we can see that while the heating power is strictly related to the square of the applied field amplitude H, increasing frequency f will always have less than an f^2 effect, with diminishing returns with larger τ. On the other hand, tissue SAR is proportional to $r^2 f^2 B_{pp}^2$ (Brown et al., 2014), therefore trading off frequency for amplitude does not change the SAR limit while heating gains may be observed from the Rosensweig equation if the frequency is too high for τ.

Another strategy is designing particles that heat more efficiently. This could help achieve the same *in vivo* heating and therapy reported in this work while lowering the required field amplitude to a safer level. For example, a very high nanoparticle SAR of 1019 W/g was reported for Zn-doped cubic SPIONs (Bauer et al., 2016b). Using the Rosensweig equation (eqn. 7.2), we can back-calculate the field amplitude required to generate the same heating achieved in our results. This calculated value is much lower at 5.2 mT and very close to the safe limit of 4.3 mT.

Lastly, because heating is most severe at the surface of the body due to the r^2 dependence (skin burns are most common), one possible way to mitigate risk from the 13 mT field is to cover the patient with a cooling surface to remove heat. This can be implemented via a cooling bag or cooling air. Because the heating is done remotely via magnetic fields, there are no electrode-tissue interface considerations.

Path to Clinical Implementation

With high contrast and high sensitivity imaging, external control over the localization of therapy and the ability to work at any depth, MPI-magnetic hyperthermia can be a powerful image-guided therapy method for clinical cancer treatment. Preclinical MPI scanners are already commercially available and the barriers to clinical implementation are few and addressable. The main challenge is maintaining high magnetic gradient strengths for large human-sized bores. We note that such gradients are already possible with current technology. For example, the gradient just outside a human 3.5 T MRI bore is approximately 7 T/m. The cost would thus be comparable to

a clinical MRI scanner. If lower heating spatial precision is acceptable, lower gradients of 1 T/m could be used, removing the need for superconducting magnets and dramatically reducing the MPI scanner cost. This would make the MPI-magnetic hyperthermia procedure much more affordable.

Another key challenge is keeping within the clinical SPION dose limits while achieving sufficient concentration for heating. It was reported that 5mg/ml was a moderate concentration for clinical magnetic hyperthermia (Jordan et al., 2009), and another clinical magnetic hyperthermia pilot study, a prostate tissue SPION concentration of up to 30 mg/ml was reached during therapy (Johannsen et al., 2005). Although concentrations of up to 75 mg/ml was injected in this study, quantitative imaging with MPI reveals that the *in vivo* concentration achieved is closer to ~ 30 mg/ml and is within the clinically relevant range. The net amount of iron injected into the tumor is 1.25 mg. Clinically, it is estimated that 0.25 – 1.0% of the total injected dose of nanoparticles reach the tumor (Wilhelm et al., 2016). Clinical doses of 510 mg Ferumoxytol was reported in prior work (Lu et al., 2010). This shows that even with limited delivery efficiency to the tumor, 1.25 – 5 mg of NPs out of the 510 mg injected is expected to reach the tumor, therefore suggesting that 1.25 mg per tumor is clinically achievable. More importantly, these numbers underscore the importance of MPI spatial localization of magnetic hyperthermia in avoiding thermal damage to healthy tissues that received the remaining 99% of the injected dose.

With this clinically relevant dose, we demonstrate in this work that robust and spatially localized temperature rise *in vivo* to $> 43^{o}$C was achieved within 7 minutes, and in the presence of active blood perfusion, suggesting that MPI-magnetic hyperthermia is viable in humans. Lower doses can be used if the heating efficiency of the SPION is further improved and the heating excitation further optimized. Much lower dosage and concentrations could be used in MPI-magnetic hyperthermia applications where only mild hyperthermia therapy is desired (as an adjuvant or sensitization procedure for chemotherapy) or in applications where no macroscopic temperature change is required (e.g. drug delivery applications).

7.8 Conclusions

Here we have described the theoretical foundation, physical construction, and testing of an MPI-magnetic hyperthermia theranostic platform. We showed experimental data using MPI gradients to deliver targeted heating on demand to components of a phantom with an ability to selectively heat

targets separated by as little as 7 mm with negligible heating of off-target sites. We have also showed the first *in vivo* experimental data using MPI image-guided localization of heat therapy in a rodent model with the use of MPI gradients for localization. We also showed the ability to sequentially target different locations *in vivo*, demonstrating arbitrary control of the heating spot. We demonstrated very good correlation of the MPI image intensity with the SAR deposited, proving that thermal dose planning can be easily performed via an MPI pre-scan. Through a luciferase assay and histological assessment, we verified that heat damage was indeed localized to the target tumor, while the off-target tumor or off-target healthy clearance organs, such as the liver, were spared. Together, these data represent an important step towards the development of a MPI-magnetic hyperthermia theranostics platform. An important next step is to develop MPI thermometry for *in vivo* implementation in order to provide a temperature feedback mechanism for complete thermal dose control. Because achieving macroscopic heating with low amplitudes remains a challenge, another important direction is to explore MPI-magnetic hyperthermia for applications in targeted drug release by using the MPI gradient localization strategy to localize actuation of the drug-containing nanocarriers. Exploring novel therapeutic approaches that do not require macroscopic temperature changes, such as activation of lysosomal pathways (Domenech et al., 2013; Creixell et al., 2011) and thermal drug delivery, are also of great interest.

7.9 Acknowledgment

I would like to thank the Rinaldi Lab from University of Florida for their close collaboration on this project. In particular, Andreina Chiu-Lam who synthesized the nanoparticles, Rohan Dhavalikar who did the hyperthermia hysteresis loop modeling and Professor Carlos Rinaldi for his extremely helpful advice and feedback on this collaborative work between UC Berkeley BISL and UF. I would also like to give special thanks to Prashant Chandrasekharan, who worked closely with me for all the animal procedures. It was a massive study and Prashant offered a lot of help and shared his many years of experience with rodent xenograft studies to help make this study possible.

Chapter 8

In Vivo Tracking and Quantification of Inhaled Aerosol using Magnetic Particle Imaging towards Inhaled Therapeutic Monitoring

8.1 Attribution

Reproduced with permission from Theranostics, in review as of April 26th 2018. Reference: Tay ZW, Chandrasekharan P, Zhou X, Yu E, Zheng B, Conolly, S. "In Vivo Tracking and Quantication of Inhaled Aerosol using Magnetic Particle Imaging towards Inhaled Therapeutics Monitoring" Theranostics 2018.

8.2 Introduction

In this chapter, we further investigate another key application for MPI - lung imaging. However, we approach this application via inhalation as the route of administration of the tracer, as opposed to previous methods in the lab to inject the nanoparticles intravenously. In this work, we show proof-of-concept that MPI can perform similar functions to that of clinical radioaerosol studies. Notably, MPI has the potential for drug tracking of inhaled therapeutics. With further improvements in resolution and sensitivity, we believe MPI can be competitive with nuclear medicine for aerosol-based imaging.

8.3 Background

Pulmonary delivery of drugs is attractive due to benefits such as rapid absorption by the massive surface area of the alveolar region, the abundant vasculature, thin air-blood barrier, and the avoidance of first pass metabolism (Ibrahim, Verma, and Garcia-Contreras, 2015). While methods for efficient drug-loaded aerosol delivery to the lung have been studied extensively, it is challenging to monitor and quantify the delivered aerosol with existing imaging modalities. Anatomical imaging techniques such as X-ray, Computed Tomography (CT) typically have low sensitivity contrast agents. While recent work on developing CT contrast agents have been promising (Kim, Jeong, and Jon, 2010; Hyafil et al., 2007), one key challenge is the high tissue background signal and thus in contrast to *in vitro* studies, *in vivo* implementation requires a high concentration or a large enough mass of contrast agent to achieve a detectable change in X-ray attenuation over the attenuation from the tissue background. Other anatomical imaging techniques such as Magnetic Resonance Imaging (MRI) and Ultrasound (US) have better sensitivity contrast agents. MRI has reported sensitivity between 0.01 – 1 mM and US has $\sim$ 1 pM sensitivity when microbubbles are used (James and Gambhir, 2012). However, both of these modalities have difficulty imaging structures containing air, such as the lung, due to air-tissue interface susceptibility changes and poor transmission of ultrasound through air respectively.

As a result, tracer imaging modalities have been the method-of-choice for imaging aerosols in the lung. A tracer modality does not receive any signal from the anatomy and thus only images the tracer agent. This enables higher sensitivity and excellent contrast. Currently, nuclear medicine imaging techniques such as Positron Emission Tomography (PET) and Gamma Scintigraphy are the gold standard for *in vivo* aerosol imaging (Dolovich and Labiris, 2004) and have reported sensitivities in the picomolar region (James and Gambhir, 2012). Nuclear medicine techniques to image inhaled aerosol have been used for a multitude of clinical applications. One such clinical test is known as pulmonary radioaerosol mucociliary clearance (PRMC) test. Here, radioaerosol (nebulized ^{99m}Tc-albumin colloid) is inhaled and the time for the lung mucociliary clearance of this aerosol measured. This PRMC metric has been found to have high sensitivity and specificity for the disease Primary Ciliary Dyskinesia (Munkholm, Nielsen, and Mortensen, 2015; Marthin et al., 2007). Gamma scintigraphy has also been used for comparative evaluation of different aerosol formulations of asthma

medication (Dolovich and Labiris, 2004). It has also been used to evaluate the lung deposition and mucociliary clearance of inhaled therapeutic nanocarriers (Weers et al., 2009). PET radioaerosol has been used to evaluate lung inflammation in diseases such as sarcoidosis, cystic fibrosis (Labiris et al., 2003), and chronic obstructive pulmonary disease (COPD) (Dolovich and Labiris, 2004).

However, there are a few limitations to nuclear medicine imaging of aerosols. One, these techniques inherently depend on the patient inhaling a radioactive tracer that poses an ionizing radiation risk, especially to the lungs which is one of the most radiosensitive organs in the body (Nikolic et al., 2010; Travis, 1987). In addition, the intrinsic nuclear degradation of the radioactive tracer, i.e. half-life of 6 hours for ^{99m}Tc, limits the length of mucociliary clearance studies. Bulk of the nuclear medicine studies conducted use 18FDG (2 h half-life) or 99mTc (6 h half-life). While longer half-life tracers such as indium-111 (2.8 day half-life) are available, this incurs a larger net radiation dose to the patient or weaker SNR. Moreover, the preparation of radiopharmaceuticals is time-consuming, expensive and requires, typically in-house, hot chemistry facilities.

To address these challenges, we propose to use a new imaging modality known as Magnetic Particle Imaging (MPI). First invented in 2005 by Gleich and Weizenecker (Gleich and Weizenecker, 2005), magnetic particle imaging (MPI) is an emerging medical imaging modality that produces a sensitive tracer image with zero ionizing radiation, robust imaging across air-tissue interfaces (Zheng et al., 2015; Zheng et al., 2016; Zhou et al., 2017; Murase et al., 2015), and safe superparamagnetic iron oxide nanoparticles (SPION) tracers (Goodwill et al., 2012d). MPI images the magnetic nanoparticle's electronic magnetization, which is 22 million times stronger than the nuclear magnetization imaged in MRI. To obtain a signal, MPI excites these SPIONs with an alternating magnetic field and measures the magnetization response (Knopp et al., 2011; Franke et al., 2016; Vogel et al., 2015a; Saritas et al., 2013b). To select which SPIONs to image, MPI uses strong background magnetic gradient fields to magnetically saturate all the SPIONs in the 3D field-of-view, leaving only a narrow field-free-region (FFR) where the SPIONs selected experiences near zero applied field and are thus magnetically unsaturated and able to be excited by the alternating magnetic field. To form a 3D image, the sensitive field-free-region is rastered over the 3D field-of-view, interrogating each point in spatial individually for presence of SPIONs. One possible trajectory of the FFP is shown in Fig. 8.1),but many other trajectories such as the Lissajous trajectory have been used (Werner,

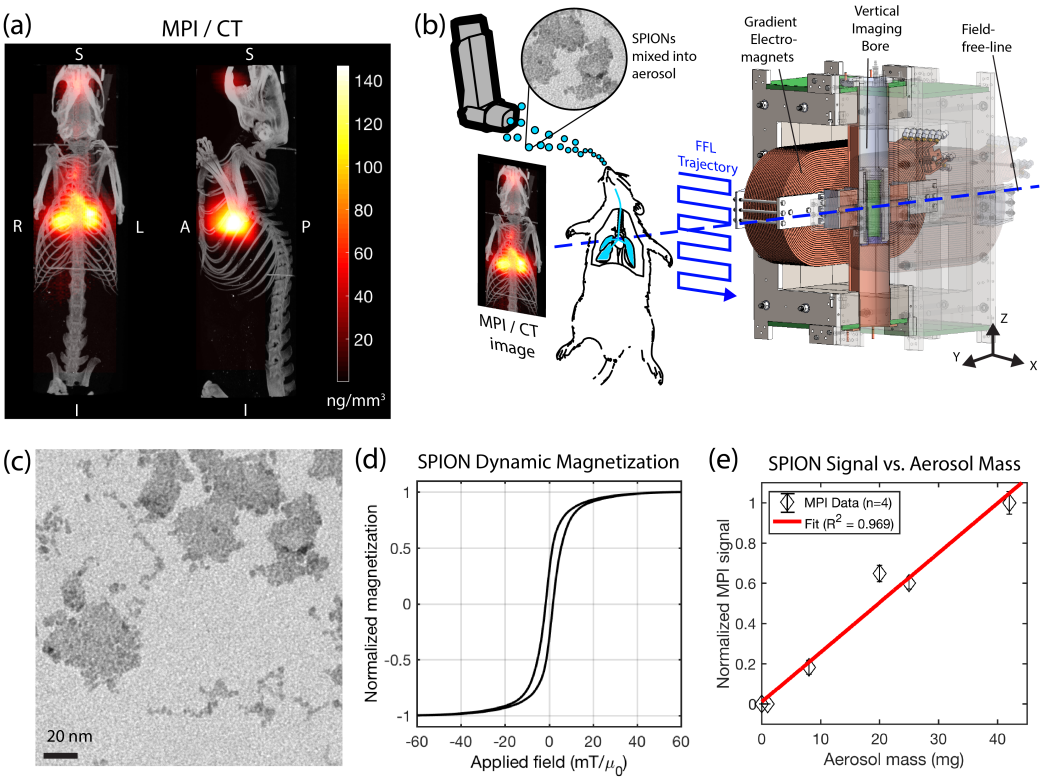

FIGURE 8.1: Magnetic Particle Imaging (MPI) applied to *in vivo* tracking of inhaled aerosol. (a) MPI / CT imaging visualizes the *in vivo* distribution of the inhaled aerosol in the lung airspace (maximum intensity projection). (b) The MPI scanner uses electromagnets to generate a field-free-line (FFL) magnetic field gradient with an effective trajectory as shown. This generates one MPI projection image and multiple projections can be used to reconstruct a 3D image. (c) TEM of the multi-core clustered superparamagnetic iron oxide nanoparticles used. (d) Dynamic magnetization curves of the SPION measured at an AC excitation field of 20.225 kHz and 40 mTpp to match the MPI drive field. (e) MPI is linearly quantitative for aerosol mass. MPI's high contrast, high sensitivity and quantitative nature enables it as a radiation-free alternative to radioaerosol scintigraphy and PET for *in vivo* quantification of therapeutic aerosol dose, visualization of biodistribution, assessment of delivery efficiency and finally timecourse evaluation of clearance rates.

Gdaniec, and Knopp, 2017; Rahmer et al., 2015). Image reconstruction occurs by solving the inverse problem with a calibrated system function (Rahmer et al., 2009) (System Matrix Method) or by gridding the MPI signal to the instantaneous location of the FFR (Goodwill and Conolly, 2010) (X-space method). The Philips-Bruker 3D Fast MPI demonstrator scanner and the Berkeley x-space scanners for the respective reconstruction methods are

described in prior work (Rahmer et al., 2015; Goodwill et al., 2012b; Goodwill et al., 2012c).

Magnetic Particle Imaging has numerous advantages that renders it suitable for *in vivo* imaging of inhaled aerosols. First, MPI is a tracer imaging modality that has high sensitivity and contrast (Them et al., 2016a; Them et al., 2016b). Recent work has reported $\sim$ 100 picogram per 1 mm^3 voxel sensitivity (Graeser et al., 2017) and high temporal resolutions of 46 fps (Ludewig et al., 2017). Second, the SPIONs in MPI do not produce ionizing radiation, are safe and have been used in clinical applications (Goodwill et al., 2012d; Lu et al., 2010). Third, because the SPIONs are magnetic nanoparticles that do not radioactively degrade over time like radiotracers, this enables months-long longitudinal imaging studies (**zheng˙2015**). This is valuable for long mucociliary clearance studies similar to those performed by the Pulmonary Radioaerosol Mucociliary Clearance (PRMC) test. In addition, the SPION formulations are stable and have long shelf-lives without the need for hot chemistry to make a fresh radiopharmaceutical for each new clinical scan or study. Lastly, MPI is fully quantitative and has zero depth attenuation, thus being able to quantify the inhaled aerosol at any depth and with no view limitations. Although the SPION magnetization response to an applied field is non-linear due to saturation, the MPI signal from the inductive receive coils is linearly proportional to the amount of iron present at the FFP. Due to these characteristics, Magnetic Particle Imaging has also been studied preclinically in many other applications such as real-time MPI image-guidance of catheters (Salamon et al., 2016; Rahmer et al., 2017), stroke diagnosis (Ludewig et al., 2017), angiography (Haegele et al., 2012), lung perfusion (Zhou et al., 2017),lung ventilation (Nishimoto et al., 2015; Banura and Murase, 2017), cancer imaging (Yu et al., 2017a), stem cell tracking (Zheng et al., 2015; Zheng et al., 2016; Fidler et al., 2015), brain perfusion imaging (Orendorff et al., 2017), magnetic hyperthermia (Hensley et al., 2016; Murase et al., 2015; Banura et al., 2016) and gut bleed detection (Yu et al., 2017a).

In this preclinical study, we demonstrate that MPI can track and quantify inhaled aerosol with high sensitivity and contrast and demonstrate its potential as a non-radioactive alternative to the nuclear medicine for applications such as the evaluating mucociliary clearance and delivery efficiency of the inhaled aerosol for future applications in inhaled therapeutic monitoring.

8.4 Methods

8.4.1 Hardware

The MPI hardware used in this study was a field-free-line 3D scanner that is detailed in prior work (Yu et al., 2017a). The drive field used was a sinusoid at 20.225 kHz and 40 mTpp. The field free line is generated by a pair of racetrack-shaped electromagnets (gradient of 6.3 x 6.3 T/m) and shifted via the same electromagnets in the trajectory described in Fig. 8.1. X-space MPI reconstruction (Yu et al., 2017a) was used for all images.

8.4.2 Nanoparticles

Superparamagnetic iron oxide nanoparticles (Perimag ™, micromod Partikeltechnologie GmbH, Rostock, Germany) was added to the aerosol mix in order to track the aerosol *in vivo* with Magnetic Particle Imaging. These multi-core nanoparticles were prepared by precipitation of iron oxide in the presence of dextran, resulting in 50% (w/w) iron oxide in a matrix of dextran (40.000 Da molecular weight). The hydrodynamic diameter is approximately 130 nm. Bright field TEM (JOEL 1200 EX) at 120 keV was performed and results shown in Fig. 8.1. Individual cores within each multi-core cluster have sizes between 4.5 – 6.5 nm. The dynamic magnetization properties at MPI scanning parameters (20.225 kHz and 40 mTpp), which are more relevant to MPI performance than static magnetization, were measured by a custom-built magnetic particle spectrometer MPS (Tay et al., 2016).

8.4.3 Ventilation Experimental Setup

To evaluate *in vivo* MPI tracking of inhaled aerosols, we constructed a controlled ventilation setup as shown in Fig. 8.2. In short, the nebulizer was connected in line between the y-junction and the output of the rodent ventilator device to inject the aerosol into the ventilation airstream to be inhaled by the rodent. SPIONs were mixed into 1x PBS or the drug formulation to a final concentration of 5 mg/ml. Due to the low concentration, the aerodynamic properties of the aerosol droplets should be negligibly affected by addition of SPIONs ($< 0.5\%$ weight change). Aerosol was generated by a vibrating mesh nebulizer (Aeroneb™Lab Nebulizer Unit, Small VMD, Kent Scientific Corporation, Connecticut, USA) and a ventilator with tunable stroke volume and rate was used (Model 683 Small Animal Ventilator, Harvard Apparatus, Holliston, MA, USA). Small doses between 0.05 - 0.5

mg/kg were used. For reference, doses of 40 mg/kg was reported in prior small animal imaging studies (Nishimoto et al., 2015) and 0.5–7.3 mg / kg in human imaging studies (Wang, 2011). Fischer 344 rats (Charles River Laboratories) weighing between 200–300 g were used for this study. Aerosol was introduced either by placement of the output tube in the mouth cavity (with depression of the tongue), or by endotracheal intubation with controlled ventilation (stroke volume and stroke rate controlled by the small animal ventilator). MPI scans were acquired by the FFL MPI scanner described above and co-registered to anatomic reference images. Anatomic references were obtained either by a projection x-ray immediately after MPI (Kubtec Xpert 40 ™cabinet x-ray unit), or a post-mortem CT scan (RS9-80 Micro CT scanner (GE), 30 min acquisition time and 93 micron isotropic resolution).

8.4.4 Animal Experimental Groups

Three groups of rats were used. In Group A (n = 3), approximately 0.3 mg/kg of SPIONs were delivered into the rodents via aerosol inhalation and MPI scans were acquired at multiple time points up to 13 days after to evaluate clearance from the lung. In Group B (n = 3), approximately 0.5 mg/kg of SPIONs was delivered by endotracheal intubation. Variation of the aerosol droplet size and ventilation rate was performed to affect delivery efficiency into the lung. In Group C (n = 3), approximately 0.3 mg/kg and 0.1 mg/kg of Doxorubicin Hydrochloride or Indocyanine Green dye (as a model therapeutic) was mixed and delivered as aerosol. The rodents were imaged with MPI and fluorescence, and imaging was repeated *ex vivo* on the lungs to evaluate MPI's ability to track deposition of inhaled therapeutics in the lung. Fluorescence imaging was performed on the IVIS Lumina ™. These animal procedures were conducted in accordance to the National Research Council Guide for the Care and Use of Laboratory Animals and approved by the UC Berkeley Animal Care and Use Committee.

8.5 Results

8.5.1 Evaluation of delivery efficiency

One of the key applications of radioaerosols is the *in vivo* evaluation of aerosol delivery efficiency (Dolovich and Labiris, 2004). Here, we show that

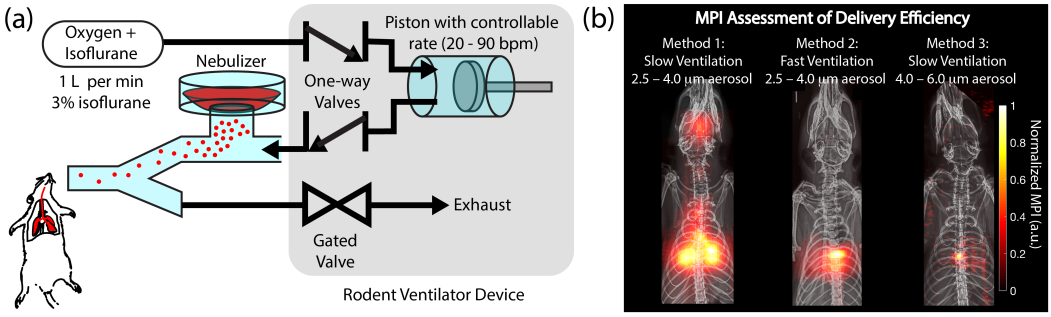

FIGURE 8.2: Magnetic Particle Imaging (MPI) is able to assess the delivery efficiency of different methods. (a) Experimental setup showing how the aerosol is delivered by controlled ventilation to the rodent. (b) MPI assessment of the delivery efficiency of three different methods. Method 1 uses a slow controlled ventilation rate. This enables the aerosol to be more evenly distributed in the lung. Method 2 uses a fast controlled ventilation rate, resulting in more inertial impactation of the aerosol in the central conducting airways as opposed to the finer airways in the lung periphery. Method 3 increases the size of the aerosol droplets and therefore significantly increases the probability of inertial impactation in the central airways, resulting in poor delivery to lung periphery.

MPI is similarly able to visualize the efficiency of different delivery methods for Group B rats (Fig. 8.2). The field of view (FOV) was 3.2 cm $\times$ 4 cm $\times$ 10 cm with acquisition time of 75 s. It is well known from prior literature that drug-aerosol deposition depends on many factors. Inhalation flow rate, the patient's breathing pattern, particle size, and airway geometry have been shown to be most dominant (Ibrahim, Verma, and Garcia-Contreras, 2015; Longest, Azimi, and Hindle, 2014). However, particle shape, density, thermodynamic state, and surface characteristics including roughness and charge may be influential as well (Kleinstreuer and Zhang, 2011). Here, we show that MPI can visualize the differences in efficiency resulting from two of the most dominant factors – inhalation flow rate and particle size. From prior literature, rapid inhalation increases the chance of impaction in the oropharynx and large conducting airways, while slow, steady inhalation increases the chance of penetration to the lung periphery. (Newman, 1985). Fig. 8.2(b) shows that MPI can visualize this effect. With fast ventilation rate as controlled by the ventilator piston stroke rate (stroke volume and rest of ventilation setup is kept the same), we observe a much larger fraction of aerosol deposited in the central, large conducting airways and lesser aerosol in the peripheral parts of the lung. For particle size, prior literature states the optimum is between 3 and 5 microns (Cheng, 2014). In Fig. 8.2(b), this effect is visualized with MPI. This was investigated by only changing the nebulizer mesh size (Aeroneb Small VMD 2.5 – 4.0 micron to Aeroneb

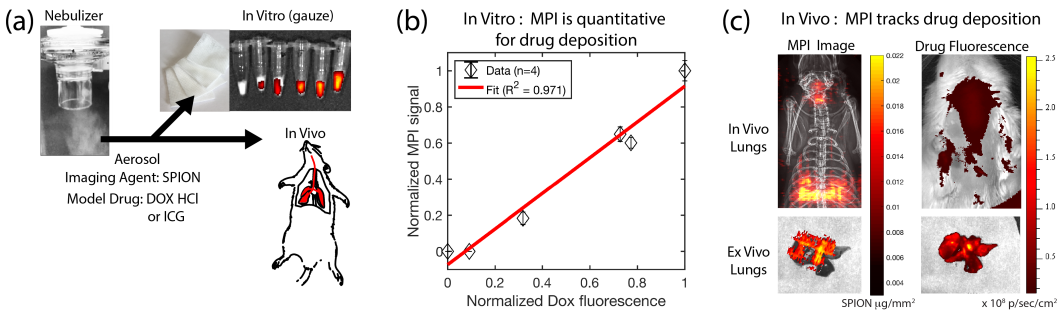

FIGURE 8.3: Magnetic Particle Imaging (MPI) is able to quantify the delivery of aerosolized therapeutics. (a) Experimental setup. The MPI imaging agent (SPIONs) is mixed with the model drug, doxorubicin hydrochloride, then aerosolized. The aerosol is inhaled by the animal or deposited on surgical gauze for the *in vitro* experiment. (b) Fluorescence measurements of deposited doxorubicin hydrochloride for the *in vitro* experiment shows good correlation with the MPI signal, confirming that the MPI image can quantify drug deposition. (c) The MPI image clearly visualizes the drug deposition *in vivo* while fluorescence imaging of the drug is difficult at depth. *Ex vivo* imaging of the lungs confirm that the MPI image and the fluorescence image match, showing that MPI images the drug distribution in the lungs and provides clearer visualization *in vivo* and at-depth.

Standard VMD 4.0 – 6.0 micron) while keeping the nebulizer type/brand and ventilation setup the same. The results show a large change in the deposition distribution where there is focal deposition in the central airways and negligible aerosol reaching the outer lung. While a limited subset of all the parameters affecting drug-aerosol deposition, these examples are a proof-of-concept demonstrating the potential of MPI as a radiation-free alternative to nuclear medicine for *in vivo* evaluation of aerosol delivery efficiency.

8.5.2 Tracking and quantification of inhaled therapeutics

Next, in order to evaluate MPI as a *in vivo* tracking agent for inhaled therapeutics, we utilize aerosols containing a mixture of both a model drug (Doxorubicin Hydrochloride or Indocyanine Green) and our SPION imaging agent. Fig. 8.3 shows the experimental setup, where the mixed aerosol is tested both *in vitro* and *in vivo*. The *in vitro* results where the aerosol is produced and deposited onto surgical gauze show that the MPI imaging signal is well-correlated with the amount of deposited DOX as measured from the fluorescence signal ($R^2 = 0.971$). Next, we evaluate *in vivo* tracking by inhalation of this mixed aerosol in Group C rats. The field of view (FOV) was 3.2 cm $\times$ 4 cm $\times$ 6 cm with acquisition time of 45 s. The MPI image

clearly visualizes the *in vivo* distribution of the aerosol while it is difficult to track the distribution with fluorescence imaging due to tissue attenuation and scatter. To address this, *ex vivo* imaging was also performed on the excised lungs. In this case, relatively good correlation of the MPI image and the fluorescence image is observed. Slight discrepancies in position may be attributed to slight shifting of the lung lobes during transfer between the scanners. The high contrast and quantitative nature of MPI shows that it has the potential to quantify *in vivo* therapeutic deposition in the lung towards assessment and monitoring of inhalation therapies.

8.5.3 Timecourse MPI to monitor clearance rates from the lung

Lastly, one key application of radioaerosols is the evaluation of lung mucociliary clearance. The PRMC metric obtained from 99mTc radioaerosol studies have been found to have high sensitivity and specificity for Primary Ciliary Dyskinesia (Munkholm, Nielsen, and Mortensen, 2015; Marthin et al., 2007). MPI is a good fit for imaging clearance over long periods of time because unlike radioaerosols, the SPION imaging agent does not radioactively decay with time. This advantage has been demonstrated in prior work for the tracking of stem cells over 90 days (Zheng et al., 2015). To evaluate MPI as a tool for measuring mucociliary clearance of delivered aerosols, we allow rats in Group A to inhale SPION aerosols and perform MPI imaging periodically over the course of 13 days. Prior literature establishes that the dominant clearance of particles larger than 17 nm median diameter occurs through the mucociliary pathway up the trachea, and down the gastrointestinal tract to finally be excreted as feces from the body (Semmler et al., 2004; Nishimoto et al., 2015). Fig. 8.4 shows the MPI timecourse study where the mucociliary clearance of the Perimag™ SPIONs (130 nm hydrodynamic size) from the lung into the gastrointestinal tract is clearly visualized. At the 2 hour time point, SPION boli are observed just above the lung. At the 14 hour time point, SPIONs are observed in the lower gastrointestinal tract. Over the course of 13 days, the MPI signal in the lungs gradually decreases as the SPIONs are cleared from the lungs. Fig. 8.5(a) verifies that clearance, rather than decay of the SPION signal, is occurring because the loss in MPI signal from the lungs is accounted for by the presence of MPI signal in the GI tract and feces. The high contrast and sensitivity of MPI enables clear visualization of the mucociliary clearance pathway and the different organs and tissues involved.

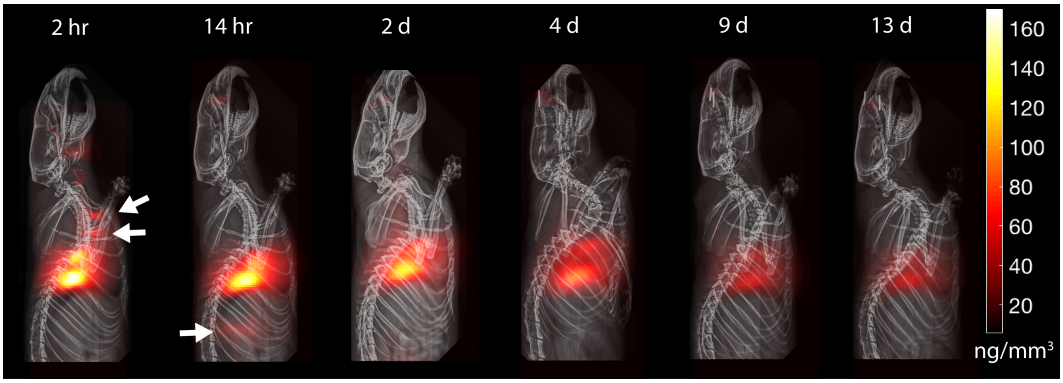

FIGURE 8.4: MPI is able to track with high contrast and sensitivity the clearance of delivered aerosol. The clearance pathway is clearly visualized by visible boli in the trachea and in the gastrointestinal tract. Because SPIONs do not radioactively decay over time, MPI is suitable for longitudinal imaging of aerosol clearance. The visible attenuation of the signal is due to mucociliary clearance from the lung, as the lost signal is accounted for by MPI signal in excreta. MPI thus has the potential to be a radiation-free alternative to current pulmonary radioaerosol mucociliary clearance clinical tests.

Because MPI is fully quantitative with zero depth attenuation, in addition to non-invasive tracking of the biodistribution through time, we are also able to model the SPION dynamics in a two compartment model. The first compartment is the lung while the gastrointestinal tract and the fecal excrement were combined into the second compartment. Fig. 8.5(a) shows the biodistribution and compartmental fitting for Group A rats. First, the MPI signal was first calibrated to to a known concentration of SPION in a similar calibration curve to that in Fig. 8.1(e). Next, regions of interest (ROI) were identified for each compartment and the measured MPI concentration is subsequently averaged. The results are finally reported as net iron in each compartment (Fig. 8.5(a)) and fitted to the exponential model described in prior work (Nishimoto et al., 2015). The equation used was

$$\mathrm{Fe} = \mathrm{Fe}_{\mathrm{total}} \cdot ((1 - k_1) \cdot e^{-k_2 t} + k_1). \tag{8.1}$$

$k_1 = 0.249$ and $k_2 = 0.261$ was obtained with the fitting ($R^2 = 0.955$). The results estimate the clearance half-life (without the offset term) as approximately 2.6 days.

To confirm presence of SPIONs in the lung and feces, *ex vivo* MPI scans of all the organs was performed. The results at 13 day in Fig. 8.5(b) show that SPIONs were only the lungs and the feces. Negligible signal was observed in the stomach and intestine because the SPIONs are spread out over a large

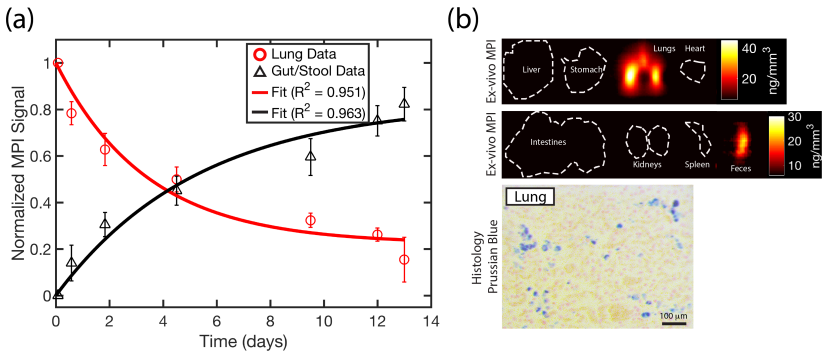

FIGURE 8.5: MPI quantification of the SPION biodistribution over time. (a) Change in biodistribution of SPIONs and two-compartment model fitting shows SPIONs are cleared from the lung and through the GI tract into excreta. The quantitative nature and high sensitivity of MPI shown here makes it a promising radiation-free alternative to radioaerosol procedures. (b) *Ex vivo* MPI validation shows SPIONs in only the lungs and excreta. Prussian Blue stains of lung histological sections verify that SPIONs were successfully delivered to the lung.

volume and slowly transferred over a long duration of digestion and therefore the effective SPION concentration is very low especially at the 13th day point when the transfer of SPIONs from the lung is much lower than the initial clearance rate. Prussian blue staining of lung sections show presence of SPIONs in the lung tissue, confirming delivery of SPION aerosol into the lung. Finally, a zoom-in MPI image of the upper respiratory tract with finer time-points show clear visualization of the mucociliary clearance (Fig. 8.5(c)).

8.6 Discussion

This study is the first proof-of-concept of MPI for evaluating delivery efficiency of aerosols as well as tracking of inhaled therapeutics. Another study has shown MPI imaging of microsprayed SPIONs endotracheally but was limited to single slice axial views and did not investigate the entire mucociliary clearance pathway (Nishimoto et al., 2015). In our study, we demonstrated that MPI can visualize the clearance pathway by detecting SPION boli in the airways, gastrointestinal tract as well as in the fecal excrement, and was able to perform two-compartment modeling of this clearance pathway and the associated kinetics.

While MPI is presented as a potential alternative to radioaerosol techniques for clinical use, several limitations exist and continued development

is required before MPI imaging of SPIONs can be fully realized for clinical use in the lung. One limitation is that MPI is less sensitive (nanomolar sensitivity) than nuclear medicine (picomolar sensitivity). This can partially be addressed by using larger doses of SPIONs and the dose-limited sensitivity of MPI will come close to that of nuclear medicine because the limiting dose of SPIONs is in the millimolar range while nuclear medicine cannot use more than micromolar concentrations of radioisotopes. Furthermore, MPI is still a relatively new technology and has not yet reached the hardware limit of sensitivity yet (Graeser et al., 2017). Another limitation is that SPIONs are about 10 – 100 nm in size and are larger than radioisotopes. However, for purposes of radioaerosol tracking, most studies use 99mTc-albumin colloid currently.

Furthermore, because SPIONs can be targeted by magnetic fields, the therapeutic aerosol can be additionally steered or moved to a target region of the lung, increasing therapeutic efficiency (Banura and Murase, 2017; Kuboyabu et al., 2016). It is evident that many cancer targeting strategies for magnetic nanoparticles are already widely investigated. MPI, with its superb sensitivity and contrast, is uniquely poised as an excellent theranostics platform, where the same administered SPIONs serve both as an imaging agent for diagnosis as well as a therapeutic agent.

8.7 Conclusions

We have showed in this work proof-of-concept that MPI can perform many of the radioaerosol study functions used in preclinical and clinical practice. While further development is necessary to be fully competitive with clinical nuclear medicine, this work shows the MPI has the potential to be radiation-free and convenient alternative to radioaerosols for therapeutic drug tracking and lung imaging.

8.8 Acknowledgments

I would like to thank Prashant Chandrasekharan for his invaluable help with some of the more difficult animal procedures such as endotracheal intubation. His advice and guidance for many of the animal experiments was critical to making this project work.

Bibliography

Alvarez-Berríos, Merlis P et al. (2013). "Hyperthermic potentiation of cisplatin by magnetic nanoparticle heaters is correlated with an increase in cell membrane fluidity". In: *Int. J. Nanomedicine* 8, pp. 1003–1013.

Alvarez-Berríos, Merlis P et al. (2014). "Magnetic fluid hyperthermia enhances cytotoxicity of bortezomib in sensitive and resistant cancer cell lines". In: *Int. J. Nanomedicine* 9, pp. 145–153.

Alvarez-Berrios, Merlis P et al. (2015). "Enhanced proteotoxic stress: one of the contributors for hyperthermic potentiation of the proteasome inhibitor bortezomib using magnetic nanoparticles". In: *Biomater Sci* 3.2, pp. 391–400.

Arami, Hamed et al. (2013). "Size-dependent ferrohydrodynamic relaxometry of magnetic particle imaging tracers in different environments". In: *Med. Phys.* 40.7, p. 071904.

Banura, Natsuo and Kenya Murase (2017). "Magnetic particle imaging for aerosol-based magnetic targeting". In: *Jpn. J. Appl. Phys.* 56.8, p. 088001.

Banura, Natsuo et al. (2016). "Heat Transfer Simulation for Optimization and Treatment Planning of Magnetic Hyperthermia Using Magnetic Particle Imaging". In: *arXiv*.

Barrera, Carola, Adriana P Herrera, and Carlos Rinaldi (2009). "Colloidal dispersions of monodisperse magnetite nanoparticles modified with poly(ethylene glycol)". In: *J. Colloid Interface Sci.* 329.1, pp. 107–113.

Bauer, L M et al. (2016a). "Eddy current-shielded x-space relaxometer for sensitive magnetic nanoparticle characterization". In: *Rev. Sci. Instrum.* 87.5, p. 055109.

Bauer, Lisa M et al. (2016b). "High-performance iron oxide nanoparticles for magnetic particle imaging–guided hyperthermia (hMPI)". In: *Nanoscale*.

Behrends, André, Matthias Graeser, and Thorsten M Buzug (2015). "Introducing a frequency-tunable magnetic particle spectrometer". In: *Current Directions in Biomedical Engineering* 1.1.

Biederer, S et al. (2009a). "Magnetization response spectroscopy of superparamagnetic nanoparticles for magnetic particle imaging". In: *J. Phys. D Appl. Phys.* 42.20, p. 205007.

Biederer, S et al. (2009b). "Magnetization response spectroscopy of superparamagnetic nanoparticles for magnetic particle imaging". In: *Journal of Physics D: Applied Physics* 42.20, p. 205007.

Brown, Robert W et al. (2014). *Magnetic resonance imaging : physical principles and sequence design*. Second edition.

Buzug, Thorsten M et al. (2012). "Magnetic particle imaging: introduction to imaging and hardware realization". In: *Z. Med. Phys.* 22.4, pp. 323–334.

Chen, D-X (2004). "High-field ac susceptometer using Helmholtz coils as a magnetizer". In: *Meas. Sci. Technol.* 15.6, p. 1195.

Cheng, Yung Sung (2014). "Mechanisms of pharmaceutical aerosol deposition in the respiratory tract". In: *AAPS PharmSciTech* 15.3, pp. 630–640.

Cho, E, G Cho, H Cho, et al. (2014). "Simulational validation of color magnetic particle imaging (cMPI)". In: *Physics in medicine and biology* 59.21, p. 6521.

Creixell, Mar et al. (2011). "EGFR-targeted magnetic nanoparticle heaters kill cancer cells without a perceptible temperature rise". In: *Acs Nano* 5.9, pp. 7124–7129.

Croft, Laura, Patrick Goodwill, and Steven Conolly (2012). "Relaxation in x-space magnetic particle imaging". In: *IEEE Trans. Med. Imaging* 31.12, pp. 2335–2342.

Croft, Laura R et al. (2016). "Low drive field amplitude for improved image resolution in magnetic particle imaging". In: *Med. Phys.* 43.1, p. 424.

Cullity, B D and C D Graham (2011). *Introduction to Magnetic Materials*. John Wiley & Sons.

Day, Emily S, Jennifer G Morton, and Jennifer L West (2009). "Nanoparticles for thermal cancer therapy". In: *J. Biomech. Eng.* 131.7, p. 074001.

Debbeler, C et al. (2015). "Evaluation of a Cotton-Mouton relaxometer for the characterization of superparamagnetic iron oxide nanoparticles". In: *Magnetic Particle Imaging (IWMPI), 2015 5th International Workshop on*. ieeexplore.ieee.org, pp. 1–1.

Deissler, R J and M A Martens (2015). "Dependence of the Magnetization Response on the Driving Field Amplitude for Magnetic Particle Imaging and Spectroscopy". In: *IEEE Trans. Magn.* 51.2, pp. 1–4.

Deissler, Robert J, Yong Wu, and Michael A Martens (2014). "Dependence of Brownian and Néel relaxation times on magnetic field strength". In: *Med. Phys.* 41.1, p. 012301.

Dhavalikar, R et al. (2016). "Finite magnetic relaxation in x-space magnetic particle imaging: comparison of measurements and ferrohydrodynamic models". In: *J. Phys. D Appl. Phys.* 49.30, p. 305002.

Dhavalikar, Rohan and Carlos Rinaldi (2014). "On the effect of finite magnetic relaxation on the magnetic particle imaging performance of magnetic nanoparticles". In: *J. Appl. Phys.* 115.7, p. 074308.

— (2016). "Theoretical predictions for spatially-focused heating of magnetic nanoparticles guided by magnetic particle imaging field gradients". In: *J. Magn. Magn. Mater.* 419, pp. 267–273.

Dieckhoff, Jan et al. (2016). "Magnetic-field dependence of Brownian and Néel relaxation times". In: *J. Appl. Phys.* 119.4, p. 043903.

Dolovich, Myrna and Renee Labiris (2004). "Imaging drug delivery and drug responses in the lung". In: *Proc. Am. Thorac. Soc.* 1.4, pp. 329–337.

Domenech, Maribella et al. (2013). "Lysosomal membrane permeabilization by targeted magnetic nanoparticles in alternating magnetic fields". In: *ACS nano* 7.6, pp. 5091–5101.

Duhan, Vikas et al. (2012). "Protocol for long duration whole body hyperthermia in mice". In: *J. Vis. Exp.* 66, e3801.

Erbe, Marlitt, Timo F Sattel, and Thorsten M Buzug (2012). "Commercialization of a magnetic particle spectrometer". In: *2012 12th IEEE International Conference on Nanotechnology (IEEE-NANO)*. IEEE, pp. 1–4.

Faes, T J et al. (1999). "The electric resistivity of human tissues (100 Hz-10 MHz): a meta-analysis of review studies". In: *Physiol. Meas.* 20.4, R1–10.

Ferguson, R Matthew, Amit P Khandhar, and Kannan M Krishnan (2012). In: *J. Appl. Phys.* 111.7, 7B318–7B3185.

Ferguson, R Matthew, Kevin R Minard, and Kannan M Krishnan (2009). "Optimization of nanoparticle core size for magnetic particle imaging". In: *J. Magn. Magn. Mater.* 321.10, pp. 1548–1551.

Ferguson, R Matthew et al. (2010). "Size-optimized magnetite nanoparticles for magnetic particle imaging". In: *Magnetic Nanoparticles*. World Scientific, pp. 53–59.

Ferguson, R Matthew et al. (2013a). "Size-Dependent Relaxation Properties of Monodisperse Magnetite Nanoparticles Measured Over Seven Decades of Frequency by AC Susceptometry". In: *IEEE Trans. Magn.* 49.7, pp. 3441–3444.

Ferguson, R Matthew et al. (2015a). "Magnetic particle imaging with tailored iron oxide nanoparticle tracers". In: *IEEE Trans. Med. Imaging* 34.5, pp. 1077–1084.

— (2015b). "Magnetic particle imaging with tailored iron oxide nanoparticle tracers". In: *IEEE Trans. Med. Imaging* 34.5, pp. 1077–1084.

Ferguson, Richard Matthew et al. (2013b). "Tailoring the magnetic and pharmacokinetic properties of iron oxide magnetic particle imaging tracers". In: *Biomed. Tech.* 58.6, pp. 493–507.

Fidler, F et al. (2015). "Stem Cell Vitality Assessment Using Magnetic Particle Spectroscopy". In: *IEEE Trans. Magn.* 51.2, pp. 1–4.

Finer, J T, R M Simmons, and J A Spudich (1994). "Single myosin molecule mechanics: piconewton forces and nanometre steps". In: *Nature* 368.6467, pp. 113–119.

Franke, Jochen et al. (2016). "System Characterization of a Highly Integrated Preclinical Hybrid MPI-MRI Scanner". In: *IEEE Trans. Med. Imaging* 35.9, pp. 1993–2004.

García-Palacios, José Luis and Francisco J Lázaro (1998). "Langevin-dynamics study of the dynamical properties of small magnetic particles". In: *Phys. Rev. B Condens. Matter* 58.22, pp. 14937–14958.

Garraud, Nicolas et al. (2017). "Design and validation of magnetic particle spectrometer for characterization of magnetic nanoparticle relaxation dynamics". In: *AIP Adv.* 7.5, p. 056730.

Gaskill, Jack D (1978). "Linear systems, Fourier transforms, and optics". In: *Linear Systems, Fourier Transforms, and Optics by Jack D. Gaskill New York, NY: John Wiley and Sons, 1978* 1.

Gleich, B et al. (2010). "Fast MPI demonstrator with enlarged field of view". In: *Proc. Int. Soc. Magn. Reson. Med. Sci. Meet. Exhib. Int. Soc. Magn. Reson. Med. Sci. Meet. Exhib.* 18, p. 218.

Gleich, Bernhard (2014). *Principles and Applications of Magnetic Particle Imaging*. Aktuelle Forschung Medizintechnik.

Gleich, Bernhard and Jurgen Weizenecker (2005). "Tomographic imaging using the nonlinear response of magnetic particles". In: *Nature* 435, pp. 1214–1217. ISSN: 7046.

Goodwill, P, E Yu, and S Conolly (2015). "Design and construction of a second generation high-resolution MPI field free line scanner". In: *Magnetic Particle Imaging (IWMPI), 2015 5th International Workshop on*. ieeexplore.ieee.org, pp. 1–1.

Goodwill, P et al. (2015). "In Vivo and Ex vivo experimental MPI angiography with high selection field strength and tailored SPIO nanoparticles". In: *Magnetic Particle Imaging (IWMPI), 2015 5th International Workshop on*. ieeexplore.ieee.org, pp. 1–1.

Goodwill, P W et al. (2011a). "Ferrohydrodynamic relaxometry for magnetic particle imaging". In: *Appl. Phys. Lett.* 98.26, p. 262502.

Goodwill, Patrick et al. (2012a). "Third Generation X-Space MPI Mouse and Rat Scanner". In: *Magnetic Particle Imaging*. Ed. by Thorsten M Buzug and Jörn Borgert. Springer Proceedings in Physics. Springer Berlin Heidelberg, pp. 261–265.

Goodwill, Patrick W and Steven M Conolly (2010). "The X-space formulation of the magnetic particle imaging process: 1-D signal, resolution, bandwidth, SNR, SAR, and magnetostimulation". In: *IEEE transactions on medical imaging* 29.11, pp. 1851–1859.

— (2011a). "Experimental demonstration of x-space magnetic particle imaging". In: *SPIE Medical Imaging*. International Society for Optics and Photonics, 79650U–79650U–6.

— (2011b). "Multidimensional x-space magnetic particle imaging". In: *IEEE transactions on medical imaging* 30.9, pp. 1581–1590.

Goodwill, Patrick W et al. (2012b). "An x-space magnetic particle imaging scanner". In: *Rev. Sci. Instrum.* 83.3, p. 033708.

Goodwill, Patrick W et al. (2012c). "Projection x-space magnetic particle imaging". In: *IEEE Trans. Med. Imaging* 31.5, pp. 1076–1085.

Goodwill, Patrick William et al. (2012d). "X-space MPI: magnetic nanoparticles for safe medical imaging". In: *Adv. Mater.* 24.28, pp. 3870–3877.

Goodwill, PW et al. (2011b). "Ferrohydrodynamic relaxometry for magnetic particle imaging". In: *Applied Physics Letters* 98.26, p. 262502.

Graeser, M, K Bente, and T M Buzug (2015). "Dynamic single-domain particle model for magnetite particles with combined crystalline and shape anisotropy". In: *J. Phys. D Appl. Phys.* 48.27, p. 275001.

Graeser, Matthias et al. (2013). "Analog receive signal processing for magnetic particle imaging". In: *Med. Phys.* 40.4, p. 042303.

Graeser, Matthias et al. (2017). "Towards Picogram Detection of Superparamagnetic Iron-Oxide Particles Using a Gradiometric Receive Coil". In: *Sci. Rep.* 7.1, p. 6872.

Haegele, Julian et al. (2012). "Magnetic particle imaging: visualization of instruments for cardiovascular intervention". In: *Radiology* 265.3, pp. 933–938.

Hensley, Daniel et al. (2015). "Preliminary experimental X-space color MPI". In: *Magnetic Particle Imaging (IWMPI), 2015 5th International Workshop on*. IEEE, pp. 1–1.

Hensley, Daniel W et al. (2016). "Combining magnetic particle imaging and magnetic fluid hyperthermia in a theranostic platform". In: *Phys. Med. Biol.*

Hensleya, Daniel et al. (2017). "A theranostic platform for localized magnetic fluid hyperthermia and magnetic particle imaging". In: *Proc. of SPIE Vol*. Vol. 10066, pp. 1006603–1006601.

Houston, William V (1927). "A Compound Interferometer for Fine Structure Work". In: *Phys. Rev.* 29.3, pp. 478–484.

Hsiao, Jong-Kai et al. (2007). "Magnetic nanoparticle labeling of mesenchymal stem cells without transfection agent: cellular behavior and capability of detection with clinical 1.5 T magnetic resonance at the single cell level". In: *Magn. Reson. Med.* 58.4, pp. 717–724.

Hufschmid, Ryan et al. (2015). "Synthesis of phase-pure and monodisperse iron oxide nanoparticles by thermal decomposition". In: *Nanoscale* 7.25, pp. 11142–11154.

Hyafil, Fabien et al. (2007). "Noninvasive detection of macrophages using a nanoparticulate contrast agent for computed tomography". In: *Nat. Med.* 13.5, pp. 636–641.

Ibrahim, Mariam, Rahul Verma, and Lucila Garcia-Contreras (2015). "Inhalation drug delivery devices: technology update". In: *Med. Devices* 8, pp. 131–139.

Ishihara, Yasutoshi et al. (2013). "Evaluation of magnetic nanoparticle samples made from biocompatible ferucarbotran by time-correlation magnetic particle imaging reconstruction method". In: *BMC Med. Imaging* 13, p. 15.

Ito, Akira, Hiroyuki Honda, and Takeshi Kobayashi (2006). "Cancer immunotherapy based on intracellular hyperthermia using magnetite nanoparticles: a novel concept of "heat-controlled necrosis" with heat shock protein expression". In: *Cancer Immunol. Immunother.* 55.3, pp. 320–328.

James, Michelle L and Sanjiv S Gambhir (2012). "A Molecular Imaging Primer: Modalities, Imaging Agents, and Applications". In: *Physiol. Rev.* 92.2, pp. 897–965.

Johannsen, M et al. (2005). "Clinical hyperthermia of prostate cancer using magnetic nanoparticles: presentation of a new interstitial technique". In: *International journal of hyperthermia* 21.7, pp. 637–647.

Jordan, Andreas et al. (1999). "Magnetic fluid hyperthermia (MFH): Cancer treatment with AC magnetic field induced excitation of biocompatible superparamagnetic nanoparticles". In: *Journal of Magnetism and Magnetic Materials* 201.1, pp. 413–419.

Jordan, Andreas et al. (2001). "Presentation of a new magnetic field therapy system for the treatment of human solid tumors with magnetic fluid hyperthermia". In: *J. Magn. Magn. Mater.* 225.1, pp. 118–126.

Jordan, Andreas et al. (2006). "The effect of thermotherapy using magnetic nanoparticles on rat malignant glioma". In: *Journal of neuro-oncology* 78.1, pp. 7–14.

Jordan, Andreas et al. (2009). "Inductive heating of ferrimagnetic particles and magnetic fluids: physical evaluation of their potential for hyperthermia". In: *International Journal of Hyperthermia* 25.7, pp. 499–511.

Khandhar, Amit P et al. (2013). "Monodisperse magnetite nanoparticle tracers for in vivo magnetic particle imaging". In: *Biomaterials* 34.15, pp. 3837–3845.

Kim, Dongkyu, Yong Yeon Jeong, and Sangyong Jon (2010). "A drug-loaded aptamer-gold nanoparticle bioconjugate for combined CT imaging and therapy of prostate cancer". In: *ACS Nano* 4.7, pp. 3689–3696.

King, Michelle A et al. (2015). "Biomarkers of multiorgan injury in a preclinical model of exertional heat stroke". In: *J. Appl. Physiol.* 118.10, pp. 1207–1220.

Kleinstreuer, Clement and Zhe Zhang (2011). "Optimal Drug-Aerosol Delivery to Predetermined Lung Sites". In: *J. Heat Transfer* 133.1, p. 011002.

Knopp, Tobias et al. (2011). "Prediction of the spatial resolution of magnetic particle imaging using the modulation transfer function of the imaging process". In: *IEEE Trans. Med. Imaging* 30.6, pp. 1284–1292.

Konkle, Justin J et al. (2013). "Projection reconstruction magnetic particle imaging". In: *IEEE transactions on medical imaging* 32.2, pp. 338–347.

Körnig, André et al. (2014). "Probing the mechanical properties of magnetosome chains in living magnetotactic bacteria". In: *Nano Lett.* 14.8, pp. 4653–4659.

Kuboyabu, Tomomi et al. (2016). "Usefulness of Magnetic Particle Imaging for Monitoring the Effect of Magnetic Targeting". In: *Open Journal of Medical Imaging* 6.02, p. 33.

Kuhlmann, C et al. (2015). "Drive-Field Frequency Dependent MPI Performance of Single-Core Magnetite Nanoparticle Tracers". In: *IEEE Trans. Magn.* 51.2, pp. 1–4.

Kuhlmann, C et al. (2016). "Signal path for a 10 kHz and 25 kHz mobility MPI system". In: *Magnetic Particle Imaging (IWMPI), 2016 6th International Workshop on*. infinite science publishing, p. 137.

Kut, Carmen et al. (2012). "Preliminary study of injury from heating systemically delivered, nontargeted dextran-superparamagnetic iron oxide nanoparticles in mice". In: *Nanomedicine* 7.11, pp. 1697–1711.

Labiris, N R et al. (2003). "Uptake of 18fluorodeoxyglucose in the cystic fibrosis lung: a measure of lung inflammation?" In: *Eur. Respir. J.* 21.5, pp. 848–854.

Lee, Jason S et al. (2011). "Hyperthermia induced by magnetic nanoparticles improves the effectiveness of the anticancer drug cis-diamminedichloroplatinum". In: *J. Nanosci. Nanotechnol.* 11.5, pp. 4153–4157.

Lele, B S and M G Kulkarni (1998). "Single step room temperature oxidation of poly (ethylene glycol) to poly (oxyethylene)dicarboxylic acid". In: *J. Appl. Polym. Sci.*

Longest, P Worth, Mandana Azimi, and Michael Hindle (2014). "Optimal delivery of aerosols to infants during mechanical ventilation". In: *J. Aerosol Med. Pulm. Drug Deliv.* 27.5, pp. 371–385.

Lu, K et al. (2017). "Multi-channel Acquisition for Isotropic Resolution in Magnetic Particle Imaging". In: *IEEE Trans. Med. Imaging* PP.99, pp. 1–1.

Lu, Kuan et al. (2013). "Linearity and shift invariance for quantitative magnetic particle imaging". In: *IEEE Trans. Med. Imaging* 32.9, pp. 1565–1575.

Lu, Min et al. (2010). "FDA report: ferumoxytol for intravenous iron therapy in adult patients with chronic kidney disease". In: *American journal of hematology* 85.5, pp. 315–319.

Ludewig, Peter et al. (2017). "Magnetic Particle Imaging for Real-Time Perfusion Imaging in Acute Stroke". In: *ACS Nano* 11.10, pp. 10480–10488.

Ludwig, F et al. (2012). "Optimization of Magnetic Nanoparticles for Magnetic Particle Imaging". In: *IEEE Trans. Magn.* 48.11, pp. 3780–3783.

Ludwig, Frank, Thilo Wawrzik, and Meinhard Schilling (2012). "Characterization of Magnetic Nanoparticles for Magnetic Particle Imaging by Magnetorelaxometry, AC Susceptibility, Magnetic Particle Spectroscopy and Static Magnetization Measurements". In: *Magnetic Particle Imaging*. Springer Proceedings in Physics. Springer Berlin Heidelberg, pp. 35–40.

Ludwig, Frank et al. (2014). "Self-consistent magnetic properties of magnetite tracers optimized for magnetic particle imaging measured by ac susceptometry, magnetorelaxometry and magnetic particle spectroscopy". In: *J. Magn. Magn. Mater.* 360.0, pp. 169–173.

Lyu, Xing et al. (2014). "Design and Optimization for a Novel Field Free Line Generation Magnet for Human Target Clinical MPI—A Preliminary Study". In: *IEEE Trans. Magn.* 50.11, pp. 1–4.

Marthin, June Kehlet et al. (2007). "Pulmonary radioaerosol mucociliary clearance in diagnosis of primary ciliary dyskinesia". In: *Chest* 132.3, pp. 966–976.

Matter, Nathaniel I et al. (2006). "Rapid polarizing field cycling in magnetic resonance imaging". In: *IEEE Trans. Med. Imaging* 25.1, pp. 84–93.

Mérida, Fernando et al. (2015). "Optimization of synthesis and peptization steps to obtain iron oxide nanoparticles with high energy dissipation rates". In: *J. Magn. Magn. Mater.* 394, pp. 361–371.

Mészáros, István (2007). "Development of a Novel Vibrating Sample Magnetometer". In: *MSF* 537-538, pp. 413–418.

Minard, Kevin R et al. (2013). "Magnetic particle detection (MPD) for in-vitro dosimetry". In: *Biosens. Bioelectron.* 43, pp. 88–93.

Munkholm, Mathias, Kim Gjerum Nielsen, and Jann Mortensen (2015). "Clinical value of measurement of pulmonary radioaerosol mucociliary clearance in the work up of primary ciliary dyskinesia". In: *EJNMMI Res.* 5.1, p. 118.

Murase, Kenya et al. (2013). "Control of the temperature rise in magnetic hyperthermia with use of an external static magnetic field". In: *Physica Medica* 29.6, pp. 624–630.

Murase, Kenya et al. (2014). "Development of a system for magnetic particle imaging using neodymium magnets and gradiometer". In: *Jpn. J. Appl. Phys.* 53.6, p. 067001.

Murase, Kenya et al. (2015). "Usefulness of Magnetic Particle Imaging for Predicting the Therapeutic Effect of Magnetic Hyperthermia". In: *Open Journal of Medical Imaging* 5.02, p. 85.

Newman, S P (1985). "Aerosol deposition considerations in inhalation therapy". In: *Chest* 88.2 Suppl, 152S–160S.

Nikolic, Boris et al. (2010). "Absorbed radiation dose in radiosensitive organs during coronary CT angiography using 320-MDCT: effect of maximum tube voltage and heart rate variations". In: *AJR Am. J. Roentgenol.* 195.6, pp. 1347–1354.

Nishimoto, Kohei et al. (2015). "Application of Magnetic Particle Imaging to Pulmonary Imaging Using Nebulized Magnetic Nanoparticles". In: *Open Journal of Medical Imaging* 5.02, p. 49.

Nohara, S et al. (2013). "Separation of Ferucarbotran: A leading candidate of MPI tracer for practical use". In: *Magnetic Particle Imaging (IWMPI), 2013 International Workshop on*, pp. 1–1.

Orendorff, Ryan et al. (2016). "First in vivo Brain Perfusion Imaging using Magnetic Particle Imaging". In: *2016 World Molecular Imaging Congress (WMIC 2016): Imaging Biology... Improving Therapy*. World Molecular Imaging Society (WMIS).

Orendorff, Ryan et al. (2017). "First in vivo traumatic brain injury imaging via magnetic particle imaging". In: *Phys. Med. Biol.* 62.9, pp. 3501–3509.

Perreard, I M et al. (2014a). "Temperature of the magnetic nanoparticle microenvironment: estimation from relaxation times". In: *Phys. Med. Biol.* 59.5, pp. 1109–1119.

Perreard, IM et al. (2014b). "Temperature of the magnetic nanoparticle microenvironment: estimation from relaxation times". In: *Physics in medicine and biology* 59.5, p. 1109.

Pouliquen, D et al. (1991). "Iron oxide nanoparticles for use as an MRI contrast agent: pharmacokinetics and metabolism". In: *Magn. Reson. Imaging* 9.3, pp. 275–283.

Prince, Jerry L and Jonathan M Links (2006). *Medical imaging signals and systems*. Pearson Prentice Hall Upper Saddle River, New Jersey.

Rahmer, J et al. (2011). "Rapid 3D in vivo magnetic particle imaging with a large field of view". In: *Proc. Int. Soc. Magn. Reson. Med. Sci. Meet. Exhib. Int. Soc. Magn. Reson. Med. Sci. Meet. Exhib.* 19, p. 3285.

Rahmer, J et al. (2015). "First experimental evidence of the feasibility of multi-color magnetic particle imaging". In: *Phys. Med. Biol.* 60.5, pp. 1775–1791.

Rahmer, Jürgen et al. (2009). "Signal encoding in magnetic particle imaging: properties of the system function". In: *BMC Med. Imaging* 9, p. 4.

— (2012). "Analysis of a 3-D system function measured for magnetic particle imaging". In: *IEEE Trans. Med. Imaging* 31.6, pp. 1289–1299.

Rahmer, Jurgen et al. (2017). "Interactive Magnetic Catheter Steering with 3D Real-Time Feedback Using Multi-Color Magnetic Particle Imaging". In: *IEEE Trans. Med. Imaging*.

Rauwerdink, Adam M and John B Weaver (2010). "Viscous effects on nanoparticle magnetization harmonics". In: *Journal of Magnetism and Magnetic Materials* 322.6, pp. 609–613.

Reeves, Daniel B and John B Weaver (2014). "Magnetic nanoparticle sensing: decoupling the magnetization from the excitation field". In: *J. Phys. D Appl. Phys.* 47.4, p. 045002.

Reilly, J P (1989). "Peripheral nerve stimulation by induced electric currents: exposure to time-varying magnetic fields". In: *Med. Biol. Eng. Comput.* 27.2, pp. 101–110.

Reimer, Peter and Thomas Balzer (2003). "Ferucarbotran (Resovist): a new clinically approved RES-specific contrast agent for contrast-enhanced MRI of the liver: properties, clinical development, and applications". In: *Eur. Radiol.* 13.6, pp. 1266–1276.

Rhoon, Gerard C van (2016). "Is CEM43 still a relevant thermal dose parameter for hyperthermia treatment monitoring?" In: *Int. J. Hyperthermia* 32.1, pp. 50–62.

Rhoon, Gerard C van et al. (2013). "CEM43C thermal dose thresholds: a potential guide for magnetic resonance radiofrequency exposure levels?" In: *Eur. Radiol.* 23.8, pp. 2215–2227.

Rieke, Viola and Kim Butts Pauly (2008). "MR thermometry". In: *J. Magn. Reson. Imaging* 27.2, pp. 376–390.

Rodrigues, Harley F et al. (2017). "Precise determination of the heat delivery during in vivo magnetic nanoparticle hyperthermia with infrared thermography". In: *Phys. Med. Biol.* 62.10, pp. 4062–4082.

Rosensweig, R E (2002a). "Heating magnetic fluid with alternating magnetic field". In: *J. Magn. Magn. Mater.* 252.Supplement C, pp. 370–374.

Rosensweig, Ronald E (2002b). "Heating magnetic fluid with alternating magnetic field". In: *Journal of magnetism and magnetic materials* 252, pp. 370–374.

Rueden, Curtis T et al. (2017). "ImageJ2: ImageJ for the next generation of scientific image data". In: *BMC Bioinformatics* 18.1, p. 529.

Salamon, Johannes et al. (2016). "Magnetic Particle / Magnetic Resonance Imaging: In-Vitro MPI-Guided Real Time Catheter Tracking and 4D Angioplasty Using a Road Map and Blood Pool Tracer Approach". In: *PLoS One* 11.6, e0156899.

Sarica, D and E U Saritas (2015). "Effects of field dependent relaxation time on x-space MPI images". In: *Magnetic Particle Imaging (IWMPI), 2015 5th International Workshop on*. ieeexplore.ieee.org, pp. 1–1.

Saritas, E U et al. (2013a). "Magnetostimulation Limits in Magnetic Particle Imaging". In: *IEEE Trans. Med. Imaging* 32.9, pp. 1600–1610.

Saritas, Emine U et al. (2013b). "Magnetic particle imaging (MPI) for NMR and MRI researchers". In: *J. Magn. Reson.* 229, pp. 116–126.

Schilling, Meinhard et al. (2013). "Magnetic particle imaging scanner with 10-kHz drive-field frequency". In: *Biomed. Tech.* 58.6, pp. 557–563.

Schindelin, Johannes et al. (2012). "Fiji: an open-source platform for biological-image analysis". In: *Nat. Methods* 9.7, pp. 676–682.

Schmale, I et al. (2011). "First phantom and in vivo MPI images with an extended field of view". In: *SPIE Medical Imaging*, pp. 796510–796510.

Schmidt, D et al. (2015). "A Phenomenological Description of the MPS Signal Using a Model for the Field Dependence of the Effective Relaxation Time". In: *IEEE Trans. Magn.* 51.2, pp. 1–4.

Schmitz, G et al. (2006). "1E-2 Experimental Characterization of Ferucarbotran (Resovist Â®) as a Photoacoustic Nanoparticle Contrast Agent". In: *Ultrasonics Symposium, 2006. IEEE*, pp. 393–396.

Schulz, Volkmar et al. (2015). "A Field Cancellation Signal Extraction Method for Magnetic Particle Imaging". In: *IEEE Trans. Magn.* 51.2 Pt 1.

Semmler, M et al. (2004). "Long-term clearance kinetics of inhaled ultrafine insoluble iridium particles from the rat lung, including transient translocation into secondary organs". In: *Inhal. Toxicol.* 16.6-7, pp. 453–459.

Shah, Saqlain A, R M Ferguson, and K M Krishnan (2014). "Slew-rate dependence of tracer magnetization response in magnetic particle imaging". In: *J. Appl. Phys.* 116.16, p. 163910.

Shahram, Morteza and Peyman Milanfar (2004). "Imaging below the diffraction limit: A statistical analysis". In: *IEEE Transactions on image processing* 13.5, pp. 677–689.

Shliomis, M and Yu L Raikher (1980). "Experimental investigations of magnetic fluids". In: *IEEE Trans. Magn.* 16.2, pp. 237–250.

Shliomis, M I (1974). "Magnetic fluids". In: *Soviet Physics Uspekhi* 17.2, p. 153.

Stehning, Christian, Bernhard Gleich, and Jürgen Rahmer (2016). "Simultaneous magnetic particle imaging (MPI) and temperature mapping using multi-color MPI". In: *International Journal on Magnetic Particle Imaging* 2.2.

Tamrazian, Arbi et al. (2011). "X-space MPI relaxometry: methods and initial data". In: *SPIE Medical Imaging*. International Society for Optics and Photonics, 79652K–79652K–6.

Tasci, T Onur et al. (2009). "Focused RF hyperthermia using magnetic fluids". In: *Medical physics* 36.5, pp. 1906–1912.

Tay, Zhi Wei et al. (2015a). "Untuned MPI relaxometer for nanoparticle characterization at arbitrary frequencies". In: *2015 5th International Workshop on Magnetic Particle Imaging (IWMPI)*. IEEE, pp. 1–1.

Tay, Zhi Wei et al. (2015b). "Untuned MPI relaxometer for nanoparticle characterization at arbitrary frequencies". In: *Magnetic Particle Imaging (IWMPI), 2015 5th International Workshop on*, pp. 1–1.

Tay, Zhi Wei et al. (2016). "A High-Throughput, Arbitrary-Waveform, MPI Spectrometer and Relaxometer for Comprehensive Magnetic Particle Optimization and Characterization." In: *Scientific reports* 6, p. 34180.

Tay, Zhi Wei et al. (2017). "The Relaxation Wall: Experimental Limits to Improving MPI Spatial Resolution by Increasing Nanoparticle Core size". In: *Biomed Phys Eng Express* 3.3.

Them, Kolja et al. (2016a). "Increasing the sensitivity for stem cell monitoring in system-function based magnetic particle imaging". In: *Phys. Med. Biol.* 61.9, pp. 3279–3290.

Them, Kolja et al. (2016b). "Sensitivity Enhancement in Magnetic Particle Imaging by Background Subtraction". In: *IEEE Trans. Med. Imaging* 35.3, pp. 893–900.

Thiesen, Burghard and Andreas Jordan (2008). "Clinical applications of magnetic nanoparticles for hyperthermia". In: *International Journal of Hyperthermia* 24.6, pp. 467–474.

Tomitaka, Asahi et al. (2015). "Variation of Magnetic Particle Imaging Tracer Performance With Amplitude and Frequency of the Applied Magnetic Field". In: *IEEE Trans. Magn.* 51.2.

Toraya-Brown, Seiko et al. (2014). "Local hyperthermia treatment of tumors induces CD8(+) T cell-mediated resistance against distal and secondary tumors". In: *Nanomedicine* 10.6, pp. 1273–1285.

Torres-Lugo, Madeline and Carlos Rinaldi (2013). "Thermal potentiation of chemotherapy by magnetic nanoparticles". In: *Nanomedicine* 8.10, pp. 1689–1707.

Travis, Elizabeth L (1987). "Relative Radiosensitivity of the Human Lung". In: *Advances in Radiation Biology*. Ed. by John T Lett and Kurt I Altman. Vol. 12. Elsevier, pp. 205–238.

Turner, R (1993). "Gradient coil design: a review of methods". en. In: *Magn. Reson. Imaging* 11.7, pp. 903–920.

Utkur, M and E U Saritas (2015). "Comparison of different coil topologies for an MPI relaxometer". In: *Magnetic Particle Imaging (IWMPI), 2015 5th International Workshop on*. ieeexplore.ieee.org, pp. 1–1.

Vogel, P et al. (2015a). "Superspeed Traveling Wave Magnetic Particle Imaging". In: *IEEE Trans. Magn.* 51.2, pp. 1–3.

Vogel, Patrick (2014). "Ultra HIgh Resolution MPI". In: *Magnetic Particle Imaging IWMPI 2014*, p. 68.

Vogel, Patrick et al. (2014). "Traveling wave magnetic particle imaging". In: *IEEE Trans. Med. Imaging* 33.2, pp. 400–407.

Vogel, Patrick et al. (2015b). "MPI—Initial Experiments With an Ultrahigh Resolution MPI". In: *IEEE Trans. Magn.* 51.2, pp. 1–4.

Vreeland, Erika C et al. (2015). "Enhanced Nanoparticle Size Control by Extending LaMers Mechanism". In: *Chem. Mater.* 27.17, pp. 6059–6066.

Wang, Yi-Xiang J (2011). "Superparamagnetic iron oxide based MRI contrast agents: Current status of clinical application". In: *Quant. Imaging Med. Surg.* 1.1, pp. 35–40.

Wawrzik, Thilo, Frank Ludwig, and Meinhard Schilling (2010). "Multivariate Magnetic Particle Spectroscopy for Magnetic Nanoparticle Characterization". In: *8th International Conference on the Scientific and Clinical Applications of Magnetic Carriers*. Vol. 1311. AIP Publishing, pp. 267–270.

Weaver, John B, Adam M Rauwerdink, and Eric W Hansen (2009). "Magnetic nanoparticle temperature estimation". In: *Med. Phys.* 36.5, pp. 1822–1829.

Webb, Andrew (2007). "Nuclear magnetic resonance of mass-limited samples using small RF coils". In: *Anal. Bioanal. Chem.* 388.3, pp. 525–528.

Weers, Jeffry et al. (2009). "A gamma scintigraphy study to investigate lung deposition and clearance of inhaled amikacin-loaded liposomes in healthy male volunteers". In: *J. Aerosol Med. Pulm. Drug Deliv.* 22.2, pp. 131–138.

Weissleder, R et al. (1989). "Superparamagnetic iron oxide: pharmacokinetics and toxicity". In: *AJR Am. J. Roentgenol.* 152.1, pp. 167–173.

Weizenecker, J et al. (2009). "Three-dimensional real-time in vivo magnetic particle imaging". In: *Phys. Med. Biol.* 54.5, pp. L1–L10.

Weizenecker, Jürgen et al. (2010). "Particle Dynamics of Mono-domain Particles in Magnetic Particle Imaging". In: *Magnetic Nanoparticles*. World Scientific, pp. 3–15.

— (2012). "Micro-magnetic simulation study on the magnetic particle imaging performance of anisotropic mono-domain particles". In: *Phys. Med. Biol.* 57.22, p. 7317.

Werner, F, N Gdaniec, and T Knopp (2017). "First experimental comparison between the Cartesian and the Lissajous trajectory for magnetic particle imaging". In: *Phys. Med. Biol.* 62.9, pp. 3407–3421.

Wilhelm, Stefan et al. (2016). "Analysis of nanoparticle delivery to tumours". In: *Nature Reviews Materials* 1, p. 16014.

Yarmolenko, Pavel S et al. (2011). "Thresholds for thermal damage to normal tissues: an update". In: *Int. J. Hyperthermia* 27.4, pp. 320–343.

Yu, E Y, P W Goodwill, and S M Conolly (2015). "Preliminary characterization of a laminated iron-core 6.3 T/m FFL magnet". In: *Magnetic Particle Imaging (IWMPI), 2015 5th International Workshop on*. ieeexplore.ieee.org, pp. 1–1.

Yu, Elaine et al. (2016). "First demonstration of in vivo Cancer Magnetic Particle Imaging with IV-administered Passive Long-circulating SPIOs". In: *2016 World Molecular Imaging Congress (WMIC 2016): Imaging Biology... Improving Therapy*. World Molecular Imaging Society (WMIS).

Yu, Elaine Y et al. (2017a). "Magnetic Particle Imaging: A Novel in Vivo Imaging Platform for Cancer Detection". In: *Nano Lett.* 17.3, pp. 1648–1654.

Yu, Elaine Y et al. (2017b). "Magnetic Particle Imaging for Highly Sensitive, Quantitative, and Safe in Vivo Gut Bleed Detection in a Murine Model". In: *ACS Nano* 11.12, pp. 12067–12076.

Zaremba, L (2001). "FDA guidance for MR system safety and patient exposures: current status and future considerations". In: *magnetic resonance procedures: health effects and safety. CRC Press, Boca Raton*, pp. 183–196.

Zheng, Bo et al. (2015). "Magnetic Particle Imaging tracks the long-term fate of in vivo neural cell implants with high image contrast". In: *Sci. Rep.* 5, p. 14055.

Zheng, Bo et al. (2016). "Quantitative Magnetic Particle Imaging Monitors the Transplantation, Biodistribution, and Clearance of Stem Cells In Vivo". In: *Theranostics* 6, pp. 291–301. ISSN: 3.

Zheng, Bo et al. (2017). "Seeing SPIOs Directly In Vivo with Magnetic Particle Imaging". In: *Mol. Imaging Biol.* 19.3, pp. 385–390.

Zhou, Xinyi Y et al. (2017). "First in vivo magnetic particle imaging of lung perfusion in rats". In: *Phys. Med. Biol.* 62.9, pp. 3510–3522.